Cavity QED in Microsphere and Fabry-Perot Cavities

Thesis by

Joseph R. Buck, Jr.

In Partial Fulfillment of the Requirements
for the Degree of
Doctor of Philosophy

California Institute of Technology
Pasadena, California

2003
(Defended May 7, 2003)

© 2003
Joseph R. Buck, Jr.
All Rights Reserved

Acknowledgements

I want to sincerely thank Jeff Kimble for his many years of guidance. He has been a wonderful mentor and provided me an incredible opportunity to be a part of his group. I am always impressed by his integrity in the pursuit of science as well as his enthusiasm for tackling difficult scientific problems. I have learned so much from Jeff and will always be grateful for the profoundly positive impact he has had on my scientific development.

I have benefited immensely from working directly on experiments with Jason Mckeever, Theresa Lynn, Kevin Birnbaum, Akira Furusawa, and Alex Kuzmich. I have also learned a great deal from working on theoretical projects with Steven van Enk and Chris Fuchs. Additionally, I would also like to thank the other members of Jeff's group that I have been fortunate to have constant interaction with during my time here: Andreea Boca, David Boozer, Warwick Bowen, Mike Chapman, Chin-wen Chou, Andrew Doherty, Nikos Georgiades, Kok Win Goh, Christina Hood, Wolfgang Lange, Ron Legere, Peter Lodahl, Hideo Mabuchi, Christoph Nagerl, Tracy Northup, Dominik Schrader, Jens Sorensen, Dan Stamper-Kurn, Quentin Turchette, David Vernooy, Jun Ye, and Tiancai Zhang. It is really quite amazing to think of the incredible group of people that have gone through Jeff's group. I hope that they have enjoyed my company as much as I have enjoyed theirs.

I would like to give a special thanks to Ron and Steven for becoming such great friends and to Glov Boi for the many hours of entertainment he has provided.

Finally, I would like to thank my wife, Jamie, for her continuous love and support during these years, and my parents for having always been supportive of my inquisitive nature.

Abstract

A long-standing ambition in the field of cavity quantum electrodynamics has been to trap single atoms inside high-Q cavities in a regime of strong coupling. Our goal has been to develop techniques for trapping that are compatible with strong coupling and that do not interfere with the cavity QED interactions. This is crucial for applications to quantum computation and communication. We have accomplished this goal by creating a trapping potential through an intracavity FORT at the 'magic' wavelength for Cesium, 935.6 nm. Unlike typical FORTs, where the signs of the AC-Stark shifts for excited and ground states are opposite, our trap causes small shifts to the relevant transition frequencies, enabling a trapping potential for the center-of-mass motion that is largely independent of the internal atomic state. This has enabled us to achieve extended trapping times ($\sim$ 3 sec) for individual Cesium atoms in cavity QED in a regime of strong coupling. Although our longest lifetimes are obtained when the probing fields are turned off, the atoms can also be continuously monitored, leading to mean trapping times of 0.4 sec, with some atoms observed for over 1 sec.

An important tool for studying atom-field interactions is a high-Q cavity with small mode volume. Considerable effort has been made in advancing our capabilities for high-Q resonators. While much of our work involves Fabry-Perot cavities, some of the highest quality optical resonators to date have been achieved with the whispering gallery modes (WGMs) of quartz microspheres ($Q \sim 8 \times 10^9$). Therefore, considerable effort has been given to understanding the usefulness of microspheres for cavity QED with strong coupling. We have also worked at manufacturing high-Q microspheres suitable for cavity QED. To this end, we have been succesful at making spheres with radius ~ 10 μm and $Q \sim 10^7$.

Contents

Acknowledgements **iii**

Abstract **v**

1 Introduction **1**

1.1 Background 1

1.2 A History of My Involvement in the Kimble Group 2

1.3 Electronics Projects 4

1.4 Organization of the Thesis 5

I Atom-Field Interactions **7**

2 Semiclassical Theory **11**

2.1 Hamiltonian 11

2.2 Dipole Approximation and Radiation Gauge 12

2.3 Rabi Oscillations 13

3 Quantum Theory **19**

3.1 Hamiltonian 19

3.2 The Jaynes-Cummings Ladder 22

4 Critical Parameters for Strong Coupling **25**

4.1 Electromagnetic Mode Volume 26

4.2 Strong Coupling Regime 27

4.3 Saturation Photon Number 28

4.4 Critical Atom Number 29
4.5 Cavity Length and the Critical Parameters 30

II Realizing Strong Coupling with Cesium in Fabry-Perot Cavities 37

5 The Cavity 41
5.1 Cavity Transmission and Losses 43
5.2 Modes of a Fabry-Perot Cavity 45
5.3 Cavity Length Stabilization 46

6 Delivering Cold Atoms to the Cavity 49
6.1 The Vacuum System 52
  6.1.1 Gas Flow in a Vacuum System 52
  6.1.2 Analysis of Gas Flow in Our Vacuum System 55
  6.1.3 Relation of Pressure to Kinetic Properties of Particles 59
  6.1.4 Mean-Free Path and Collision Times 60
  6.1.5 Collisional Lifetime for Background in Our System 61
6.2 Magneto-Optical Traps 62
  6.2.1 Optical Molasses 62
  6.2.2 Magneto-Optical Trap 64
  6.2.3 Sub-Doppler Cooling in a MOT 66

7 Dipole Force Traps 71
7.1 Classical Dipole Force 71
7.2 Two-Level Atom 72
7.3 Multi-Level Alkali Atoms 74
7.4 State Insensitive Trap 74
7.5 Trap Vibrational Frequencies 77
7.6 Scattering Processes and Population Transfer in the FORT 79
7.7 Heating Due to FORT Intensity Fluctuations 79

8 Realizing Trapping with an Intracavity FORT 83

8.1 The Experimental Setup 84

8.1.1 Delivering Atoms to the Cavity Mode Volume 87

8.1.2 Atom Transits 89

8.2 Trapping in an 869 nm FORT 91

8.3 Trapping in a 906 nm FORT 91

8.4 Trapping in a 936 nm FORT 92

8.5 Continuous Observation of Trapped Atoms 96

III Cavity QED with Dielectric Microspheres 103

9 Electromagnetic Properties of Dielectric Spheres 107

9.1 Modes of a Microsphere 107

9.2 Electromagnetic Mode Volume 110

9.3 Losses in Dielectric Spheres 113

9.3.1 Intrinsic Radiative Losses 114

9.3.2 Material Loss Mechanisms 115

10 Strong Coupling with Dielectric Spheres 125

10.1 The Strong Coupling Regime 125

10.2 Strong Coupling with Cesium 127

10.3 Progress in Small Sphere Manufacture 129

10.4 Comparing Microspheres and Fabry-Perot Cavities 130

IV Brownian Motion of Mirrors in High-Finesse Fabry-Perot Cavities 141

11 Brownian Motion and Harmonic Oscillators 145

11.1 Effect of Displacement on Cavity Output 145

11.1.1 Fabry-Perot Finesse 145

11.1.2 Power Fluctuations for Length Changes 146

11.1.3 Important Assumptions 146
11.2 Simple Harmonic Oscillator in Thermodynamic Equilibrium 147
11.2.1 Classical Harmonic Oscillator 148
11.2.2 Quantum Harmonic Oscillator 148
11.2.3 Effective Mass Coefficients 149
11.3 Spectral Density Function for Displacement 150
11.3.1 Velocity Damping 150
11.3.2 Structural Damping 151
11.4 Measuring Brownian Motion in Fabry-Perot Cavities 152
11.4.1 Shot Noise in Photodetectors 152
11.4.2 Measuring Displacements Due to Brownian Motion 153
11.4.3 Sensitivity of the Mechanical System 154

12 Normal Modes of Oscillation and Cavity Output 157

12.1 Normal Modes of a Cylinder 158
12.1.1 Longitudinal Modes of a Bar 158
12.1.2 Wave Equation in an Elastic Cylinder 162
12.1.3 Corrections to Cylinder Modes 163
12.1.4 Finite Element Analysis for a Cylinder 166
12.2 Normal Modes of Our Mirrors 167

V Applications of Cavity QED to Communication Theory: Superadditivity 175

13 Superadditivity for a Binary Quantum Alphabet: Introduction 177

14 Deriving Superadditivity for Two-Shot Collective Measurements 181

14.1 Quantum Shannon Noisy Coding Theorem 181
14.2 Limiting Cases for C_n 182
14.3 R_2: Rate for Two-Shot Collective Measurements 183
14.4 Measurement Basis and Limit for R_2 187

15 Experimental Proposal for Achieving Superadditivity 191

15.1 Basis for Experiment 191

15.2 Experimental Protocol 193

15.2.1 Mapping the Photon States to an Atom 194

15.2.2 Transforming the Measurement Basis 195

15.2.3 Measuring the Projection in the Physical Basis 196

Bibliography 197

List of Figures

3.1 The Jaynes-Cummings Ladder 23
3.2 Vacuum-Rabi Splitting 24

4.1 Progress in Strong Coupling 32
4.2 Electromagnetic Mode Volume for a Fabry-Perot Cavity 33
4.3 Critical Parameters in Cavity QED 34
4.4 Coupling Coefficient for a Fabry-Perot Cavity 35

5.1 Geometry of Our Mirrors 42
5.2 The Cavity 44

6.1 Schematic for Differential Vacuum System 50
6.2 Vacuum Chamber for Our Experiment 51
6.3 Relating Conductance, Throughput and Pumping Speed for a Tube . . 54
6.4 A Simple Model for Gas Flow in Our System 58
6.5 Force on an Atom in Counterpropagating Red-Detuned Fields 65
6.6 Restoring Force in a MOT 67
6.7 Polarization Gradient Cooling 69

7.1 Simplified Illustration of the ‘Magic’ Wavelength 76
7.2 AC Stark Shifts for Cesium in a Linear FORT 78
7.3 Depolarization of State Populations in Our FORT 81

8.1 Schematic of the Trapping Experiment 85
8.2 Optical Layout for the Trapping Experiment 86
8.3 Lab 11 Trapping Experiment 88

8.4 Transits from the Upper and Lower MOTs 90
8.5 Lifetime Plot for our 906 nm FORT 93
8.6 Lifetime Plots for our 935.6 nm FORT 95
8.7 Continuous Observation of a Trapped Atom 98
8.8 Observing the Number of Intracavity Atoms 99
8.9 Lifetime Plots for One and Two Intracavity Atoms 100
8.10 Determining the Optimal Detuning for Intracavity Cooling 101

9.1 Mode Function for a Dielectric Microsphere 109
9.2 Electromagnetic Mode Volume and the Cutoff Parameter 111
9.3 Dimensionless Volume Parameter 118
9.4 Electromagnetic Mode Volume for a Dielectric Microsphere 119
9.5 Index of Refraction for Fused Silica 120
9.6 Radiative Quality Factors for Dielectric Microspheres 121
9.7 Quality Factor Due to Bulk Absorption 122
9.8 Quality Factors for Dielectric Microspheres 123

10.1 Dimensionless Parameter β 133
10.2 Dimensionless Parameter $\frac{1}{\sqrt{\beta}}$ 134
10.3 Coupling Coefficient for Dielectric Microspheres 135
10.4 Saturation Photon Number for Microsphere Resonators 136
10.5 Critical Atom Number for Microsphere Resonators 137
10.6 Comparison of the Critical Parameters for Microsphere Resonators . . 138
10.7 Comparison of Microsphere and Fabry-Perot Cavities 139

12.1 Spectral Density Function for a Bar 160
12.2 Thermal Displacement Noise for a Bar 161
12.3 Spectral Density Function for Elastic Modes of a Cylinder 164
12.4 Thermal Displacement Noise for Elastic Modes of a Cylinder 165
12.5 Spectral Density Function for Modes of a Cylinder 168
12.6 Thermal Displacement Noise for Modes of a Cylinder 169

12.7 Geometry of Our Mirrors 171
12.8 Spectral Density Function for Modes of Our Mirror 172
12.9 Thermal Displacement Noise for Modes of Our Mirror 173
12.10 Comparison of Calculated and Measured Thermal Noise 174

13.1 C_∞/C_1 for Nonorthogonal States 179

14.1 Effective Alphabet Projection 186
14.2 Comparison of Superadditivity 188
14.3 Difference in Communication Rates $(R_2 - C_1)$ 189

15.1 Transition Diagram for Experimental Implementation 194

Chapter 1

Introduction

1.1 Background

The last decade has seen an incredible number of advances in quantum information science. The areas of quantum computation and communication have grown into mature fields with many research fronts. These advances have benefited from the progress in atomic and optical physics made possible by the realization of optical trapping and cooling techniques.

Our ultimate goal is to study the interaction of individual atoms and photons. The model for single atom-photon interactions in a regime of strong coupling was described by E. T. Jaynes and F. W. Cummings forty years ago [1]. However, the experimental realization of this model with trapped atoms has only been achieved relatively recently [2]. We accomplish this by trapping individual atoms inside a high-Q Fabry-Perot cavity in a regime of strong coupling [3]. Diverse avenues have been pursued for creating the trapping potential for atom confinement, including the use of additional far off-resonant trapping beams [2, 4] and of the cavity QED light itself [5, 6]. Our goal has been to develop techniques for trapping that are compatible with strong coupling and that do not interfere with the cavity QED interactions. This is crucial for applications to quantum computation and communication [7, 8, 9, 10, 11, 12].

Our trapping potential was provided by an intracavity FORT at the ‘magic’ wavelength for Cesium, 935.6 nm [13, 14, 15, 16]. Unlike typical FORTs, where the signs of the AC-Stark shifts for excited and ground states are opposite, our trap causes small shifts to the relevant transition frequencies, enabling a trapping potential for the center-of-mass motion that is largely independent of the internal atomic state. This has enabled us to achieve extended trapping times (~ 3 sec) for individual Cesium atoms in cavity QED in a regime of strong coupling. Although our longest lifetimes are obtained when the probing fields are turned off, the atoms can also be continuously monitored, leading to mean trapping times of 0.4 sec, with some atoms observed for over 1 sec. This trap represents an improvement by a factor of 10^2 beyond the first realization of trapping in cavity QED [2], and by roughly 10^4 beyond prior results for atomic trapping [5] and localization [6] by way of the cavity QED field itself.

An important tool for studying atom-field interactions is a high-Q cavity with small mode volume. Considerable effort has been made by Jeff's group to advance our capabilities for high-Q resonators. While much of our work involves Fabry-Perot cavities, some of the highest quality optical resonators to date have been achieved with the whispering gallery modes (WGMs) of quartz microspheres ($Q \sim 8 \times 10^9$) [17, 18]. Therefore, considerable effort has been given to understanding the usefulness of microspheres for cavity QED with strong coupling. We have also worked at manufacturing high-Q microspheres suitable for cavity QED. To this end, we have been succesful at making spheres with radius ~ 10 μm and $Q \sim 10^7$.

1.2 A History of My Involvement in the Kimble Group

I joined Jeff's group in the Fall of 1996. It was an exciting time, with the recent advances in quantum computation and information theory. My first task was to work with a visiting scientist, Akira Furusawa, on a project to develop an apparatus for performing Raman Spectroscopy on trapped Cesium atoms. We realized that we would need several lasers for the metrology beams and MOT. Unhappy with the current electronics and mechanical setup of our homemade diode laser systems, I spent some time improving the system. This ended up being a side project of mine for the rest of my time at Caltech. Along the way, there were significant contributions made by postdocs Jun Ye and Christoph Nagerl.

Akira became interested in Quantum Teleportation and began to pursue that while I began to work on microspheres. Hideo Mabuchi had started this work in the group, and it was continued by David Vernooy along with Erik Streed, Akira Furusawa, and Nikos Georgiades [19, 18, 20]. We also benefited from continued interaction with Vladimir Ilchenko. My work focused on understanding the limits of microspheres for achieving cavity QED in the strong coupling regime. We investigated this theoretically while I worked on manufacturing and testing small spheres (radius $\sim 10\ \mu$m) with high quality factors (Q$\sim 10^7$).

During this time, I became interested in quantum communication theory, and began working on a project with two postdocs, Steven van Enk and Chris Fuchs. We devised an experimental proposal for achieving superadditive communication capacities with a binary quantum alphabet [21]. The hope was to develop a protocol that could be implemented in the atom-cavity system that already existed in the group. While this work represents an important step in understanding the use of entanglement to improve detection sensitivity, the effect is small and would be difficult to implement in our current system.

Akira and Jens succeeded in achieving the first unconditional quantum teleportation of an optical coherent state, by utilizing squeezed-state entanglement. After they left, I switched to the teleportation experiment to continue their work. Akira visited to help me, and we finally worked directly together on an experiment.

After this I moved to Lab 1 to work with Theresa Lynn and Kevin Birnbaum on a cavity QED experiment. The hope was to achieve continuous feedback control for the dynamics of an atom trapped in a high finesse Fabry-Perot cavity. Unfortunately, the experiment developed problems requiring a new cavity and vacuum system. At that point the decision was made to rebuild the experiment in a dual chamber configuration as had been implemented in Lab 11.

The cavity QED experiment in Lab 11 had been rebuilt by David Vernooy and Jun Ye. Their work involved using an intracavity FORT at 869 nm to trap single atoms with a lifetime of $\tau \sim 28$ ms. This work was then continued by Jason McKeever, and two postdocs, Dan Stamper-Kurn and Christoph Nagerl. After Dan and Christoph left, Kevin and I joined Jason part-time to continue the work. In addition, a new post-doc, Alex Kuzmich, joined the experiment. Kevin eventually went back to Lab 1 full-time and Alex pursued a different experiment in Lab 2. Jason and I worked many long hours continuing the experiment before finally achieving our first successful advance with a 906 nm FORT. While toiling away on the experiment, we managed to keep each other entertained and even refined our French. The Lab 11 experiment is now being continued by Jason, Dave Boozer, and Andreea Boca.

1.3 Electronics Projects

During my time in Jeff's group, I have spent a great deal of time improving the electronics we use for conducting our experiments. This work is well documented in my 'electronics notebook' and will not be reproduced in this thesis. In this section, I will describe some of the work that is documented there.

The diode laser systems we use in our group have continuously evolved over time. There are three main components to the system: the current controller, temperature controller, and FET modulation board. The current controllers can be traced back to the work of K. G. Libbrecht and J. L. Hall [22]. I made some improvements to the circuit and generalized it to act as either a current source or sink depending on the particular laser diode being used. The temperature controllers can be traced back to the work of Bradley et al. [23]. The FET modulation board is used for high-speed feedback to the laser diode. This type of circuit was first implemented by Christoph Nagerl. I improved the circuit and designed a board that incorporates the laser diode protection circuitry. This board has a 3 dB point of ~ 5.5 MHz, so the bandwidth will be limited by the capacitance of the laser diode. Overall, I am pleased with the system, however, if I was going to spend time on one of the elements, it would be the temperature control.

Another useful circuit for the lab is a high-voltage offset controller. This is useful for applying a voltage offset to PZTs used for length and angle control. Christoph first used high-voltage DC-DC converters for this purpose, and I designed a board incorporating these and filtering for the output.

Jun Ye and I worked on making high-speed photodetectors ($\sim$ 280 MHz) to be used for balanced heterodyning in our experiments. Now many people use these detectors for performing the RF-locking of a laser to Cesium. While these circuits are overkill for this purpose, they are relatively easy to mass produce, since we have many of these boards and all of the components.

Another circuit I will mention here is a rate meter for pulses from the photon counting modules we have recently incorporated into our cavity QED experiment. This circuit is essentially an integrator. However, our purposes require a low-noise, high-speed circuit. This is due to the nature of the pulses (width$\sim$ 33 ns, height$\sim$ 4.3 V) and the low rates we require. The circuit has a buffered output, so the photon counting module can be hooked up to the rate meter box as well as a counting card in the computer. While the data stored by the computer provides a complete record of the pulse arrival time, the rate meter output provides a real-time signal that can be used for control of the experiment. This circuit is documented in my Lab notebook.

1.4 Organization of the Thesis

This thesis is comprised of five parts. There is a little redundancy in the material covered in some of the parts, allowing each to be read independently. Part I is an overview of atom-photon interactions with emphasis on the strong coupling regime of an atom-cavity system. The chapters comprising Part I are not intended to be an exhaustive exposition on the topic, but rather provide a consistent framework for the work presented throughout the rest of this thesis.

Part II describes our recent work in implementing an intracavity FORT at the ‘magic’ wavelength of 935.6 nm [13, 14, 15, 16]. This has allowed us to achieve extended trapping times ($\sim$ 3 sec) for individual Cesium atoms in cavity QED in a regime of strong coupling by realizing a trapping potential for the center-of-mass motion that is largely independent of the internal atomic state. This has also facilitated the demonstration of a scheme for extended continuous observation of a strongly coupled trapped atom. The mean trapping time for a continuously observed atom is ~ 0.4 sec, with some atoms observed for over 1 sec.

An important tool for studying atom-field interactions is a high-finesse cavity with small mode volume. The work described in Part II utilized a Fabry-Perot cavity. However, some of the highest quality optical resonators to date have been achieved with the whispering gallery modes (WGMs) of quartz microspheres [17, 18], making them a natural candidate for use in cavity QED. Part III describes our work [24] towards understanding the limits of microspheres for cavity QED in the strong coupling regime. In addition, details are given about the fabrication of small microspheres with radii $a \sim 10\mu$m. The experimental results for Q are compared with those from our theoretical analysis. We also present a detailed comparison for the state of the art and future prospects for achieving strong coupling in cavity QED for both microsphere and Fabry-Perot cavities.

Part IV describes an interesting problem that arose during our work to trap single atoms in a Fabry-Perot cavity. It turns out that our system is sensitive to the thermally excited motion of the cavity mirrors. We were able to see these effects in our system, and the results have been confirmed by Theresa and Kevin in a similar cavity setup. While thermal noise is important in many mechanical measurements [25], it was not obvious that it would be important in our intracavity FORT trapping experiments.

Finally, Part V describes an experimental proposal for achieving superadditive communication capacities with a binary quantum alphabet [21]. This work represents an important step in understanding the use of entanglement to improve detection sensitivity.

Part I

Atom-Field Interactions

The chapters comprising Part I are not intended to be an exhaustive exposition on the topic of atom-field interactions. Instead they are meant to give an overview and provide a consistent framework for the notation used throughout the rest of this thesis.

An effort is made to show the difference between the quantum and semiclassical theories of atom-field interactions involving the electromagnetic field. The semiclassical theory uses a classical electromagnetic field coupled to a quantized atom. Many situations including most aspects of the photoelectric effect can be understood using the semiclassical theory. In the full quantum theory, quantum mechanics is used for both the light and the atoms. This was first discussed by Dirac [26]. The semiclassical theory sometimes yields the same results as the completely quantum mechanical calculation. However, the semiclassical theory has the advantage that the radiative processes can be treated in terms of classical models.

An important tool for studying atom-field interactions is a high-finesse cavity with small mode volume. The properties of Fabry-Perot cavities are detailed in Part II, and the properties of microsphere resonators are detailed in Part III. With a sufficiently small mode-volume and cavity loss rate, we will see that the single-photon Rabi frequency for a single, two-level atom coupled to the cavity can be made much larger than the cavity and atomic decay rates. In this regime, the atom is said to be strongly coupled to the cavity.

For an atom in the strong coupling regime, there are two parameters that become useful for characterizing the atom-cavity system. These are the saturation photon number and the critical atom number. The saturation photon number is the number of photons required to saturate the atomic transition. The critical atom number corresponds to the number of intracavity atoms required to have an appreciable effect on the transmission of a probe through the cavity. In the strong coupling regime, these parameters are less than unity. In a system with both parameters much less than unity, the interaction of an individual atom and photon can be nonlinear.

Chapter 2

Semiclassical Theory

A two-state description of an atom coupled to a single mode of the electromagnetic field is valid if the two atomic states are resonant or nearly resonant with the driving field and all other fields are highly detuned. Here I will discuss the semiclassical theory of the interaction of an individual two-state atom coupled to a single mode of the field. In the semiclassical treatment, the atom is treated as a quantum two-state system and the field is treated classically.

The two-state atom is analogous to a spin-$\frac{1}{2}$ system with two possible states. In the dipole approximation, when the field wavelength is larger than the atomic size, the atom-field interaction is mathematically equivalent to a spin-$\frac{1}{2}$ particle interacting with a time-dependent magnetic field. The particle then undergoes optical Rabi oscillations under the action of the driving electromagnetic field. If there is atomic decay, the oscillations are damped.

2.1 Hamiltonian

The Hamiltonian for an electron of charge e and mass m is given as [27]

$$H = \frac{1}{2m}\left[\mathbf{p} - e\mathbf{A}(\mathbf{r},t)\right]^2 + eU(\mathbf{r},t) + V(r), \tag{2.1}$$

where $\mathbf{p}$ is the momentum operator, $\mathbf{A}(\mathbf{r},t)$ is the vector potential of the external field, $U(\mathbf{r},t)$ is the scalar potential of the external field, and $V(r)$ is the electrostatic potential (typically the atomic binding potential). $\mathbf{A}(\mathbf{r},t)$ and $U(\mathbf{r},t)$ are the gauge dependent potentials. The gauge independent quantities are the electric and magnetic fields

$$\mathbf{E} = -\nabla U - \frac{\partial \mathbf{A}}{\partial t}, \tag{2.2}$$

$$\mathbf{B} = \nabla \times \mathbf{A}. \tag{2.3}$$

2.2 Dipole Approximation and Radiation Gauge

If we work in the radiation gauge, we have the following for the potentials of the external field

$$U(\mathbf{r},t) = 0, \tag{2.4}$$

and

$$\nabla \cdot \mathbf{A} = 0. \tag{2.5}$$

$\mathbf{p} = -i\hbar\nabla$ and Equation 2.5 imply that

$$[\mathbf{p}, \mathbf{A}] = 0. \tag{2.6}$$

Schrödinger's Equation is

$$H\psi(\mathbf{r},t) = i\hbar\frac{\partial \psi(\mathbf{r},t)}{\partial t}, \tag{2.7}$$

where H is now given by

$$H = -\frac{\hbar^2}{2m}\left[\nabla - \frac{ie}{\hbar}\mathbf{A}(\mathbf{r}_0,t)\right]^2 + V(r). \tag{2.8}$$

We now define a new wave function $\phi(\mathbf{r},t)$ as

$$\psi(\mathbf{r},t) = \exp\left[\frac{ie}{\hbar}\mathbf{A}(\mathbf{r}_0,t)\cdot\mathbf{r}\right]\phi(\mathbf{r},t). \tag{2.9}$$

Substituting this into Schrödinger's Equation above yields

$$i\hbar\left[\frac{ie}{\hbar}\frac{\partial \mathbf{A}}{\partial t}\cdot\mathbf{r}\phi(\mathbf{r},t)+\frac{\partial\phi(\mathbf{r},t)}{\partial t}\right]=\left[\frac{p^2}{2m}+V(r)\right]\phi(\mathbf{r},t) \tag{2.10}$$

Equations 2.2 and 2.4 imply that $\mathbf{E}=-\frac{\partial A}{\partial t}$. Therefore, rearranging Equation 2.10 we now have

$$i\hbar\frac{\partial\phi(\mathbf{r},t)}{\partial t}=\left[\frac{p^2}{2m}+V(r)-e\mathbf{r}\cdot\mathbf{E}(\mathbf{r}_0,t)\right]\phi(\mathbf{r},t). \tag{2.11}$$

Therefore, the Hamiltonian can now be expressed as

$$H=\frac{p^2}{2m}+V(r)-e\mathbf{r}\cdot\mathbf{E}(\mathbf{r}_0,t). \tag{2.12}$$

This Hamiltonian is obtained from the radiation gauge Hamiltonian above by applying the gauge transformation $\xi(\mathbf{r},t)=-\frac{e}{\hbar}\mathbf{A}(\mathbf{r}_0,t)\cdot\mathbf{r}$. It can be expressed as the sum of an unperturbed Hamiltonian H_{un} and an interaction Hamiltonian H_{int} where

$$H=H_{\text{un}}+H_{\text{int}}, \tag{2.13}$$

where

$$\begin{aligned} H_{\text{un}} &= \frac{p^2}{2m}+V(r), && (2.14)\\ H_{\text{int}} &= -e\mathbf{r}\cdot\mathbf{E}(\mathbf{r}_0,t). && (2.15)\end{aligned}$$

2.3 Rabi Oscillations

Now consider the interaction of a single-mode radiation field of angular frequency ω_{field} with a two-state atom. Let $|g\rangle$ be the ground state and $|e\rangle$ the excited state of the two-state atom. These are the eigenstates of the unperturbed Hamiltonian, H_{un}, of Equation 2.14. The eigenvalues are E_g and E_e for the ground and excited states respectively. The wave function can now be expressed as a superposition of these eigenstates

$$|\psi(t)\rangle = C_g(t)|g\rangle + C_e(t)|e\rangle, \tag{2.16}$$

where C_g and C_e are the probability amplitudes for finding the atom in the ground and excited states respectively.

The completeness theorem implies that $|g\rangle\langle g| + |e\rangle\langle e| = \mathbf{1}$. Therefore, the unperturbed Hamiltonian of Equation 2.14 can be expressed as

$$H_{un} = E_g|g\rangle\langle g| + E_e|e\rangle\langle e|, \tag{2.17}$$

where E_g and E_e are the energies of the ground and excited states, respectively. The angular frequency for the atomic transition, ω_{atom}, would then be given by

$$\omega_{\text{atom}} = \frac{E_e - E_g}{\hbar}. \tag{2.18}$$

In the dipole approximation we can express the field as $E(t) = E_0\cos(\omega_{\text{field}}t)$, where E_0 is the amplitude and ω_{field} is the angular frequency of the field. The interaction part of the Hamiltonian can be expressed as

$$H_{\text{int}} = -erE(t) = -(D_{ge}|g\rangle\langle e| + D_{eg}|e\rangle\langle g|)E(t), \tag{2.19}$$

where $D_{ge} = D_{eg}^* = e\langle g|r|e\rangle$ is the matrix element of the electric dipole moment. Defining the Rabi frequency to be

$$\Omega_R = \frac{e\,|\langle g|r|e\rangle|\,E_0}{\hbar}, \tag{2.20}$$

we can now express the interaction Hamiltonian in terms of the Rabi frequency

$$H_{\text{int}} = -\hbar\Omega_R\left(e^{i\phi}|g\rangle\langle e| + e^{-i\phi}|e\rangle\langle g|\right)\cos(\omega_{\text{field}}t), \tag{2.21}$$

where ϕ is the phase of the dipole matrix element, that is, $D_{ge} = |D_{ge}|e^{i\phi}$.

Integrating the Schrödinger Equation gives

$$|\psi(t)\rangle = U(t)|\psi(0)\rangle, \tag{2.22}$$

where the unitary time evolution operator is defined by

$$\frac{\partial U(t)}{\partial t} = -\frac{i}{\hbar} H U(t), \tag{2.23}$$

and

$$U(0) = 1. \tag{2.24}$$

In the interaction picture, the state vector's time dependence is due purely to the interaction energy given by the interaction Hamiltonian. We define the state vector, $|\psi_I(t)\rangle$, in the interaction picture to be

$$|\psi_I(t)\rangle = U_0^\dagger(t)|\psi(t)\rangle, \tag{2.25}$$

with

$$U_0(t) = \exp\left(-\frac{i}{\hbar} H_{\mathrm{un}} t\right), \tag{2.26}$$

and H_{un} is the the unperturbed Hamiltonian. Therefore, if we define the interaction picture Hamiltonian $\mathcal{V}(t)$ to be

$$\mathcal{V}(t) = U_0^\dagger(t) H_{int} U_0(t), \tag{2.27}$$

the state vector $|\psi_I(t)\rangle$ in the interaction picture evolves according to

$$\frac{\partial}{\partial t}|\psi_I(t)\rangle = -\frac{i}{\hbar}\mathcal{V}(t)|\psi_I(t)\rangle. \tag{2.28}$$

This is solved by the state

$$|\psi_I(t)\rangle = U_I(t)|\psi_I(0)\rangle, \tag{2.29}$$

where

$$U_I(t) = \mathcal{T} \exp\left[-\frac{i}{\hbar}\int_0^t \mathcal{V}(\tau)d\tau\right] \tag{2.30}$$

is the time evolution operator in the interaction picture, and $\mathcal{T}$ is the time ordering operator. This is a shorthand notation for

$$\mathcal{T} \exp\left[-\frac{i}{\hbar}\int_0^t \mathcal{V}(\tau)d\tau\right] = 1 - \frac{i}{\hbar}\int_0^t \mathcal{V}(\tau_1)d\tau_1 + \left(\frac{i}{\hbar}\right)^2 \int_0^t d\tau_1 \int_0^{t_1} \mathcal{V}(\tau_1)\mathcal{V}(\tau_2)d\tau_2 + \dots \tag{2.31}$$

Now for our case of a two-state atom interacting with a monochromatic electromagnetic field of angular frequency ω_{field}, the unperturbed Hamiltonian H_{un} is given by Equation 2.17 so that we have

$$\begin{aligned} U_0(t) &= \exp\left(-\frac{i}{\hbar}H_{\text{un}}t\right) \\ &= \exp\left(-\frac{i}{\hbar}E_g t\right)|g\rangle\langle g| + \exp\left(-\frac{i}{\hbar}E_e t\right)|e\rangle\langle e|. \end{aligned} \tag{2.32}$$

Therefore, the interaction picture Hamiltonian is given by

$$\begin{aligned} \mathcal{V}(t) = &\quad -\hbar\Omega_R U_0^\dagger(t)\left(e^{-i\phi}|g\rangle\langle e| + e^{i\phi}|e\rangle\langle g|\right)U_0(t)\cos(\omega t) \\ = &\quad -\frac{\hbar\Omega_R}{2}\left[e^{-i\phi}|g\rangle\langle e|e^{i\Delta t} + e^{i\phi}|e\rangle\langle g|e^{-i\Delta t}\right. \\ &\quad \left. + e^{-i\phi}|g\rangle\langle e|e^{i(\omega_{\text{atom}}+\omega_{\text{field}})t} + e^{i\phi}|e\rangle\langle g|e^{-i(\omega_{\text{atom}}+\omega_{\text{field}})t}\right], \end{aligned} \tag{2.33}$$

where $\Delta = \omega_{\text{atom}} - \omega_{\text{field}}$ is the detuning between the atom and driving field. The interaction picture Hamiltonian contains terms proportional to $e^{\pm i(\omega_{\text{atom}}+\omega_{\text{field}})t}$, which vary very rapidly compared to the other terms. Their average over a timescale larger than the inverse optical driving frequency is quite small. The Hamiltonian can be simplified by making the "Rotating Wave Approximation" and neglecting these terms. This simplified Hamiltonian is

$$\mathcal{V}(t) = -\frac{\hbar\Omega_R}{2}\left(e^{-i\phi}|g\rangle\langle e|e^{i\Delta t} + e^{i\phi}|e\rangle\langle g|e^{-i\Delta t}\right). \tag{2.34}$$

The time evolution operator for the case of zero detuning $\Delta = 0$, is found by noting that

$$\mathcal{V}^{2n}(t) = \left(\frac{\hbar\Omega_R}{2}\right)^{2n} [\,|g\rangle\langle g| + |e\rangle\langle e|\,]^n\,, \tag{2.35}$$

and

$$\mathcal{V}^{2n+1}(t) = \left(\frac{\hbar\Omega_R}{2}\right)^{2n+1} \left[e^{-i\phi}|g\rangle\langle g| + e^{i\phi}|e\rangle\langle e|\,\right]. \tag{2.36}$$

The time evolution operator $U_I(t)$ is given by

$$U_I(t) = \cos\left(\frac{\Omega_R t}{2}\right)(|g\rangle\langle g| + |e\rangle\langle e|) + i\sin\left(\frac{\Omega_R t}{2}\right)\left(e^{-i\phi}|g\rangle\langle g| + e^{i\phi}|e\rangle\langle e|\right). \tag{2.37}$$

This time-evolution operator and Equation 2.29 yield the time evolution for a given initial state $|\phi_I(0)\rangle$. For example, if the atom is initially in the ground state $|\phi_I(0)\rangle = |g\rangle$,

$$|\phi(t)\rangle = \cos\left(\frac{\Omega_R t}{2}\right)|g\rangle + i\sin\left(\frac{\Omega_R t}{2}\right)e^{i\phi}|e\rangle. \tag{2.38}$$

The probability for the atom to be in the ground and excited states is given by

$$\begin{aligned} P_g &= |\langle g|\phi(t)\rangle|^2 = \cos^2\left(\frac{\Omega_R t}{2}\right), \\ P_e &= |\langle e|\phi(t)\rangle|^2 = \sin^2\left(\frac{\Omega_R t}{2}\right). \end{aligned} \tag{2.39}$$

We see that the angular frequency of population transfer occurs at the Rabi frequency Ω_R. This example illustrates the usefulness of the interaction picture in solving for the time evolution of a system.

Chapter 3

Quantum Theory

With a sufficiently small mode volume, the dynamics of the interaction of a single radiation mode of the field with a single, two-level atom can be very different for a full quantum theory than those of a semiclassical theory. Here I discuss the interaction of a quantized radiation field with a two-level atom approximated using the dipole and rotating wave approximations. For a more careful treatment of this topic see Reference [28].

3.1 Hamiltonian

The Hamiltonian for a single electron atom is given by [27]

$$H = H_{\text{atom}} + H_{\text{field}} - e\overrightarrow{r} \cdot \overrightarrow{E}, \tag{3.1}$$

where H_{atom} is the energy of the atom, H_{field} is the energy of the field, $\overrightarrow{r}$ is the electron position, and E is the electric field. Note that the field is assumed to be uniform over the atom.

The Hamiltonian for the modes of a cavity can be expressed as [29]

$$H_{\text{cavity}} = \sum_n \hbar\omega_n \left(a_n^\dagger a_n + \frac{1}{2} \right), \tag{3.2}$$

where $a^\dagger$ is the field creation operator, a is the field annihilation operator, and ω is the frequency of the cavity field.

The Hamiltonian for the atom is given by

$$H_{\text{atom}} = \sum_i E_i |i\rangle\langle i| = \sum_i E_i \sigma_{ii}, \tag{3.3}$$

where E_i is the energy of the eigenstate $|i\rangle$, and $|i\rangle$ forms a complete set of atomic eigenstates.

Now the interaction term is found by noting that

$$e\overrightarrow{r} = \sum_{i,j} e|i\rangle\langle i|\overrightarrow{r}|j\rangle\langle j| = \sum_{i,j} e\langle i|\overrightarrow{r}|j\rangle\sigma_{ij}, \tag{3.4}$$

where σ_{ij} is the atomic transition operator $|i\rangle\langle j|$, and $e\langle i|\overrightarrow{r}|j\rangle$ is the electric dipole transition matrix element. If we place the atom at the origin, the electric field operator, $\overrightarrow{\mathcal{E}}$, can be expressed as

$$\overrightarrow{\mathcal{E}} = \sum_n \hat{\varepsilon}_n \mathcal{E}_n (a_n + a_n^\dagger), \tag{3.5}$$

where

$$\mathcal{E}_n = \sqrt{\frac{\hbar\omega_n}{2\epsilon_0 V_n}}, \tag{3.6}$$

$\hat{\varepsilon}_n$ is the unit polarization vector, ϵ_0 is the permittivity of free space, and V_n is the electromagnetic mode volume.

If we let

$$g_n^{ij} = -\frac{e\langle i|\overrightarrow{r}|j\rangle\sigma_{ij} \cdot \hat{\varepsilon}_n}{\hbar}\sqrt{\frac{\hbar\omega_n}{2\epsilon_0 V_n}}, \tag{3.7}$$

the Hamiltonian for the system can now be expressed as

$$H = \sum_n \hbar\omega_n \left(a_n^\dagger a_n + \frac{1}{2}\right) + \sum_i E_i \sigma_{ii} + \hbar \sum_{i,j}\sum_n g_n^{ij}\sigma_{ij}\left(a_n^\dagger + a_n\right). \tag{3.8}$$

For an individual two-level atom interacting with a single cavity mode, we denote the ground state by $|g\rangle$ and the excited state by $|e\rangle$. The electric dipole transition matrix is only non-zero for $\Delta l = \pm 1$. Therefore,

$$g^{ii} = 0. \tag{3.9}$$

Also,

$$g^{ij} = g^{ji}. \tag{3.10}$$

If we let $g_0 = g^{eg} = g^{ge}$, the Hamiltonian is reduced to

$$H = \hbar\omega\left(a^\dagger a + \frac{1}{2}\right) + E_g\sigma_{gg} + E_e\sigma_{ee} + \hbar g_0\left(\sigma_{eg} + \sigma_{ge}\right)\left(a^\dagger + a\right). \tag{3.11}$$

Now, we can rearrange this further by noting a few relations. First, the atomic states form a complete basis,

$$\sum_n |n\rangle\langle n| = \sum_n \sigma_{nn} = 1. \tag{3.12}$$

In the case of a two level atom we have

$$\sigma_{gg} + \sigma_{ee} = 1. \tag{3.13}$$

We now define the following operators [29]

$$\sigma^\dagger = \begin{pmatrix} 0 & 1 \\ 0 & 0 \end{pmatrix}, \sigma = \begin{pmatrix} 0 & 0 \\ 1 & 0 \end{pmatrix}, \sigma_z = \begin{pmatrix} 1 & 0 \\ 0 & -1 \end{pmatrix}, \tag{3.14}$$

where $\sigma^\dagger$ is the atomic raising operator, σ is the lowering operator, and σ_z is the inversion operator. If we now make the rotating wave approximation, that is, neglect all terms that do not conserve energy, we are left with the following Hamiltonian

$$H = \hbar\omega\left(a^\dagger a + \frac{1}{2}\right) + \frac{1}{2}\hbar\omega\sigma_z + \hbar g_0\left(a^\dagger\sigma + a\sigma^\dagger\right). \tag{3.15}$$

We refer to g_0 as the coupling coefficient, since it determines the strength of the atom-field interaction term in the Hamiltonian. This coefficient corresponds to one half the single-photon Rabi frequency discussed in Section 2.3, that is, $g_0 = \frac{\Omega_R}{2}$.

This Hamiltonian now corresponds with the Jaynes-Cummings model [1] for a single, stationary two-level atom in an electromagnetic field. It is realized in the limit of negligible dissipation and no detunings.

The Jaynes-Cummings model can be extended to allow the presence of dissipation and detunings to give a master equation for the evolution of the density operator, ρ, for the joint state of the atom and cavity. With the electric dipole and rotating wave approximations [16]

$$H = \hbar(\omega_c - \omega_p)\hat{a}^\dagger\hat{a} + \hbar(\omega_a - \omega_p)\hat{\sigma}^\dagger\hat{\sigma} + \hbar g(\overrightarrow{r})[\hat{a}\hat{\sigma}^\dagger + \hat{a}^\dagger\hat{\sigma}] + \hbar\varepsilon(\hat{a} + \hat{a}^\dagger), \tag{3.16}$$

where ε is the driving probe field of frequency ω_p.

3.2 The Jaynes-Cummings Ladder

The previous section contains a derivation of the Hamiltonian for the Jaynes-Cummings model of a single, stationary two-level atom in an electromagnetic field. Diagonalizing Equation 3.15 yields

$$|\pm\rangle_n = \frac{1}{\sqrt{2}}(|g, n\rangle \pm |e, n-1\rangle) \tag{3.17}$$

with (g, e) denoting the atomic ground and excited states. These states form the Jaynes-Cummings ladder and represent the atom and cavity equally sharing an excitation with corresponding energy eigenvalues $(n\hbar\omega \pm \sqrt{n}\hbar g_0)$. Measurements of the structural properties for weak excitation yields a double peaked vacuum Rabi transmission spectrum (see Figure 3.2), which comes from the $\pm\hbar g_0$ splitting in the energy eigenstates for a single excitation. This was first directly observed in [30].

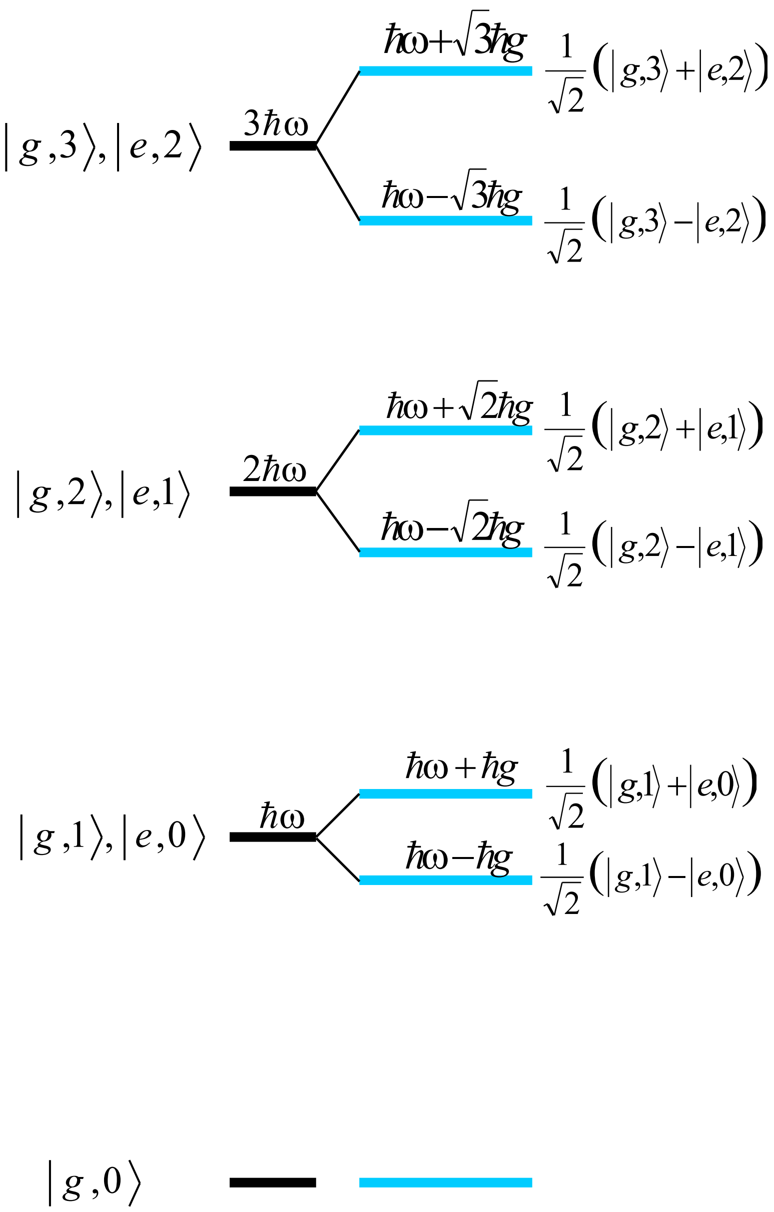
|g,3⟩,|e,2⟩
3ħω
ħω+√3ħg
1/√2 (|g,3⟩+|e,2⟩)
ħω−√3ħg
1/√2 (|g,3⟩−|e,2⟩)
|g,2⟩,|e,1⟩
2ħω
ħω+√2ħg
1/√2 (|g,2⟩+|e,1⟩)
ħω−√2ħg
1/√2 (|g,2⟩−|e,1⟩)
|g,1⟩,|e,0⟩
ħω
ħω+ħg
1/√2 (|g,1⟩+|e,0⟩)
ħω−ħg
1/√2 (|g,1⟩−|e,0⟩)
|g,0⟩

Figure 3.1: The Jaynes-Cummings Ladder
The ‘ladder’ of eigenvalues for the fully quantum treatment of a single, two-level atom coupled to a cavity, where the cavity is on resonance with the atomic transition. In the case of zero atom-cavity coupling, $g_0 = 0$, the eigenstates $|g, n\rangle$ and $|e, n-1\rangle$ are degenerate, where g and e refer to the atomic ground state and atomic excited state respectively, and n refers to the number of intracavity photons present. The energy splittings are $\pm\sqrt{n}\hbar g_0$.

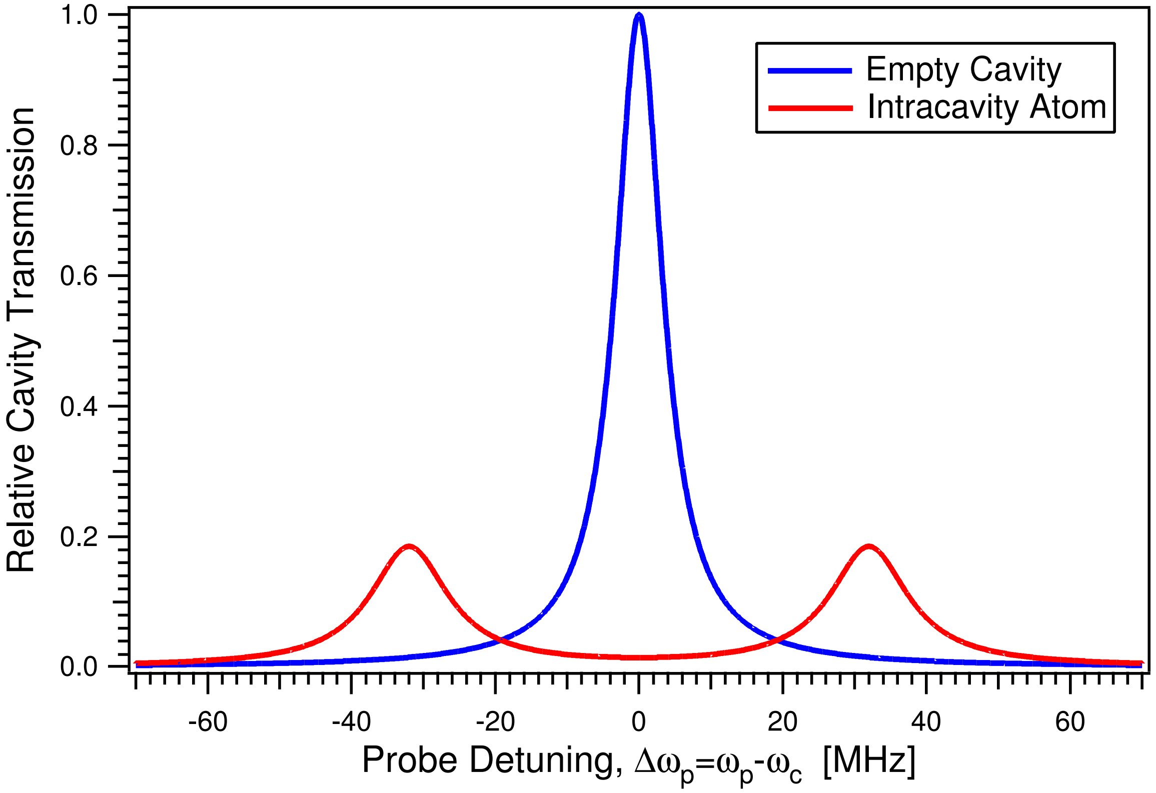

Figure 3.2: Vacuum-Rabi Splitting

The double peaked Vacuum-Rabi transmission spectrum due to the $\pm\hbar g_0$ splitting in the energy eigenstates for a single excitation of one intracavity atom. This plot is for the case of zero cavity detuning, $\omega_c = \omega_a$, where ω_c is the resonance of the cavity and ω_a is the atomic resonance. The blue line is the relative transmission of a probe through the empty cavity as a function of probe detuning $\Delta\omega_p = \omega_p - \omega_c$, where ω_p is the frequency pf the probe. In the empty cavity case, the half-width half-maximum point occurs for $\omega_p = \kappa$, where κ is the cavity decay rate. The red line is the relative transmission of a probe through the cavity with a single intracavity atom coupled to the cavity mode with coupling coefficient g_0. The energy splitting is $\pm\hbar g_0$, so the two peaks occur for $\Delta\omega_p = \pm g_0$. These plots are made using the parameters of our system in the weak field limit: the coupling coefficient $\frac{g_0}{2\pi} = 32$ MHz, the cavity decay rate $\frac{\kappa}{2\pi} = 4$ MHz, and the atomic spontaneous decay rate $\frac{\gamma_\perp}{2\pi} = 2.61$ MHz.

Chapter 4

Critical Parameters for Strong Coupling

There are two dimensionless parameters useful in describing the atom-cavity system in the strong coupling regime, the saturation photon number and the critical atom number. A critical atom number of N_0 indicates that the insertion of N_0 atoms into the cavity mode has a significant effect on the transmission of a probe field through the cavity. If there is a single atom in the cavity, the saturation photon number, n_0, gives the number of photons it takes to saturate the the atomic transition.

Most quantum systems have large critical parameters. For example, a typical laser has a threshold photon number $\sqrt{n_0} \sim 10^3 - 10^4$, so that adding or removing a single photon has little effect. Similarly, in a cavity QED system with large critical parameters, the effect of individual photons or atoms is small. As the critical parameters are reduced, however, we move to a regime where individual quanta are important. When the critical parameters are less than unity, they serve to determine the "quality" of the atom-cavity system by showing the relative importance of a single quanta on the system.

For an atom-cavity system to be in the strong coupling regime, these parameters must be less than unity. In that case, the interaction of a single intracavity atom and photon will be nonlinear. There has been steady progress over the years in the Kimble group to drive these parameters to smaller values. Figure 4.1 illustrates this progress.

4.1 Electromagnetic Mode Volume

For a Gaussian standing wave inside a Fabry-Perot cavity, the electromagnetic mode has a spatial dependence of

$$\psi(\overrightarrow{r}) = \sin\left(\frac{2\pi x}{\lambda}\right)\exp\left[-\frac{y^2+z^2}{w_0^2}\right], \tag{4.1}$$

where w_0 is the cavity waist and the mirrors are located at $x = 0, L$. The electromagnetic mode volume, V_m, is found by integrating over the cavity mode

$$\begin{aligned} V_{\mathrm{m}} &= \int |\psi(\overrightarrow{r})|^2 dV \\ &= \int_0^{L_{\mathrm{eff}}}\int_0^{2\pi}\int_0^{\infty} \cos^2\left(\frac{2\pi x}{\lambda}\right) r e^{-\frac{2r^2}{w_0^2}} dr d\theta dx \\ &= \frac{\pi w_0^2}{4} L_{\mathrm{eff}}, \end{aligned} \tag{4.2}$$

where L_{eff} is an effective length for the cavity. Here we have assumed that the cavity has hard edges at $x = 0, L_{\mathrm{eff}}$ and the mode is a pure sinusoidal standing wave. In fact, the mirrors are composed of a mirror substrate with a stack of ~ 35 dielectric layers each $\frac{\lambda}{4}$ thick. For very short cavities, there will be significant penetration of the electromagnetic mode into the dielectric stack. As the length is decreased, this leakage has a greater impact on the mode volume. The cavity used in our experiment has a length of ~ 40 μm. The dielectric stack is ~ 5 μm thick, so a careful analysis would have to include these effects on our cavity mode. These effects are discussed in greater detail in Reference [35].

If we neglect penetration of the mode into the mirror substrates, the mode volume $V_{\mathrm{m}} = \frac{\pi w_0^2}{4} L$. The cavity waist, w_0, for a symmetric Fabry-Perot cavity is given by

$$w_0^2 = \frac{L\lambda}{2\pi}\sqrt{\frac{2R-L}{L}}, \tag{4.3}$$

where L is the cavity length and R is the radius of curvature of the mirrors. Therefore, for the case of no penetration of the mode into the cavity mirrors, the mode volume is given by

$$V_{\mathrm{m}} = \frac{\lambda}{8}\sqrt{L^3(2R - L)}. \tag{4.4}$$

Figure 4.2 shows this dependence on cavity length of the mode volume for the parameters of our system. In our cavity, the radius of curvature of the mirrors is $R = 0.2$ m, and the wavelength is $\lambda = 852$ nm.

4.2 Strong Coupling Regime

As we have seen earlier, the coherent atom-field coupling coefficient is given by

$$g(\overrightarrow{r}) = g_0 \sin\left(\frac{2\pi x}{\lambda}\right) \exp\left[-\frac{y^2 + z^2}{w_0^2}\right], \tag{4.5}$$

where

$$g_0 = d \cdot E = d\sqrt{\frac{\hbar\omega}{2\varepsilon_0 V_{\mathrm{m}}}}, \tag{4.6}$$

d is the atomic dipole matrix element, ω is the transition frequency, V_{m} is the cavity mode volume, and $2g_0$ is the single-photon Rabi frequency. The position dependence is due to the standing wave structure of the cavity mode.

One might assume that the cavity mode volume, V_{m}, should be made as small as possible in order to improve the coupling coefficient, and hence the strength of the atom-cavity coupling. However, this is not the case. In the regime of strong coupling, the atom and cavity must be considered as a coupled system whose structure and dynamics approach those of the Jaynes-Cummings model. The regime of strong coupling is achieved when the coherent evolution rate of the single quanta dominates any dissipation in the system. The dissipation rates are set by the atomic dipole decay rate, $\gamma_\perp$, and the cavity field decay rate, κ. In the case of Fabry-Perot cavities, the electromagnetic mode volume is minimized by decreasing the cavity length, L. However, as the cavity length is decreased, the cavity field decay rate is *increased*. Therefore, we shall see later that the atom-cavity system is not optimized by simply minimizing the cavity mode volume.

Since the atomic decay is purely radiative, the rate for decay of atomic inversion $\gamma_{\|} = 2\gamma_{\perp}$. Also, $\gamma_{\|}$ is essentially the same as for an atom in free space, since the solid angle subtended by the cavity mode is small, ($\sim 10^{-5}$). It is also important to note that the cavity decay, κ, does not necessarily lead to decoherence, since this light could in principle be measured or reintroduced to the cavity to maintain coherence.

4.3 Saturation Photon Number

The saturation intensity, I_{sat}, for an atomic transition is [36]

$$I_{\text{sat}} = \frac{4\pi^2 \hbar c \gamma}{3\lambda^3}. \tag{4.7}$$

The intracavity intensity for n photons in a mode volume V_{m} is

$$I_{\text{photon}} = \frac{n\hbar\omega c}{V_{\text{m}}}. \tag{4.8}$$

Therefore, the number of intracavity photons, n_0, required to saturate the transition is given by

$$n_0 = \frac{2\pi\gamma V_{\text{m}}}{3c\lambda^2}. \tag{4.9}$$

This parameter, n_0, is referred to as the saturation photon number. From earlier we know that the Rabi frequency, Ω_R, is given by

$$\begin{aligned} \Omega_R &= \frac{e\left|\langle g|r|e\rangle\right| E_0}{\hbar}, \\ &= \sqrt{\frac{\omega}{2\epsilon_0 V_{\text{m}}\hbar}}\, e\left|\langle g|r|e\rangle\right|, \\ &= \sqrt{\frac{3c\gamma\lambda^2}{4\pi V_{\text{m}}}}. \end{aligned} \tag{4.10}$$

Because the coupling coefficient $g_0 = \frac{\Omega_R}{2}$, we can now express the saturation photon number in terms of the coupling coefficient

$$n_0 = \frac{\gamma^2}{2g^2}. \tag{4.11}$$

Therefore, we see that n_0 is a dimensionless parameter that corresponds to the number of intracavity photons required to saturate the transition of an intracavity atom. When $n_0 \ll 1$, the atomic transition is saturated by a single intracavity photon.

4.4 Critical Atom Number

The critical atom number, N_0, corresponds to the number of atoms required to have an appreciable effect on the intracavity field. The effective coupling coefficient for multiple intracavity atoms in the weak field limit is given by $g_{\text{eff}} = g_0\sqrt{N}$. If we assume that the atom has an appreciable effect on the system when the splitting is greater than the geometric mean of the cavity decay rate, κ, and the spontaneous decay rate, γ, the critical atom number will scale roughly as

$$N_0 \sim \frac{\kappa\gamma}{g^2}. \tag{4.12}$$

$C = N_0^{-1}$ is the single atom cooperativity parameter [37]. Cooperative spontaneous radiation, also referred to as superradiance, occurs as a result of the mutual coupling of atoms through the electromagnetic field. The rate that each excited atom radiates is significantly influenced by the presence of the other atoms. When multiple atoms are very close together, this can lead to an enhanced rate for the spontaneous decay. The cooperativity parameter then arises from solving the Maxwell-Bloch equations for a system of N two-state atoms coupled to a classical electromagnetic field [38]. The single atom cooperativity parameter is $C = \frac{g^2}{2\kappa\gamma}$. Therefore, the critical atom number is given by

$$N_0 = \frac{2\kappa\gamma}{g^2}. \tag{4.13}$$

4.5 Cavity Length and the Critical Parameters

The saturation photon number and critical atom number are useful because of their physical meaning. However, one can define a new dimensionless parameter,

$$\beta = \frac{8\pi^2 V_{\mathrm{m}}}{3\lambda_0^3}\frac{1}{\left|\vec{\Psi}(r)\right|^2}, \tag{4.14}$$

that corresponds to the cavity mode volume in units of λ^3 weighted by the inverse of the strength of the mode function at the atomic position. This enables the equations for the saturation photon number and critical atom number to be expressed as:

$$n_0 = \frac{\beta}{4Q_{\mathrm{atom}}}, \tag{4.15}$$

and

$$N_0 = \frac{\beta}{Q_{\mathrm{cavity}}}, \tag{4.16}$$

where

$$Q_{\mathrm{atom}} = \frac{\pi c}{\lambda_0 \gamma_\perp}, \tag{4.17}$$

and

$$Q_{\mathrm{cavity}} = \frac{\pi c}{\lambda_0 \kappa} = \frac{2\mathcal{F}L}{\lambda_0}. \tag{4.18}$$

This parameter, β, then also determines the coupling coefficient in the following manner:

$$g(r) = \sqrt{\frac{2\pi c \gamma_\perp}{\beta \lambda_0}}. \tag{4.19}$$

Therefore, we see that one can use a single parameter, β, combined with the properties of the atom to be used (λ_0 and $\gamma_\perp$) and the quality factor of the resonator, Q_{cavity}, to determine the three parameters (n_0, N_0, g_0) of importance in determining the quality of an atom-cavity system.

For a Fabry-Perot cavity, if we neglect penetration of the mode into the mirror substrates, we know from Section 4.1 that the mode volume for a symmetric Fabry-

Perot cavity is given by

$$V_{\mathrm{m}} = \frac{\pi \omega_0^2}{4} L = \frac{\lambda}{8}\sqrt{L^3(2R-L)}, \tag{4.20}$$

where L is the cavity length and R is the radius of curvature of the mirrors. Therefore, at the maximum of the electromagnetic mode function, we have

$$\beta = \frac{2\pi^3 \omega_0^2 L}{3\lambda^3} = \frac{\pi^2}{3\lambda^2}\sqrt{L^3(2R-L)}, \tag{4.21}$$

We can now see how the three parameters scale with cavity length:

$$n_0 = \frac{\pi^2 \omega_0^2 \gamma}{6\lambda^2 c} L = \frac{\pi\gamma}{12\lambda c}\sqrt{L^3(2R-L)}, \tag{4.22}$$

$$N_0 = \frac{\pi^3 \omega_0^2}{3\lambda^2 \mathcal{F}} = \frac{\pi^2}{6\lambda\mathcal{F}}\sqrt{L(2R-L)}, \tag{4.23}$$

and

$$g_0 = \sqrt{\frac{3\lambda^2 c\gamma}{\pi^2 \omega_0^2 L}} = \left(\frac{6\lambda c\gamma}{\pi}\right)^{\frac{1}{2}} \left(\frac{1}{L^3(2R-L)}\right)^{\frac{1}{4}}, \tag{4.24}$$

where L is the cavity length, γ is the atomic decay rate, and $\mathcal{F}$ is the cavity finesse. Figure 4.3 is a plot of the saturation photon number and critical atom number as a function of cavity length for the parameters of our cavity. Figure 4.4 shows the dependence of the coupling coefficient, g_0, on cavity length. The cavity used in our experiment has a finesse of $\mathcal{F} \approx 4.2 \times 10^5$ for $\lambda = 852$ nm, cavity length $L \approx 44.6\ \mu$m, and mirror radius of curvature $R = 0.2$ m. $\frac{\gamma_\perp}{2\pi} = 2.61$ MHz is the transverse decay rate for the D_2 transition in Cesium at $\lambda = 852$ nm.

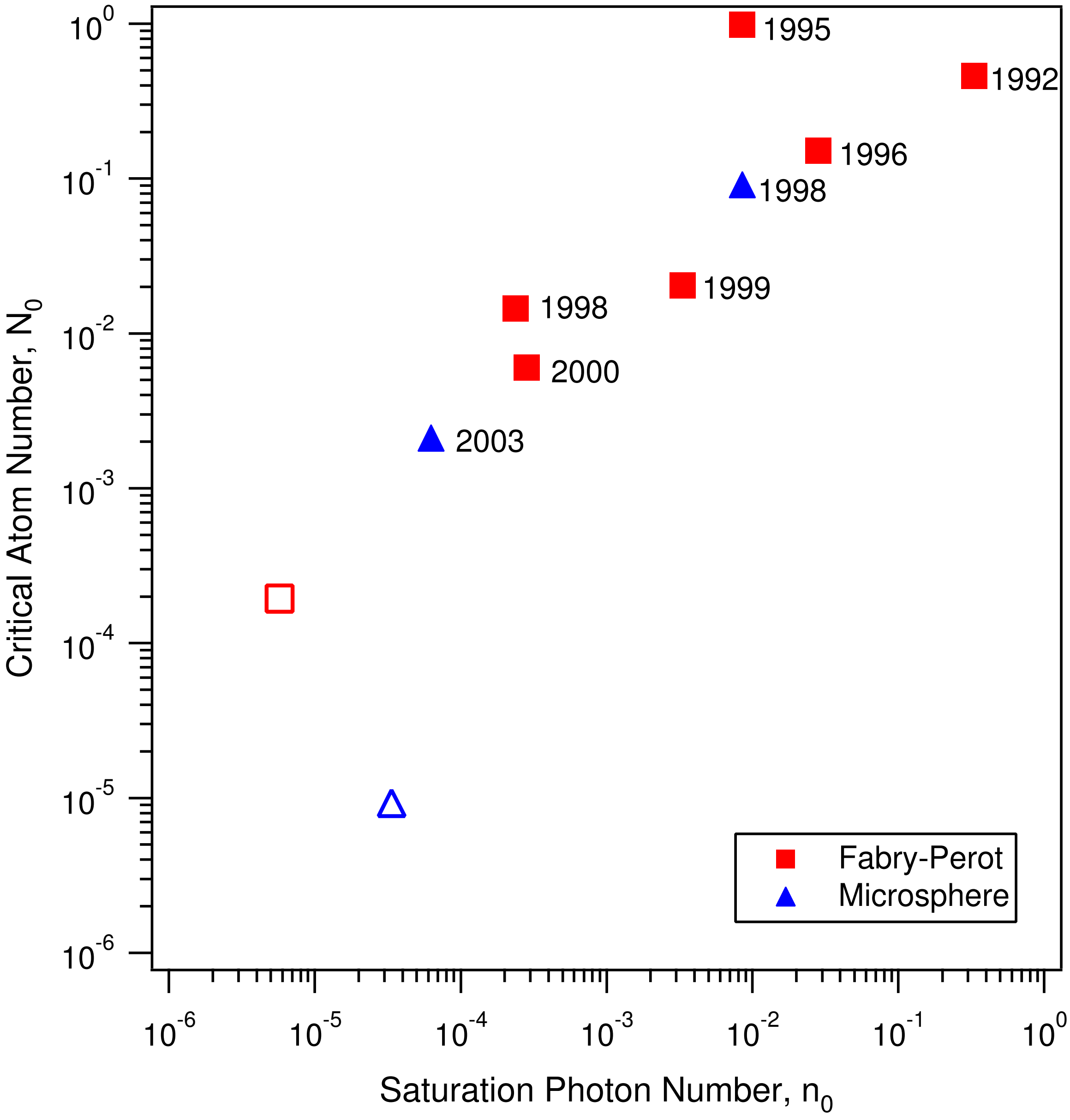

Figure 4.1: Progress in Strong Coupling

Progress on improving the strong coupling of atoms and cavities in the Kimble group. ■ represents published results for Fabry-Perot cavities [31, 30, 32, 5, 2, 33]. ▲ represents published results for Microsphere cavities [18, 24]. □ represents the ultimate limit for Fabry-Perot cavities discussed in Reference [34]. △ represents the ultimate limit for Microsphere resonators discussed in Reference [24] and Part III of this thesis.

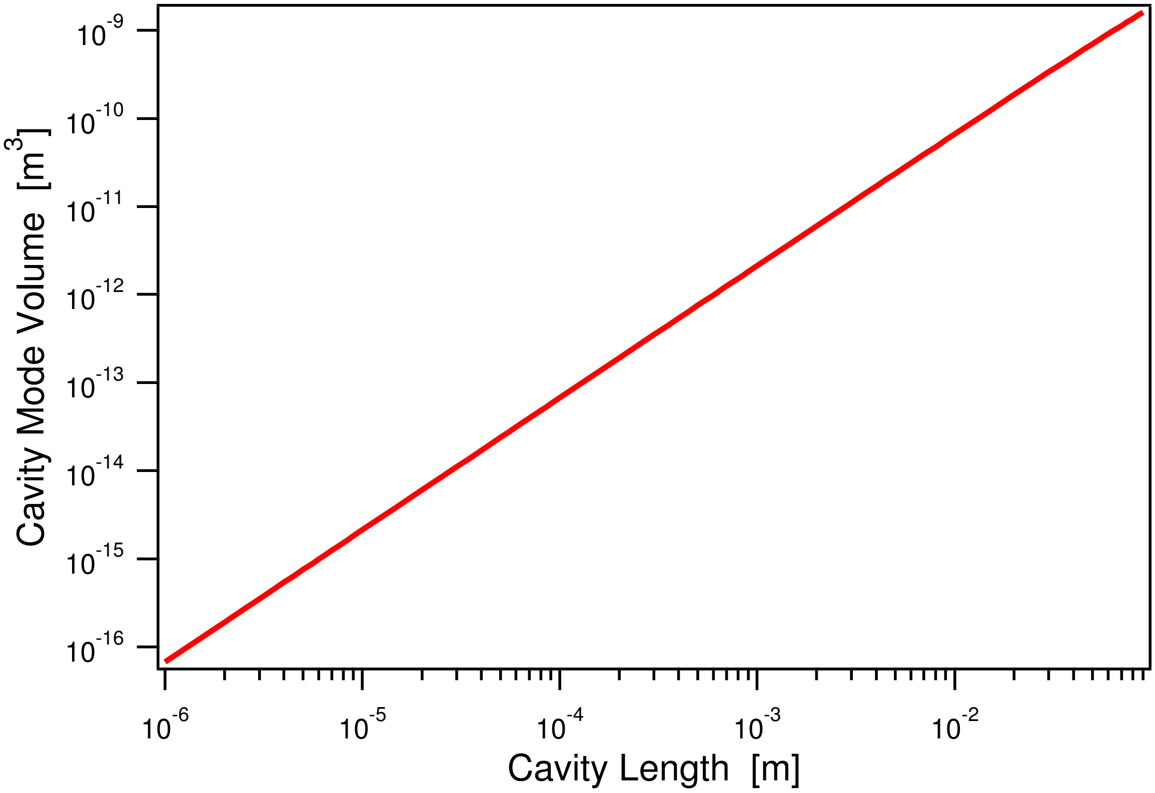

Figure 4.2: Electromagnetic Mode Volume for a Fabry-Perot Cavity
The electromagnetic mode volume, V_{m} (see Equation 4.4), for a Fabry-Perot cavity as a function of cavity length, L. This plot assumes that there is no penetration of the cavity mode into the mirrors. The parameters for our system are used, that is, a wavelength of $\lambda = 852$ nm and radius of curvature for the mirrors of $R = 0.2$ m.

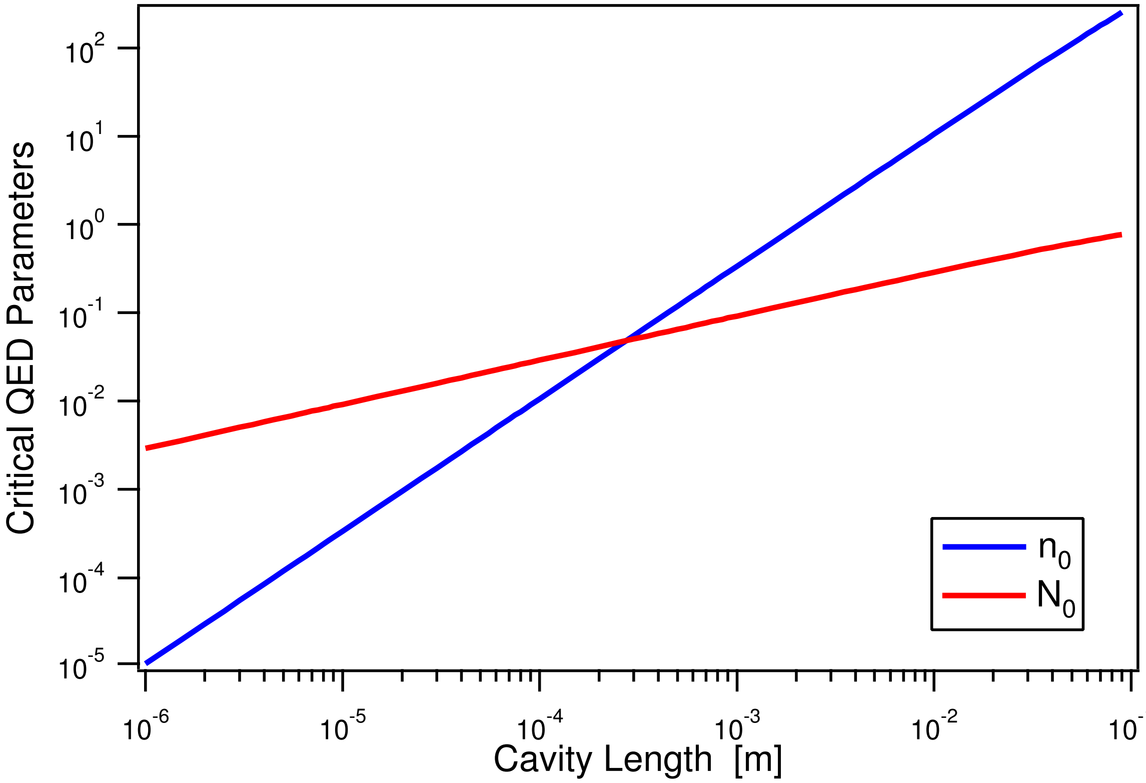

Figure 4.3: Critical Parameters in Cavity QED

This plot shows the two parameters, (n_0, N_0), of importance to cavity QED as a function of cavity length. These plots assume there is no penetration of the cavity mode into the mirrors. The blue line represents the saturation photon number, n_0, of Equation 4.22, and the red line represents the critical atom number, N_0, of Equation 4.23. The parameters for our system are used to generate this plot: the transverse spontaneous decay rate for the D_2 transition in Cesium is $\frac{\gamma_\perp}{2\pi} = 2.61$ MHz for a wavelength $\lambda = 852$ nm, the cavity finesse $\mathcal{F} = 4.2 \times 10^5$, and the radius of curvature of the mirrors is $R = 0.2$ m. The two curves cross for a cavity length of $L = 273.7$ μm with $n_0 = N_0 = 4.81 \times 10^{-2}$.

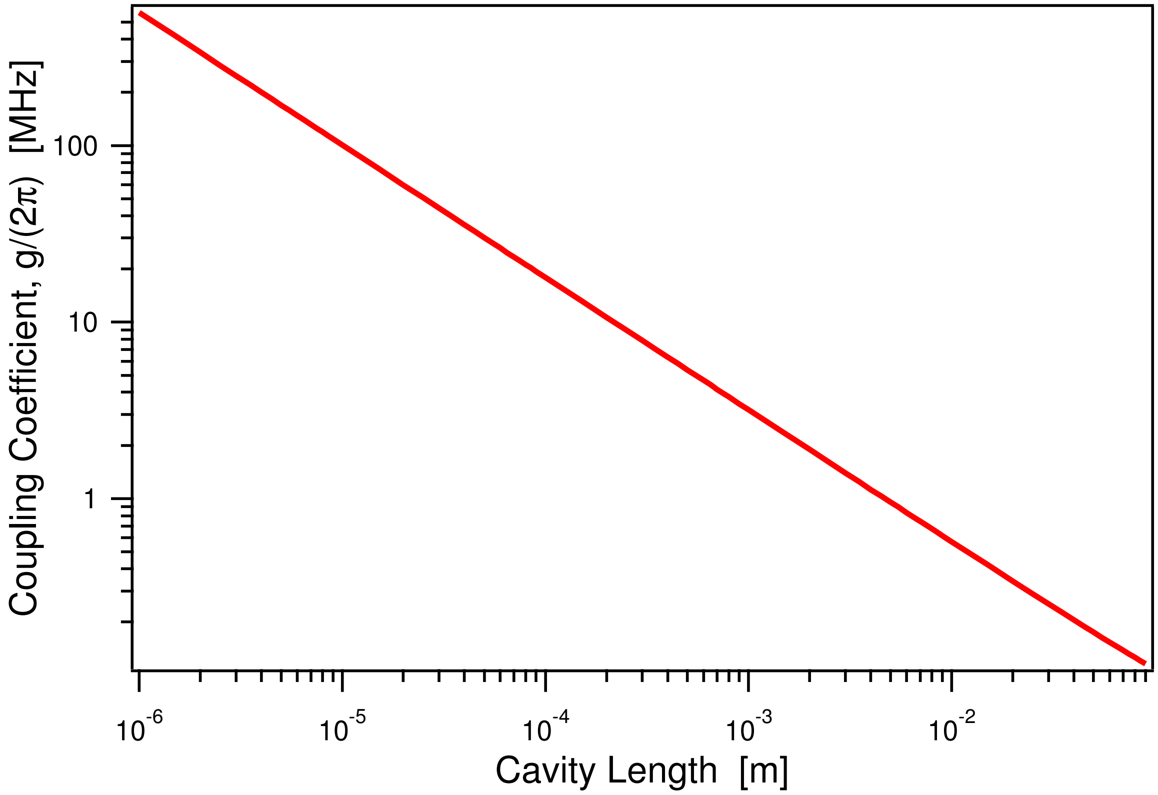

Figure 4.4: Coupling Coefficient for a Fabry-Perot Cavity
The coupling coefficient, $\frac{g_0}{2\pi}$, for a Fabry-Perot cavity as a function of cavity length (see Equation 4.24). The plot is made for the parameters of our system: the transverse spontaneous decay rate for the D_2 transition in Cesium is $\frac{\gamma_\perp}{2\pi} = 2.61$ MHz for a wavelength $\lambda = 852$ nm, and the radius of curvature of the mirrors is $R = 0.2$ m.

Part II

Realizing Strong Coupling with Cesium in Fabry-Perot Cavities

Our ultimate goal is to study the interaction of individual atoms and photons described by the Jaynes-Cummings model (see Part I). We accomplish this by trapping individual atoms inside a high-Q Fabry-Perot cavity in a regime of strong coupling [3]. Diverse avenues have been pursued for creating the trapping potential for atom confinement, including the use of additional far off-resonant trapping beams [2, 4], of the cavity QED light itself [5, 6], and of single trapped ions in high-finesse optical cavities [39, 40]. Our goal is to develop techniques for trapping that are compatible with strong coupling and that do not interfere with the cavity QED interactions. This is crucial for applications to quantum computation and communication [7, 8, 9, 10, 11, 12].

Our work [4] utilizes an intracavity FORT and represents an important step forward by achieving extended trapping times ($\sim$ 3 sec) for individual Cesium atoms in cavity QED in a regime of strong coupling, realizing a trapping potential for the center-of-mass motion that is largely independent of the internal atomic state, and demonstrating a scheme that allows continuous observation of a strongly coupled trapped atom. Our trap represents an improvement by a factor of 10^2 beyond the first realization of trapping in cavity QED [2], and by roughly 10^4 beyond prior results for atomic trapping [5] and localization [6] by way of the cavity QED field itself. Although our longest lifetimes are obtained when near-resonant fields are turned off, atoms can also be continuously monitored, leading to mean trapping times of 0.4 sec, with some atoms observed for over 1 sec. These observations as well as cooling and trapping protocols are facilitated by the choice of a “magic” wavelength for the FORT [13, 14, 15, 16]. Unlike typical FORTs, where the signs of the AC-Stark shifts for excited and ground states are opposite, our trap causes small shifts to the relevant transition frequencies, thereby providing advantages for coherent state manipulation of the atom-cavity system.

Chapter 5

The Cavity

Our cavity consists of two spherical mirrors with radius of curvature $R \sim 20$ cm on fused silica substrates with diameter $D \sim 3$ mm. These substrates are turned down to have a diameter of ~ 1 mm at the mirror face. (See Figure 5.1 for an illustration of the geometry of our mirrors.) The flat surface of the substrate is anti-reflection coated and the curved surface has a high reflectivity coating consisting of 35 alternating layers $\lambda/4$ thick of Ta_2O_5, $n = 2.041$ and SiO_2, $n = 1.455$.

The minimum cavity length is limited to

$$L_{\text{min}} = 2R - \sqrt{4R^2 - D^2}, \tag{5.1}$$

where R corresponds to the mirror radius of curvature, and D is the diameter of the substrate at the mirror surface. With a 20 cm radius of curvature, the minimum cavity length for a 3 mm diameter substrate would be $L_{\text{min}} \sim 11.3$ μm, and for a 1 mm diameter substrate it would be $L_{\text{min}} \sim 1.3$ μm. Turning down the mirror substrate also allows a greater clearance for the transverse beams we need to deliver to the cavity mode from the side.

There is a practical limit to how much we can turn down the mirror face. If the mirror face is too small, there will be losses due to the transmission of the Gaussian beam through an aperture. The transmission (power) of an aperture with radius a

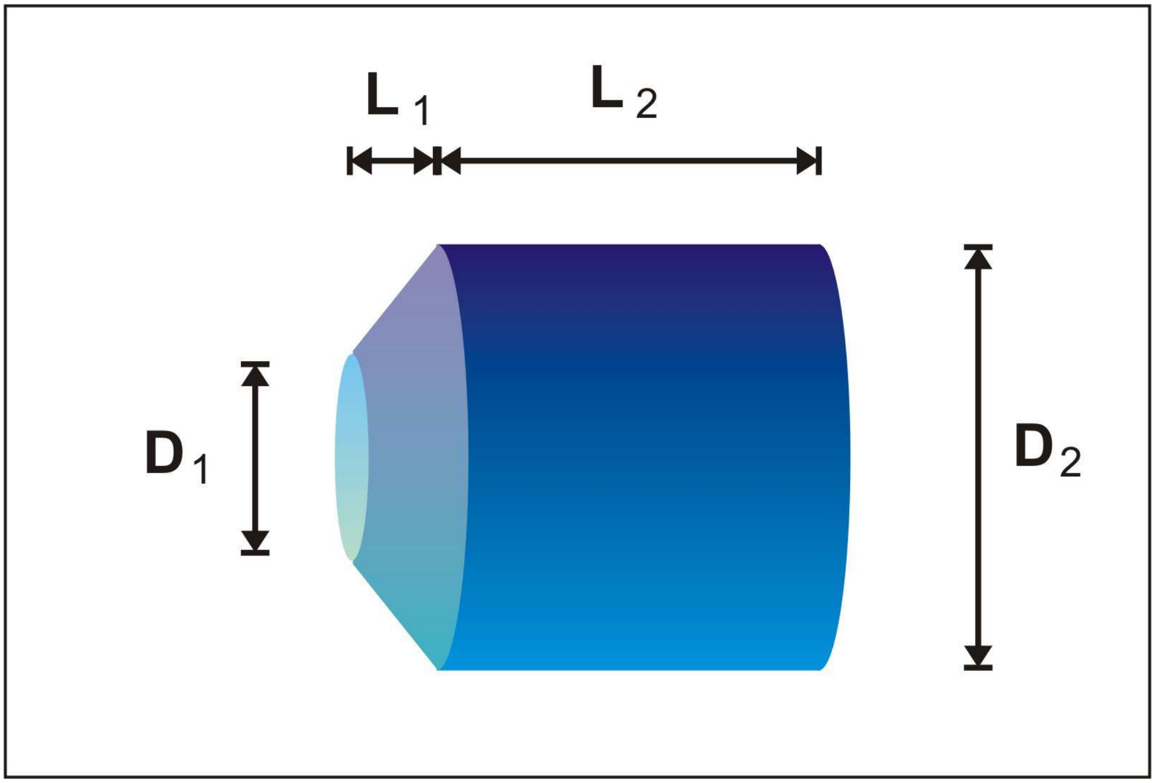

Figure 5.1: Geometry of Our Mirrors

The geometry of the mirrors comprising our Fabry-Perot cavity. A mirror is made of a BK7 substrate with an anti-reflective coating on one side and a dielectric high reflecting coating on the other side. The diameter is 2.98 mm($R_2 = \frac{D_2}{2} = 1.49$ mm), the total length is 3.85 mm, the length before the taper is $L_1 = 2.91$ mm, the length of the tapered section is $L_2 = 0.94$ mm, and the radius of the front face is $R_1 = \frac{D_1}{2} = 0.5$ mm. The radius of curvature for the mirror surface is 20 cm.

for a beam with waist w at the aperture is given by [41]

$$T = 1 - e^{-\frac{2a^2}{w^2}}. \tag{5.2}$$

These losses reach 1 ppm when $a \approx 2.63w$. In our case, the beam waist at the mirror is $w \sim 23\ \mu$m, so the aperture transmission losses will be negligible.

Figure 5.2 is a picture showing the cavity setup. The mirrors are glued to aluminum v-blocks which are placed on shear-mode piezoelectric transducers. This allows the cavity length to be actively controlled. These are then glued to a solid copper base which is placed on a vibration isolation stack inside the chamber. More details concerning cavity construction can be found in Christina Hood's thesis [35].

5.1 Cavity Transmission and Losses

The loss, l, for the highly reflecting coating of our mirrors is given by

$$l = A + S, \tag{5.3}$$

where A is the absorptive loss, and S is the scattering loss. The cavity transmission, I_{trans}, is

$$I_{\text{trans}} = \frac{4T_1T_2}{(T_1 + T_2 + l_1 + l_2)^2}, \tag{5.4}$$

where T is the transmission of the coating and the subscript refers to mirrors 1 and 2, respectively. The cavity finesse is

$$\mathcal{F} = \frac{2\pi}{T_1 + T_2 + l_1 + l_2} = \frac{\pi}{T + l}, \tag{5.5}$$

where the second part is for the case of equivalent mirrors.

For an incident input power of P_{in}, the transmitted power, P_t, is given by [34]

$$P_t = \epsilon P_{in} I_{\text{trans}} = \epsilon P_{in} T_1 T_2 \left(\frac{\mathcal{F}}{\pi}\right)^2, \tag{5.6}$$

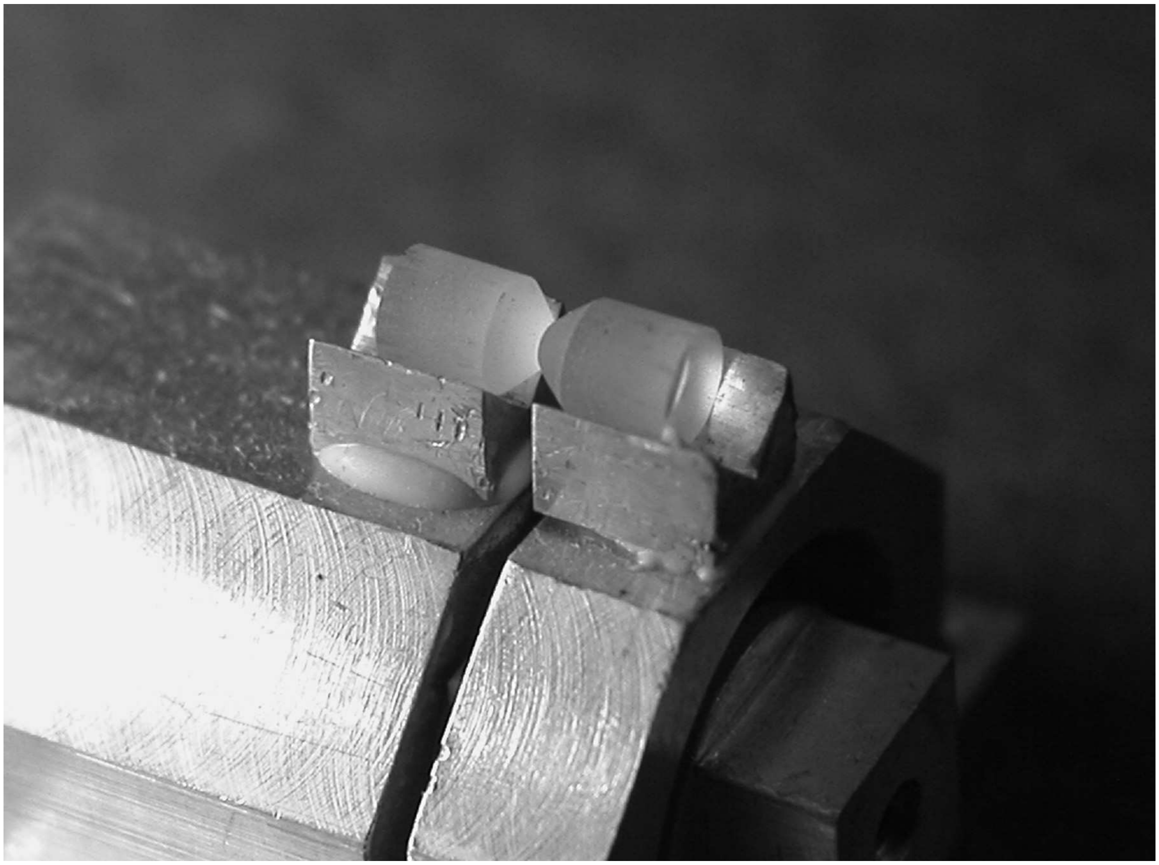

Figure 5.2: The Cavity

A picture of the cavity setup. The mirrors are glued to aluminum v-blocks which are placed on shear-mode piezoelectric transducers. These are then glued to a solid copper base which is placed on a vibration isolation stack inside the chamber.

where ϵ is the mode matching factor. The reflected power, P_r, is given by

$$P_r = (1-\epsilon)P_{in} + \epsilon P_{in}(l_1 + l_2 + T_1 - T_2)^2 \left(\frac{\mathcal{F}}{2\pi}\right)^2. \tag{5.7}$$

A little rearranging yields

$$\frac{P_t}{P_r - P_{in}} = \frac{T^2 \left(\frac{\mathcal{F}}{\pi}\right)^2}{l^2 \left(\frac{\mathcal{F}}{\pi}\right)^2 - 1}. \tag{5.8}$$

Equations 5.5 and 5.8 allow us to infer the transmission and losses for the mirrors comprising a cavity *after* it has been constructed. Jun Ye performed these measurements for our cavity with $P_{in} = 54$ μW, $P_r = 42.6$ μW, and $P_t = 4.82$ μW. Our finesse is $\mathcal{F} \sim 4.2 \times 10^5$ implying $T + l \sim 7.5$ ppm. Equation 5.8 then infers that $T \sim 4.5$ ppm and $l = 3.0$ ppm.

5.2 Modes of a Fabry-Perot Cavity

For a Gaussian standing wave inside a Fabry-Perot cavity with mirrors located at $x = (0, L)$, the electromagnetic mode has a spatial dependence of

$$\psi(\overrightarrow{r}) = \sin\left(\frac{2\pi x}{\lambda}\right) \exp\left[-\frac{y^2 + z^2}{w_0^2}\right], \tag{5.9}$$

where w_0 is the cavity waist. For a symmetric Fabry-Perot cavity, the cavity waist is given by

$$w_0 = \sqrt{\frac{L\lambda}{2\pi}\sqrt{\frac{2R - L}{L}}}, \tag{5.10}$$

where L is the cavity length and R is the radius of curvature of the mirrors.

The electromagnetic mode volume, V_m, is found by integrating over the cavity mode

$$\begin{aligned} V_{\mathrm{m}} &= \int |\psi(\overrightarrow{r})|^2 dV \\ &= \int_0^{L_{\mathrm{eff}}} \int_0^{2\pi} \int_0^{\infty} \sin^2\left(\frac{2\pi x}{\lambda}\right) r e^{-\frac{2r^2}{w_0^2}} dr d\theta dx \\ &= \frac{\pi w_0^2}{4} L_{\mathrm{eff}}, \end{aligned} \tag{5.11}$$

where L_{eff} is an effective length for the cavity. Here we have assumed that the cavity has hard edges at $x = (0, L_{\mathrm{eff}})$ and the mode is a pure sinusoidal standing wave. In fact, the mirrors are composed of a mirror substrate with a stack of ~ 35 dielectric layers each $\frac{\lambda}{4}$ thick. For very short cavities, there will be significant penetration of the electromagnetic mode into the dielectric stack. As the length is decreased, this leakage has a greater impact on the mode volume. The cavity used in our experiment has a length of ~ 45 μm. The dielectric stack is ~ 5 μm thick, so a careful analysis would have to include these effects on our cavity mode. These effects are discussed in greater detail in Reference [35].

If we neglect penetration of the mode into the mirror substrates, $L = L_{eff}$ and the mode volume is given by

$$\begin{aligned} V_{\mathrm{m}} &= \frac{\pi w_0^2}{4} L, \\ &= \frac{\lambda}{8}\sqrt{L^3(2R - L)}. \end{aligned} \tag{5.12}$$

Our cavity has length $L \sim 45$ μm and radius of curvature $R \sim 0.2$ m. Therefore, for a wavelength of $\lambda = 852$ nm, the cavity mode volume is $\sim 2.0 \times 10^4$ $\mu\mathrm{m}^3$.

5.3 Cavity Length Stabilization

In order to keep the cavity on resonance (or at a specified detuning), the length needs to be stabilized. For a Fabry-Perot cavity, we have the following relation between changes in the resonance frequency, ω, and cavity length, L,

$$\frac{\Delta L}{L} = -\frac{\Delta\omega}{\omega} \tag{5.13}$$

If we wish to stabilize the cavity to within $\frac{2\kappa}{A}$ of the cavity linewidth 2κ, the length must be stabilized to within

$$\Delta L = \frac{\kappa\lambda L}{\pi c A} = \frac{\lambda}{2A\mathcal{F}}. \tag{5.14}$$

In our setup, the cavity has linewidth $2\kappa \approx 8$ MHz and finesse $\mathcal{F} \approx 4.2 \times 10^5$. In order to stabilize the cavity to within one hundredth of its linewidth, the length would need to be stabilized to within $\Delta L \sim 1 \times 10^{-14}$ m.

We use the TEM_{00} longitudinal mode of our cavity located two orders above the cavity QED mode, with a wavelength of $\sim$ 836 nm. The mirrors are attached to piezoelectrics allowing us to actively servo the cavity length. This allows us to arbitrarily control the probe and trapping beams without interfering with the cavity length stabilization. The locking laser and cavity QED probe are referenced to each other through the use of a separate transfer cavity (see Figure 8.2).

Chapter 6

Delivering Cold Atoms to the Cavity

This chapter discusses the vacuum system used for our experiment as well as the Magneto-Optical Trap (MOT) used to deliver cold atoms to our cavity. These may at first appear to be disparate topics; however, they complement each other in forming a tool crucial to our experiment. Collisions with background gas will provide the ultimate limit to any trapping experiment. Therefore, a good vacuum is necessary for achieving long trap lifetimes.

Unfortunately, loading a MOT from the background cesium gas in a high vacuum would take a prohibitively long time. We use the trick of differential pumping to support a pressure differential between two connected chambers with pressures P_{upper} and P_{lower}, where the subscript refers to the upper and lower chamber. Figure 6.1 is a schematic of this setup, and Figure 6.2 is a picture of the actual chamber with the associated MOT optics. Our setup supports a pressure ratio of $\frac{P_{\text{upper}}}{P_{\text{lower}}} \sim 26$. This allows a suitable pressure in the upper chamber for loading a MOT from background gas in a timely fashion, while maintaining a high vacuum in the lower chamber. The cold atoms trapped in the upper MOT can then be efficiently transferred to a MOT in the lower chamber. Finally, the cloud of cold atoms in the lower MOT can be dropped into the cavity. As we shall see, this process allows cold atoms to be delivered to the cavity in a timely fashion while maintaining the high vacuum necessary for achieving long trap lifetimes.

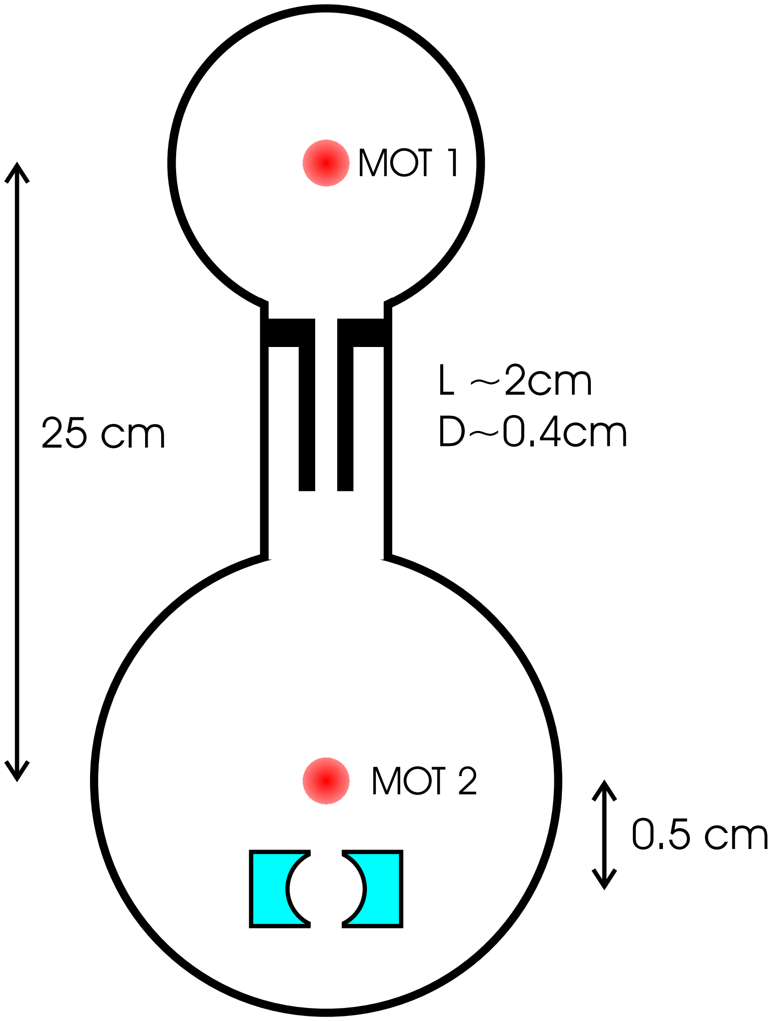

Figure 6.1: Schematic for Differential Vacuum System
The dual-chamber vacuum system used in our setup. The upper and lower chambers are at pressures $P_{\text{upper}} \sim 1.07 \times 10^{-8}$ Torr and $P_{\text{lower}} \sim 4.06 \times 10^{-10}$ Torr, respectively (inferred from measurements with an ion guage). The two chambers are connected by a tube of length $L \approx 2$ cm and diameter $D \approx 0.4$ cm which supports a ratio of pressures $\frac{P_{\text{upper}}}{P_{\text{lower}}} \sim 26$ (see Section 6.1.2).

The chamber and MOT setup used in our experiment was constructed by David Vernooy and Jun Ye. The details of construction and setup of the system are given in detail in David's Thesis [42]. The information contained in this chapter instead describes the possible effects of background gas on trapped atoms in our cavity. Magneto-Optical Traps are also discussed to understand the technology involved in delivering cold atoms to our cavity.

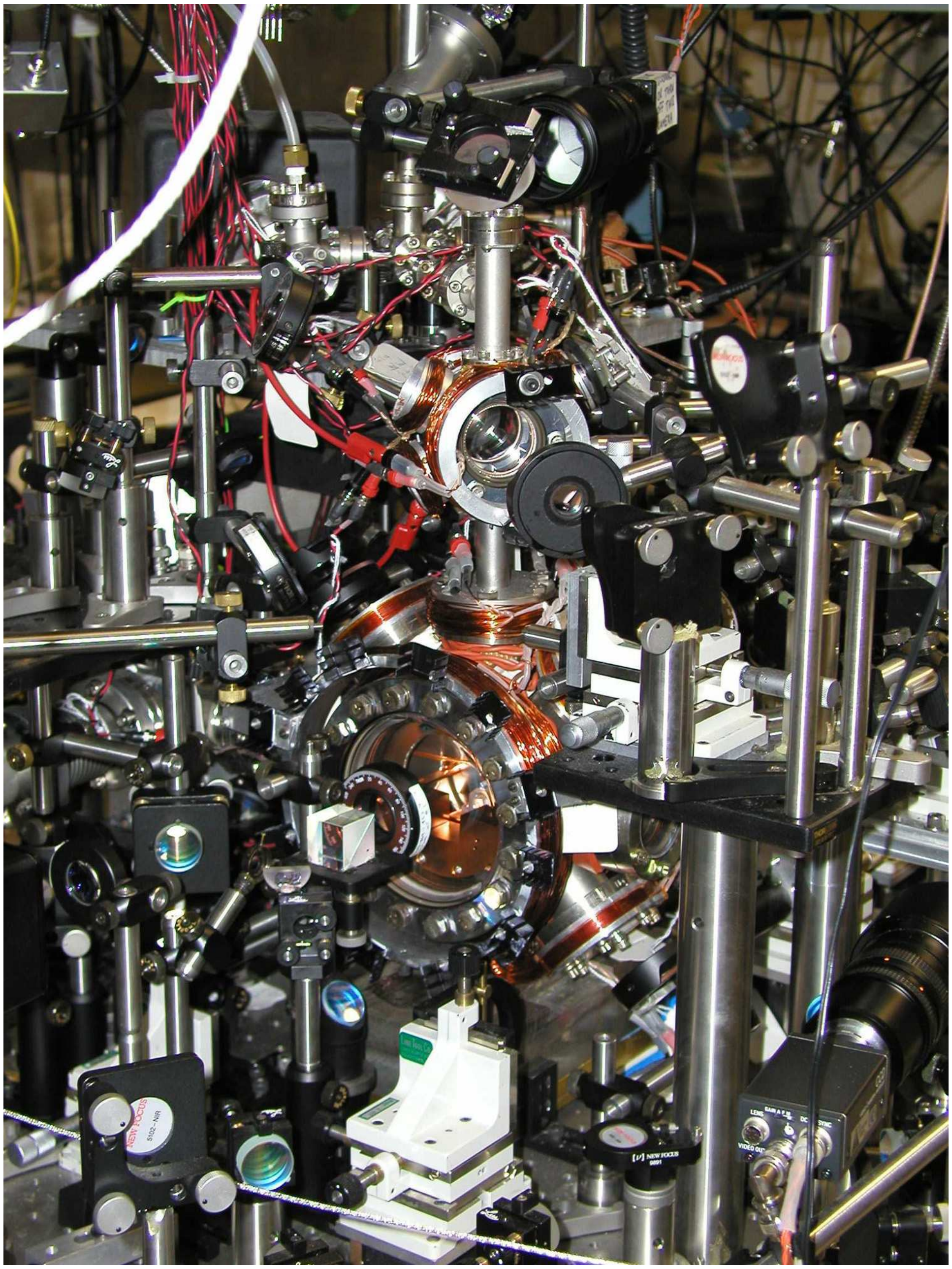

Figure 6.2: Vacuum Chamber for Our Experiment

The two chambers used to create the differential system for our experiment. The optics and magnet coils associated with the upper and lower MOTs can also be seen.

6.1 The Vacuum System

We are interested in the relation of the vacuum properties to the corresponding background gas. This is necessary to understand the effects of the background gas on our trap lifetime. Clearly, if a Cesium atom at room temperature collides with a cold atom trapped in our cavity, it will not remain trapped. Therefore, this type of interaction will constitute the ultimate limit for our trap lifetime.

6.1.1 Gas Flow in a Vacuum System

There are three useful quantities for understanding gas flow in a vacuum system. They are the pumping speed, S, the conductance, C, and the throughput, Q. The pumping speed is given by

$$S \equiv \frac{dV}{dt}, \tag{6.1}$$

corresponding to the volume rate of flow through a cross section of the vacuum system. This quantity is usually denoted in units of $[\frac{\text{liter}}{\text{sec}}]$, and vacuum pumps are typically specified by this parameter at their inlet.

The throughput is defined as the product of the pressure and pumping speed at a given cross section of the system. This is proportional to the mass rate of flow through that cross section, which can be verified as

$$Q \equiv PS = P\frac{dV}{dt} = n_v k_B T\frac{dV}{dt} = \frac{k_B T}{m} m n_v \frac{dV}{dt} = \frac{k_B T}{m}\frac{dM}{dt} \propto \frac{dM}{dt}, \tag{6.2}$$

where P and S respectively are the pressure and pumping speed at the cross section in question, n_v is the number of particles per unit volume at the point, k_B is Boltzman's constant, T is the temperature of the gas, m is the mass of a Cesium atom, and $\frac{dM}{dt}$ is the total mass rate of flow through the cross section.

The final quantity needed to analyze a vacuum system is the conductance, C, of a section of tube, defined as the proportionality constant between the driving force applied (i.e., the pressure differential) and the throughput:

$$Q = (P_1 - P_2)C. \tag{6.3}$$

Figure 6.3 shows the simplest setup of a tube with conductance C where the pressure and pumping speed at each end are (P_1, S_1) and (P_2, S_2). If we assume there are no sources inside the tube, the mass throughput will be uniform throughout the tube, so that

$$Q = \begin{cases} S_1 P_1 \\ C(P_1 - P_2) \\ S_2 P_2. \end{cases} \tag{6.4}$$

Some rearranging also reveals the relation

$$\frac{1}{S_1} = \frac{1}{S_2} + \frac{1}{C}. \tag{6.5}$$

For a vacuum pump located at point 2 and connected to a chamber at point 1 by a tube of conductance C, Equation 6.5 would yield the net pumping speed at the chamber. This is extremely useful in checking the suitability of a connection tube for a given system. It is best to overdesign the connection so that it does not severely degrade the pump performance. As an example, we consider the situation of a pump with speed $S_2 = 200\ \frac{\text{liter}}{\text{sec}}$ connected to a tube with conductance $C = 14\ \frac{\text{liter}}{\text{sec}}$. In this case, the net speed at the chamber is $\sim 13\ \frac{\text{liter}}{\text{sec}}$. This is not a good design, since the large capacity of the pump is wasted. This also demonstrates the importance of proper gauge placement. If the pressure is monitored at the pump, the pressure on the other end of the connection tube can be very different. A little algebra yields

$$P_1 = P_2 \left(1 + \frac{S_2}{C}\right). \tag{6.6}$$

In our example, the pressure at the chamber would be a factor of ~ 15 higher than that measured at the pump. This illustrates the importance of gas flow analysis in

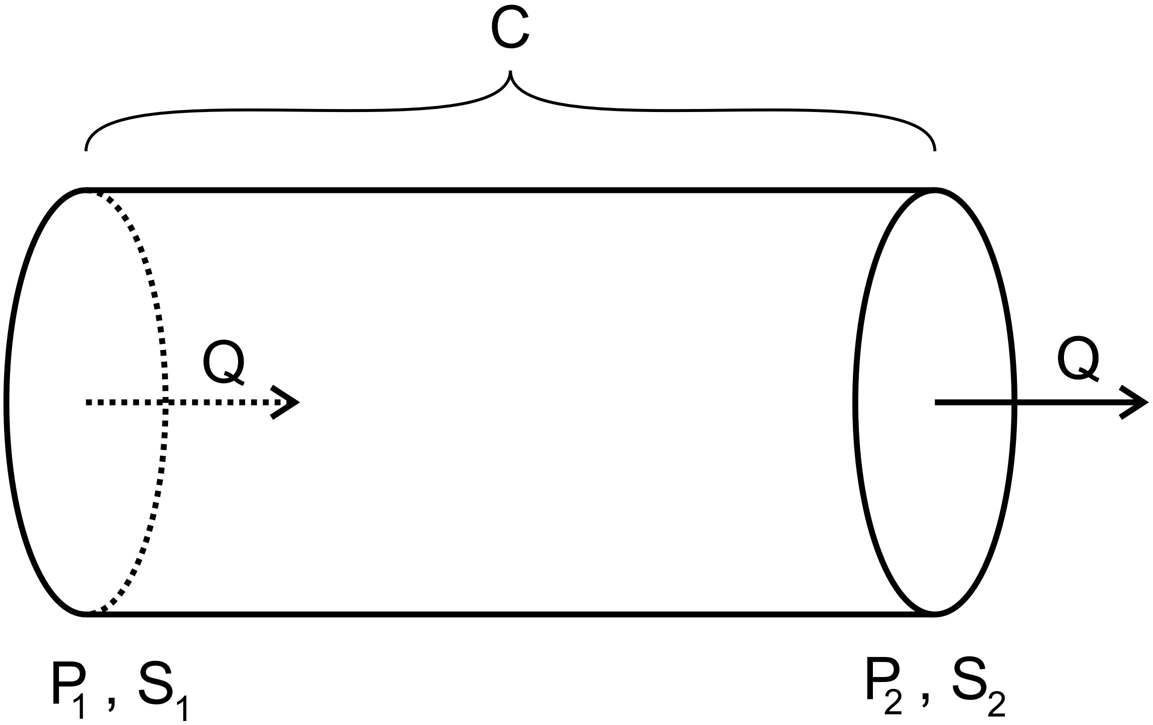

Figure 6.3: Relating Conductance, Throughput and Pumping Speed for a Tube
The pumping speed, S, throughput, Q, and conductance, C, are useful parameters in analyzing the gas flow in a vacuum system. The relations between them are explored in Section 6.1.1.

designing connection tubes and monitoring the pressure.

The conservation of mass throughput, Q, can be used to derive the network equations for tubes connected in series or parallel. For two tubes connected in series, the net conductance is

$$C_{\text{series}} = \frac{C_1 C_2}{C_1 + C_2}, \tag{6.7}$$

while the net conductance for tubes connected in parallel is

$$C_{\text{parallel}} = C_1 + C_2. \tag{6.8}$$

When the mean free path for collisions of the gas is much greater than the dimensions of the vacuum chamber, the process for gas flow is referred to as molecular flow. In this case, the momentum transfer occurs between the gas particles and the wall of the container with very little interaction between the particles. Therefore, the conductance in this region does not depend on the pressure, but only the geometry of the system. For a tube of circular cross section in the regime of molecular flow, the conductance for air at 20° C is given by

$$C \approx (1.2 \times 10^5)\frac{D^3}{L}, \tag{6.9}$$

where D and L are the tube diameter and length respectively in [m], and C has the units $[\frac{\text{liter}}{\text{sec}}]$.

6.1.2 Analysis of Gas Flow in Our Vacuum System

We need to know the pressure inside our lower chamber (see Figure 6.1) in order to determine the lifetime for trapped atoms due to collisions with a background gas. A simplified model of our system is found by assuming there are no sources in the lower chamber or the tubes connecting the chambers and pump. There are additional sources, such as outgassing throughout the chamber as well as the atoms that are dropped from the upper and lower MOT. However, this model will at least put a bound on how good our pressure can be and give us an idea of the expected collisional lifetimes.

The simplified model is illustrated in Figure 6.4. In this model, we have neglected the conductance of the lower chamber, since it is of significantly larger cross section than the tubes connected to it. Because we have assumed there are no extra sources in the lower chamber or the tubes connecting the chambers, the mass throughput, Q, is constant throughout the system. We will account for some of the imperfections of this model by assuming there is a base pressure throughout the system, P_0, when there is no mass flow through the system. This modifies Equation 6.2 to yield

$$Q = (P - P_0)S. \tag{6.10}$$

These conditions give the following for the mass throughput

$$Q = \begin{cases} (P_P - P_0)S_P \\ C_3(P_I - P_P) \\ (P_I - P_0)S_I \\ C_2(P_L - P_I) \\ (P_L - P_0)S_L \\ C_1(P_U - P_L) \\ (P_U - P_0)S_U, \end{cases} \tag{6.11}$$

where P_P and S_P are the pressure and pumping speed at the ion pump, P_I and S_I are the measured pressure and pumping speed at the ion gauge, P_L and S_L are the pressure and pumping speed in the lower chamber, P_U and S_U are the pressure and pumping speed of the upper chamber, P_0 is the base pressure in the system, C_1 is the conductance of the tube connecting the upper and lower chamber, C_2 is the conductance of the tube connecting the lower chamber to the T for the ion gauge, and C_3 is the conductance for the tube connecting the T to the ion pump. A little algebra then yields the following for the pumping speeds throughout the system

$$\begin{aligned} \frac{1}{S_I} &= \frac{1}{C_3} + \frac{1}{S_P}, \\ \frac{1}{S_L} &= \frac{1}{C_2} + \frac{1}{C_3} + \frac{1}{S_P}, \\ \frac{1}{S_U} &= \frac{1}{C_1} + \frac{1}{C_2} + \frac{1}{C_3} + \frac{1}{S_P}. \end{aligned} \tag{6.12}$$

A little more rearranging yields the following results for the pressures:

$$P_P = \frac{1}{C_3 + S_P}(C_3 P_I + S_P P_0), \tag{6.13}$$

$$P_L = P_0 + \left(\frac{1}{C_2} + \frac{1}{C_3} + \frac{1}{S_P}\right)\frac{C_3 S_P}{C_3 + S_P}(P_I - P_0), \tag{6.14}$$

and

$$P_U = P_0 + \left(\frac{1}{C_1} + \frac{1}{C_2} + \frac{1}{C_3} + \frac{1}{S_P}\right) \frac{C_3 S_P}{C_3 + S_P}(P_I - P_0). \tag{6.15}$$

The ratio of the upper chamber pressure to the lower chamber is given by

$$\frac{P_U}{P_L} = 1 + \frac{\frac{C_3 S_P}{C_1(C_3+S_P)}(P_I - P_0)}{P_0 + \left(\frac{1}{C_2} + \frac{1}{C_3} + \frac{1}{S_P}\right)\frac{C_3 S_P}{C_3+S_P}(P_I - P_0)}. \tag{6.16}$$

In our system (see Figure 6.4), the pumping speed of the ion pump is $S_P \approx 200\ \frac{\text{liter}}{\text{sec}}$. P_I is the pressure measured with the ion gauge and is typically $P_I \sim 2.5 \times 10^{-10}$ Torr. The background pressure is inferred from the pressure obtained when the system has been depleted of Cesium by closing the valve and pumping for some time, so that $P_0 \sim 1.0 \times 10^{-10}$ Torr. The tube connecting the upper chamber to the lower chamber has a length of $L_1 \sim 2 \times 10^{-2}$ m and diameter $D_1 \sim 4 \times 10^{-3}$ m. The conductance of this tube is $C_1 \sim 0.384\ \frac{\text{liter}}{\text{sec}}$. The tube connecting the lower chamber to the T for the ion gauge has a length of $L_2 \sim 1.524 \times 10^{-1}$ m, diameter $D_2 \sim 3.175 \times 10^{-2}$ m, and conductance $C_2 \sim 25.2\ \frac{\text{liter}}{\text{sec}}$. The tube connecting the T for the ion gauge to the ion pump has a length of $L_3 \sim 1.27 \times 10^{-1}$ m, diameter $D_3 \sim 3.175 \times 10^{-2}$ m, and conductance $C_3 \sim 30.24\ \frac{\text{liter}}{\text{sec}}$.

For a measured ion gauge pressure of $P_I = 2.5 \times 10^{-10}$ Torr and background pressure $P_0 = 1.0 \times 10^{-10}$ Torr, the parameters of our system yield a lower chamber pressure of $P_L \approx 4.06 \times 10^{-10}$ Torr and an upper chamber pressure of $P_U \approx 1.07 \times 10^{-8}$ Torr. The ratio of pressures supported by the differential pumping hole in this case is then 26.3.

These calculations show some important features of our system. Since the example of bad system design discussed in Section 6.1.1 corresponds to the actual parameters for our chamber, we see that while we have a large capacity ion pump with speed $S_P \sim 200\ \frac{\text{liter}}{\text{sec}}$, it is strangled by the connection tube to give a pumping speed at the lower chamber of $S_L \sim 12.9\ \frac{\text{liter}}{\text{sec}}$. The other important feature is the tube connecting the upper and lower chamber. The conductance is very small, $C_1 \sim 0.384\ \frac{\text{liter}}{\text{sec}}$. In this case, the small conduction is intentional. We want to be able to have a low

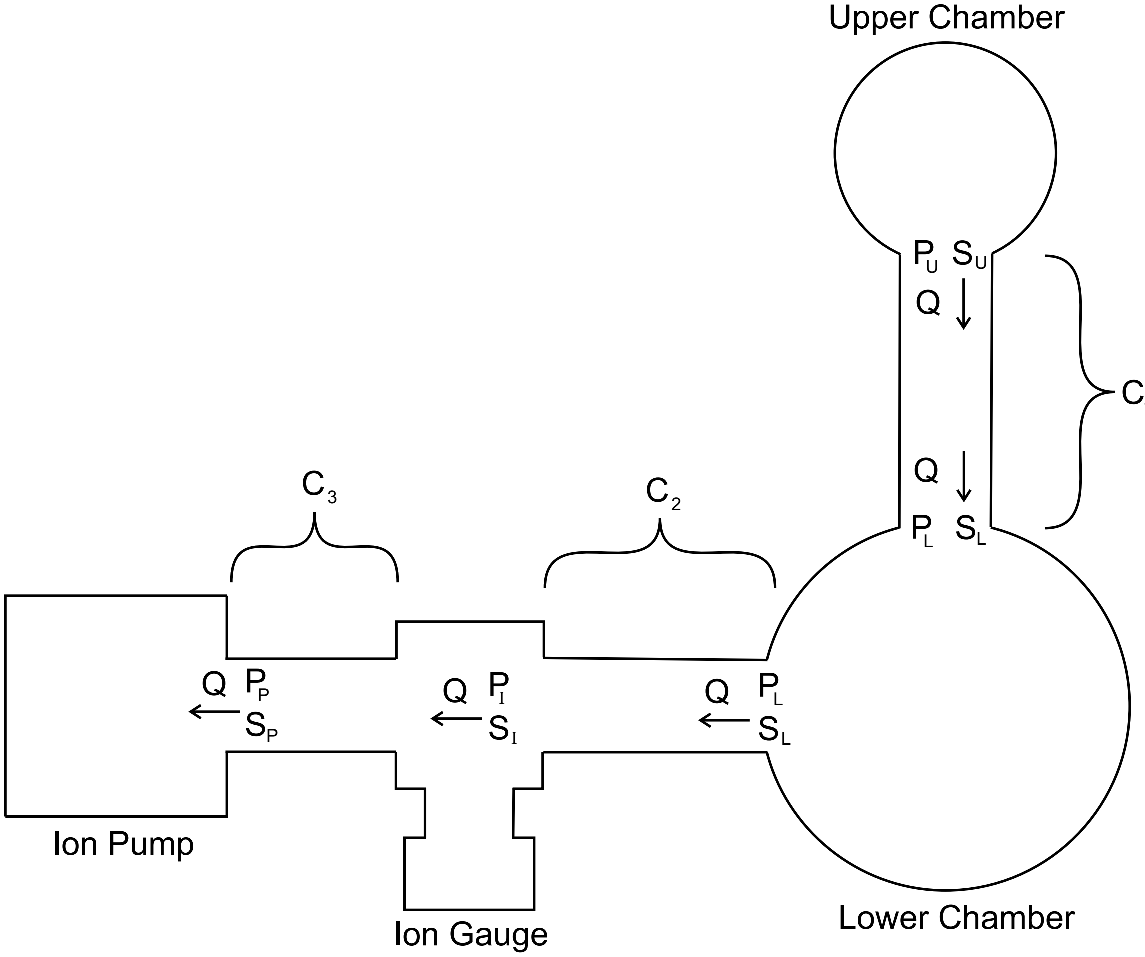
Upper Chamber
P_U S_U
Q
C_1
Q
P_L S_L
C_3
C_2
Q P_P
S_P
Q P_I
S_I
Q P_L
S_L
Ion Pump
Ion Gauge
Lower Chamber

Figure 6.4: A Simple Model for Gas Flow in Our System
In our simplified model, we assume that the only source is the upper chamber, so that the throughput, Q, is constant from the upper chamber to the lower ion pump. We also assume that the conductance of the lower chamber is infinite. This approximation is not unreasonable, since the cross section is much larger than the tubes connecting the pump and chambers. These approximations allow us to put a bound on the pressure in the lower chamber. (See Section 6.1.2)

pressure in the lower chamber for long trap lifetimes, while keeping a higher pressure in the upper chamber for efficient loading of a MOT from the background gas. This connection is referred to as a *differential pumping hole*, because it allows for a large differential in pressures. Our setup allows a pressure ratio of $\frac{P_{\text{upper}}}{P_{\text{lower}}} \approx 26$. This allows us to load the upper MOT in a reasonable time while maintaining a good vacuum in the lower chamber.

6.1.3 Relation of Pressure to Kinetic Properties of Particles

A simple kinetic calculation of the pressure is given by

$$\begin{aligned} P &= \frac{\overline{F}}{A} = \frac{1}{A}\overline{\frac{d(mv_\perp)}{dt}} = \frac{1}{A}\overline{\frac{d(mv_\perp)}{dx}v_\perp} = \frac{1}{A}(mn_v A\overline{v_\perp^2}) \\ &= mn_v\overline{v_\perp^2} = \frac{1}{3}mn_v v_{rms}^2 = \frac{1}{3}\rho v_{rms}^2, \end{aligned} \tag{6.17}$$

where F is the force on the wall, A is the area of the wall, m is the mass of the particles comprising the gas, $\overline{v_\perp}$ is the average velocity of the particle perpendicular to the wall, n_v is the number of particles per unit volume, ρ is the mass per unit volume, and v_{rms} is the root-mean-squared velocity of the particles.

The Maxwell-Boltzmann distribution of velocities is given by

$$N(v) = 4\pi N \left(\frac{m}{2\pi k_B T}\right)^{3/2} v^2 e^{-\frac{mv^2}{2k_B T}}, \tag{6.18}$$

where T is the temperature, k_B is Boltzmann's constant, m is the mass of the particles, and N is the total number of particles in the sample which can be verified by integrating the distribution

$$N = \int_0^\infty N(v)dv. \tag{6.19}$$

The average velocity is found to be

$$\overline{v} = \frac{\int_0^\infty N(v)vdv}{N} = \sqrt{\frac{8k_B T}{\pi m}}. \tag{6.20}$$

The root-mean-square velocity is given by

$$v_{rms} = \sqrt{\overline{v^2}} = \sqrt{\frac{\int_0^\infty N(v)v^2dv}{N}} = \sqrt{\frac{3k_BT}{m}}. \tag{6.21}$$

6.1.4 Mean-Free Path and Collision Times

Assuming the particles comprising a gas have a collisional cross section of σ, in a time t a particle sweeps out a volume σvt. Let n_v be the number of particles per unit volume. On average, the number of collisions in time $\bar{t}$ is given by $\sigma\overline{v}_{\text{rel}}\bar{t}n_v$, where $\overline{v}_{\text{rel}}$ is the average relative velocity. The mean time between collisions, $\bar{t}$, is given by

$$\bar{t} = \frac{1}{\sigma n_v \overline{v}_{\text{rel}}}. \tag{6.22}$$

Note that the mean time between collisions depends on the average *relative* velocity. Therefore, for collisions within the background gas, $\overline{v}_{\text{rel}} = \overline{v}\sqrt{2}$, where the $\sqrt{2}$ is due to the relative motion of the particles, and $\overline{v}$ is given by Equation 6.20. For collisions with a stationary atom, $\overline{v}_{\text{rel}} = \overline{v}$.

The mean distance between collisions is referred to as the mean free path, $\overline{L}$. From the preceding discussion we see that

$$\overline{L} = \overline{v}\bar{t} = \frac{\overline{v}}{\sigma n_v \overline{\overline{v}_{\text{rel}}}} = \frac{1}{\sqrt{2}\sigma n_v}, \tag{6.23}$$

where $\overline{v}$ is the average velocity in the gas (Equation 6.20), and $\overline{v}_{\text{rel}} = \overline{v}\sqrt{2}$ is the mean relative velocity of particles in the gas.

From Section 6.1.3 we know that the number of particles per unit volume can be related to the pressure as follows

$$n_v = \frac{P}{k_BT}, \tag{6.24}$$

where P is the pressure, k_B is Boltzmans's constant, and T is the temperature. The mean free path can now be expressed as

$$\overline{L} = \frac{k_B T}{\sigma P \sqrt{2}}, \tag{6.25}$$

where σ is the collisional cross section of the particles.

There are two types of collisions that will be important for our situation. First, collisions within the gas for which the mean collision time is

$$\overline{t}_{\text{gas}} = \frac{1}{\sigma n_v \overline{v_{\text{rel}}}} = \frac{k_B T}{\sqrt{2}\sigma P \overline{v}} = \frac{1}{\sigma P}\sqrt{\frac{k_B T \pi m}{16}}, \tag{6.26}$$

where the average velocity is given by Equation 6.20. In the second case, for interactions between stationary particles and the background gas, the relative velocity is increased by a factor $\sqrt{2}$. The mean time between collisions $\overline{t}_{\text{stat}}$ for this stationary particle case is

$$\overline{t}_{\text{stat}} = \frac{1}{\sigma P}\sqrt{\frac{k_B T \pi m}{8}}. \tag{6.27}$$

6.1.5 Collisional Lifetime for Background in Our System

The collisional lifetime, τ_{coll}, for almost stationary atoms in our trap interacting with a background gas is described precisely by the second case above. Therefore, $\tau_{\text{coll}} = \overline{t}_{\text{stat}}$, where $\overline{t}_{\text{stat}}$ is given by Equation 6.27. For a given temperature, the collisional lifetime depends inversely on the pressure, illustrating the importance of pressure on trap lifetimes.

We assume the background gas in our system is Cesium, with mass $m = 2.206 \times 10^{-25}$ kg and collisional cross section $\sigma \approx 2 \times 10^{-17}$ m^2 [43]. In many vacuum systems the pressure is measured in Torr, defined as $\frac{1}{760}$ of a standard atmosphere. (The following conversion is useful: 1 Torr $= 1.33322 \times 10^2$ $\frac{\text{N}}{\text{m}^2}$.) For a pressure of $P \sim 1 \times 10^{-10}$ Torr $\approx 1.333 \times 10^{-8}$ $\frac{\text{N}}{\text{m}^2}$ at room temperature ($300K$), we would have a collisional lifetime $\tau_{\text{coll}} \sim 71$ sec. Unfortunately, as we have seen in Section 6.1.2, the pressure in the lower chamber of our system is at least $P \sim 4.06 \times 10^{-10}$ Torr. The collisional lifetime for a trapped atom in this case would be limited to $\tau_{\text{coll}} \sim 17$ sec.

Unfortunately, we have no direct measurement of the residual pressure in the narrow cylinder between the mirror substrates (diameter 1 mm and length 40 μm). However, this places an upper bound on our expected lifetime. Therefore, our measured trap lifetime of $\sim$ 3 sec [4] may be limited by collisions with the background gas. This demonstrates the extreme importance of the vacuum system in conducting trapping experiments with long lifetimes. Other possible limits to the lifetime are discussed in Chapter 7.

6.2 Magneto-Optical Traps

The basic techniques involved in laser cooling and trapping have become a standard tool in atomic physics. The Magneto-Optical Trap (MOT) in particular forms the starting point for many experiments. There are many references describing the various types of Magneto-Optical traps and the theory behind their operation (see Reference [36]). This section is not intended to be an exhaustive reference on laser cooling and trapping. I will only discuss the principles involved, since these concepts are important for my later discussion of trapping atoms in our cavity.

6.2.1 Optical Molasses

Optical cooling of atomic motion arises from the transfer of momentum from a light field to a recoiling atom through the scattering of photons. Cooling is achieved by making this process velocity dependent. When this is extended to three dimensions, the light field acts as a viscous medium and is referred to as an *optical molasses*.

To understand the optical molasses, we start by examining the one-dimensional case of a two-level atom with resonance ω_a in the field of a laser with frequency ω_L propagating to the right. When the atom absorbs a photon, it is given a momentum kick of in the direction of propagation of the laser. When it spontaneously emits a photon, the direction is random. Therefore, over many cycles of absorption and emission, the recoil momentum for spontaneous emission will average to zero. This causes the atom to experience a net force along the direction of propagation of the laser given by

$$< F >= R_{sc}\frac{\hbar\omega}{c}, \tag{6.28}$$

where R_{sc} is the number of spontaneous scattering events per second given by

$$R_{sc} = \frac{\gamma\frac{I}{I_{\text{sat}}}}{1+\frac{I}{I_{\text{sat}}}+\left(\frac{\Delta}{\gamma}\right)^2}, \tag{6.29}$$

I is the intensity of the field, I_{sat} is the saturation intensity, γ is the spontaneous decay rate (HWHM), and $\Delta = \omega_L - \omega_a$ is the detuning of the laser from the atomic resonance. At low intensities the scattering rate is proportional to the intensity. As the intensity increases the scattering rate shows power broadening and the rate saturates.

The velocity of the atom leads to a Doppler shift, so the atom sees a laser frequency of $\omega_L\left(1-\frac{v}{c}\right)$, where v is the velocity of the atom anti-parallel to the field propagation. The scattering probability is related to the detuning, so the maximum scattering occurs when the Doppler shifted frequency matches the atom's resonance frequency. This occurs when $v = \frac{c}{\omega_L}\Delta$, where $\Delta = \omega_L - \omega_a$ is the detuning of the laser from the atomic resonance. The average force discussed above will have a velocity dependence due to the Doppler shift given by

$$< F >= \frac{\hbar\omega}{c}\frac{\gamma\frac{I}{I_{\text{sat}}}}{1+\frac{I}{I_{\text{sat}}}+\left(\frac{\Delta-\mathbf{k}\cdot\mathbf{v}}{\gamma}\right)^2}, \tag{6.30}$$

where $\mathbf{k}$ is the wave vector of the incident photon. Figure 6.5 shows the force on an atom as a function of velocity. The maximum force occurs for velocity $v = \frac{c\Delta}{\omega_L}$. When $\omega_L < \omega_a$ ($\Delta < 0$), the laser is red detuned and the force opposes the atom's forward motion. If a similarly detuned beam is directed to counterpropagate with the first, it will oppose the atom's backward motion. In this way, the atom will experience an average velocity dependent force, which is zero if it is not moving (also shown in Figure 6.5). This velocity dependent force can be extended to three dimensions with 3 orthogonal sets of counterpropagating beams acting as a viscous medium to slow down the atom. This configuration is referred to as an optical molasses. While the molasses leads to cooling, the atom performs a random walk in momentum space as it emits spontaneously. These fluctuations limit the lowest temperature achievable when the laser beam is present, corresponding to the Doppler cooling limit with temperature

$$T_D = \frac{\hbar\gamma}{k_B}. \tag{6.31}$$

For the D_2 line in Cesium, $\frac{\gamma}{2\pi} \approx 2.61$ MHz, so the Doppler limit is $\sim 125\ \mu$K.

The process relies on having many cycles of absorption and emission for the transition used for cooling. For an excited two-level atom, the atom will trivially return to the ground state through spontaneous emission and can be re-excited by the same beam. When such a transition exists in a real atom, it is referred to as a cycling transition. In a real atom, other levels could interfere with the Doppler cooling process by interfering with the necessary cycling (in the next section we will also see that they can sometimes lead to sub-Doppler cooling). Alkali atoms with nuclear spin I and total angular momentum F have the transition from the $S_{\frac{1}{2}}$ ground state with $F = I + \frac{1}{2}$ to the $P_{\frac{3}{2}}$ state with $F = I + \frac{3}{2}$ that satisfies the cycling condition. The excited state cannot decay to the other hyperfine level ($F = I - \frac{1}{2}$) of the ground state because of the $\Delta F = 0, \pm 1$ selection rule. This transition is the D_2 line and is commonly used for the trapping of alkali atoms, with saturation intensities $I_{\text{sat}} \sim 1\ \frac{\text{mW}}{\text{cm}^2}$.

6.2.2 Magneto-Optical Trap

Although the optical molasses will cool the atoms, they will still diffuse out of the region if there is no position dependence to the damping/friction force. While there are multiple ways to induce a position dependence, one method relies on the Zeeman shift produced by a magnetic field. The position dependent force is created by applying an inhomogeneous magnetic field and appropriately polarized laser beams to the region. The magnetic field regulates the rate at which an atom in a particular position scatters photons, creating a position dependent force [36].

Consider the simplified case of an atom with $J = 0$ ground state and $J = 1$ excited

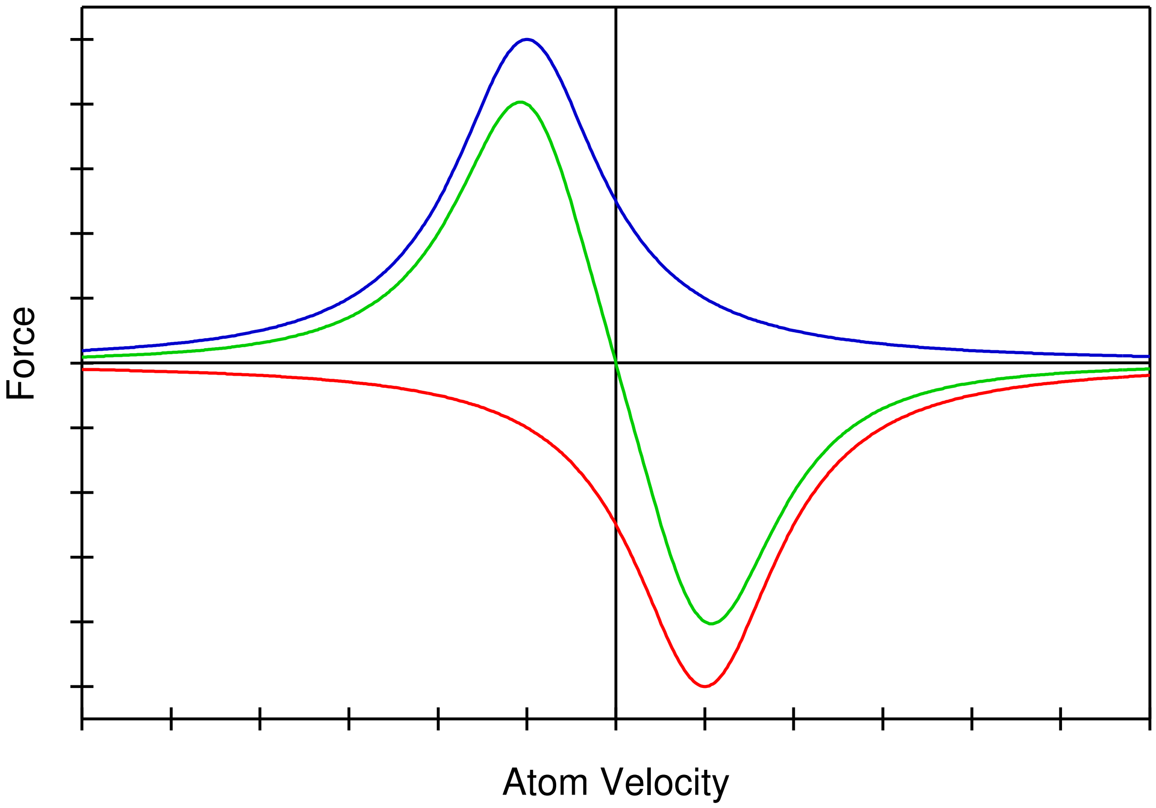

Figure 6.5: Force on an Atom in Counterpropagating Red-Detuned Fields
The one-dimensional case of a two-level atom in counterpropagating fields with detuning $\Delta = \omega_L - \omega_a < 0$. The blue line shows the force on an atom in a field propagating to the right, the red line shows the force for a field propagating to the left, and the green line shows their sum, which is the net force on the atom for the two counterpropagating fields. These forces are velocity dependent because of the Doppler shifts due to the atomic motion. For a single beam, the maximum force occurs at speed $v = \frac{c\Delta}{\omega_L}$. For the combined beams, the force is zero when the atom is not moving. This effect leads to Doppler cooling of the atoms.

state illuminated by counterpropagating beams with opposite circular polarization. Conservation of angular momentum dictates that the σ^- beam can only excite transitions to the $m_F = -1$ state, while the σ^+ beam can only excite transitions to the $m_F = +1$ state.

A quadrupole magnetic field can be created by using two anti-Helmholtz coils. This field is zero at the origin and is proportional to the distance from the origin, for small displacements. The degenerate excited state energy levels will be split by an amount $(\frac{1}{2}\mu_B g B m_F)$, where μ_B is the Bohr magneton, B is the magnitude of the magnetic field, g is the Landé g-factor, and m_F is the magnetic sublevel of the atom. If the optical beams and magnetic field are oriented as shown in Figure 6.6A, the Zeeman shift is linear in x. When the atom moves to the right of the origin, the magnetic field it sees increases causing the $m_F = +1(-1)$ state to go up (down) in energy. If the laser frequency is red detuned to be below all of the split levels, the level with the least detuning will scatter the most. In this case, it will be the $m_F = -1$ state with the σ^- light which is propagating to the left, opposite the atom's motion (see Figure 6.6B, $B > 0$ case). This will tend to push the atom back towards the center. If the atom moves to the left of the origin, the opposite happens and the atom is once again pushed back to the center of the trap where the magnetic field is zero. In this way, a restoring force can be created to confine the atoms to the origin. This idea can be extended to three dimensions by using three orthogonal pairs of counterpropagating beams to create a linear restoring force in each direction. Damping in the trap is then provided by the optical molasses created by the same beams as discussed in the previous section.

6.2.3 Sub-Doppler Cooling in a MOT

As we have seen in the previous sections, Doppler cooling methods are limited in their ability to cool an atom. If one wishes to cool beyond the Doppler limit, other mechanisms must be employed. While there are many possible methods of performing sub-Doppler cooling, I will discuss one method referred to as Polarization Gradient

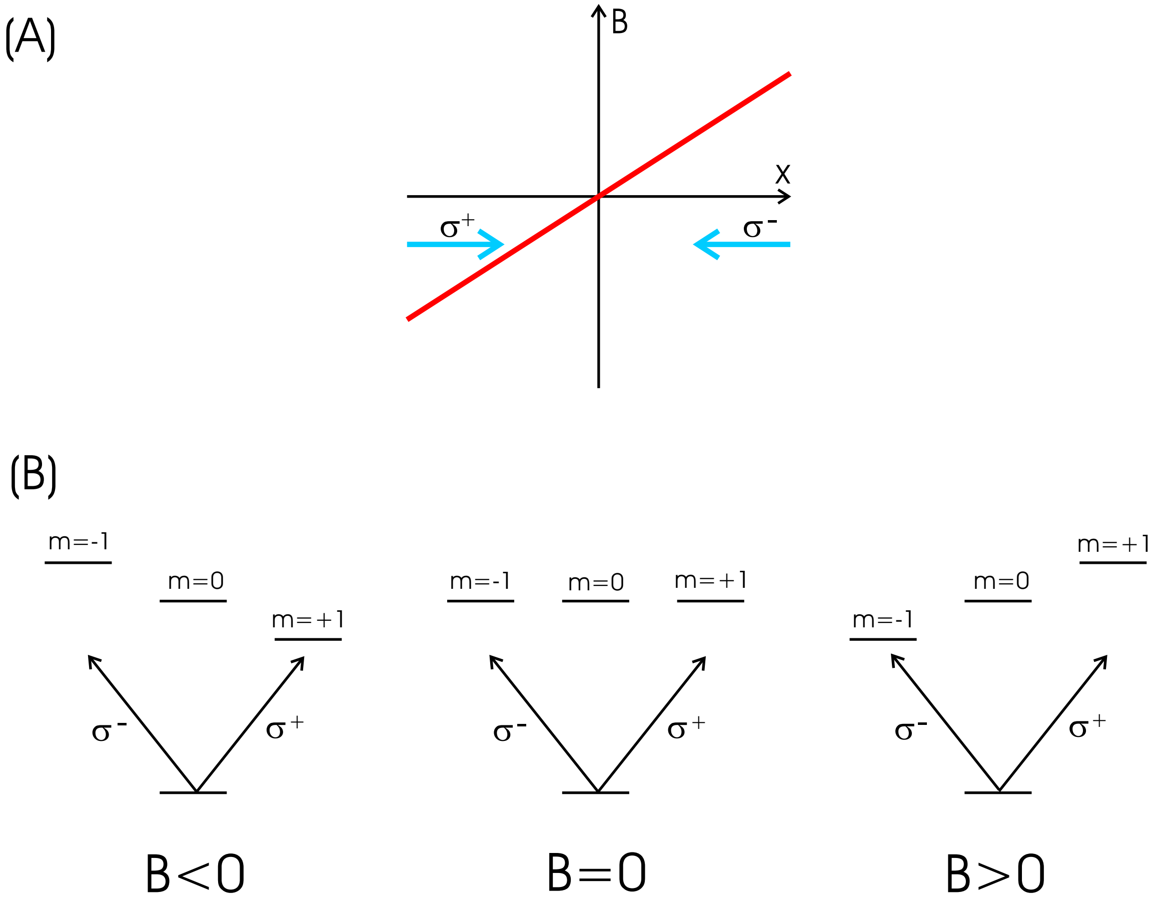
(A)
B
x
σ+
σ-
(B)
m=-1
m=0
m=+1
σ-
σ+
B<0
m=-1
m=0
m=+1
σ-
σ+
B=0
m=+1
m=0
m=-1
σ-
σ+
B>0

Figure 6.6: Restoring Force in a MOT

The one-dimensional case of a two-level atom in a position-dependent magnetic field with counterpropagating opposite circularly polarized beams. As the atom moves from the origin, the magnetic field causes Zeeman splitting affecting the scattering rates. A position-dependent restoring force is created.

Cooling (PGC).

The following example is discussed in detail in References [44] and [45]. Consider an atom with ground state $J = \frac{1}{2}$ and excited state $J = \frac{3}{2}$ confined to move along two orthogonal linearly polarized counterpropagating beams. The atom will see a position-dependent polarization for the field. Over a distance of $\lambda/2$, the polarization will vary from purely σ^+ to linear at 45° with respect to the two beams, to purely σ^-, to linear at $-45°$, returning to σ^+. This is just one method of creating a light field with polarization gradients.

The light will induce Stark shifts in the different magnetic sublevels of the ground level, yielding a position and internal-state dependent potential. When the light field is σ^+, the shift of the $m = +\frac{1}{2}$ sublevel is larger than that of the $m = -\frac{1}{2}$ sublevel. When the light is σ^-, the opposite is true. Therefore, the ground state shifts for the two cases will change as shown in Figure 6.7. In addition, the different polarizations will induce different optical pumping effects: The σ^+ light tends to put the population into the $m = +\frac{1}{2}$ state, whereas the σ^- light tends to put the population into the $m = -\frac{1}{2}$ sublevel.

In this way, as the atom moves due to its thermal energy, it is forced to climb a potential hill. If it has enough energy to reach the top of a neighboring hill, it will be optically pumped to the other sublevel where it is again at the minimum of the potential. As the atom moves away from this point, it once again climbs a potential hill. As shown in Figure 6.7, each optical pumping event results in the absorption of light at a lower frequency than the emitted light, leading to a dissipation of energy. This process will continue until the kinetic energy is too small to climb the next hill. This process is often referred to as Sisyphus Cooling because the atoms are forced to always move ‘uphill.’

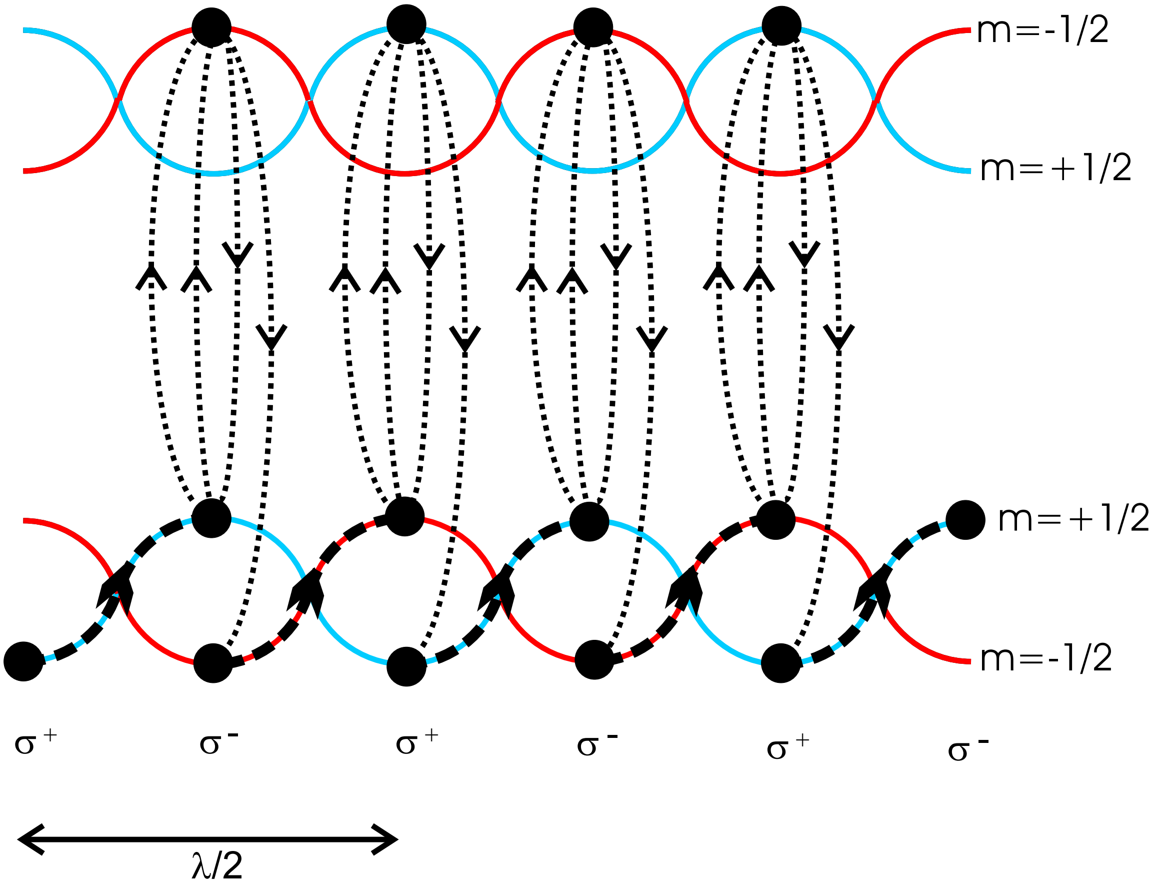

Figure 6.7: Polarization Gradient Cooling
An atom with ground state $J = \frac{1}{2}$ and excited state $J = \frac{3}{2}$ is confined to move along two orthogonal linearly polarized counterpropagating beams. These beams create an alternating polarization gradient of σ^+ and σ^-. The σ^+ light tends to pump the atom to $m = +\frac{1}{2}$, while the σ^- light tends to pump the atom to $m = -\frac{1}{2}$. The polarization gradient also creates a position and internal state dependent potential. This potential combined with the optical pumping leads to the Sisyphus cooling described in Section 6.2.3. As shown in the diagram, each optical pumping event results in the absorption of light at a lower frequency than the emitted light, leading to a dissipation of energy.

Chapter 7

Dipole Force Traps

While a cavity QED probe can be used to trap an intracavity atom [5], we prefer to decouple the trap and probe fields. In addition, we would like to create a trapping potential that is independent of the atom's internal state. Optical dipole traps are far detuned and rely on the electric dipole interaction with far detuned light, implying low optical excitation of the transition. In addition, we will see that the multiple levels of a real atom can be exploited to create a trap that is insensitive to the atomic state.

7.1 Classical Dipole Force

When a dielectric is placed in an electric field $\overrightarrow{E}$, it becomes polarized with a dipole moment $\overrightarrow{p}$ given by

$$\overrightarrow{p} = \alpha \overrightarrow{E}, \tag{7.1}$$

where α is the polarizability of the dielectric. The force on the induced dipole moment is given by

$$\overrightarrow{F}_{\text{dip}} = (\overrightarrow{p} \cdot \nabla)\overrightarrow{E} = \nabla \left(\overrightarrow{p} \cdot \overrightarrow{E} \right). \tag{7.2}$$

Because the dipole potential is related to the dipole force by

$$\overrightarrow{F}_{\text{dip}} = -\nabla U_{\text{dip}}, \tag{7.3}$$

we now can express the dipole potential as

$$U_{\text{dip}} = -\overrightarrow{p} \cdot \overrightarrow{E} = -\alpha \left|\overrightarrow{E}\right|^2 . \tag{7.4}$$

If the electric field is due to electromagnetic radiation, we can now see that the dipole potential will be proportional to the intensity, I, of the electromagnetic field,

$$U_{\text{dip}} \propto -I. \tag{7.5}$$

This implies that a trapping potential could be produced with a spatially varying intensity profile. This potential is not stable, however, since scattering with the detuned field leads to heating. Fortunately, as we shall see in the next section, the scattering rate can be made arbitrarily small.

7.2 Two-Level Atom

The dipole potential for a two-level atom in the limit of large detuning and negligible saturation is given by [46]

$$U_{\text{dip}} = \frac{3\pi c^2 \gamma}{\omega_0^3} \frac{I}{\Delta} \propto \frac{I}{\Delta}, \tag{7.6}$$

where ω_0 is the atomic resonance frequency, ω_{trap} is the frequency of the trapping light, $\Delta = (\omega_{\text{trap}} - \omega_0)$ is the detuning of the trapping field, I is the intensity of the trapping light, and γ is the spontaneous decay rate (HWHM) for the transition. For a red detuned field ($\Delta < 0$) we have an attractive potential, $U_{\text{dip}} < 0$, and the atom will be attracted to the maximum of the field intensity. The scattering rate, R_{sc}, for this transition in the same regime is given by

$$R_{\text{sc}} = \frac{6\pi c^2 \gamma^2}{\hbar \omega_0^3} \frac{I}{\Delta^2} \propto \frac{I}{\Delta^2} \propto \frac{U_{\text{dip}}}{\Delta}. \tag{7.7}$$

For a desired potential, U_{dip}, as the detuning, Δ, is increased, the intensity, I, can be increased to maintain the same potential depth. However, the scattering rate will decrease. In this way, the scattering rate can be made arbitrarily small for a given trap depth. The practical limits to this in a real atom are the other atomic levels that are present, making it difficult to have arbitrarily large detunings for a trapping potential.

The trap depth, U_0, is often quoted in terms of the resulting AC Stark shift, δ_{AC}, through the relation [47]

$$U_0 = \hbar\delta_{AC}, \tag{7.8}$$

where the AC Stark shift is given by [46]

$$\delta_{AC} = \frac{3\pi c^2\gamma}{\hbar\omega_0^3}\frac{I}{\Delta}. \tag{7.9}$$

The spontaneous scattering rate can then be expressed as

$$R_{sc} = \frac{2\gamma}{\Delta}\delta_{AC}. \tag{7.10}$$

Both absorption and spontaneous emission contribute to the heating of the trapped atom [46]. At large detunings, the heating due to absorption corresponds to an increase in thermal energy in the direction light propagation equal to the recoil energy, E_{rec}, per scattering event. Spontaneous emission also results in an increase in energy equal to the recoil energy per scattering event, however, this occurs in a random direction. In this way, the longitudinal motion will be heated on average by $\frac{4}{3}E_{rec}$ per scattering process, whereas the two transverse directions are each heated by by $\frac{1}{3}E_{rec}$. The overall heating corresponds to an increase of $2E_{rec}$ in a time R_{sc}^{-1}.

If we assume that a spontaneously scattered photon leads to heating by twice the recoil energy, E_{rec}, we have a lifetime of [48]

$$\tau = \frac{U_0}{2E_{rec}R_{sc}}, \tag{7.11}$$

where the recoil energy is given by

$$E_{rec} = \frac{\hbar^2 k^2}{2m} = \frac{2\hbar^2\pi^2}{m\lambda^2}. \tag{7.12}$$

7.3 Multi-Level Alkali Atoms

There are several references for the general results of a multi-level atom in a FORT [46, 48, 47, 49, 50]. Here we will consider the results for the ground state of alkali atoms, where spin-orbit coupling leads to the D-line doublet with $S_{1/2} \rightarrow (P_{1/2}, P_{3/2})$. The coupling to the nuclear spin then produces the hyperfine structure of the ground and excited states. In this case, the potential and spontaneous scattering rate of a ground state with total angular momentum F and magnetic quantum number m_F is given by [46]

$$\begin{aligned} U(\mathbf{r}) &= \frac{\pi c^2\gamma}{w_0^3}\left(\frac{2+Pg_Fm_F}{\Delta_{2,F}} + \frac{1-Pg_Fm_F}{\Delta_{1,F}}\right) I(\mathbf{r}), \\ R_{\rm sc}(\mathbf{r}) &= \frac{2\pi c^2\gamma^2}{\hbar w_0^3}\left(\frac{2}{\Delta_{2,F}^2} + \frac{1}{\Delta_{1,F}^2}\right) I(\mathbf{r}), \end{aligned} \tag{7.13}$$

where $P = (1, 0, -1)$ for transitions $(\sigma^+, \pi, \sigma^-)$ respectively, $\Delta_{1,F}$ is the detuning of the FORT light from the $P_{1/2}$ state, $\Delta_{2,F}$ is the detuning of the FORT light from the $P_{3/2}$ state, (F, m_F) are the hyperfine and magnetic sublevels, and g_F is the Landé g-factor. This result is valid for both linear and circular polarization as long as all optical detunings stay large compared with the excited state hyperfine splitting.

7.4 State Insensitive Trap

In order to create a trapping potential, spatial variations in the fields which create AC Stark shifts are necessary. However, this makes spectroscopy difficult, since they change the ground and excited states differently. For a two-state atom, a field that causes an AC Stark shift for the ground state would cause the opposite shift in the excited state. Therefore, for a trapping potential of the ground state, the excited state is actually repelled. This leads to the unfortunate consequence that the effective detuning between an atomic transition and the cavity mode becomes a strong function of the atom's position within the trap, which interferes with the cavity QED interactions [16]. However, due to the specific multi-level structure of Cs, the wavelength of the trapping laser can be tuned to a region where this problem is eliminated [13, 14, 15]. Ideally we would like to have both the excited and ground state trapped with the same shifts, so that optical transitions will not lead to additional heating beyond the recoil heating.

We can use the multiple atomic levels to our advantage by choosing the appropriate trapping laser wavelength that couples to several excited states. In this way, we can manipulate the AC Stark Shifts of multiple levels to produce a potential with the same shift in the ground and excited state [46]. A simplified illustration of this scenario is depicted in Figure 7.1. Imagine a three-level system $(|g\rangle, |e\rangle, |c\rangle)$ where $|g\rangle$ is the ground state, $|e\rangle$ is the excited state, and $|c\rangle$ is another state. If we have a field, Ω, red-detuned from the $|g\rangle \rightarrow |e\rangle$ transition by Δ_{ge}, the AC Stark shift of the ground state is $U_{ge} \propto -\frac{\gamma_e I}{\Delta_{ge}}$, where γ_e is the spontaneous decay rate of $|e\rangle$ and I is the intensity of the field. The AC Stark shift for the state $|e\rangle$ due to this field has the opposite sign as that of the ground state, $-U_{ge}$. The applied field has a similar effect on the $|e\rangle \rightarrow |c\rangle$ transition. In that case, the AC Stark shift of the state $|e\rangle$ is $U_{ec} \propto -\frac{\gamma_c I}{\Delta_{ec}}$, where γ_c is the spontaneous decay rate of $|c\rangle$. The AC Stark shift of the state $|c\rangle$ due to this field is $-U_{ec}$. If the wavelength is chosen appropriately, such that $U_{ec} = 2U_{ge}$, the AC Stark shift of the ground and excited states will be equal (see Figure 7.1). This is a desirable situation for spectroscopy, since the spatial dependance of the trapping field will have no effect on the transition frequency. The trapping wavelength that achieves this situation is referred to as the 'magic' wavelength [13, 14, 15].

In Cesium we can use the $6S_{1/2}$, $6P_{3/2}$ and $6D_{5/2}$ atomic levels to achieve the scenario described in Figure 7.1. In the range $920 - 950$ nm the ground state is relatively unchanged, while the excited state is strongly affected because it couples to a higher lying state. This is similar to the scheme proposed in Reference [51] and implemented in Reference [52]. Around the 'magic' wavelength $\lambda_F = 935.6$ nm, the

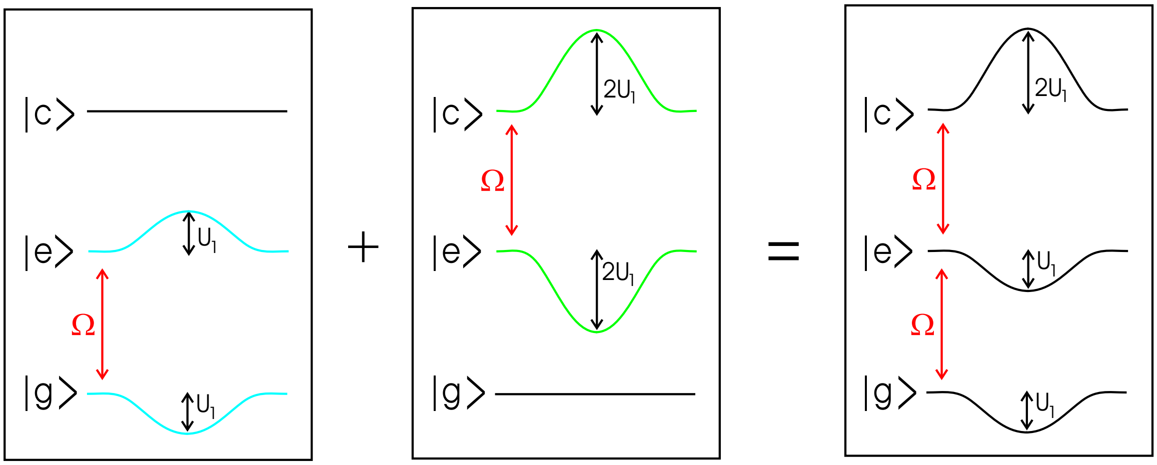

Figure 7.1: Simplified Illustration of the ‘Magic’ Wavelength

Imagine a three-level system ($|g\rangle, |e\rangle, |c\rangle$) where $|g\rangle$ is the ground state, $|e\rangle$ is the excited state, and $|c\rangle$ is another state. A FORT is created with a field, Ω, red-detuned from the $|g\rangle \rightarrow |e\rangle$ transition by Δ_{ge}, to produce an trapping potential in the ground state of U_1. The AC Stark shift for the state $|e\rangle$ due to this field has the opposite sign as that of the ground state to create a repulsive potential, $-U_1$. The applied field has a similar effect on the $|e\rangle \rightarrow |c\rangle$ transition. If the wavelength is chosen such that the potential created for the $|e\rangle$ state is $2U_1$, the potential for the $|c\rangle$ state will be $-2U_1$. The resultant potential for the excited state due to these two effects is U_1. In this situation, the AC Stark shift of the ground and excited states will be equal.

sum of the AC Stark shifts coming from different allowed optical transitions results in the ground, $6S_{1/2}$, and excited, $6P_{3/2}$, states both being shifted downwards by comparable amounts, $\delta_{6S_{1/2}} \simeq \delta_{6P_{3/2}}$. The AC-Stark shifts remain slightly dependent on the hyperfine and magnetic quantum numbers of the $6P_{3/2}$ states, as shown in Figure 7.2. Jeff computed these shifts using an extended model that includes counter-rotating terms and the following couplings: $6S_{1/2} \rightarrow nP_{1/2,3/2}$, for $n = (6-11)$; $6P_{3/2} \rightarrow nS_{1/2}$ for $n = (6-15)$; $6P_{3/2} \rightarrow nD_{3/2,5/2}$ for $n = (5-11)$. The relevant parameters are taken from References [35] and [53].

7.5 Trap Vibrational Frequencies

In the harmonic approximation for a standing wave dipole force trap, the oscillation frequency for the trapped atom in the axial direction will be

$$\omega_{\mathrm{ax}} = 2\pi\sqrt{\frac{2\hbar\delta_{AC}}{m\lambda^2}}, \tag{7.14}$$

where m is the mass of the atom and δ_{AC} is the maximum AC stark shift (in radians per second) of the trap. In the radial direction, the oscillation frequency is

$$\omega_{\mathrm{rad}} = \sqrt{\frac{4\hbar\delta_{AC}}{mw_0^2}}, \tag{7.15}$$

where w_0 is the beam waist.

For our case of Cesium, $m = 2.206 \times 10^{-25}$ kg, in a FORT with wavelength $\lambda = 935.6$ nm and trap depth $\frac{\delta_{AC}}{2\pi} = 47$ MHz, the axial and radial oscillation frequencies are $\nu_{\mathrm{ax}} \sim 570$ kHz and $\nu_{\mathrm{rad}} \sim 5.2$ kHz, respectively.

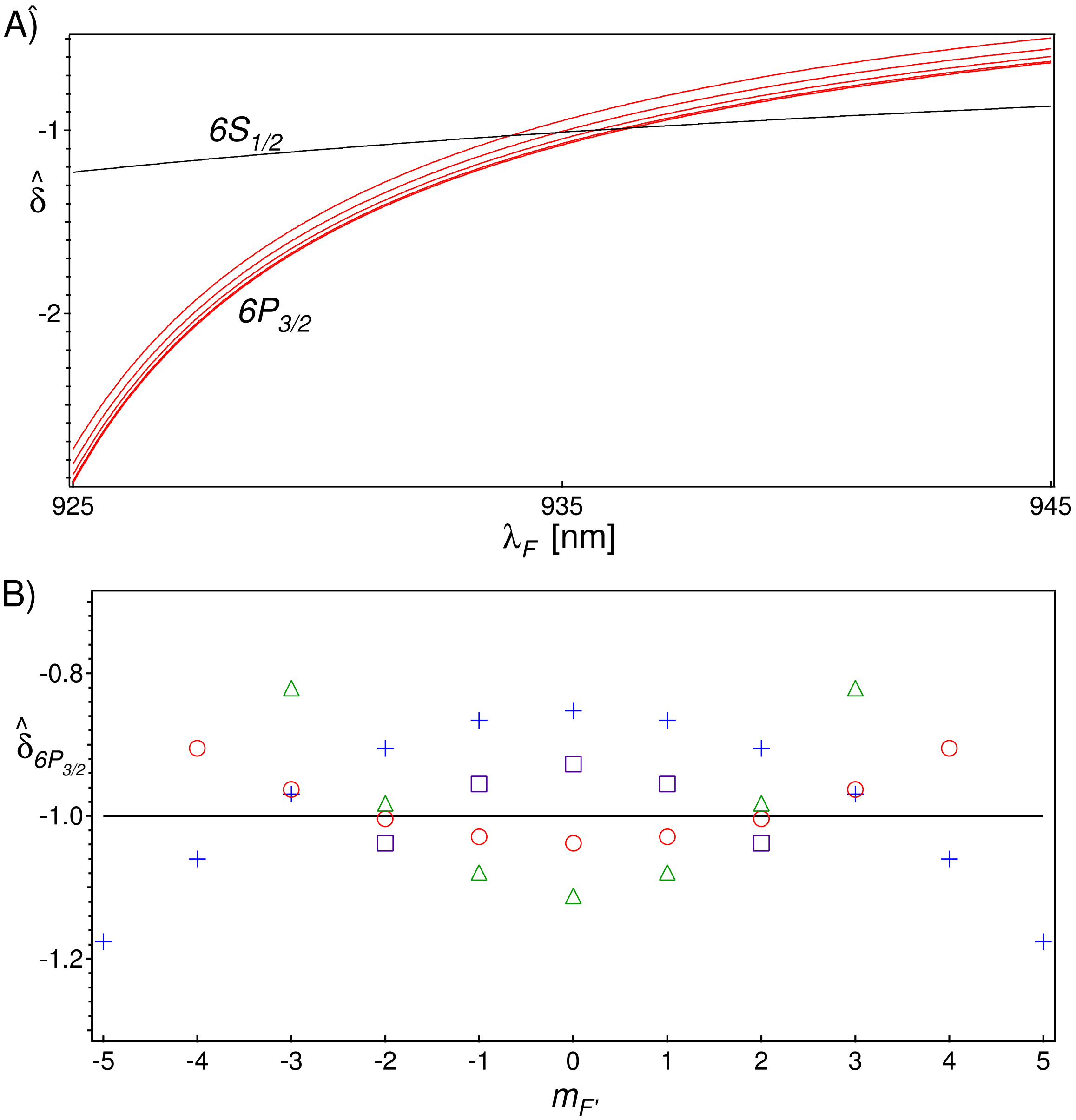

Figure 7.2: AC Stark Shifts for Cesium in a Linear FORT

A) The AC-Stark shifts $(\hat{\delta}_{6S_{1/2}}, \hat{\delta}_{6P_{3/2},F'=4})$ as functions of FORT wavelength λ_F for atomic Cs for a linearly polarized FORT. In each case, the normalization is $\hat{\delta} = \delta/[\delta_{6S_{1/2}}(\lambda_F = 935.6 \text{ nm})]$.

B) The AC Stark shift $\hat{\delta}_{6P_{3/2}}$ versus $m_{F'}$ for each of the levels $6P_{3/2}, F' = (2, 3, 4, 5)$ for $\lambda_F = 935.6$ nm. The normalization is $\hat{\delta} = \delta/[\delta_{6S_{1/2}}(\lambda_F = 935.6 \text{ nm})]$.

7.6 Scattering Processes and Population Transfer in the FORT

There are off-resonant scattering processes driven by the FORT light that transfer the population between the $6S_{1/2}, F = (3, 4)$ ground-state hyperfine levels for Cesium atoms trapped in our FORT. Therefore, we typically have repump light present in the trap that maintains the $F = 4$ population. Figure 7.3 shows a lifetime plot for the trapped Cesium atoms in the presence of the $F = 3 \rightarrow 4$ repump light. In this experiment, the trap lifetime was $\tau_{\text{trap}} \approx 2.7$ sec. In order to check the timescales for the off-resonant scattering rates, we initially deplete the $F = 4$ population and monitor the re-equilibration of the population between $F = (3, 4)$. Figure 7.3 also shows a plot of the change in population due to scattering as a function of time for the case of no repump light. In that case we see that the population equilibrates between the $F = 3$ and $F = 4$ states with a timescale of $\tau_{\text{eq}} = 0.14 \pm 0.03$ sec. David Boozer performed a numerical simulation based upon the relevant scattering rates in our FORT that predicts $\tau_{\text{eq}} \sim 0.10$ sec for atoms trapped exactly at the peak FORT intensity and with an unpolarized initial state in the $F = 3$ manifold.

7.7 Heating Due to FORT Intensity Fluctuations

Intensity fluctuations of the trapping field lead to parametric heating of the trapped atom [54, 55]. This heating is characterized by an exponential temperature growth at the rate

$$\Gamma_p \equiv \frac{1}{\tau_p} = \pi^2 \nu_{tr}^2 S_e(2\nu_{tr}), \tag{7.16}$$

where $S_e(2\nu_{tr})$ is the power spectral density of fractional intensity fluctuations evaluated at twice the (harmonic) trap frequency ν_{tr}. In our FORT, the relevant harmonic frequencies are $\nu_a = 570$ kHz for motion along the x-axis of the cavity and $\nu_r = 5.2$ kHz in the radial $y - z$ plane. However, due to the anharmonic shape of the FORT potential, as a trapped atom heats, its motion will include a wide spectrum of frequencies below (ν_a, ν_r). We therefore estimate a lower bound to the FORT lifetime due to this heating mechanism by taking the maximum value of Γ_p over the frequency range of interest, leading to $\tau_p^{axial} > 1.6$ s and $\tau_p^{radial} > 10^4$ s, suggesting that parametric heating in the radial direction is not an issue; however, axial heating could be important. Subsequent measurements of the FORT lifetime were performed in which the intensity noise was reduced below the shot-noise level of our detection system, giving a lower bound of $\tau_p^{axial} > 9$ s. Unfortunately, the measured lifetime was only $\tau = (3.1 \pm 0.4)$ s, indicating that other mechanisms are at least partially responsible for the observed decay rates.

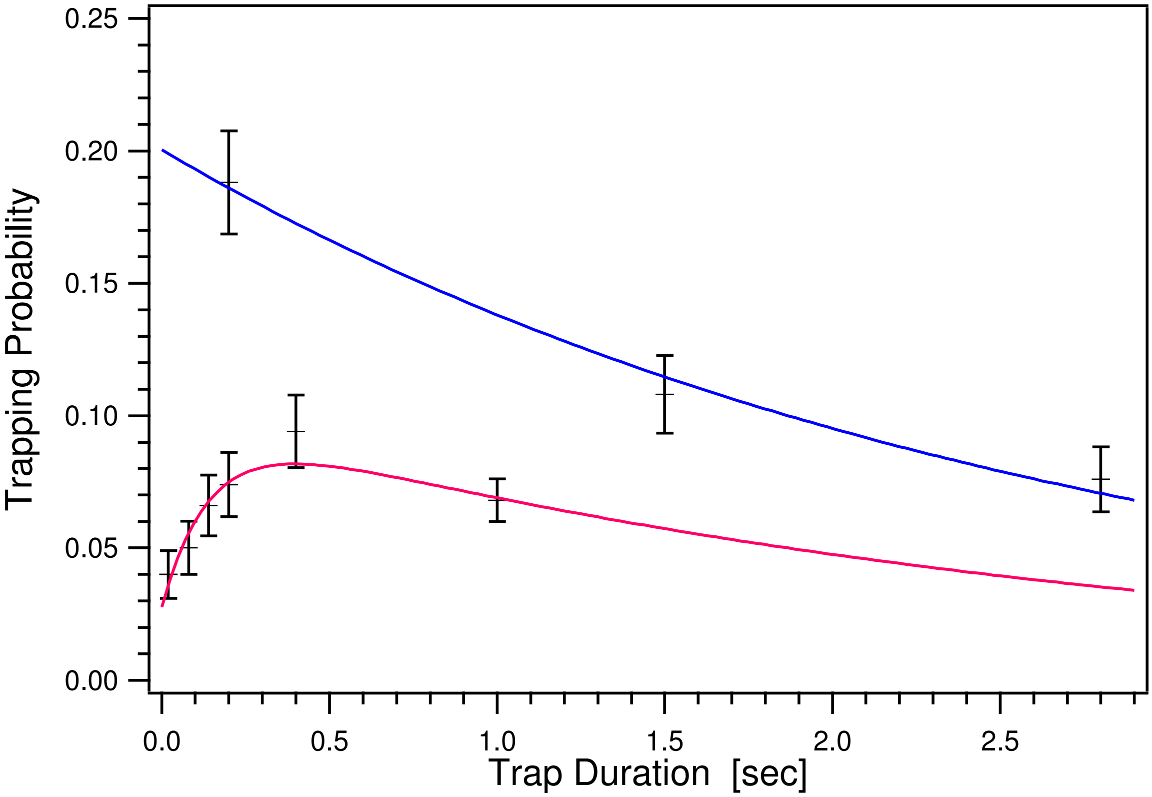

Figure 7.3: Depolarization of State Populations in Our FORT

The blue trace is a lifetime curve for atoms trapped in our FORT in the presence of $F = 3 \rightarrow 4$ repump light. In that case, the exponential decrease in the population is due to atoms leaving the trap. A fit to $y = Ae^{-t/\tau}$ for the data yields $A = 0.20 \pm 0.01$ and $\tau_{\text{trap}} = 2.7 \pm 0.3$ sec. The red trace is for the case of no repump light and an initial depletion of the $F = 4$ state population. Because we are able to detect the atoms in the $F = 4$ state, we can monitor the population as a function of time. The resulting curve will be due to both the decrease in atoms leaving our trap and an increase in the $F = 4$ population (Our detection scheme is not sensitive to atoms in the $F = 3$ state.) For the lower trace, a fit of $y = Ae^{-t/\tau_{\text{trap}}} - Be^{-t/\tau_{\text{eq}}}$, where A and τ_{trap} are obtained from the previous lifetime fit, yields $B = 0.072 \pm 0.01$ and $\tau_{\text{eq}} = 0.14 \pm 0.03$ sec. This timescale agrees well with that obtained from simulations of the scattering rates.

Chapter 8

Realizing Trapping with an Intracavity FORT

This chapter discusses the details of our experiments to trap single atoms in a high-finesse Fabry-Perot cavity. We achieve this trapping through the use of an intracavity far off resonance dipole force trap (FORT). In the course of this experiment, we have constructed FORT trapping potentials at various wavelengths (constrained by the free spectral range of our cavity). In the current version, by making use of the 'magic' wavelength for Cesium described in Chapter 7, we have been able to create an external potential for the center-of-mass motion that is only weakly dependent on the atom's internal state. This has enabled long trapping lifetimes $\tau \simeq 3$ sec. In addition, it has allowed us to perform continuous, real-time observations of single trapped atoms in a regime of strong coupling with mean duration 0.4 sec and with individual events lasting $\simeq 1$ sec.

The principal parameters for our system relevant to cavity QED are the Rabi frequency, $2g_0$, for a single quantum of excitation and the amplitude decay rates (κ, γ) due to cavity losses and atomic spontaneous emission. For our system, $\frac{g_0}{2\pi} = 24$ MHz, $\frac{\kappa}{2\pi} = 4.2$ MHz, and $\frac{\gamma}{2\pi} = 2.6$ MHz, where g_0 is for the $(6S_{1/2}, F = 4, m_F = 4) \rightarrow (6P_{3/2}, F' = 5, m'_F = 4)$ transition in atomic Cs at $\lambda_0 = 852.4$ nm. We are able to meet the requirements of strong coupling, $g_0 \gg (\kappa, \gamma)$, discussed in Chapter 4. The saturation photon and critical atom number are respectively $n_0 \equiv \frac{\gamma^2}{2g_0^2} \simeq 0.006$ and $N_0 \equiv \frac{2\kappa\gamma}{g_0^2} \simeq 0.04$.

The small transition shifts for our FORT should enable the application of a variety of laser cooling schemes to achieve atomic confinement in the Lamb-Dicke regime. The realization of this FORT also sets the stage for further advances in quantum information science via photon-atom interactions. For example, for an atom trapped in our FORT, the rate of optical information [56] is $\mathcal{R} \equiv \frac{g_0^2}{\kappa} \sim 10^9\ \frac{1}{\text{sec}} \gg (\kappa, \gamma)$, leading to information about atomic dynamics at a rate that far exceeds that from either cavity decay at the rate κ or spontaneous scattering at the rate γ (as in fluorescence imaging). This suggests new possibilities for sensing and control of the quantum dynamics of an individual system.

8.1 The Experimental Setup

Our experimental setup is schematically depicted in Figures 8.1 and 8.2. The input to the cavity consists of cavity QED probe, FORT-trapping, and cavity-locking beams, all of which are directed to separate detectors at the output. Figure 8.2 shows a schematic for the optical layout used to derive these beams. Because of a small stress-induced birefringence in the cavity mirrors, we attempt to align the directions of linear polarization for the FORT and cavity QED fields along an axis that coincides with one of the cavity eigen-polarizations [34]. The transmitted probe beam is monitored using heterodyne detection, allowing real-time detection of individual cold atoms within the cavity mode [32]. The cavity length is actively controlled using a cavity resonance at $\lambda_C = 835.8$ nm, so the length is stabilized and tunable independently of all other intracavity fields [2].

Figure 8.1 also shows the transverse beams used for cooling and repumping of the atoms. They are comprised of two additional orthogonal pairs of counter-propagating beams in a $\sigma^+ - \sigma^-$ configuration, illuminating the region between the cavity mirrors along directions at $\pm 45°$ relative to $\hat{y}, \hat{z}$ (the "$y - z$ beams") and contain cooling light tuned to the red of the $F = 4 \rightarrow F' = 5$ transition and repumping light near the $F = 3 \rightarrow F' = 3$ transition. These beams eliminate the free-fall velocity to capture atoms in the FORT and provide for subsequent cooling of trapped atoms.

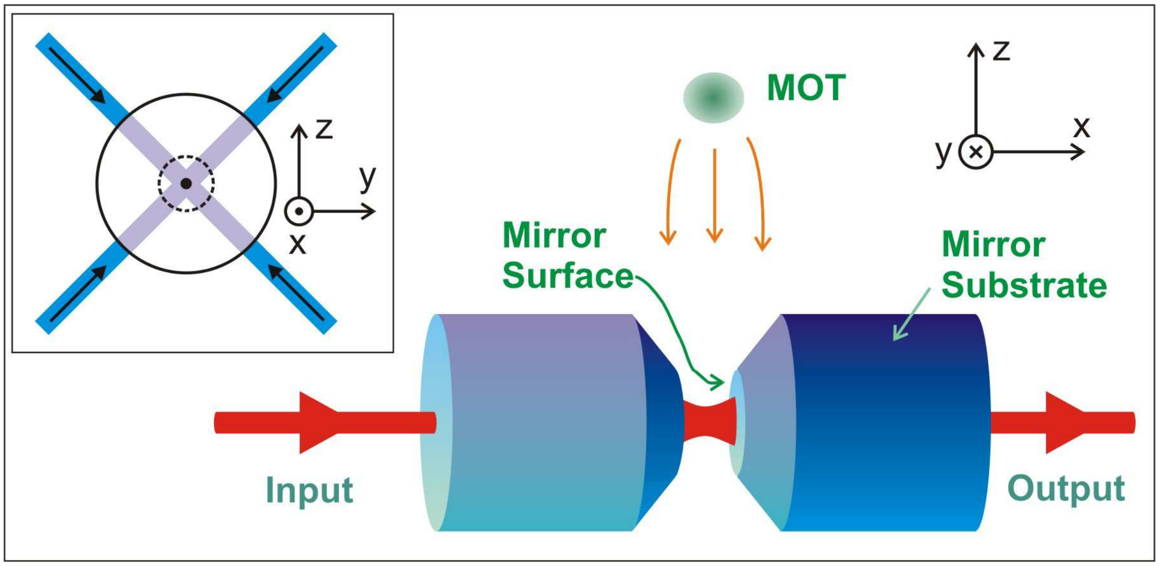

Figure 8.1: Schematic of the Trapping Experiment
An overview of our experiment to trap single atoms in a high-finesse Fabry-Perot cavity. The input to the cavity consists of cavity QED probe, FORT-trapping, and cavity-locking beams, all of which are directed to separate detectors at the output. Relevant cavity parameters are length $l = 43.0\ \mu$m, waist $w_0 = 23.9\ \mu$m, and finesse $\mathcal{F} = 4.2 \times 10^5$ at 852 nm. The inset illustrates the transverse beams used for cooling and repumping. They are comprised of two additional orthogonal pairs of counter-propagating beams in a $\sigma^+ - \sigma^-$ configuration, illuminating the region between the cavity mirrors along directions at $\pm 45°$ relative to $\hat{y}, \hat{z}$ (the "$y - z$ beams") and contain cooling light tuned to the red of the $F = 4 \rightarrow F' = 5$ transition and repumping light near the $F = 3 \rightarrow F' = 3$ transition. These beams eliminate the free-fall velocity to capture atoms in the FORT and provide for subsequent cooling of trapped atoms.

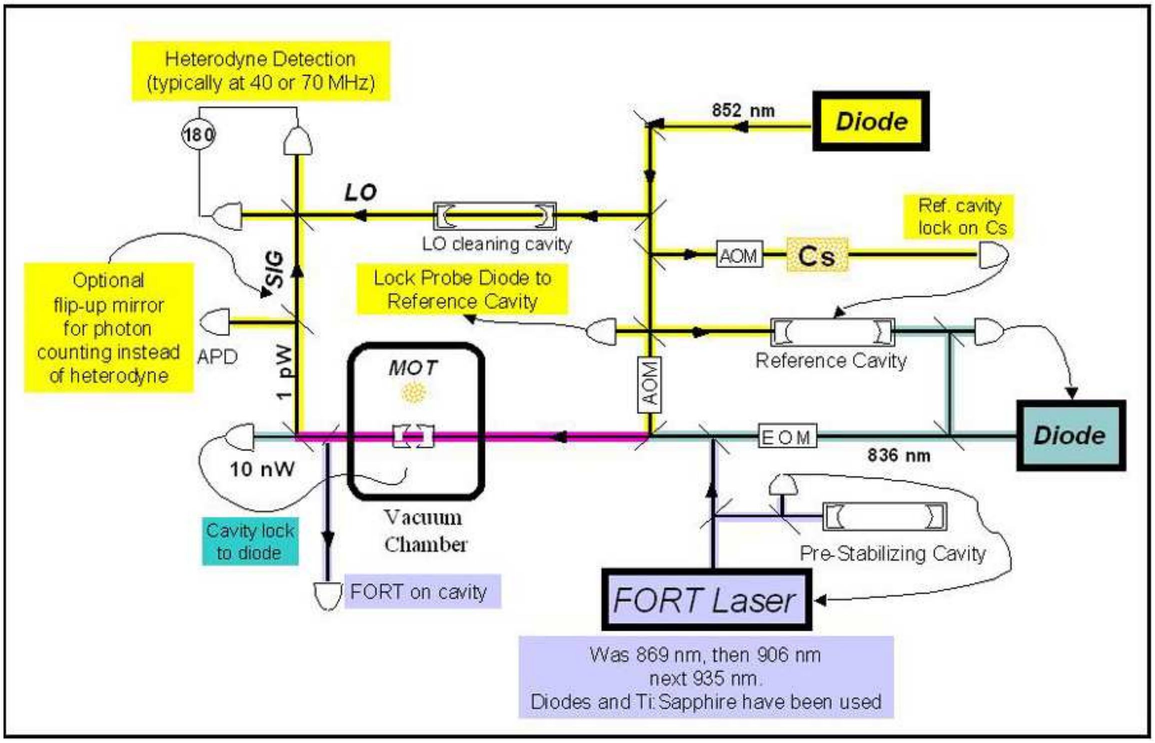
Heterodyne Detection
(typically at 40 or 70 MHz)
180
LO
SIG
LO cleaning cavity
852 nm
Diode
Ref. cavity
lock on Cs
AOM
Cs
Optional
flip-up mirror
for photon
counting instead
of heterodyne
Lock Probe Diode to
Reference Cavity
APD
1 pW
MOT
AOM
Reference Cavity
Diode
EOM
836 nm
10 nW
Vacuum
Chamber
Cavity lock
to diode
FORT on cavity
Pre-Stabilizing Cavity
FORT Laser
Was 869 nm, then 906 nm
next 935 nm.
Diodes and Ti:Sapphire have been used

Figure 8.2: Optical Layout for the Trapping Experiment

The input to the cavity consists of cavity QED probe, FORT-trapping, and cavity-locking beams, all of which are directed to separate detectors at the output. The transmitted probe beam is monitored using heterodyne detection, allowing real-time detection of individual cold atoms within the cavity mode. The cavity length is actively controlled using a cavity resonance at $\lambda_C = 835.8$ nm, so the length is stabilized and tunable independently of all other intracavity fields. This beam is referenced to the correct wavelength for the cavity through the use of a separate transfer cavity locked to the appropriate Cesium transition.

We estimate the (incoherent) sum of the four intensities to be $I_{4-5} \sim 60\ \frac{\text{mW}}{\text{cm}^2}$ for the cooling and $I_{3-3} \sim 40\ \frac{\text{mW}}{\text{cm}^2}$ for the repumping light, with uncertainties of roughly a factor of 2.

While the principles involved in realizing our trapping system are relatively straightforward, the implementation of this seemingly simple protocol is fairly involved. This can be illustrated best by comparing the schematic shown in Figure 8.2 to a picture of the actual experiment in Figure 8.3.

8.1.1 Delivering Atoms to the Cavity Mode Volume

As discussed in Chapter 6, we use a dual MOT system in order to deliver cold Cesium atoms to our cavity. We first collect approximately 10^8 Cesium atoms in the upstairs MOT (as estimated by Jun and David [42]). They are cooled with polarization gradient cooling before being dropped through the differential pumping hole (see Figure 6.1). These atoms are then captured in the lower MOT approximately 5 mm above the cavity, where they are again cooled to through polarization gradient cooling. The transfer efficiency of this process is approximately 10% [42].

After being released from the lower MOT, the freely falling atoms pick up energy when they are dropped from a height h, corresponding to a temperature of

$$T_D = \frac{mgh}{k_B}. \tag{8.1}$$

Therefore, the atoms have a temperature of ~ 0.8 mK when they reach the cavity. Because this is much larger than the Doppler temperature for Cesium ($\sim 125\ \mu$K), it would at first appear unnecessary to further cool the sample in the lower MOT. However, the expansion of the MOT as it falls is governed by its temperature. Therefore, in order to efficiently deliver atoms to the cavity mode volume, the MOT must be made as cold as possible to reduce the expansion. Similarly, the cloud of atoms from the upper MOT must be able to drop through the differential pumping hole to be efficiently transferred to the lower MOT.

We are able to control the density of atoms delivered to the cavity mode volume

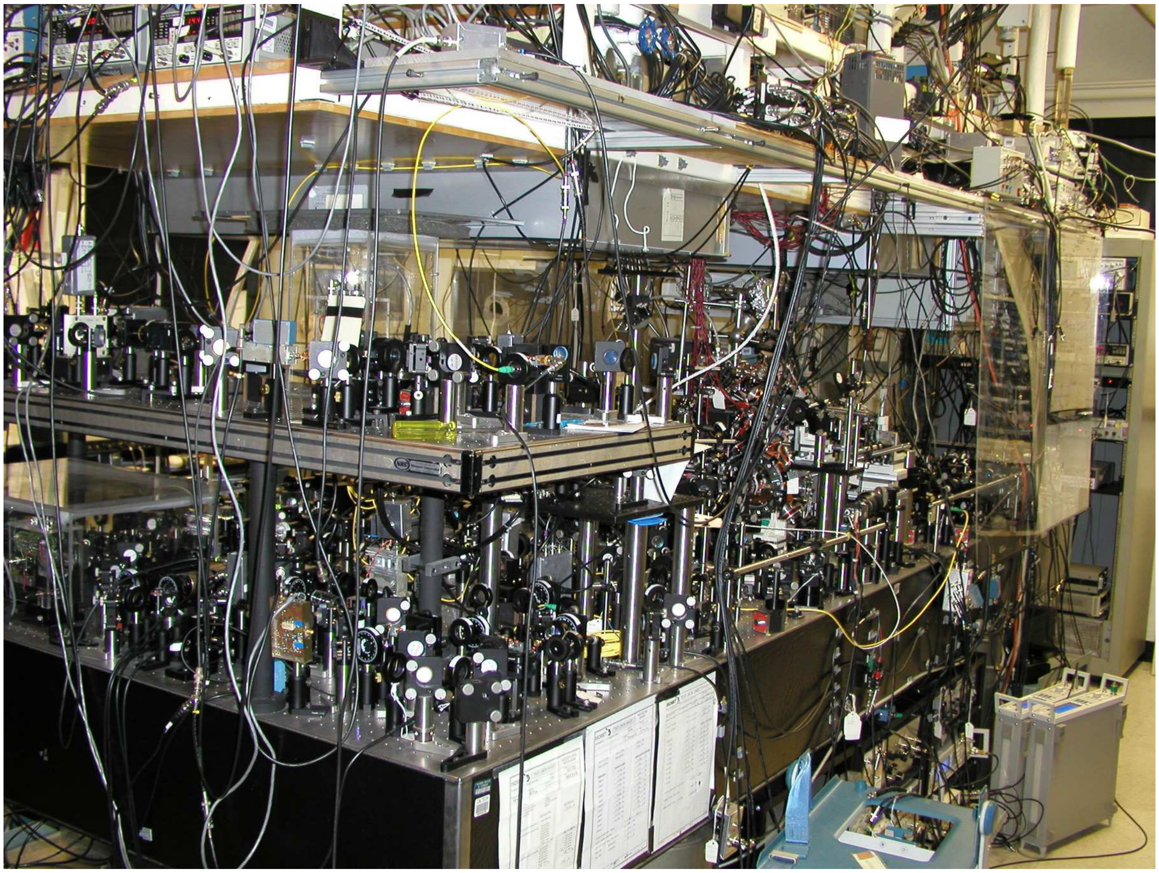

Figure 8.3: Lab 11 Trapping Experiment
A picture of the actual setup for our experiment. This can be contrasted to the optical layout depicted in Figure 8.2, demonstrating the complexity of the apparatus currently necessary for experimentally achieving the simple situation of a single atom coupled to a high-finesse cavity in a regime of strong coupling.

by changing the number of initial atoms in the upper MOT. This is accomplished by controlling the upper MOT loading time. The freely falling atoms arrive at the cavity mode over an interval of about 10 ms, and the density of intracavity atoms can be controlled over the range $0.011 \leq \bar{N} \leq 0.30$. Estimates of $\bar{N}$ are obtained from the mean number of atom transit events (each of duration $\simeq 150\mu$s) during the interval $\simeq$ 10ms from the falling MOT atoms, in the absence of trapping.

8.1.2 Atom Transits

Transits occur because the presence of an intracavity atom modifies the intracavity field (see Chapter 4) which is then measured by monitoring the probe transmission through the cavity. The trajectory of an atom can be monitored, since the output is dependent on the spatially dependent coupling coefficient

$$g(\overrightarrow{r}) = g_0 \sin\left(\frac{2\pi x}{\lambda}\right) \exp\left[-\frac{y^2+z^2}{w_0^2}\right], \tag{8.2}$$

where

$$g_0 = d \cdot E = d\sqrt{\frac{\hbar\omega}{2\varepsilon_0 V_{\mathrm{m}}}}, \tag{8.3}$$

d is the atomic dipole matrix element, ω is the transition frequency, V_{m} is the cavity mode volume, and $2g_0$ is the single-photon Rabi frequency. The spatial dependence is due to the standing wave structure of the cavity mode.

From the previous section we know that the atoms dropped from the lower MOT have a kinetic energy of $\frac{E_K}{k_B} \simeq 0.8$ mK, corresponding to a velocity of $v \simeq 0.22$ m/s. For a cavity mode waist of $w_0 \sim 20$ μm, this will translate into a cavity mode transit time of $\delta t = \frac{2w_0}{v} \simeq 175$ μs. For atoms dropped from the upper MOT at a height of $h \sim 25$ cm without lower MOT trapping, the transit time will be reduced to ~ 25 μs. Figure 8.4 shows typical transits from the upper and lower MOTs.

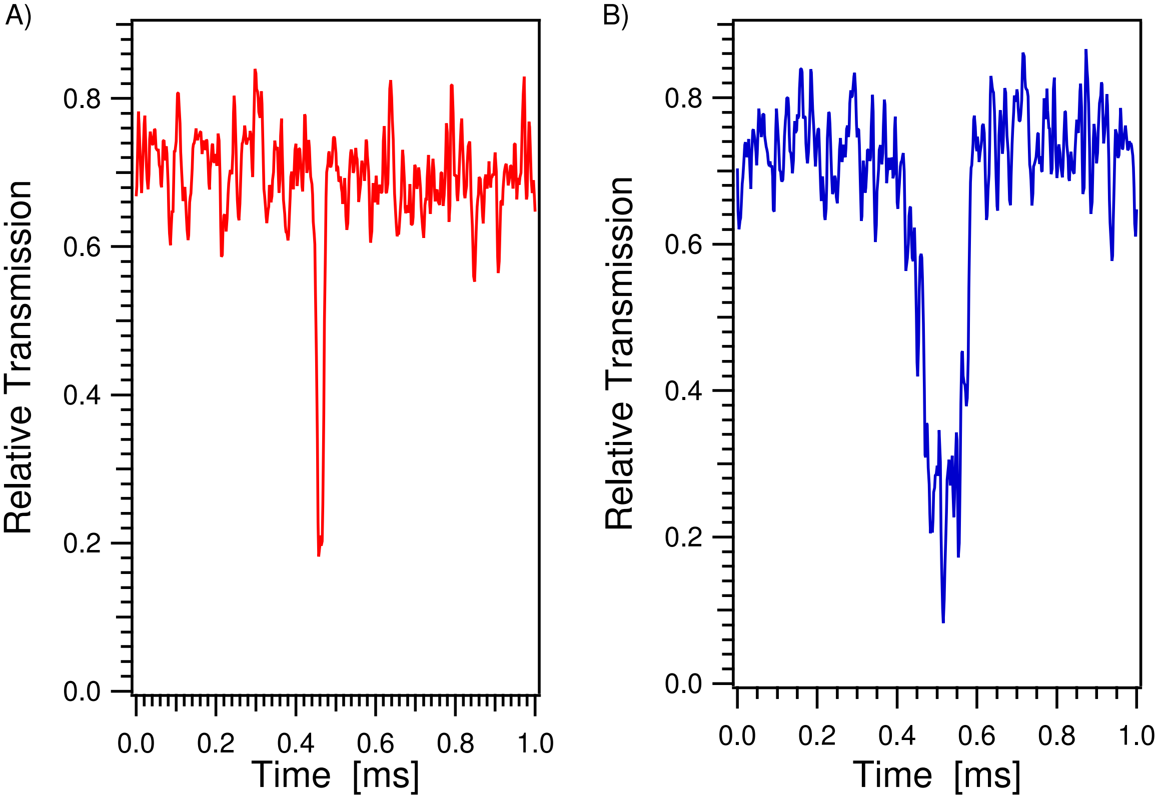

Figure 8.4: Transits from the Upper and Lower MOTs

The red trace on the left (A) is a typical transit for atoms dropped from the upper MOT at a height of ∼ 25 cm. The blue trace on the right is a typical transit for atoms dropped from the lower MOT at a height of ∼ 5 mm. Average transit times for the upper and lower MOT are respectively ∼ 25 μs and ∼ 175 μs. For this data the probe and cavity were on resonance with the $F = 4 \rightarrow F' = 5$ transition.

8.2 Trapping in an 869 nm FORT

The intracavity FORT in our experiment was first implemented by David Vernooy and Jun Ye [2, 42]. Their setup used a FORT wavelength of $\lambda_F = 869$ nm (two longitudinal modes below the cavity QED mode in our cavity) with the FORT triggered *ON* by a transit detected by the probe beam. Without triggering the FORT, the atoms would not become trapped, since the FORT provides a nearly conservative potential. Before triggering the FORT, the atom's free-fall energy is dissipated by the optical molasses created by the transverse lattice beams discussed earlier.

In this experiment, the cavity QED interaction employed the $(F, m_F) = (4, 4) \rightarrow (F', m_{F'}) = (5, 5)$ cycling transition using σ^+ light. Therefore, a σ^+ FORT was implemented for simplicity. In this case, the $F = 4, m_F = (-3, -4)$ and $F = 3, m_F = 3$ states are not trapped. This has serious consequences for the atoms in the implementation of cavity QED on the $(6S_{1/2}, F = 4) \rightarrow (6P_{3/2}, F = 4)$ transition since they are off-resonantly scattered from $F = 4$ through $F' = 4$ into the $F = 3$ state. This makes repumping of the atomic population out of this state critical on timescales comparable to the inverse scattering rate.

The lifetime in this experiment, $\tau = 28$ ms, was attributed to parametric heating caused by intensity fluctuations of the trapping field [54, 55]. Since then, we have invested considerable effort to understand and eliminate this heating mechanism [57], which is characterized by an exponential temperature growth (see Chapter 7).

8.3 Trapping in a 906 nm FORT

As discussed in the previous section and Chapter 7, intensity fluctuations of the trapping field lead to parametric heating of the trapped atoms. Therefore, we have endeavored to improve the stability of the trapping lasers and cavity. However, in Part IV we will see that an important source of intensity fluctuations is Brownian motion of the cavity mirrors. Our system is sensitive to this motion because of the high finesse of our cavity. Because this noise scales as the square of the cavity finesse, we just need to change the FORT wavelength to a cavity mode with lower finesse. For our cavity, the finesse at the three trapping wavelengths we have implemented is $\mathcal{F}_{869} \approx 3.3 \times 10^5$, $\mathcal{F}_{906} \approx 5.9 \times 10^4$, and $\mathcal{F}_{936} \approx 2.2 \times 10^3$. Another suspect that cannot be discounted is the presence of stray light, which we have also endeavored to eliminate. For our setup, we require a mean intracavity photon number $\bar{n} \ll 10^{-5}$ for light near the cavity QED resonance, which is not trivial to diagnose.

As discussed in Chapter 7, we ultimately want to use a trapping wavelength of 935.6 nm. However, it was simpler to implement a FORT wavelength of 906 nm as an intermediate step to check our ideas for improving the lifetime. This was due to the optics we already had in the setup to deliver the FORT light to the cavity, as well as the limitations of the Ti:Sapphire laser we were using to implement this light. Figure 8.5 is the lifetime plot for the 906 nm FORT. From this plot we see that the lifetime was improved to $\tau \sim 90$ ms. This improvement allowed us to locate other sources of noise and stray light. The next step was to move to a trapping wavelength of 935.6 nm as described in the next section.

8.4 Trapping in a 936 nm FORT

We were fortunate that our cavity has a TEM_{00} longitudinal mode located nine orders below the cavity QED mode, at the 'magic' wavelength $\lambda_F = 935.6$ nm, allowing the implementation of an internal-state insensitive FORT. We implemented this wavelength using a grating feedback diode laser system. Our cavity linewidth at this wavelength is FWHM = 1.6 GHz, corresponding to a cavity finesse $\mathcal{F} \sim 2200$. This implies that a mode-matched input power of 1.2 mW gives a peak AC-Stark shift $\delta_{6S_{1/2}} = -47$ MHz for all states in the $6S_{1/2}$ ground manifold, corresponding to a trap depth $\frac{U_0}{k_B} = 2.3$ mK, which was used for all of our experiments. In addition, the noise due to thermally driven oscillations of our mirrors is reduced even further at this wavelength, since it scales as the square of the cavity finesse.

In order to probe the atoms, we use the $F = 4 \rightarrow F' = 5$ transition for cavity QED interactions with zero detuning of the cavity from the bare atomic resonance,

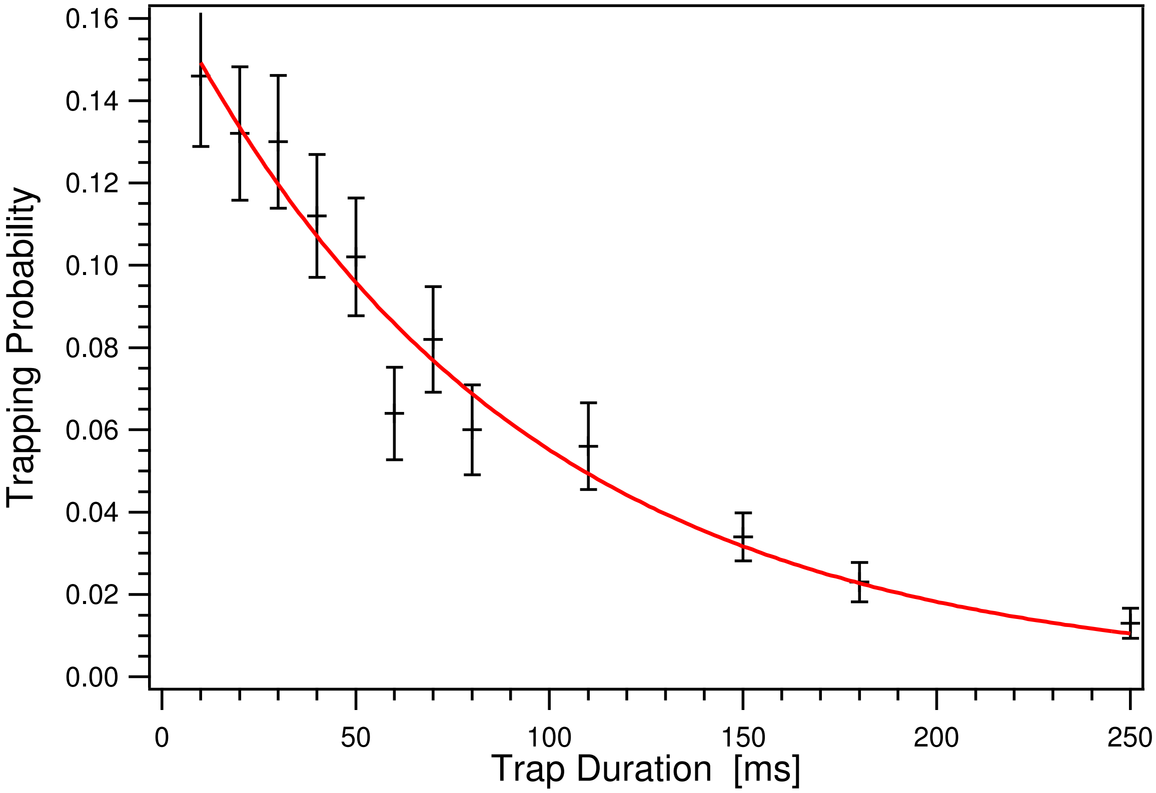

Figure 8.5: Lifetime Plot for our 906 nm FORT
Detection probability P as a function of trapping time t_T. An exponential fit (solid line) yields a lifetime $\tau \approx 90$ ms.

$\Delta_C \equiv \omega_C - \omega_{4\to5} = 0$. In contrast to Section 8.2, here the FORT is *ON* continuously without switching, which makes a cooling mechanism necessary to load atoms into the trap (due to the conservative nature of the potential). The initial detection of a single atom falling into the cavity mode is performed with a probe beam tuned to the lower sideband of the vacuum-Rabi spectrum ($\Delta_p = \omega_p - \omega_{4\to5} = -20$ MHz), generating an *increase* in transmitted probe power when an atom approaches a region of optimal coupling [33]. This increase triggers *ON* a pulse of transverse cooling light from the $y - z$ beams, detuned 41 MHz red of $\omega_{4\to5}$. During the subsequent trapping interval, all near-resonant fields are turned *OFF* (including the transverse cooling light), both via acousto-optical switches and mechanical shutters. After a variable delay t_T, the cavity QED probe field is switched back *ON* to detect whether the atom is still trapped, where now $\Delta_p = 0$, resulting in a sharp *decrease* in transmission when an atom is present.

Data collected in this manner are shown in Figure 8.6, which displays the conditional probability P to detect an atom given an initial single-atom triggering event versus the time delay t_T. The two data sets shown in Figure 8.6 yield comparable lifetimes, the upper having been acquired with mean intracavity atom number $\bar{N} = 0.30$ atoms and the lower with $\bar{N} = 0.019$. The offset in P between the two curves in Figure 8.6 arises primarily from the reduction in duration, δt, of the cooling pulses, from 100 μs to 5 μs, which results in a reduced capture probability. In addition to determining the lifetime, such measurements with various loading conditions allow us to investigate the probability of trapping an atom other than the "trigger" atom and of capturing more than one atom. For example, with $\delta t = 5$ μs as in the lower set, we have varied $0.011 \lesssim \bar{N} \lesssim 0.20$ with no observable change in either P_T or the trap lifetime τ. Since a conservative upper bound on the relative probability of trapping a second atom is just $\frac{\bar{N}}{2}$ (when $\bar{N} \ll 1$), these data strongly support the conclusion that our measurements are for single trapped atoms. Quite generally, we routinely observe lifetimes in the range 2 sec $< \tau <$ 3 sec depending upon the parameters chosen for trap loading and cooling.

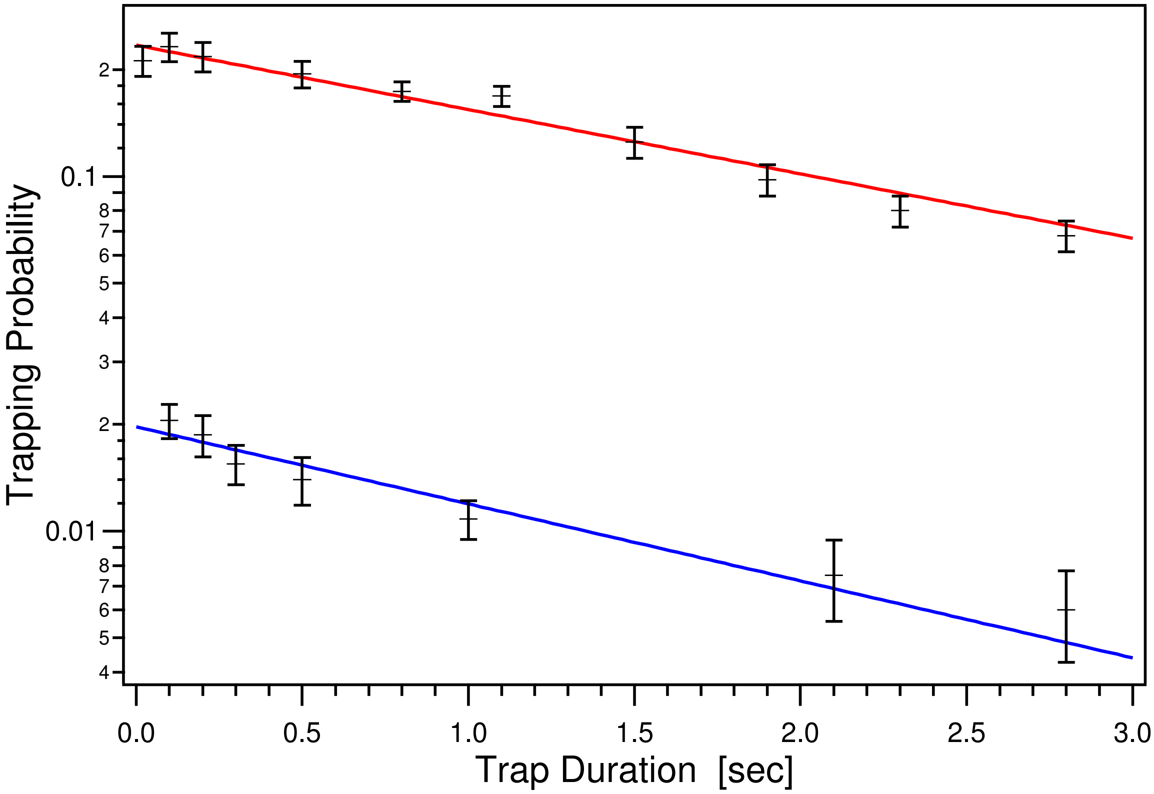

Figure 8.6: Lifetime Plots for our 935.6 nm FORT

Detection probability P as a function of trapping time t_T. The upper data set is for mean intracavity atom number $\bar{N} \approx 0.30$, while the lower set is for $\bar{N} \approx 0.019$ atoms. Exponential fits (solid lines) yield lifetimes $\tau_{\text{upper}} = (2.4 \pm 0.2)$ sec and $\tau_{\text{lower}} = (2.0 \pm 0.3)$ sec. (Note: Because of the lowered probability for having an intracavity atom in the lower trace, the data collection for this trace took 38 hours of continuous observation!)

8.5 Continuous Observation of Trapped Atoms

The results presented in the previous section were obtained “in the dark” with the atom illuminated only by the FORT laser at λ_F and the cavity-locking laser at λ_C. Toward the goals of continuous observation of single trapped atoms over long times and of implementing Λ-schemes in cavity QED [7, 8, 9, 58], we next present results from a second protocol used with our state-insensitive 935.6 nm FORT. In this scheme, the cavity is on resonance with the $F = 4 \rightarrow F' = 4$ transition ($\Delta'_C \equiv \omega_C - \omega_{4\rightarrow 4} = 0$). Atoms falling into the cavity mode are detected by a reduction in probe transmission through the cavity ($\Delta'_p = \omega_p - \omega_{4\rightarrow 4} = 0$), with the probe then triggered *OFF*. Here, the repumping light from the transverse $y-z$ beams is always *ON*, with fixed detuning Δ_3 with respect to the $F = 3 \rightarrow F' = 3$ resonance. Cooling light from the $y - z$ beams to drive $F = 4 \rightarrow F' = 5$ is no longer used. After a delay of 80 ms following a trigger event (which allows other atoms to fall through the cavity and be lost), the probe beam is switched back *ON*, and sets $t = 0$. As before, the FORT is left *ON* continuously.

An example of the resulting probe transmission is shown in Figure 8.7, which displays the continuous observation of a single trapped atom. In these experiments, unlike those of Figure 8.6, we use a lower detection bandwidth (1 kHz instead of 30 kHz) since the probe power is much weaker ($\bar{m}_e \simeq 0.02$ instead of $\simeq 0.5$ for the empty cavity). This reduced time resolution for the trigger in the presence of continuous probing and repumping fields means that we trap more than one atom with increased frequency, as evidenced by probe transmission below the level $\bar{m}_1$ of Figure 8.7. In such cases, the probe transmission versus t is observed always to increase in a discontinuous “staircase” of steps, presumably due to the loss of successive atoms, with the last level before $\bar{m}_e$ corresponding to $\bar{m}_1$, which we then associate with a single atom. An example of this staircase is shown in Figure 8.8. For independent heating of each atom, we would expect a lifetime of each level in Figure 8.8 to be given by

$$\tau_n = \frac{\tau_1}{n}, \tag{8.4}$$

where τ_n is the lifetime for the level corresponding to n intracavity atoms. Figure 8.9 shows a lifetime plot for the first two levels, $n = (1, 2)$, taken from $1,000$ drops. An exponential fit yields $\tau_1 = 278$ ms and $\tau_1 = 146$ ms.

Given that the FORT is *ON* continuously, it is remarkable that a falling atom can be trapped and observed over long intervals as in Figure 8.7 in the *absence* of transverse cooling light on the $F = 4 \rightarrow F' = 5$ transition. Since we have not seen such striking phenomena under similar conditions for cavity QED with the $F = 4 \rightarrow F' = 5$ transition, it seems likely that a cycle between hyperfine ground levels $F = 3 \Leftrightarrow 4$ is involved in a cooling process involving the repumping and cavity QED beams. We observe a strong dependence of the trapping and continuous observation times on the detuning of the $y - z$ repumping beams near $F = 3 \rightarrow F' = 3$, with an optimal value $\Delta_3 \simeq 25$ MHz to the *blue*, which strongly suggests blue Sisyphus cooling as has been employed in “gray” optical molasses [59]. Figure 8.10 shows the method used to determine this optimal detuning. The cavity QED probe is also a critical component, since without it, observations as in Figure 8.7 are not possible, although it is not clear whether this beam is acting as a simple “repumper” or is functioning in a more complex fashion due to strong coupling.

We see that we can efficiently load multiple atoms into our cavity. Now that we have the means for determining the number of intracavity atoms, we should be able to efficiently load a single cold atom into our cavity. This could be achieved by first intentionally loading many atoms, then applying some heating to ‘boil’ out all but one atom. We can then apply our cooling to the remaining atom to have a single, cold, trapped atom with nearly every MOT drop.

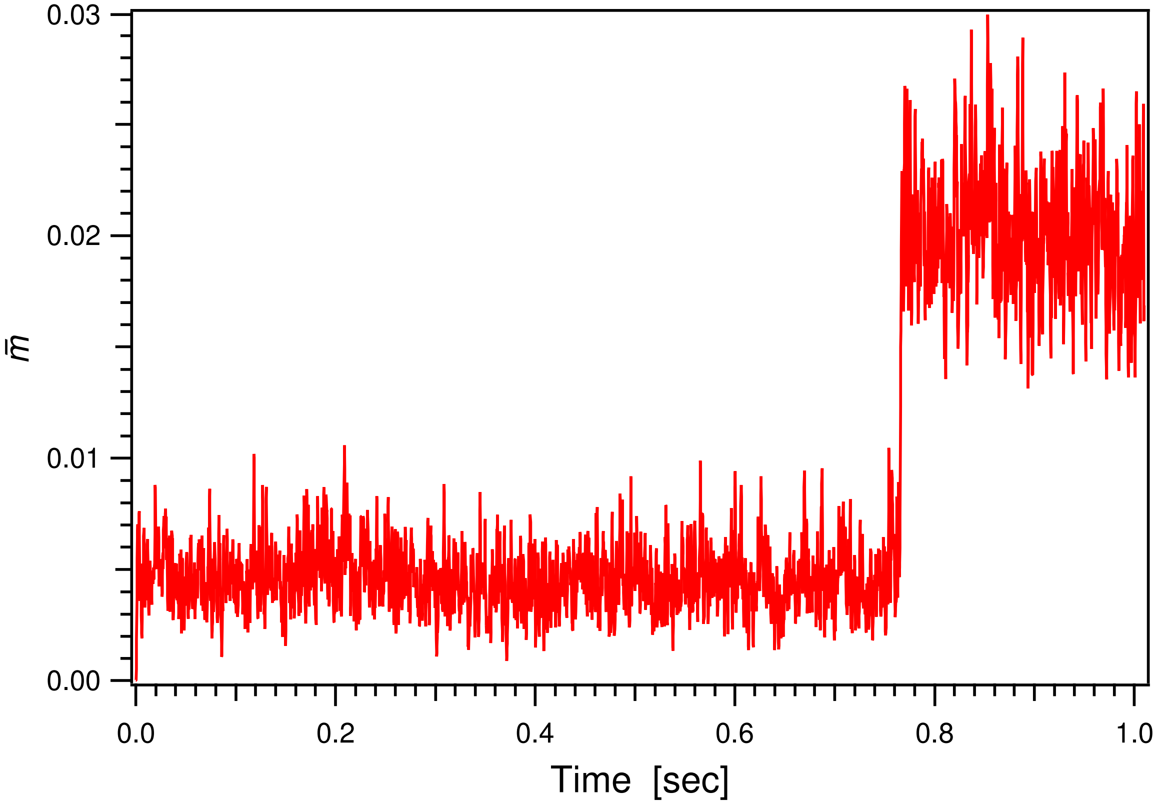

Figure 8.7: Continuous Observation of a Trapped Atom
A single atom trapped inside the cavity is continuously observed for $\sim$ 0.8 sec. The average lifetime for continuously observed atoms is $\sim$ 0.4 sec. Displayed is the strength of the intracavity field $\bar{m} = |\langle\hat{a}\rangle|^2$ deduced from the heterodyne current as a function of time t, where the initial trigger event occurred at $t = -80$ ms. The RF detection bandwidth is 1 kHz, $\Delta'_C = 0 = \Delta'_p$, and $\Delta_3 = 25$ MHz (*blue* detuned).

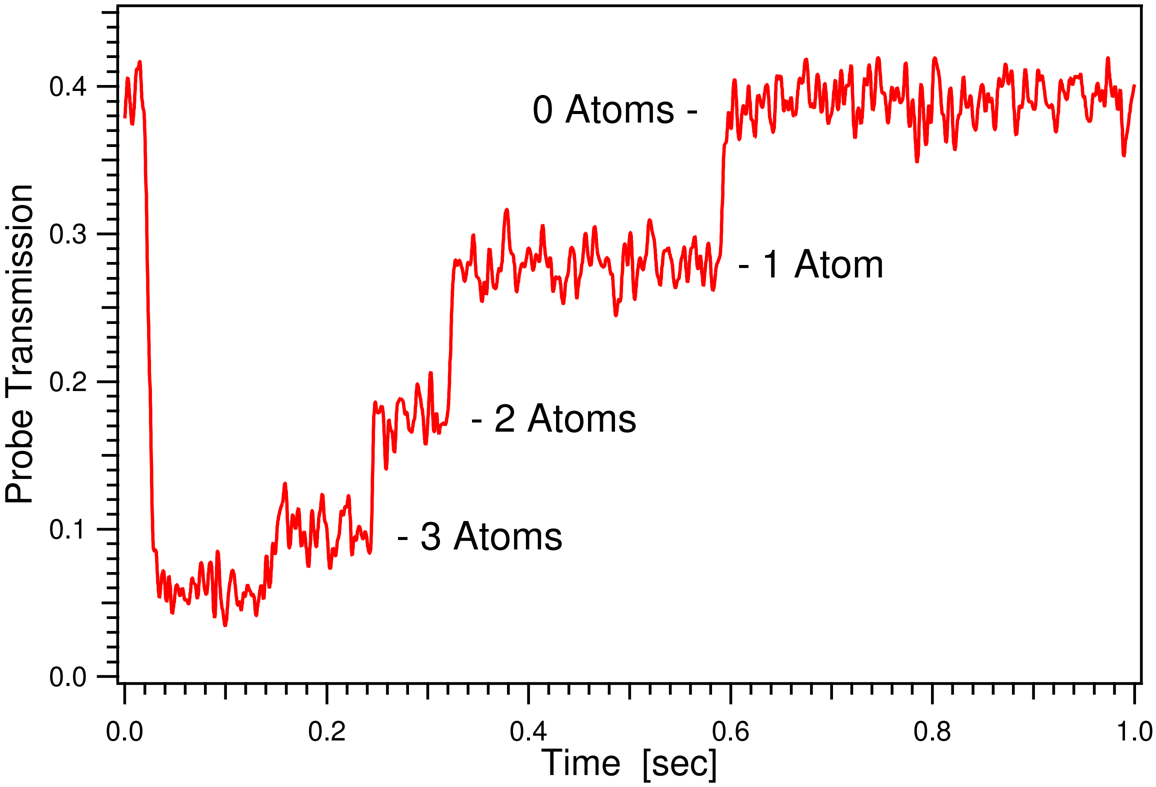

Figure 8.8: Observing the Number of Intracavity Atoms
We are now able to load multiple atoms into the FORT and resolve the intracavity atom number. Displayed is the strength of the intracavity field $\bar{m} = |\langle \hat{a} \rangle|^2$ deduced from the heterodyne current as a function of time t, with an RF detection bandwidth of 1 kHz, $\Delta'_C = 0 = \Delta'_p$, and $\Delta_3 = 25$ MHz (*blue* detuned).

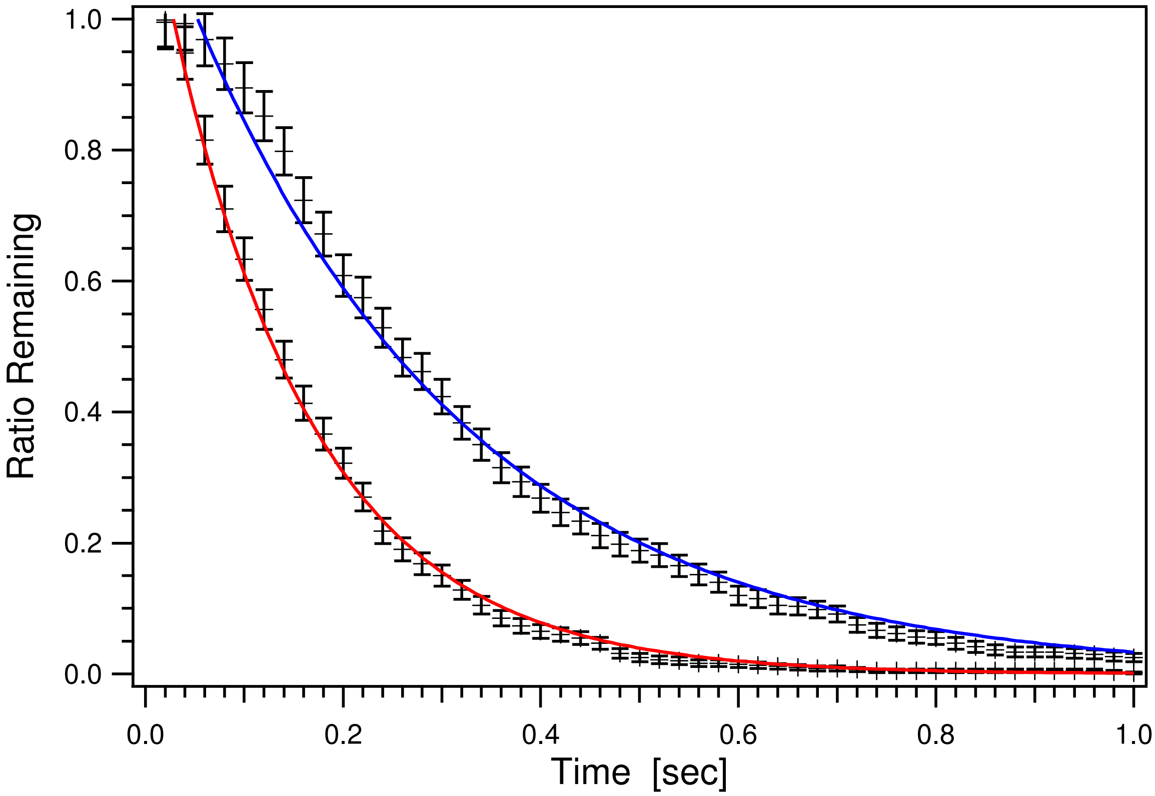

Figure 8.9: Lifetime Plots for One and Two Intracavity Atoms

We expect the lifetime for a given level in Figure 8.8 to be given by $\tau_n = \frac{\tau_1}{n}$. We used $1,000$ traces taken with the same parameters as that shown in Figure 8.8. The upper trace is the lifetime for the one-atom level, with an exponential fit of $\tau_1 \sim 278$ ms. The lower trace is for the two-atom level, with an exponential fit of $\tau_2 \sim 146$ ms. This is in good agreement with our expectations.

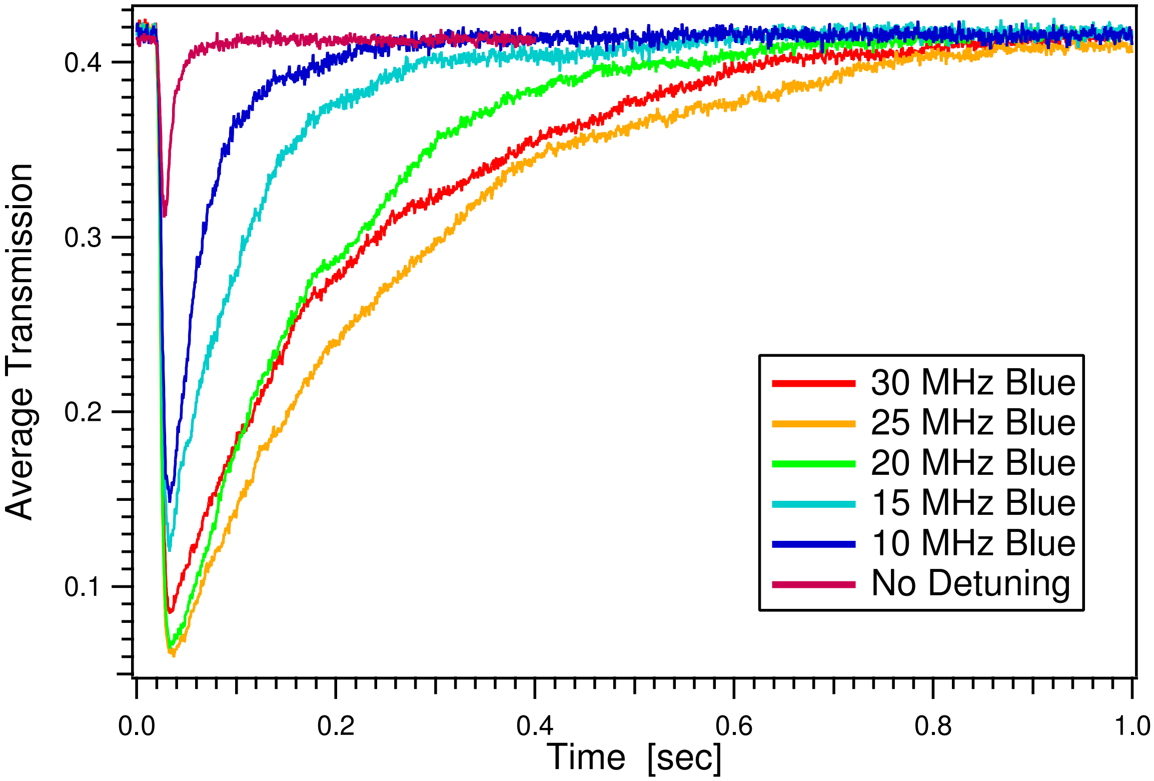

Figure 8.10: Determining the Optimal Detuning for Intracavity Cooling
As discussed in Section 8.5, we are now able to load multiple atoms into the FORT and resolve the intracavity atom number. This plot is an average of $1,000$ traces obtained in the same manner as shown in Figure 8.8. Displayed is the strength of the intracavity field $\bar{m} = |\langle \hat{a} \rangle|^2$ deduced from the heterodyne current as a function of time t, with an RF detection bandwidth of 1 kHz and $\Delta'_C = 0 = \Delta'_p$. The detuning, Δ_3, of the repump light from the $F = 3 \rightarrow F' = 3$ transition for each trace is shown in the legend. A deeper trace implies that more atoms are loaded into the trap on average. We deduce the optimal detuning for the repump light to be $\Delta_3 = 25$ MHz.

Part III

Cavity QED with Dielectric Microspheres

Motivated by the pioneering work of Braginsky and Ilchenko [60], some of the highest quality optical resonators to date have been achieved with the whispering gallery modes (WGMs) of quartz microspheres [17, 18]. Over the wavelength range $630 - 850$ nm, quality factors $Q \approx 8 \times 10^9$ have been realized, and cavity finesse $\mathcal{F} = 2.3 \times 10^6$ demonstrated [17, 18]. Such high quality factors make the WGMs of small dielectric spheres a natural candidate for use in cavity QED [19, 61, 60, 62, 63, 64, 65, 66, 67, 68, 69, 70, 71, 72, 73, 74, 75, 76].

While much of the work regarding quartz microspheres has centered around achieving the ultimate quality factors [17, 18], the quality factor of the resonator is but one of the factors that determines the suitability of the WGMs for investigations of cavity quantum electrodynamics in a regime of strong coupling. In this case, the coherent coupling coefficient, g, for a single atom interacting with the cavity mode must be much larger than all other dissipative rates, including the cavity decay rate, κ, and the rate of atomic spontaneous emission, γ; namely $g \gg (\kappa, \gamma)$. Note that $2g = \Omega$ gives the Rabi frequency associated with a single quantum of excitation shared by the atom-cavity system [77, 56]. The atom-field interaction can be characterized by two important dimensionless parameters: the saturation photon number, $n_0 \propto \frac{\gamma^2}{g^2}$, and the critical atom number, $N_0 \propto \frac{\kappa\gamma}{g^2}$. Since these parameters correspond respectively to the number of photons required to saturate an intracavity atom and the number of atoms required to have an appreciable effect on the intracavity field, strong coupling requires that $(n_0, N_0) \ll 1$. Ideally one would hope to minimize both of these parameters in any particular resonator. Unfortunately, within the context of our current understanding of the loss mechanisms of the WGMs [18], the critical parameters (n_0, N_0) cannot be minimized simultaneously in a microsphere.

Motivated by these considerations, in these chapters we explore possible limits for the critical parameters (n_0, N_0) for the WGMs of quartz microspheres. Following the analysis of References [61, 19, 74], we study the particular case of a single atom coupled to the *external* field of a WGM near the sphere's surface. We show that there are radii that minimize (n_0, N_0) individually, and that there is an "optimal" sphere size that minimizes the geometric mean, $\sqrt{n_0 \times N_0}$, of these two cavity QED parameters and allows both parameters to be near their respective minima. We also report our progress in the fabrication of small microspheres with radii $a \sim 10\mu$m, and compare our experimental results for Q with those from our theoretical analysis. Finally, we present a detailed comparison for the state of the art and future prospects for achieving strong coupling in cavity QED for both microsphere and Fabry-Perot cavities. Throughout the presentation, an attempt is made to develop a general formalism that can be applied to diverse systems. However, detailed analysis is given for the case of an individual Cesium atom coupled to the WGMs of quartz microspheres.

Chapter 9

Electromagnetic Properties of Dielectric Spheres

9.1 Modes of a Microsphere

Solving for the mode structure of the resonances of a dielectric sphere in vacuum is a classic problem in electricity and magnetism, and the resulting field distributions have been known for some time [78]. The electric field of the TM, *electric type*, modes inside and outside a sphere of refractive index n at free-space wavelength λ_0 are respectively,

$$\begin{aligned}\vec{E}_{\text{in}}(r,\theta,\phi) \propto \quad & l(l+1)\frac{j_l(kr)}{kr}P_l^m(\cos\theta)e^{im\phi}\widehat{r} \\ + \quad & \frac{[krj_l(kr)]'}{kr}\frac{\partial P_l^m(\cos\theta)}{\partial\theta}e^{im\phi}\widehat{\theta} \\ + \quad & \frac{im}{\sin\theta}\frac{[krj_l(kr)]'}{kr}P_l^m(\cos\theta)e^{im\phi}\widehat{\phi} \end{aligned} \tag{9.1}$$

and,

$$\begin{aligned}\vec{E}_{\text{out}}(r,\theta,\phi) \propto \quad & l(l+1)\frac{h_l^{(1)}\left(\frac{kr}{n}\right)}{\frac{kr}{n}}P_l^m(\cos\theta)e^{im\phi}\widehat{r} \\ + \quad & \frac{\left[\frac{kr}{n}h_l^{(1)}\left(\frac{kr}{n}\right)\right]'}{\frac{kr}{n}}\frac{\partial P_l^m(\cos\theta)}{\partial\theta}e^{im\phi}\widehat{\theta} \\ + \quad & \frac{im}{\sin\theta}\frac{\left[\frac{kr}{n}h_l^{(1)}\left(\frac{kr}{n}\right)\right]'}{\frac{kr}{n}}P_l^m(\cos\theta)e^{im\phi}\widehat{\phi}\,. \end{aligned} \tag{9.2}$$

where a is the radius of the sphere, $k = \frac{2\pi n}{\lambda_0}$ is the wave vector inside the sphere, $j_l(x)$ is the spherical Bessel function, $h_l^{(1)}(x)$ is the spherical Hankel function, $(\widehat{r}, \widehat{\theta}, \widehat{\phi})$ are unit vectors, and the $'$ refers to differentiation with respect to the argument. Note that the TM modes have a predominantly radial electric field vector.

In order to satisfy the boundary conditions at the surface of the microsphere, the tangential components of the mode function immediately inside and outside the sphere must be equal. However, there is a discontinuity in the radial component of the electric field at the dielectric boundary (as can be seen from Figure 9.1.) The eigenmodes are determined by solving for the roots of a characteristic equation [78], which can be reduced to

$$\frac{j_{l-1}(ka)}{j_l(ka)} - \frac{n h_{l-1}^{(1)}\left(\frac{ka}{n}\right)}{h_l^{(1)}\left(\frac{ka}{n}\right)} + \frac{n^2 l}{ka} - \frac{l}{ka} = 0 \; . \tag{9.3}$$

Throughout this paper, we normalize the mode functions such that their maximum value is unity. This condition then yields for the $l = m$ modes of the sphere

$$\begin{aligned} \vec{\Psi}_{\text{in}}(r,\theta,\phi) = \quad & N(l+1)\frac{j_l(kr)}{kr}\sin^l(\theta)e^{il\phi}\widehat{r} \\ + \quad & NF(r)\cos\theta\sin^{l-1}\theta e^{il\phi}\widehat{\theta} \\ + \quad & iNF(r)\sin^{l-1}\theta e^{il\phi}\widehat{\phi} \end{aligned} \tag{9.4}$$

and,

$$\begin{aligned} \vec{\Psi}_{\text{out}}(r,\theta,\phi) = \quad & NB(l+1)\frac{h_l^{(1)}\left(\frac{kr}{n}\right)}{\frac{kr}{n}}\sin^l\theta e^{il\phi}\widehat{r} \\ + \quad & NBH(r)\cos\theta\sin^{l-1}\theta e^{il\phi}\widehat{\theta} \\ + \quad & iNBH(r)\sin^{l-1}\theta e^{il\phi}\widehat{\phi}, \end{aligned} \tag{9.5}$$

where

$$F(r) = \frac{j_l(kr)}{kr} + \frac{l}{2l+1}j_l(kr) - \frac{l+1}{2l+1}j_{l+1}(kr), \tag{9.6}$$

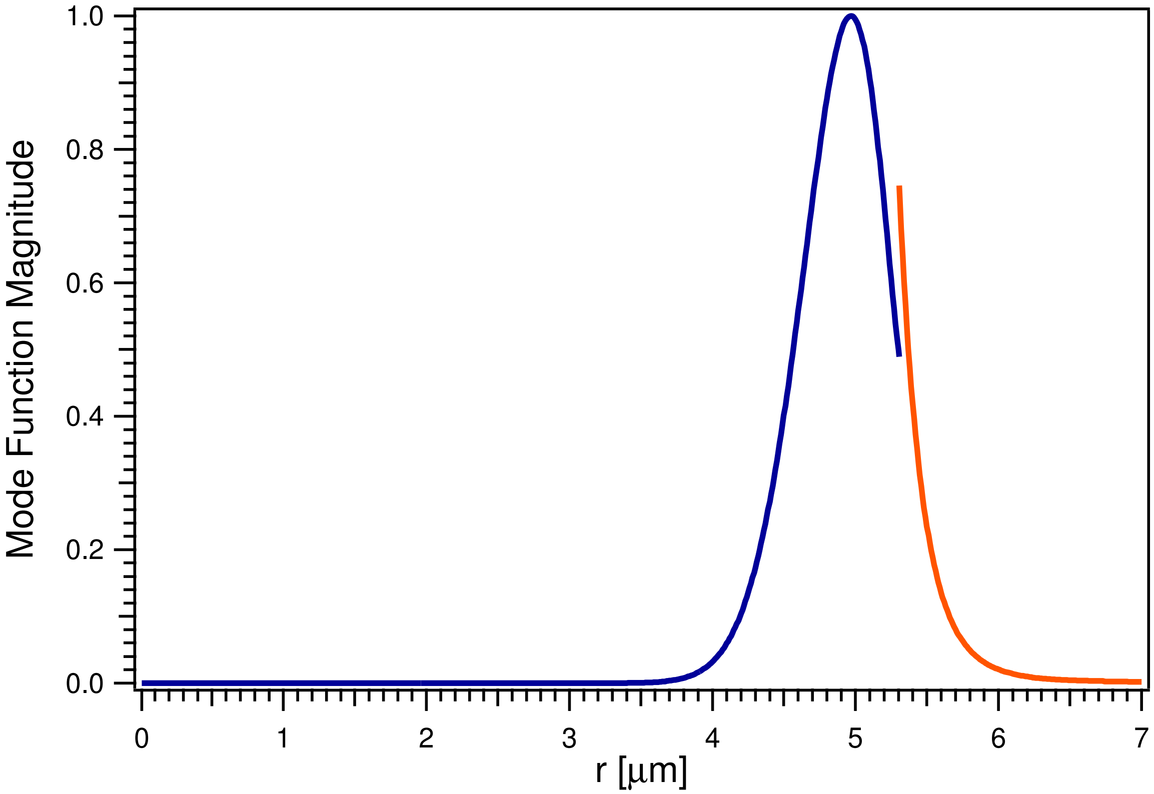

Figure 9.1: Mode Function for a Dielectric Microsphere
The magnitude of the normalized mode function as a function of radius for the TM mode of a 5.305 μm radius sphere ($p = 1, l = m = 50$) with $\theta = \frac{\pi}{2}$ and $\phi = 0$ for a wavelength of $\lambda_0 = 852.359$ nm and index of refraction $n = 1.45246$. In our case, the function is normalized to have a maximum value of unity. Note that there is a discontinuity at the surface.

$$
\begin{aligned}
H(r) = \quad & \frac{h_l^{(1)}\left(\frac{kr}{n}\right)}{\frac{kr}{n}} + \frac{l}{2l+1} h_{l-1}^{(1)}\left(\frac{kr}{n}\right) \\
& - \frac{l+1}{2l+1} h_{l+1}^{(1)}\left(\frac{kr}{n}\right),
\end{aligned} \tag{9.7}
$$

$$
B = \frac{\frac{j_l(ka)}{ka} + \frac{l}{2l+1} j_l(ka) - \frac{l+1}{2l+1} j_{l+1}(ka)}{\frac{h_l^{(1)}\left(\frac{ka}{n}\right)}{\frac{ka}{n}} + \frac{l}{2l+1} h_{l-1}^{(1)}\left(\frac{ka}{n}\right) - \frac{l+1}{2l+1} h_{l+1}^{(1)}\left(\frac{ka}{n}\right)}, \tag{9.8}
$$

and N is the normalization factor. Because we will require the field outside the sphere to be as large as possible, we will choose the $p = 1$ modes. Also, because the coherent coupling constant $g \propto \frac{1}{\sqrt{V_{\vec{P}}}}$, where $V_{\vec{P}}$ is the cavity mode volume, we choose the $l = m$ modes, since they yield the smallest electromagnetic mode volume, as will be explained in the next section.

9.2 Electromagnetic Mode Volume

The effective mode volume $V_{\vec{P}}$ associated with the electromagnetic field distribution $\vec{\Psi}(r, \theta, \phi)$ [19] is given by

$$V_{\vec{P}} = \int_{V_Q} \varepsilon\left(\vec{r}\right) \left|\vec{\Psi}_{\vec{P}}(\vec{r})\right|^2 \mathrm{d}V \ , \tag{9.9}$$

where

$$\varepsilon\left(\vec{r}\right) = \begin{cases} n^2 & \text{if } r < a, \\ 1 & \text{if } r > a. \end{cases} \tag{9.10}$$

and $\vec{P}$ corresponds to the (p, l, m) mode. V_Q is the quantization volume discussed in Ref. [19]. Because the WGMs are the modes of an open resonator, the mode volume, $V_{\vec{P}}$, diverges as $r_Q \to \infty$. However, this divergence is logarithmic, and $V_{\vec{P}}$ is quite insensitive to the choice of r_Q for a large range of values. Figure 9.2 shows that for the optimal sphere size discussed in Section 10.2, where $l = 76$, $V_{\vec{P}}$ varies by less than 1% for $1 < \frac{2\pi n}{\lambda_0}(r_Q - a) < 10^4$. As long as the quantization radius r_Q is chosen large enough to include the effects of the evanescent field, the mode volume is relatively insensitive to the particular choice of quantization radius.

Using the relations developed in Section 9.1 and the arguments outlined in Ref. [79], it is relatively straightforward to see that the modes of a dielectric sphere of finite dielectric constant and radius must radiate. Since the resonator is finite, it is contained entirely within a sphere of radius R. Outside of this sphere, the field can be expanded in terms of a fundamental set of solutions obtained by separating the vector wave equation in polar coordinates. The radial dependence of these solutions is given by the Hankel functions of the first and second kind, whose orders are half-odd-integers, and whose arguments are kr with $k = \frac{2\pi}{\lambda}$. The Hankel functions of the second kind represent waves coming in toward the origin from infinity. Since we do not have these in our case, their coefficients would be zero. Therefore, only the Han-

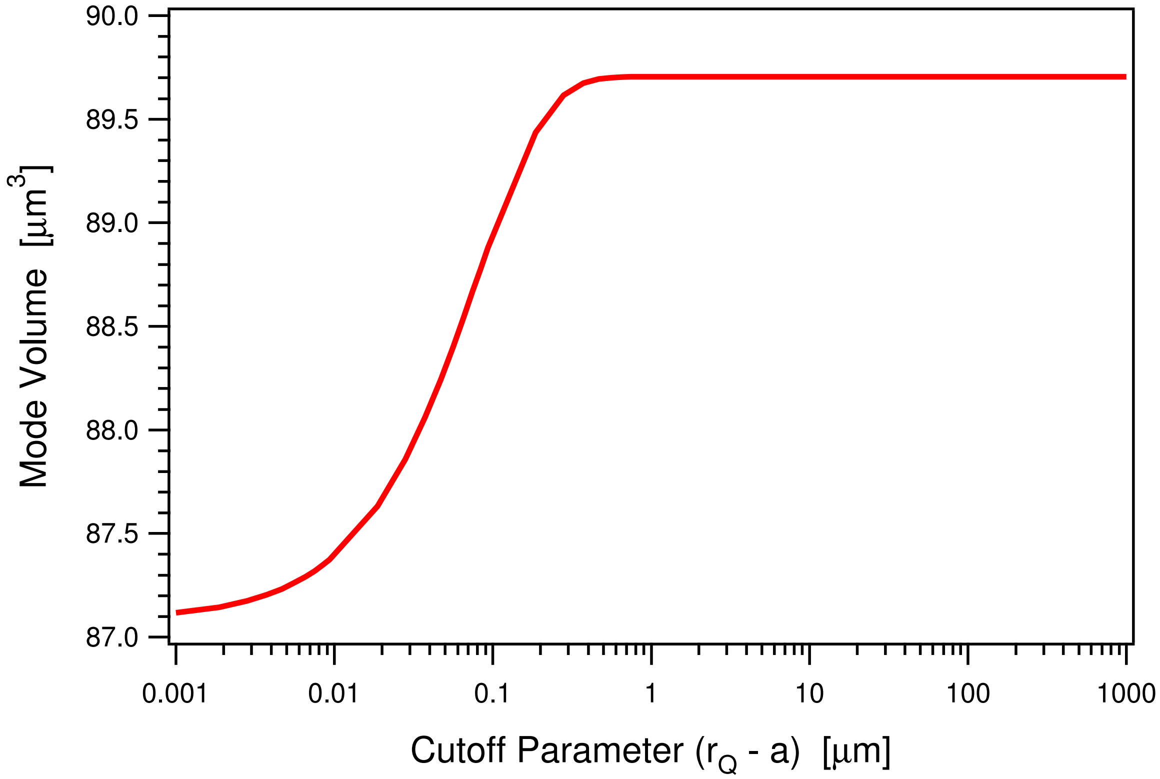

Figure 9.2: Electromagnetic Mode Volume and the Cutoff Parameter
Semi-log plot of the mode volume as a function of cutoff parameter $(r_Q - a)$ for the optimal sphere size discussed in Section 10.2. Here r_Q is the quantization radius and $a = 7.83038$ μm is the sphere radius for the $l = m = 76$ mode for a wavelength of 852 nm. Note that $V_{\vec{P}}$ varies by less than 1% for $1 < \frac{2\pi n}{\lambda_0}(r_Q - a) < 10^4$. Therefore, the mode volume is insensitive to the choice of quantization radius as long as the evanescent field is included.

kel functions of the first kind would have nonzero coefficients. If the power radiated was zero, then all of the coefficients would have to vanish for this solution outside the sphere. Therefore, the field would vanish everywhere outside the sphere and just outside the surface of the resonator. At the surface, the boundary conditions are such that the tangential components of the electric intensity E and the normal component of the dielectric displacement D must be continuous. For a finite dielectric constant, the field must then vanish everywhere just inside the outer surface of the resonator. Therefore, the only non-radiating solutions are everywhere zero.

As discussed more extensively in References [77, 56] the interaction between the internal atomic degrees of freedom and the intracavity field is characterized by the coherent coupling constant $g(r, \theta, \phi)$, where

$$g(r, \theta, \phi) \equiv g_0 \vec{\Psi}^{(p,l,m)}(r, \theta, \phi) \tag{9.11}$$

and

$$g_0 \propto \frac{1}{\sqrt{V_{\vec{P}}}}. \tag{9.12}$$

Note that in the absence of damping, $2g(\vec{r})$ gives the frequency for Rabi nutation associated with a single photon in the cavity for an atom initially in the ground state located at position $\vec{r}$ within the mode. Therefore, in order to maximize the coupling strength, one must endeavor to minimize the cavity mode volume.

In order to derive an answer that can be applied to different wavelengths, one can define a dimensionless mode volume parameter, $\tilde{V}$, and plot as a function of a dimensionless sphere size parameter, $\tilde{x}$, defined as:

$$\tilde{V} = \frac{V_{\vec{P}}}{(\frac{\lambda_0}{2\pi n})^3} \tag{9.13}$$

and

$$\tilde{x} = \frac{2\pi n a}{\lambda_0}, \tag{9.14}$$

where $V_{\vec{P}}$ is the cavity mode volume, n is the index of refraction at the free-space wavelength λ_0, and a is the sphere radius. The plots then only depend on the index of refraction (see Figure 9.3).

Naively, one might assume that the sphere should be made as small as possible in order to minimize the electromagnetic mode volume, and hence to provide a maximum for g_0 and hence globally for $g(\vec{r})$. However, as shown in Figures 9.3 and 9.4, the mode volume for the TM modes of a quartz microsphere actually passes through a minimum at some particular radius a_0. This behavior can be understood by noting that for $a < a_0$, the intrinsic, radiative losses are increasing rapidly and ultimately cause the mode to no longer be well-confined by the sphere, with a concomitant increase of the mode volume. Note that in Figure 9.3 and subsequent figures, we give results for $n \sim 1.45$ corresponding to fused silica, as well as for $n = 2.00$ and $n = 3.00$. These latter cases serve to illuminate the role of n as well as being applicable to other materials (i.e., the index of refraction for GaAs is $n = 3.4$ for $\lambda = 1550$ nm [80]). For a very low-OH fused silica microsphere at $\lambda_0 = 852$ nm (the wavelength of the D_2 transition in atomic Cesium) with index of refraction $n = 1.45246$, the minimum mode volume $V_{\vec{P}}^{\mathrm{min}} \approx 28.4\mu\mathrm{m}^3$ occurs for radius $a \approx 3.73\mu$m corresponding to mode numbers $p = 1, l = m = 34$ (see Figure 9.4). One might at first believe that this value for the radius represents the optimal sphere size for use as a cavity with single atoms. However, while the mode volume $V_{\vec{P}}$ plays an important role in determining the coupling constant (Equation 9.12), it is not the only parameter relevant to cavity QED with single atoms in a regime of strong coupling. As discussed in the next sections, the quality factor, Q, of a WGM has a strong dependence on the sphere radius, and must also be considered in an attempt to optimize the critical atom and saturation photon numbers.

9.3 Losses in Dielectric Spheres

For fused silica spheres with radius $a \gtrsim 15$ μm, the effect of intrinsic radiative losses can be safely neglected, since they allow quality factor $Q \gtrsim 10^{21}$, as illustrated in Figure 9.6. Such large values of Q greatly exceed those imposed by technical constraints of material properties, such as bulk absorption and surface scattering.

However, as one moves to very small spheres with radius $a \lesssim 10$ μm, the intrinsic radiative Q falls steeply enough to become the dominant loss mechanism even in the face of other technical imperfections. When assessing the usefulness of microspheres for cavity QED, one must account for the entire set of loss mechanisms to determine the optimal size for the microsphere, which is the subject to which we now turn our attention.

The quality factors of the WGMs of fused silica microspheres are determined by several different loss mechanisms. The overall quality factor can then be calculated by adding the different contributions in the following way [17]:

$$Q^{-1} = Q_{\mathrm{rad}}^{-1} + Q_{\mathrm{mat}}^{-1}, \tag{9.15}$$

$$Q_{\mathrm{mat}}^{-1} = Q_{\mathrm{s.s.}}^{-1} + Q_{\mathrm{w}}^{-1} + Q_{\mathrm{bulk}}^{-1}, \tag{9.16}$$

where Q_{rad} is due to purely radiative losses for an ideal dielectric sphere and Q_{mat} results from non-ideal material properties. The principal mechanisms contributing to Q_{mat} are scattering losses from residual surface inhomogeneities ($Q_{\mathrm{s.s.}}$), absorption losses due to water on the surface of the sphere (Q_{w}), and bulk absorption in the fused silica (Q_{bulk}). The intrinsic material losses are known very accurately, since they arise from absorption in the material at the wavelength of concern [81]. Considerably greater uncertainty is associated with the losses due to surface scattering and absorption due to adsorbed material on the surface of the sphere, of which water is likely the principal component. We will adopt the models for these losses presented in References [17, 18], extrapolated to the regime of small spheres of interest here.

9.3.1 Intrinsic Radiative Losses

The contribution to the quality factor for purely radiative effects, Q_{rad}, can be derived by following the arguments presented in Ref. [82]. These losses are due to the leakage of light from the resonator due to its finite dielectric constant and radius of curvature. The results can then be compared to numerical results obtained by Lorenz-Mie theory [83]. We find from Ref. [82] that

$$Q_{\mathrm{rad}} = \frac{1}{2}\left(l + \frac{1}{2}\right) n^{1-2b} \left(n^2 - 1\right)^{1/2} e^{2T_l}, \tag{9.17}$$

where

$$T_l = \left(l + \frac{1}{2}\right)\left(\eta_l - \tanh \eta_l\right), \tag{9.18}$$

$$\eta_l = \operatorname{arccosh}\left\{ n \left[1 - \frac{1}{l + \frac{1}{2}} \left(t_p^0 \xi + \frac{l^{1-2b}}{\sqrt{l^2 - 1}} \right) \right]^{-1} \right\}, \tag{9.19}$$

$$\xi = \left[\frac{1}{2}\left(l + \frac{1}{2}\right)\right]^{\frac{1}{3}}, \tag{9.20}$$

and

$$b = \begin{cases} 0 & \text{TE modes,} \\ 1 & \text{TM modes.} \end{cases} \tag{9.21}$$

Also, n is the index of refraction and t_p^0 is the p^{th} zero of the Airy function Ai. This p corresponds to the mode number (p, l, m). In our case, we are only interested in the $p = 1$ modes of the sphere to maximize the electromagnetic field outside the sphere while maintaining a small mode volume. Note that these expressions for Q_{rad} become invalid in the limit of small l mode numbers. The error in the mode functions used to derive these results reaches 1% for $l = 18$. However, the error is less than 0.2% for $l = 76$ (This is the optimal sphere size discussed in Section 10.2). Fortunately, the expressions are valid in the regimes for which we are concerned. This has been confirmed by making comparisons with numerical values obtained using Lorenz-Mie scattering theory.

From Figure 9.6, we see that the radiative Q falls approximately exponentially as the radius a is decreased, and can become quite important as the sphere size is decreased below 10 μm. For example, for a 15 μm radius sphere and a wavelength $\lambda_0 = 852.359$ nm, $Q_{\text{rad}} \approx 2 \times 10^{21}$. Therefore, the net quality factor would most certainly be dominated by other loss mechanisms in Equation 9.15. However, for a 7 μm radius sphere, $Q_{\text{rad}} \approx 4 \times 10^{8}$, and the radiative losses can play a crucial role in the characteristics of the spheres that are optimal for use in cavity QED.

9.3.2 Material Loss Mechanisms

The quality factor due to bulk absorption, Q_{bulk}, in fused silica is actually known very well, since this depends only on the absorption of the material at the wavelength of concern [17]:

$$Q_{\text{bulk}} = \frac{2\pi n}{\alpha \lambda_0}, \tag{9.22}$$

where n is the index of refraction, and α is the absorption coefficient of the material. From Figure 9.7 we see that for very low-OH fused silica, the absorption coefficient at 852 nm is $\alpha \approx 4.5 \times 10^{-4}\mathrm{m}^{-1}$ [81]. This would correspond to a quality factor of $Q_{\text{bulk}} \sim 2.4 \times 10^{10}$. Fused silica has a minimum in its absorption coefficient of $\alpha \approx 1.5 \times 10^{-5}\mathrm{m}^{-1}$ at 1550 nm, which yields a quality factor of $Q_{\text{bulk}} \sim 3.8 \times 10^{11}$.

The quality factor due to surface scattering, $Q_{\text{s.s.}}$, and absorption by adsorbed water, Q_{w}, has also been studied and modelled, albeit for larger spheres with $a \gtrsim 600\ \mu\text{m}$. For losses due to surface scattering, we follow the work of References [17, 18] and take

$$Q_{\text{s.s.}} \sim \frac{3\varepsilon(\varepsilon+2)^2}{(4\pi)^3(\varepsilon-1)^{5/2}}\frac{\lambda_0^{7/2}(2a)^{1/2}}{(\sigma B)^2}, \tag{9.23}$$

where $\varepsilon = n^2$ is the dielectric constant and $\sigma B \sim 5\ \text{nm}^2$ is an empirical parameter determined by the size and correlation length of the distribution of residual surface inhomogeneities. This quantity was reported in Ref. [18] based upon atomic force microscopy measurements of a microsphere.

The quality factor due to water adsorbed on the surface, Q_{w}, is given by [18]

$$Q_{\text{w}} \sim \sqrt{\frac{\pi}{8n^3}}\frac{(2a)^{1/2}}{\delta\lambda_0^{1/2}\beta_w}, \tag{9.24}$$

where $\delta \sim 0.2$ nm is an estimated thickness for the water layer, and $\beta_w \sim 4.33\ \text{m}^{-1}$ is the absorption coefficient of water at 852 nm.

Combining these various results, we display in Figure 9.8 a curve for the quantity Q_{mat} as a function of sphere radius, a, for a wavelength $\lambda_0 = 852$ nm. This same figure shows the quality factor, Q_{rad}, set by intrinsic radiative losses (Equation 9.17), as well as the overall quality factor, $Q = \frac{Q_{\text{rad}}Q_{\text{mat}}}{Q_{\text{rad}}+Q_{\text{mat}}}$. From this plot, we see that the radiative losses dominate the overall quality factor below a radius of $a \lesssim 8\ \mu\text{m}$, while the losses due to material properties are most significant for $a \gtrsim 8\ \mu\text{m}$. Because of the extremely steep dependence of Q_{rad} on sphere size, the point of transition from material to radiative dominated loss should be reasonably insensitive to details of the models employed to describe the material losses. Although we focus our attention here on the wavelength appropriate to the particular case of the D_2 transition in atomic Cesium, a similar analysis could be carried out for other wavelengths of interest using the above formalism, as for example the $2S \rightarrow 2P$ transition at 1.083 μm in metastable Helium.

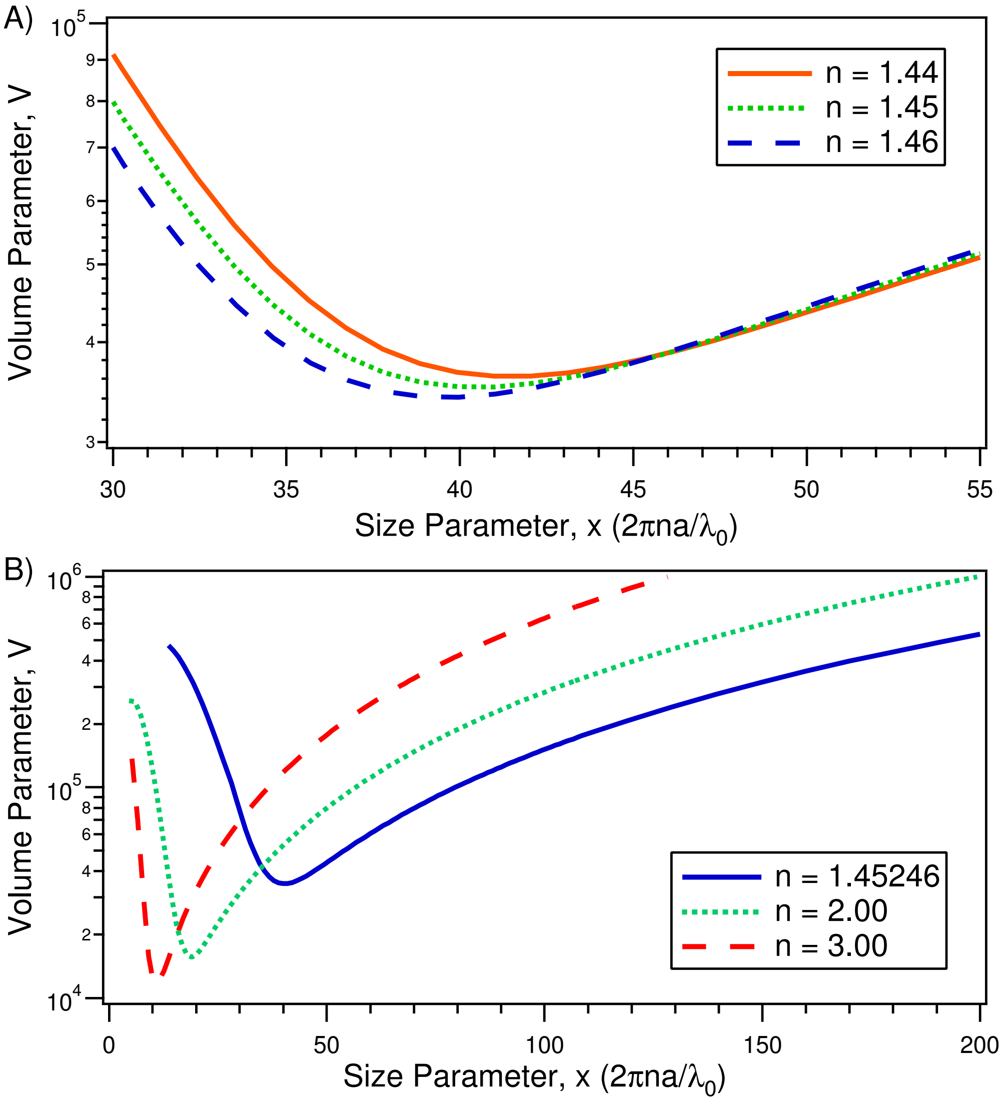

Figure 9.3: Dimensionless Volume Parameter

(a) The dimensionless volume parameter, $\tilde{V}$ (defined by Equation 9.13), as a function of the dimensionless size parameter, $\tilde{x}$ (defined by Equation 9.14). The solid line is for an index of refraction $n = 1.45246$, the index of refraction for fused silica at $\lambda_0 = 852$ nm, with a minimum of $\tilde{V} = 34883.4$ for $\tilde{x} = 39.9469$ ($l = m = 34$). The dotted line is for an index of refraction $n = 2.00$, with a minimum of $\tilde{V} = 15596.2$ for $\tilde{x} = 18.9864$ ($l = m = 14$). The dashed line is for an index of refraction $n = 3.00$, with a minimum of $\tilde{V} = 11546.4$ for $\tilde{x} = 10.2748$ ($l = m = 6$). (b) Because the index of refraction for fused silica varies from $n = 1.444$ at $\lambda_0 = 1550$ nm to $n = 1.458$ for $\lambda_0 = 600$ nm (see Figure 9.5), this plot of the dimensionless volume parameter, $\tilde{V}$, as a function of the dimensionless size parameter, $\tilde{x}$, is made for that range of values. The solid line is for an index of refraction $n = 1.44$, with a minimum of $\tilde{V} = 36247.5$ for $\tilde{x} = 40.9812$, ($l = m = 35$). The dotted line is for an index of refraction $n = 1.45$, with a minimum of $\tilde{V} = 35161.1$ for $\tilde{x} = 41.0036$, ($l = m = 35$). The dashed line is for an index of refraction $n = 1.46$, with a minimum of $\tilde{V} = 34129.1$ for $\tilde{x} = 39.9631$, ($l = m = 34$).

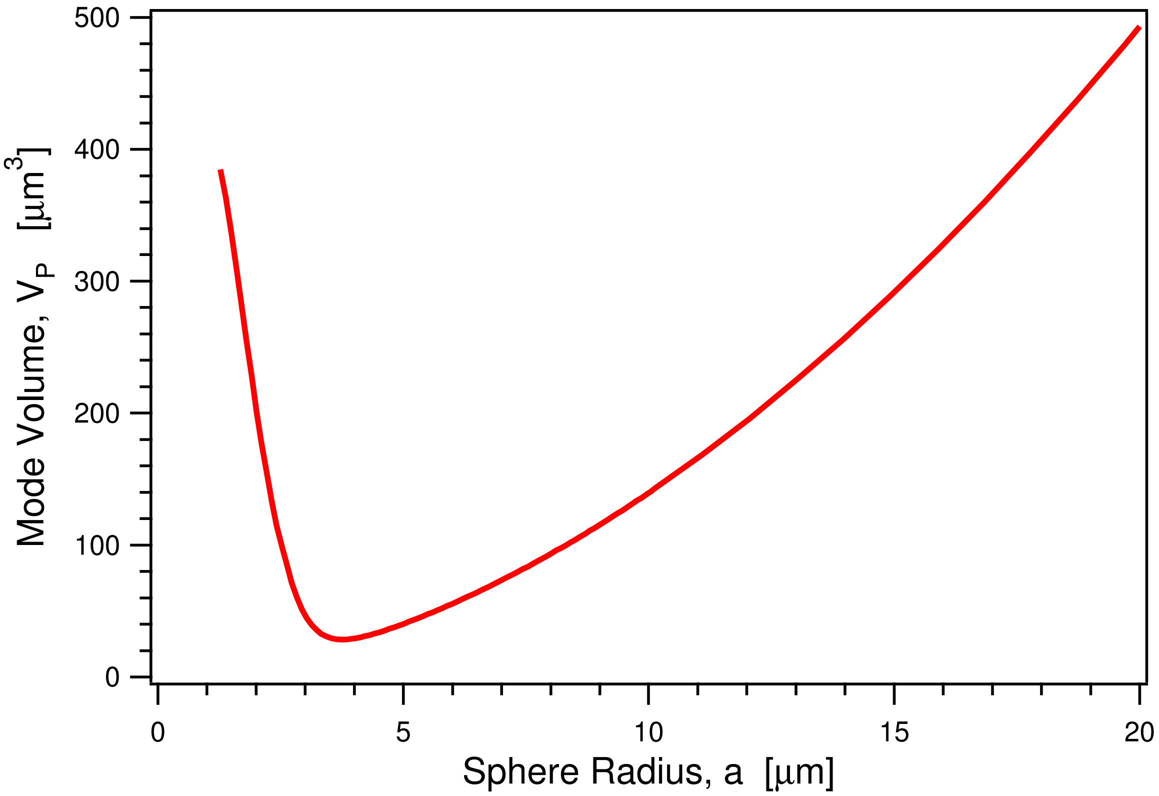

Figure 9.4: Electromagnetic Mode Volume for a Dielectric Microsphere
The electromagnetic mode volume, $V_{\vec{P}}$, for the TM modes of a very low-OH fused silica microsphere as a function of sphere radius at the wavelength $\lambda_0 = 852$ nm for the D_2 line of atomic Cesium. The minimum, 28.4 μm^3, occurs for radius $a_0 \approx 3.73$ μm corresponding to mode numbers $p = 1$ and $l = m = 34$.

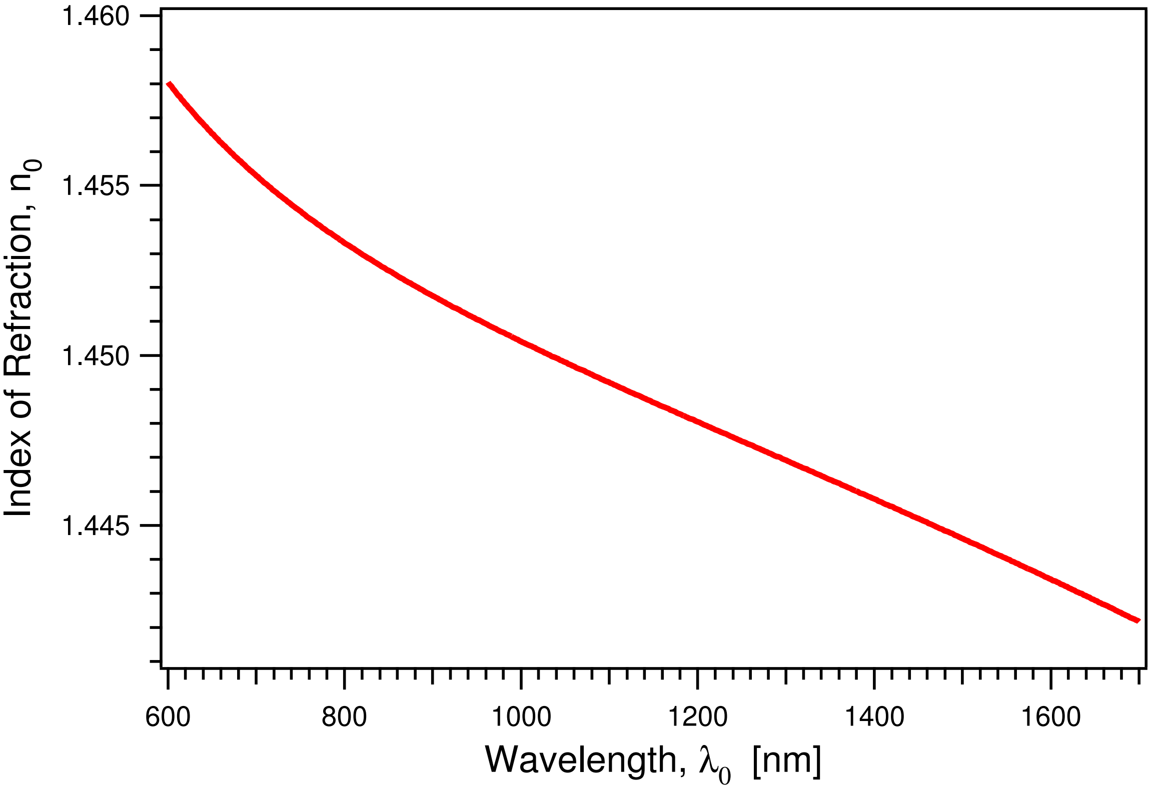

Figure 9.5: Index of Refraction for Fused Silica
The index of refraction of very low-OH fused silica as a function of wavelength.

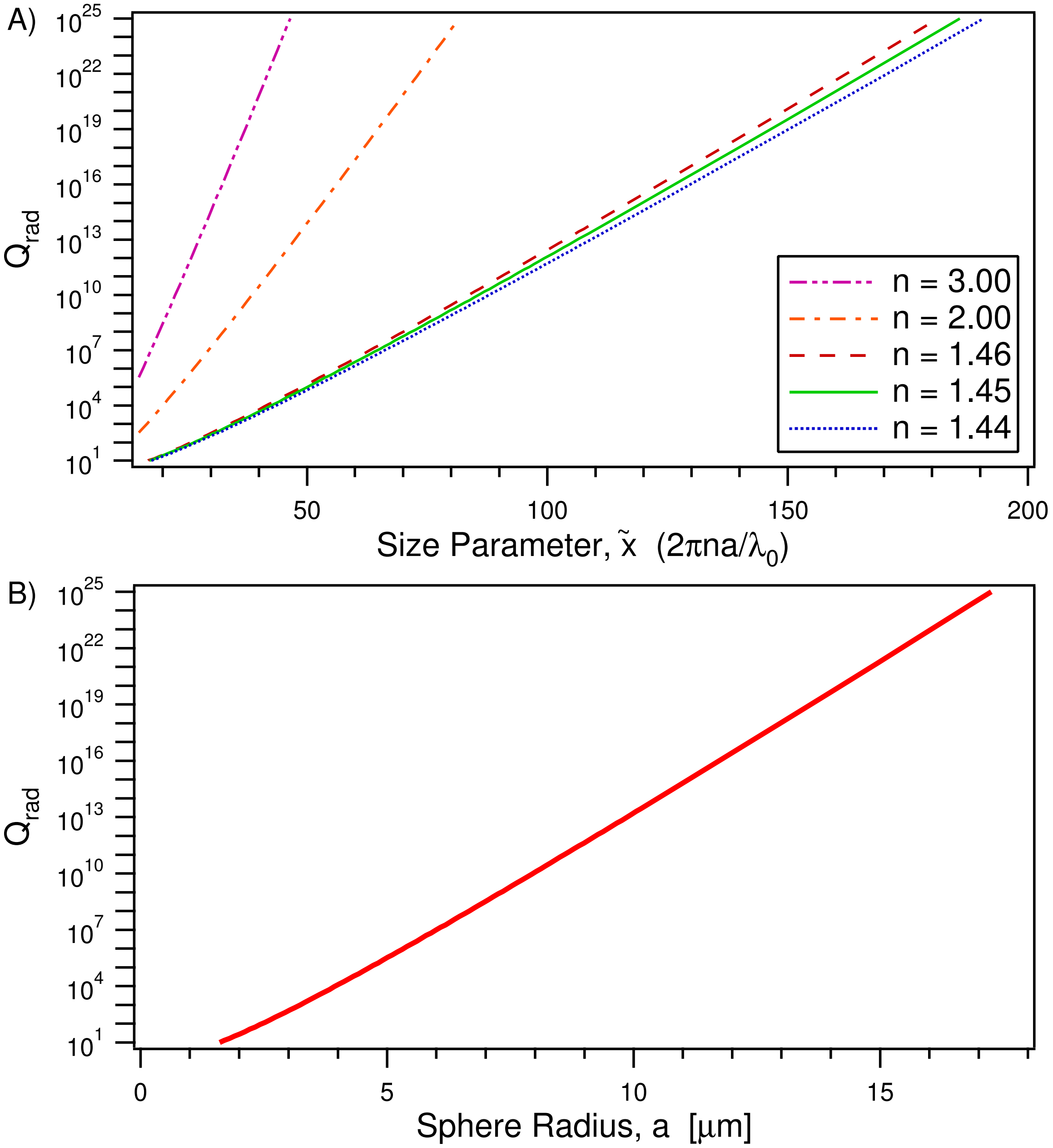

Figure 9.6: Radiative Quality Factors for Dielectric Microspheres
(a) Semi-log plot of the radiative quality factor, Q_{rad}, for various indices of refraction as a function of the dimensionless size parameter, $\tilde{x} = \frac{2\pi na}{\lambda_0}$. (b) Semi-log plot of the radiative quality factor, Q_{rad}, as a function of sphere radius for a wavelength of $\lambda_0 = 852.359$ nm (index of refraction is $n = 1.45246$).

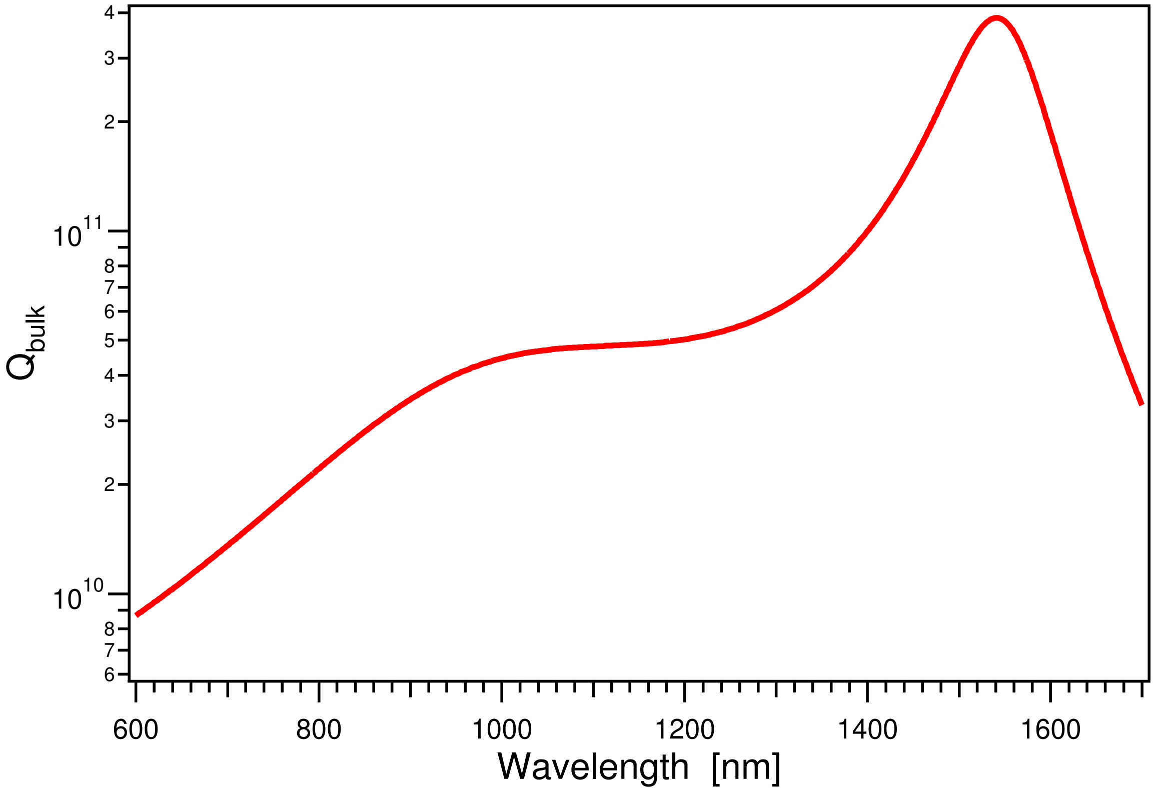

Figure 9.7: Quality Factor Due to Bulk Absorption
The quality factor, Q_{bulk}, from Equation 9.22 for a very low-OH fused silica microsphere as a function of wavelength. Because fused silica has a minimum in absorption at 1550 nm, there is a maximum for the quality factor due to bulk absorption of $Q_{\text{bulk}} \sim 3.8 \times 10^{11}$. At 852 nm, the quality factor due to bulk absorption is $Q_{\text{bulk}} \sim 2.4 \times 10^{10}$.

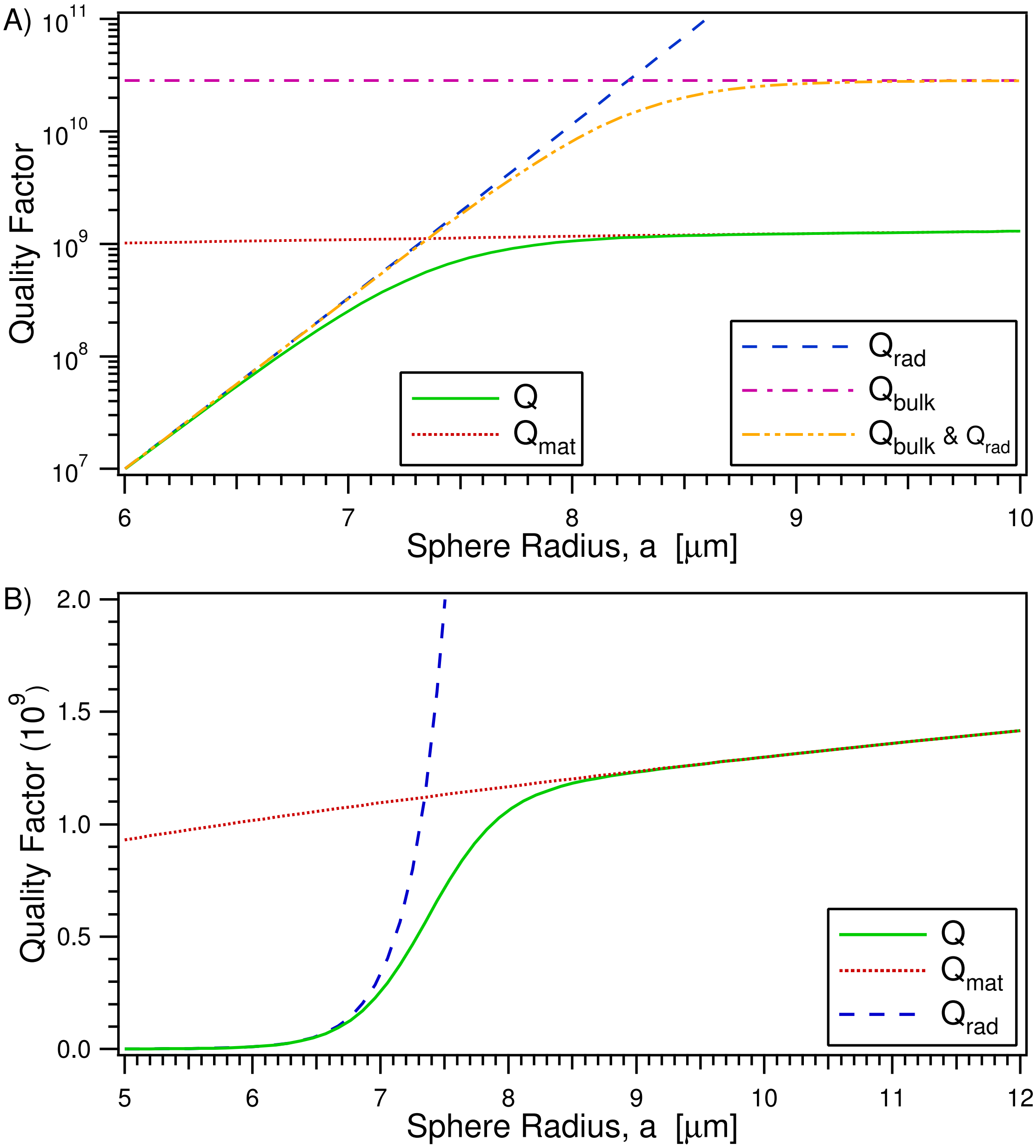

Figure 9.8: Quality Factors for Dielectric Microspheres

(a) Semi-log plot of the quality factors due to the various loss mechanisms discussed in Section 9.3 for a very low-OH fused silica microsphere as a function of sphere radius for the $l = m$, TM modes at a wavelength of $\lambda_0 = 852$ nm. In particular, traces are shown for the quality factor due to purely radiative losses (Q_{rad}), the bulk absorption of fused silica (Q_{bulk}), both radiative losses and bulk absorption, the three loss mechanisms comprising Q_{mat}: (Q_{bulk}, $Q_{\mathrm{s.s.}}$, Q_{w}), and the predicted Q due to all four loss mechanisms. (b) This linear plot zooms in on the region of interest at the transition where the radiative losses become the dominant loss mechanism. The plot contains the quality factor due to purely radiative losses (Q_{rad}), the three loss mechanisms comprising Q_{mat}: (Q_{bulk}, $Q_{\mathrm{s.s.}}$, Q_{w}), and the predicted Q due to all four loss mechanisms.

Chapter 10

Strong Coupling with Dielectric Spheres

10.1 The Strong Coupling Regime

The ultimate goal that we consider here is to employ the WGMs of quartz microspheres as cavity modes for achieving strong coupling to atoms within the setting of cavity QED. The atom of choice in our work is Cesium, and in particular, the D_2 ($F = 4 \mapsto F' = 5$) transition in Cesium at $\lambda_0 = 852.359$ nm as an illustrative example. Such an analysis allows a direct comparison with the state of the art in Fabry-Perot cavities [34].

The coupling coefficient $g(\vec{r})$ is the coupling frequency of a single atom to a particular cavity mode and corresponds to one-half the single-photon Rabi frequency [77, 56]. For an atom located just at the outer surface of the microsphere (i.e., in vacuum) and interacting with a whispering gallery mode $\vec{P} = (p, l, m)$, the coupling coefficient is given by [19]

$$g(a) \equiv g_a = \gamma_\perp \left| \vec{\Psi}_{\mathrm{out}}(a) \right| \sqrt{\frac{V_0}{V_{\vec{P}}}}, \tag{10.1}$$

where a is the sphere radius, $\frac{\gamma_\perp}{2\pi} = 2.61$ MHz is the transverse spontaneous decay rate for our transition in Cesium, $V_0 = \frac{3c\lambda_0^2}{4\pi\gamma_\perp}$ is the effective volume of the atom for purely radiative interactions, and $V_{\vec{P}}$ is the electromagnetic mode volume of the whispering gallery mode designated by $\vec{P} = (p, l, m)$.

Armed with a knowledge of g, we are now able to determine certain dimensionless parameters relevant to the strong coupling regime of cavity QED. In particular, we consider an atom-cavity system to be in the strong coupling regime when the single-photon Rabi frequency, $2g$, for a single intracavity atom dominates the cavity field decay rate, κ, the atomic dipole decay rate, $\gamma_\perp$, and the inverse atomic transit time, T^{-1} [77, 56]. We will defer further discussion of T^{-1}, however, this requirement relates to the need for atomic localization [19, 61]. In the strong coupling regime, important parameters for characterizing the atom-cavity system are the two dimensionless parameters: the saturation photon number, n_0, and the critical atom number, N_0. The saturation photon number, given by

$$n_0 \equiv \frac{\gamma_\perp^2}{2g^2}, \tag{10.2}$$

corresponds to the number of photons required to saturate an intracavity atom [77, 56]. The critical atom number, defined by

$$N_0 \equiv \frac{2\gamma_\perp \kappa}{g^2}, \tag{10.3}$$

corresponds to the number of atoms required to have an appreciable effect on the intracavity field [77, 56]. Ideally, one hopes to minimize simultaneously both the critical atom number, N_0, and the saturation photon number, n_0, which corresponds to simultaneous maxima for both $\frac{g^2}{\kappa\gamma_\perp}$ and $\frac{g^2}{\gamma_\perp^2}$.

The saturation photon number and critical atom number are useful because of their physical meaning. However, one can define a new dimensionless parameter

$$\beta = \frac{8\pi^2 V_{\vec{P}}}{3\lambda_0^3} \frac{1}{\left|\vec{\Psi}_{\text{out}}(a)\right|^2}, \tag{10.4}$$

that corresponds to the cavity mode volume in units of λ^3 weighted by the inverse of the strength of the mode function at the atomic position. This enables the equations for the saturation photon number and critical atom number to be expressed as:

$$n_0 = \frac{\beta}{4Q_{\text{atom}}}, \tag{10.5}$$

and

$$N_0 = \frac{\beta}{Q_{\text{cavity}}}, \tag{10.6}$$

where

$$Q_{\text{atom}} = \frac{\pi c}{\lambda_0 \gamma_\perp}, \tag{10.7}$$

and

$$Q_{\text{cavity}} = \frac{\pi c}{\lambda_0 \kappa}. \tag{10.8}$$

This parameter, β, then also determines the coupling coefficient in the following manner:

$$g(a) = \sqrt{\frac{2\pi c \gamma_\perp}{\beta \lambda_0}}. \tag{10.9}$$

Therefore, we see that one can use a single parameter, β, combined with the properties of the atom to be used (λ_0 and $\gamma_\perp$) and the quality factor of the resonator, Q_{cavity}, to determine the three parameters (n_0, N_0, g_0) of importance in determining the quality of an atom-cavity system.

Figures 10.1 and 10.2 are plots of this dimensionless parameter β and of $\frac{1}{\sqrt{\beta}}$ as functions of the dimensionless size parameter $\tilde{x} = \frac{2\pi n a}{\lambda_0}$ for a few values of index of refraction. Because the index of refraction for fused silica varies from $n = 1.444$ at $\lambda_0 = 1550$ nm to $n = 1.458$ for $\lambda_0 = 600$ nm (see Figure 9.5), Figures 10.1b and 10.2b are made for that range of values. From Figures 10.1 and 10.2 one sees that there is a minimum for β and a maximum for $\frac{1}{\sqrt{\beta}}$ that depends on the index of refraction.

10.2 Strong Coupling with Cesium

The results of the previous section can now be used to determine the saturation photon number, n_0, the critical atom number, N_0, and the coupling coefficient, $g(a)$, for any atomic transition. In our case, we are concerned with the D_2 transition in Cesium ($\lambda_0 = 852.359$ nm). For this transition, the spontaneous transverse decay rate is $\frac{\gamma}{2\pi} = 2.61$ MHz. Also, at this wavelength the index of refraction for fused silica is $n = 1.45246$. This allows one to compute the coupling coefficient, $g(a) = \sqrt{\frac{2\pi c\gamma_\perp}{\beta\lambda_0}}$. Figure 10.3 shows that there is a maximum of $\frac{g}{2\pi} = 749.986$ MHz for a radius $a = 3.63\mu$m, ($l = m = 33$). Interestingly, because we are restricted to having the atom couple to the *external* field of the microsphere, the maximum in the coupling coefficient, $g(a)$, does not coincide with the minimum for the mode volume, $V_{\vec{P}}$ (see Figures 9.4 and 10.3.)

The saturation photon number, n_0, is proportional to the dimensionless parameter β as shown in Equation 10.5. Since the factor of proportionality is a constant that depends only on the properties of the particular atom of concern, the curve is determined by that of β along with the quality factor of the atomic resonance (in our case Cesium), which is given by Equation 10.7 to be $Q_{atom} = 6.738 \times 10^7$. Figure 10.4 is a plot of the saturation photon number for the D_2 transition in Cesium as a function of sphere size. Figure 10.4 shows that there is a minimum for the saturation photon number of $n_0 = 6.05527 \times 10^{-6}$ for a sphere radius of $a = 3.63163\mu$m ($l = m = 33$).

The critical atom number, N_0, is also proportional to the dimensionless parameter β as shown in Equation 10.6. However, its factor of proportionality is the quality factor of the resonator, Q_{cavity}, which has a very strong dependence on the sphere radius, a, in the region below 10μm (see Figure 9.8). Therefore, the minimum for the critical atom number does not occur for the same sphere size as for the saturation photon number. Figure 10.5 is a plot of the critical atom number as a function of sphere size. Using for Q_{cavity} the model that incorporates all of the loss mechanisms discussed in section 9.3 (radiative losses, bulk absorption, surface scattering, and absorption due to water on the surface), we find that the minimum for the critical atom number $N_0 = 8.99935 \times 10^{-6}$ occurs for a sphere radius of $a = 8.12015\mu$m ($l = m = 79$). At this radius, the coupling coefficient is $\frac{g}{2\pi} = 304.16$ MHz.

Unfortunately, as illustrated in Figure 10.6, the minima for the two parameters, n_0 and N_0, do not occur for the same sphere radius. However, if one uses the minimum of the geometric mean of the two parameters, each can have a value near its respective minimum. The minimum of the geometric mean occurs for a sphere radius $a = 7.83038 \mu\mathrm{m}$ ($l = m = 76$). For this sphere size, the coupling coefficient is $\frac{g}{2\pi} = 318.333$ MHz, the saturation photon number is $n_0 = 3.36107 \times 10^{-5}$, and the critical atom number is $N_0 = 9.27834 \times 10^{-6}$. Therefore, each cavity QED parameter can be made to achieve simultaneously a value near its respective minimum.

10.3 Progress in Small Sphere Manufacture

A large portion of the work being done on microspheres has been to push the quality factors of the spheres to record levels [17, 18]. This effort has produced some of the highest finesse ($\mathcal{F} = 2.3 \times 10^6$) optical cavities to date with quality factors $Q \sim 10^{10}$ [17, 18]. However, we have seen that Q is not the only relevant factor in determining the suitability of the WGMs for cavity QED in a regime of strong coupling. In general, the preceding analysis demonstrates the requirement to push to microspheres of small radius, $a \lesssim 10\mu\mathrm{m}$. Unfortunately, the experiments that have achieved the highest quality factors and which have investigated certain material loss mechanisms are of rather larger size, and hence not optimal for cavity QED in a regime of strong coupling. For example, the experiment of Ref. [18] achieved a quality factor of $Q = 7.2 \times 10^9$ at 850 nm in a sphere of radius $a = 340\mu\mathrm{m}$.

To explore the possibilities of cavity QED with strong coupling in substantially smaller spheres, we have undertaken a program to study fabrication techniques for quartz microspheres with $a \lesssim 30\mu\mathrm{m}$, while still maintaining high quality factors. We have been able to fabricate $10\mu\mathrm{m}$ radius spheres using an oxygen-hydrogen microtorch to melt the ends of very low-OH fused silica rods to form a sphere on the end of a stem. Light is then coupled to the sphere using frustrated total internal reflection of a prism, as in References [19, 18, 20]. Our observations demonstrate that spheres of this size can be made consistently to have quality factors $Q \gtrsim 0.8 \times 10^7$. While this is encouraging progress, the resulting Q is two orders of magnitude smaller than the theoretical maximum of approximately 1.3×10^9 for this size based upon the model discussed in Section 9.3.

One possible reason for this discrepancy could be the importance of minimizing the ellipticity of the small spheres. Because the small resonators fabricated by our technique have a stem protruding out of them, they are far from spherical. When coupling to an $l = m$ mode in spheres with $a \gtrsim 100\mu$m and hence large l, the mode is tightly confined to the equator; therefore, the poles do not have an appreciable impact on the mode structure or quality factor. In this case, it is not of critical importance to have the best sphere possible, but rather the best great circle possible to achieve large quality factors. However, this is not the case in small spheres with $a \lesssim 10\mu$m. As a decreases, the $l = m$ modes occupy an increasingly larger proportion of the sphere in polar angle, and the ellipticity of the sphere becomes increasingly important in determining the mode structure as well as the Q. However, while there is certainly room for improvement in our fabrication technique and in the resulting mode structures and quality factors, we shall see in the next section that the current results have promising implications.

10.4 Comparing Microspheres and Fabry-Perot Cavities

Figure 10.7 offers a comparison of the state of the art for Fabry-Perot and microsphere cavities for cavity QED, as well as projections of likely limits for each. It is interesting to note that in our projections for the limiting cases of each, microspheres allow for a significant improvement in the critical atom number, N_0, relative to Fabry-Perot cavities. On the other hand, a principal advantage of Fabry-Perot cavities relative to microspheres would seem to be significant improvements in the saturation photon number, n_0. The specific specific task at hand would then dictate which technology to apply.

As shown in Figure 10.7, there has already been some progress in coupling atoms to the external fields of a microsphere [20]. The sphere employed for the work of Ref. [20]

had a radius of $a \approx 60\ \mu$m, and quality factor $Q \lesssim 5 \times 10^7$, corresponding to a mode volume of $V_{\vec{P}} \approx 3.7 \times 10^3\ \mu\text{m}^3$, coupling coefficient $g_a/(2\pi) \approx 24$ MHz, saturation photon number $n_0 = 5.54 \times 10^{-3}$, and critical atom number $N_0 = 2.99 \times 10^{-2}$. If instead this experiment were to be implemented with a smaller sphere with 10μm radius and with quality factor $Q \sim 0.8 \times 10^7$ such as we have manufactured and described in Section 10.2, the following parameters would be achieved: a mode volume of $V_{\vec{P}} \approx 1.4 \times 10^2\ \mu\text{m}^3$, coupling coefficient $g_a/(2\pi) \approx 233$ MHz, saturation photon number $n_0 \approx 6.27 \times 10^{-5}$, and critical atom number $N_0 \approx 2.11 \times 10^{-3}$. Therefore, we see that currently achievable quality factors in spheres of radius 10μm already would allow for impressive results in cavity QED with single atoms.

By comparison, the state of the art for Fabry-Perot cavities has already achieved the following results for the TEM_{00} modes [5]: a cavity finesse of $\mathcal{F} = 4.8 \times 10^5$, a mode volume of $V_\text{m} \approx 1.69 \times 10^3\ \mu\text{m}^3$, coupling coefficient $g_0/(2\pi) \approx 110$ MHz, saturation photon number $n_0 \approx 2.82 \times 10^{-4}$, and critical atom number $N_0 \approx 6.13 \times 10^{-3}$. If one then looks at possible limits of Fabry-Perot technology for cavity QED as analyzed in Ref. [34], the following may be possible; a cavity of length $\lambda_0/2$ with a cavity finesse of $\mathcal{F} = 7.8 \times 10^6$ yields coupling coefficient $g_0/(2\pi) \approx 770$ MHz, saturation photon number $n_0 \approx 5.7 \times 10^{-6}$, and critical atom number $N_0 \approx 1.9 \times 10^{-4}$.

It is encouraging that the currently achievable results for small sphere manufacture would already allow the WGMs to compete favorably with the current state of the art in Fabry-Perot cavity QED. However, if one were able to manufacture and couple to spheres at the optimal size $a \approx 7.83\mu$m with a $Q \sim 9.76 \times 10^8$ (the theoretical maximum predicted from the analysis of Section 9.3), the following results could be achieved: a mode volume of $V_{\vec{P}} \approx 90\ \mu\text{m}^3$, coupling coefficient $g_a/(2\pi) \approx 318$ MHz, saturation photon number $n_0 \approx 3.36 \times 10^{-5}$, and critical atom number $N_0 \approx 9.28 \times 10^{-6}$. This would represent a significant improvement over the current Fabry-Perot technology and be competitive with the likely limits of Fabry-Perot technology. However, even short of achieving this stated maximum Q for the WGMs, impressive results can already be attained. With a quality factor $Q \sim 0.8 \times 10^7$ at the optimal sphere radius $a \approx 7.83\ \mu$m, one would obtain these same results (i.e., $g_a/(2\pi) \approx 318$ MHz and saturation photon number $n_0 \approx 3.36 \times 10^{-5}$), except that the critical atom number, N_0, would increase to $N_0 \approx 1.13 \times 10^{-3}$. This is still an impressive gain over the current capabilities of Fabry-Perot cavities for the saturation photon number, with room for improvement in the critical atom number.

Overall, we thus find that the technologies of microspheres and Fabry-Perot resonators each have their advantages and disadvantages. However, there is one notable advantage of microspheres; they can be made cheaply and relatively simply given sufficient training and skill. By contrast, the Fabry-Perot cavities considered here require specialized coating runs with expensive equipment and considerable expertise, which is to be found at only a few locations worldwide. This alone makes microspheres an attractive alternative to Fabry-Perot cavities for cavity QED. Another unique advantage of the WGMs is the ability to control the cavity decay rate, κ, by controlling the coupling efficiency into and out of the microsphere (e.g., by adjusting the distance between a coupling prism and the microsphere [84].) Furthermore, as one moves to the limit of small cavities, the open geometry of microspheres offers a considerable advantage when compared to the geometry of Fabry-Perot cavities. Such possibilities combined with our projected values of the critical parameters, (n_0, N_0), shown in Figure 10.7 point to the competitiveness of microspheres with current and future Fabry-Perot technology and demonstrate their potential as a powerful tool for cavity QED in the regime of strong coupling.

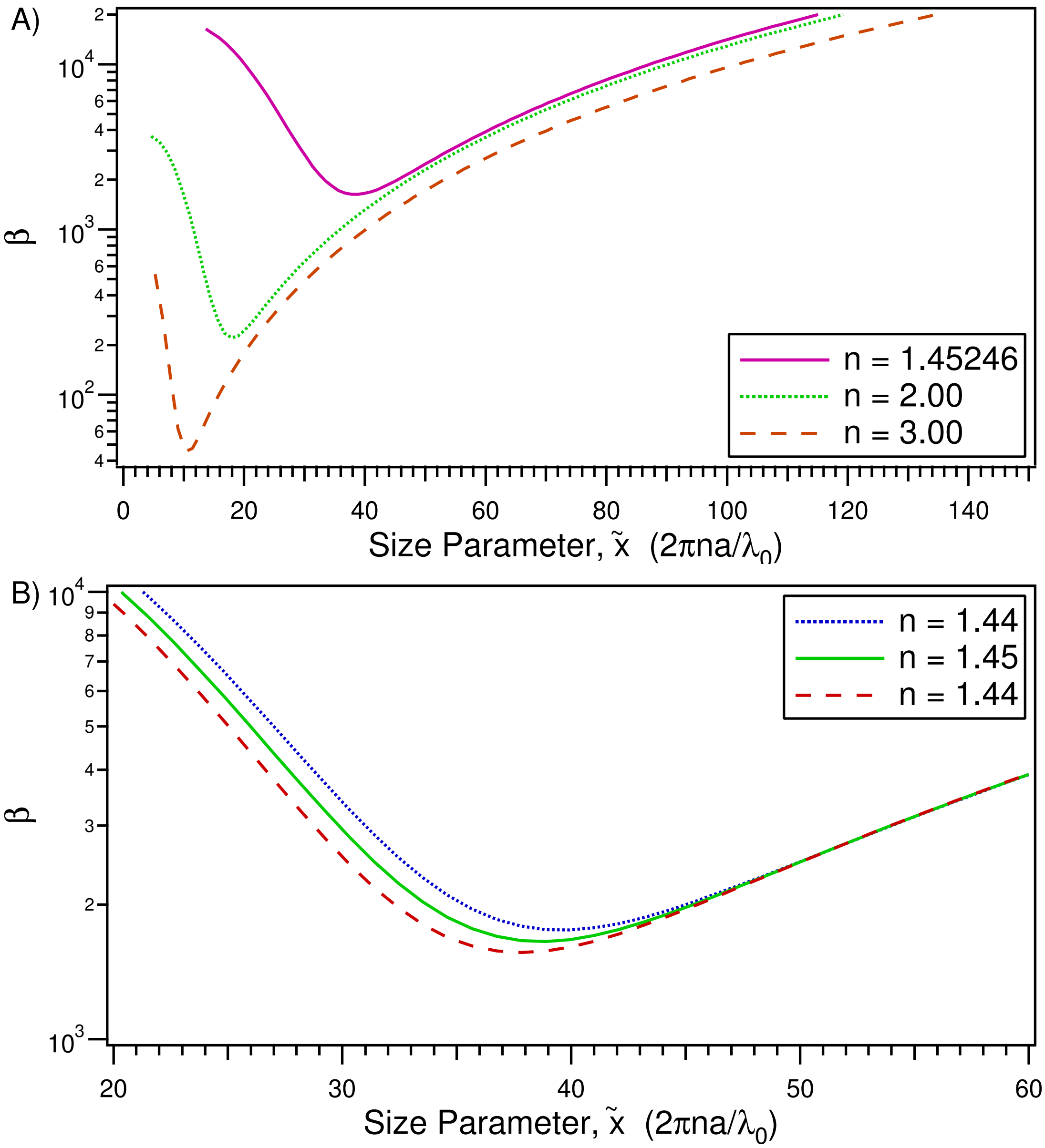

Figure 10.1: Dimensionless Parameter β

(a) The dimensionless parameter β as a function of the dimensionless size parameter $\tilde{x} = \frac{2\pi na}{\lambda_0}$. For an index of refraction $n = 1.45246$ (i.e., the index of refraction for fused silica at $\lambda_0 = 852$ nm), there is a minimum of $\beta = 1632.01$ for $\tilde{x} = 38.8833$, $(l = m = 33)$. For an index of refraction $n = 2.00$, there is a minimum of $\beta = 221.124$ for $\tilde{x} = 17.8763$, $(l = m = 13)$. For an index of refraction $n = 3.00$, there is a minimum of $\beta = 45.3744$ for $\tilde{x} = 10.2748$, $(l = m = 6)$. (b) Because the index of refraction for fused silica varies from $n = 1.444$ at $\lambda_0 = 1550$ nm to $n = 1.458$ for $\lambda_0 = 600$ nm (see Figure 9.5), this plot is made for that range of values. For an index of refraction $n = 1.44$, there is a minimum of $\beta = 1753.92$ for $\tilde{x} = 39.9188$, $(l = m = 34)$. For an index of refraction $n = 1.45$, there is a minimum of $\beta = 1653.7$ for $\tilde{x} = 38.8778$, $(l = m = 33)$. For an index of refraction $n = 1.46$, there is a minimum of $\beta = 1561.45$ for $\tilde{x} = 37.8348$, $(l = m = 32)$.

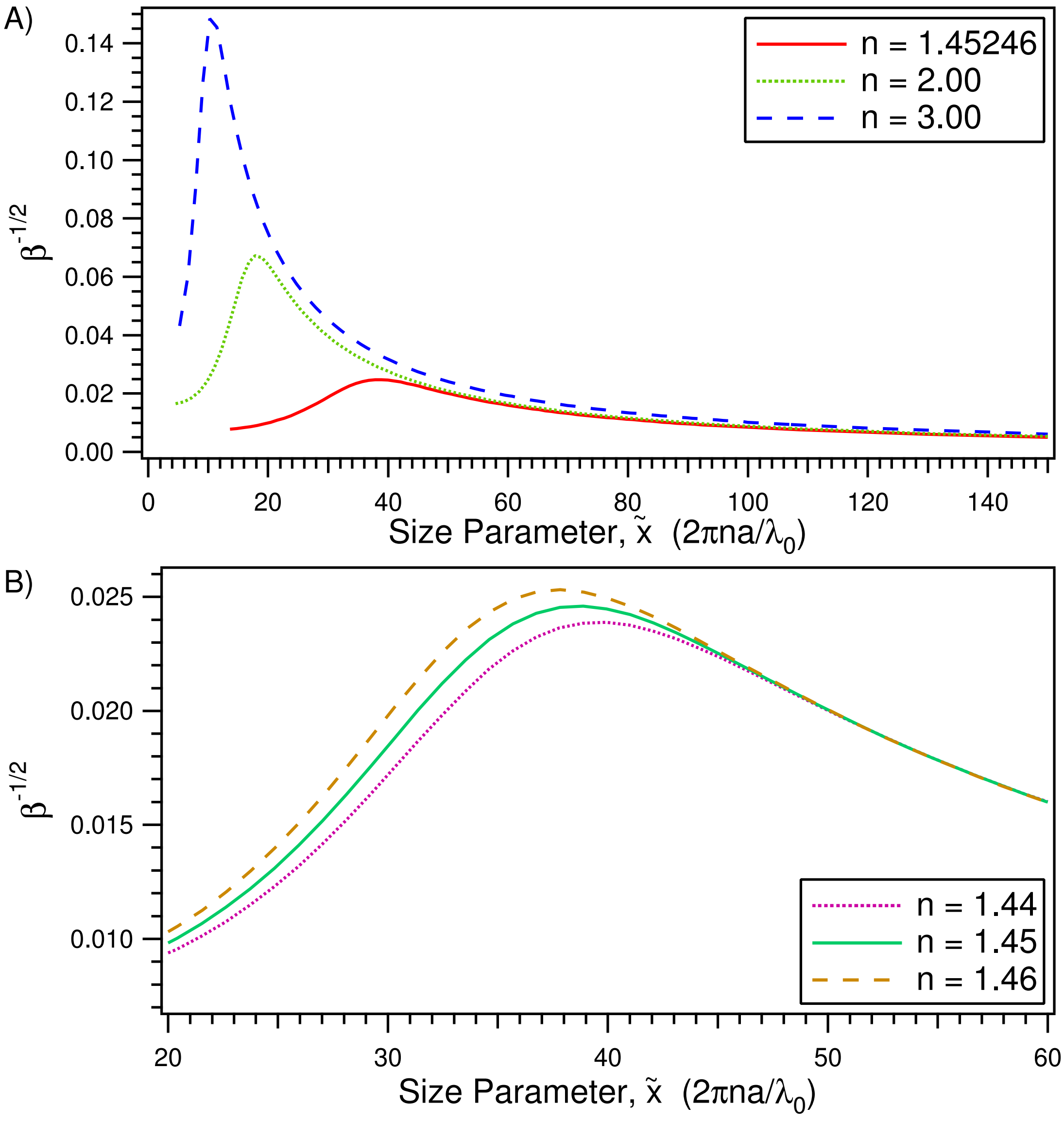

Figure 10.2: Dimensionless Parameter $\frac{1}{\sqrt{\beta}}$

(a) The dimensionless parameter $\frac{1}{\sqrt{\beta}}$ as a function of the dimensionless size parameter $\tilde{x} = \frac{2\pi na}{\lambda_0}$. For an index of refraction $n = 1.45246$ (i.e., the index of refraction for fused silica at $\lambda_0 = 852$ nm), there is a maximum of $\frac{1}{\sqrt{\beta}} = 0.0247536$ for $\tilde{x} = 38.8833$, ($l = m = 33$). For an index of refraction $n = 2.00$, there is a maximum of $\frac{1}{\sqrt{\beta}} = 0.0672484$ for $\tilde{x} = 17.8763$, ($l = m = 13$). For an index of refraction $n = 3.00$, there is a maximum of $\frac{1}{\sqrt{\beta}} = 0.148455$ for $\tilde{x} = 10.2748$, ($l = m = 6$). (b) Because the index of refraction for fused silica varies from $n = 1.444$ at $\lambda_0 = 1550$ nm to $n = 1.458$ for $\lambda_0 = 600$ nm (see Figure 9.5), this plot is made for that range of values. For an index of refraction $n = 1.44$, there is a maximum of $\frac{1}{\sqrt{\beta}} = 0.0238779$ for $\tilde{x} = 39.9188$, ($l = m = 34$). For an index of refraction $n = 1.45$, there is a minimum of $\frac{1}{\sqrt{\beta}} = 0.0245908$ for $\tilde{x} = 38.8778$, ($l = m = 33$). For an index of refraction $n = 1.46$, there is a minimum of $\frac{1}{\sqrt{\beta}} = 0.0253068$ for $\tilde{x} = 37.8348$, ($l = m = 32$).

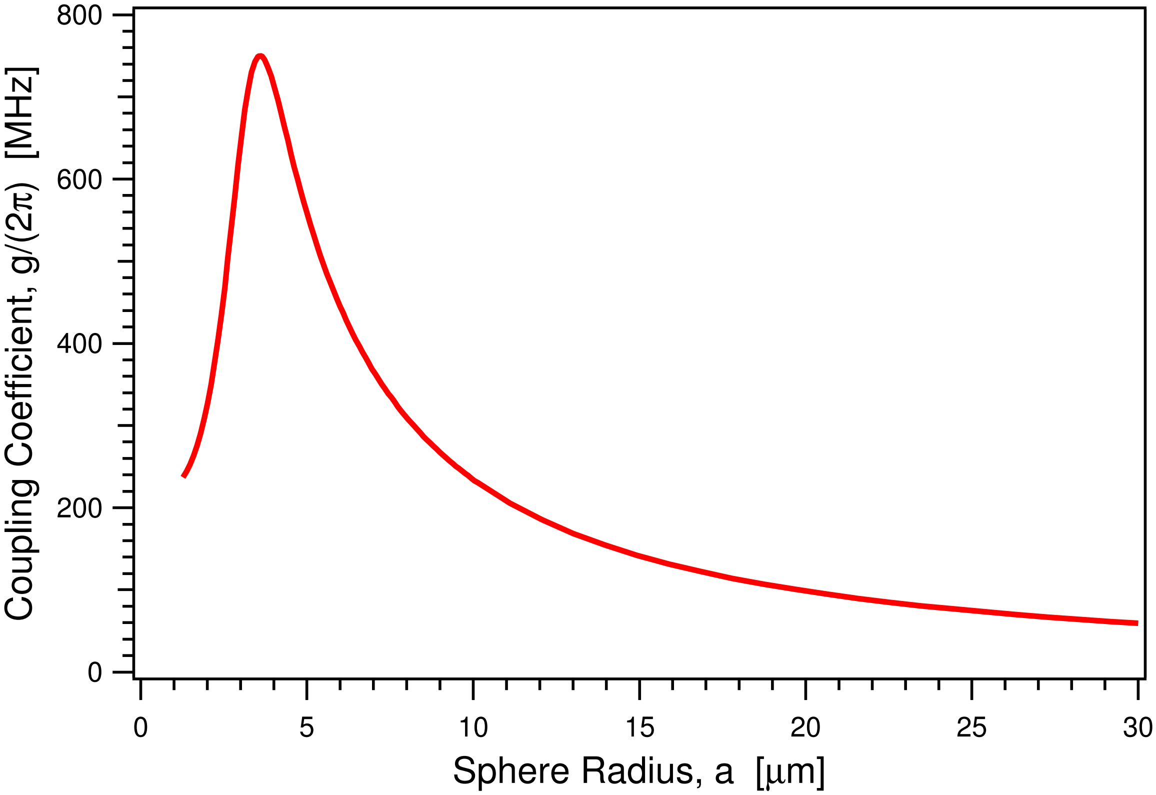

Figure 10.3: Coupling Coefficient for Dielectric Microspheres
The coupling coefficient, $\frac{g}{2\pi}$, as a function of sphere size for the D_2 transition in Cesium ($\lambda_0 = 852.359$ nm). There is a maximum of $\frac{g}{2\pi} = 749.986$ MHz for a sphere radius of $a = 3.63163\mu$m, ($l = m = 33$). Note that the maximum for $\frac{g}{2\pi}$ does not coincide with the minimum for the cavity mode volume, $V_{\vec{P}}$ (see Figure 9.4).

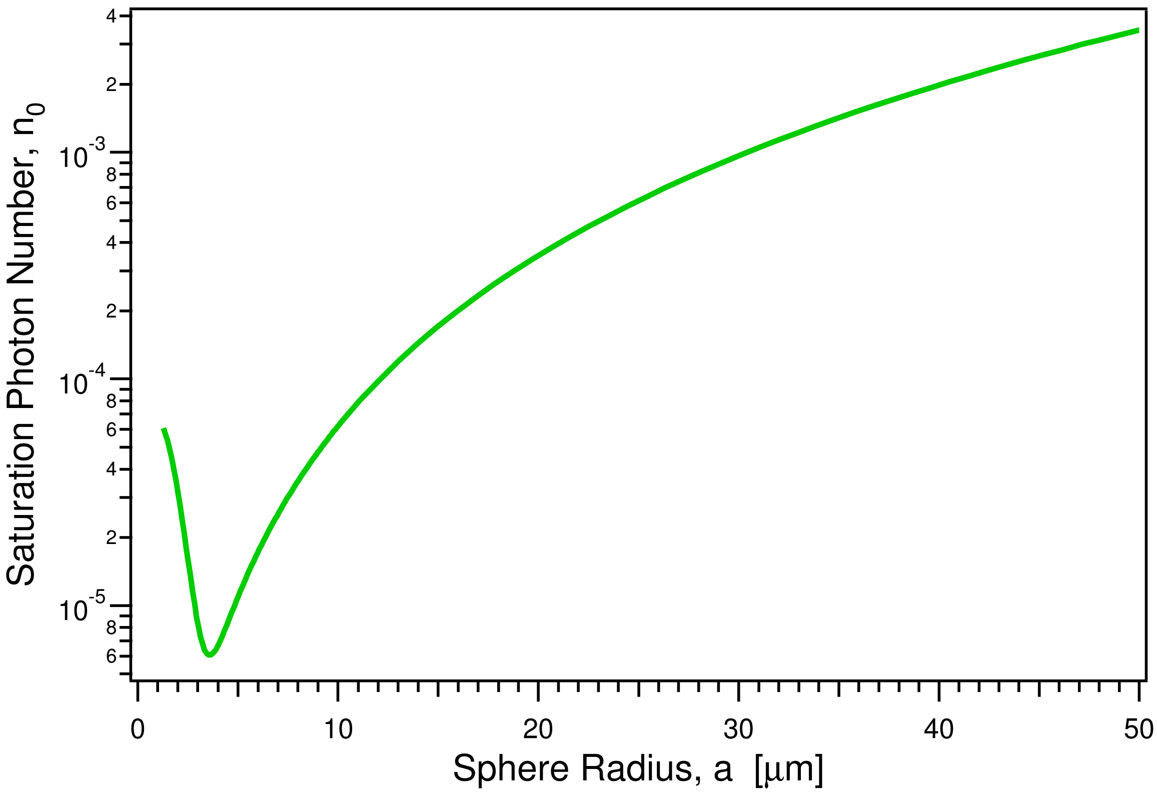

Figure 10.4: Saturation Photon Number for Microsphere Resonators
The saturation photon number, n_0, as a function of sphere size for the D_2 transition in Cesium ($\lambda_0 = 852.359$ MHz). There is a minimum $n_0 = 6.05527 \times 10^{-6}$ for a sphere radius of $a = 3.63163\mu$m ($l = m = 33$). At this radius, the coupling coefficient is $\frac{g}{2\pi} = 749.986$ MHz.

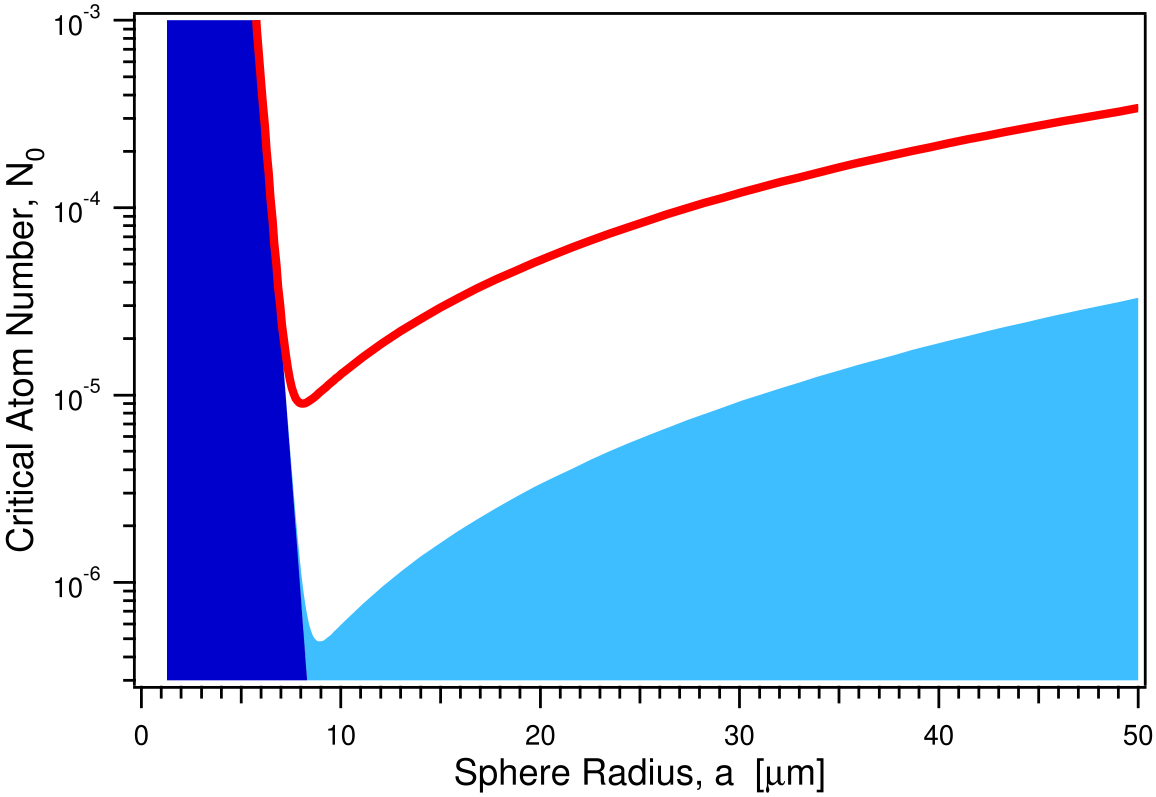

Figure 10.5: Critical Atom Number for Microsphere Resonators
The critical atom number, N_0, as a function of sphere size for the D_2 transition in Cesium ($\lambda_0 = 852.359$ MHz). There is a minimum $N_0 = 8.99935 \times 10^{-6}$ for a sphere radius of $a = 8.12015\mu$m ($l = m = 79$). At this radius, the coupling coefficient is $\frac{g}{2\pi} = 304.16$ MHz. This plot of the critical atom number incorporates the model for the quality factor of the resonator, Q_{cavity}, outlined in section 9.3, for the four loss mechanisms: bulk absorption, surface scattering, absorption due to water on the surface, and radiative losses. The dark blue region is bounded by the effects of purely radiative losses. The light blue region is bounded by the effects of both radiative losses and bulk absorption.

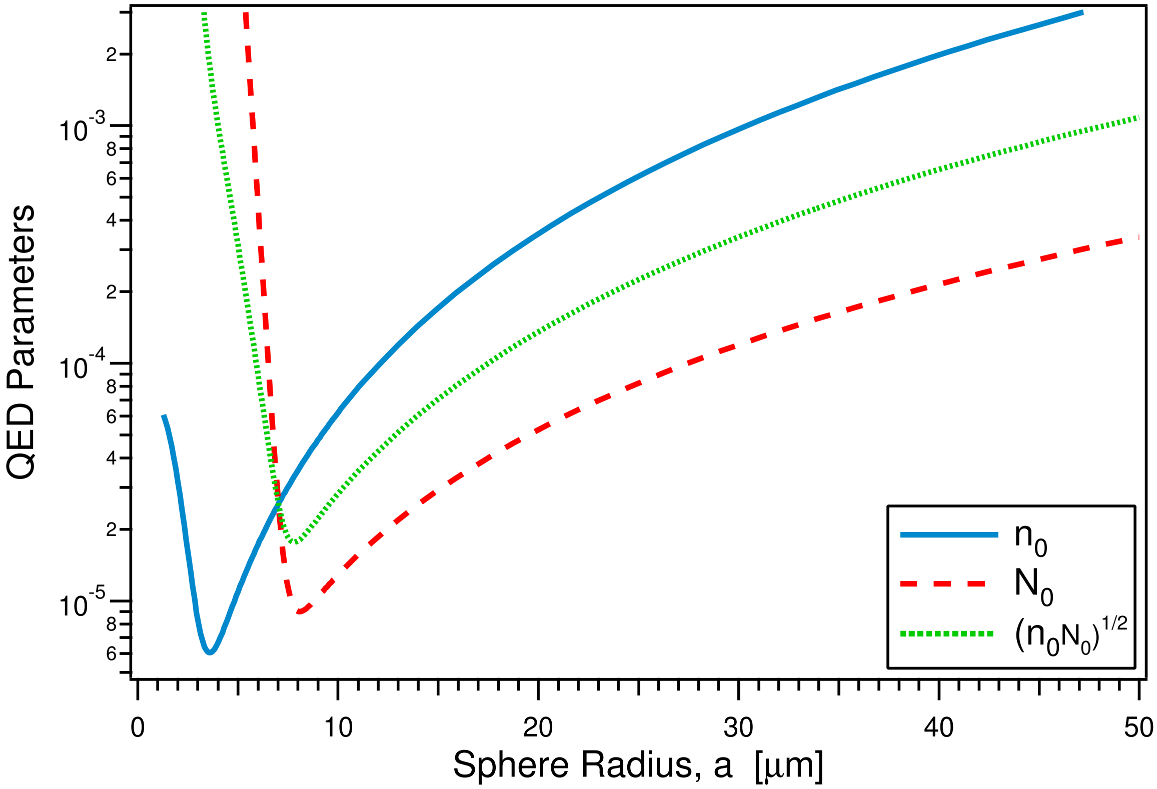

Figure 10.6: Comparison of the Critical Parameters for Microsphere Resonators This plot shows the two parameters, (n_0, N_0), of importance to cavity QED as a function of sphere radius. The geometric mean of these two parameters is also plotted. The solid line represents the saturation photon number, n_0, the dashed line gives the critical atom number, N_0, and the dotted line shows the geometric mean of the two parameters, $\sqrt{n_0 \times N_0}$. The minimum of each plot corresponds to the following dimensionless parameters: $n_0 = 6.05527 \times 10^{-6}$ for $a = 3.63163\mu\mathrm{m}$ $(l = m = 33)$, and $N_0 = 8.99935 \times 10^{-6}$ at $a = 8.12015\mu\mathrm{m}$ $(l = m = 79)$. The two curves cross at $a = 7.03\mu\mathrm{m}$ with $n_0 = N_0 = 2.56 \times 10^{-5}$. The geometric mean of these two parameters, $\sqrt{n_0 \times N_0}$, is minimized for $a = 7.83038\mu\mathrm{m}$ $(l = m = 76)$. For this radius, the parameters are: $n_0 = 3.36107 \times 10^{-5}$ and $N_0 = 9.27834 \times 10^{-6}$. Note that the curve for N_0 assumes the model for the Q discussed in this paper, and that the coupling coefficient $g\left(\vec{r}\right)$ is evaluated at the maximum of the mode function for $r = a$.

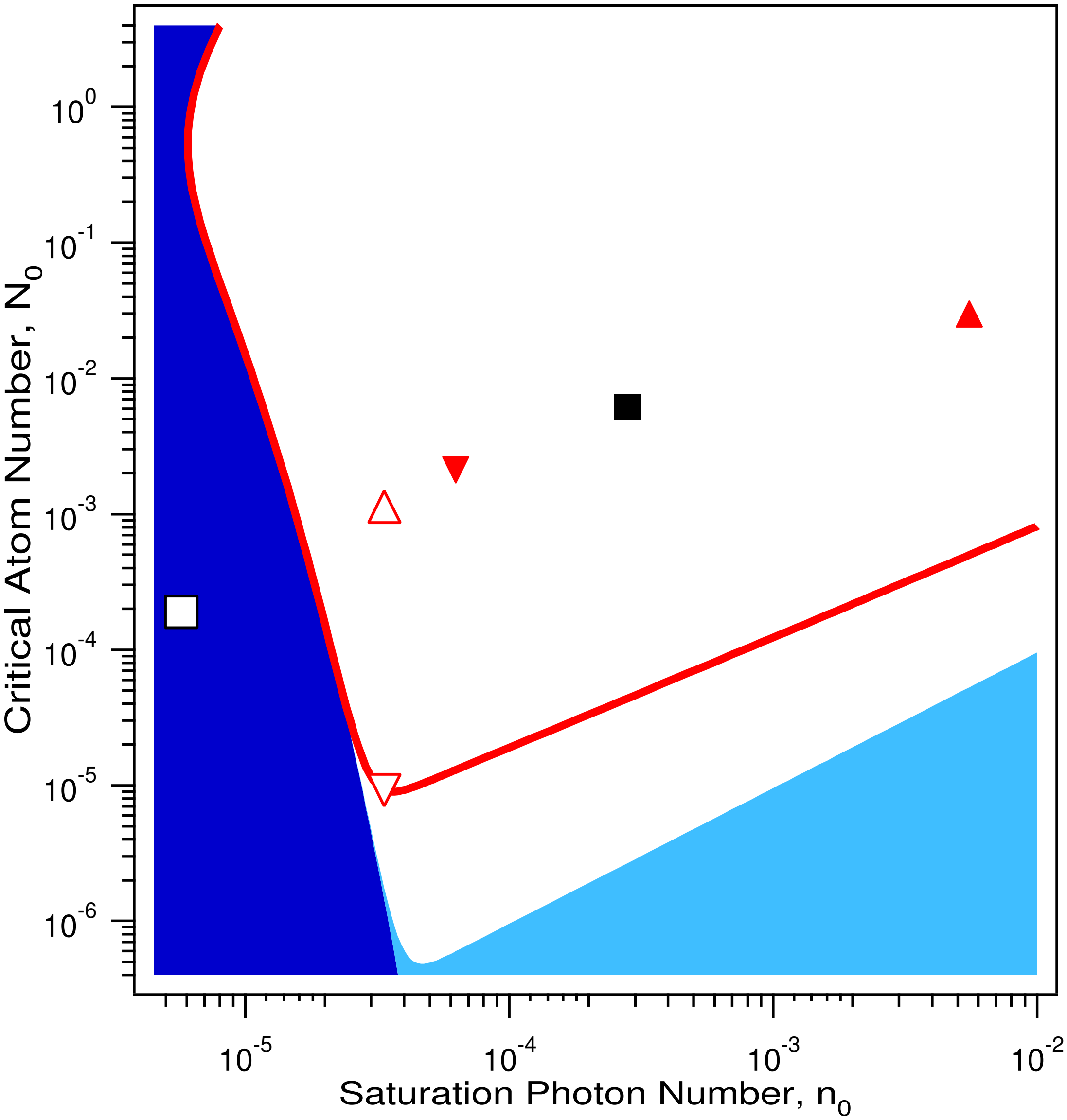

Figure 10.7: Comparison of Microsphere and Fabry-Perot Cavities
The solid line gives a parametric plot of the critical atom number, N_0, and the saturation photon number, n_0, for fused-silica microspheres and the D_2 transition of atomic Cesium, incorporating the loss mechanisms outlined in section 9.3. The dark blue region is bounded by the effects of radiative losses. The light blue region is bounded by the effects of bulk absorption and radiative losses. This plot also offers a comparison of experimental and theoretical cavity QED parameters for microsphere and Fabry-Perot cavities. ■ represents the current state of the art for cavity QED in Fabry-Perot cavities as in Ref. [5]. □ is a projection of the practical limit for Fabry-Perot cavities based upon Ref. [34]. ▲ represents the 60μm radius sphere implemented for cavity QED in Ref. [20]. ▼ is the current state of the art in 10μm microspheres based upon the results presented in section 10.2. △ is the currently achievable Q with the optimal sphere size of 7.83μm based upon the analysis of sections 9.3 and 10.1. ▽ is the theoretically achievable $Q \sim 9.76 \times 10^8$ at the optimal sphere size, $a \approx 7.83\mu$m.

Part IV

Brownian Motion of Mirrors in High-Finesse Fabry-Perot Cavities

Thermal noise is important in many mechanical measurements [25]. It is of course crucial in experiments designed to measure the small displacement of an interferometer. For example, the Laser Interferometer Gravitational-Wave Observatory (LIGO) relies on measuring the gravitational-wave strain $h(t) = \frac{\Delta L}{L}$ with a sensitivity of $h(t) \approx 10^{-23}$. For a length $L = 4$ km, this implies a sensitivity in cavity length of $\Delta L \approx 10^{-19}$ m [85]. In the simplest case for the LIGO interferometer, the Brownian motion of the suspended mirrors can be decomposed into suspension and internal thermal noises. The internal thermal noise results in thermally induced deformations of the mirror surface. Measurements of displacement are complicated by the fact that the modes depend on the spatial matching between light and internal acoustic modes as well as the shape of each eigenmode of the mirror [86]. The energy associated with these displacements is determined by the equipartion theorem. For an acoustic mode of a macroscopic object, an energy equal to $k_B T$ corresponds to a very small displacement.

As we have seen in Chapter 5, Fabry-Perot cavities can be made to have a very high finesse ($\mathcal{F} \sim 1 \times 10^6$). We have also seen that our atom-trapping experiments rely on being able to servo the cavity length to an accuracy exceeding $\Delta L \sim 10^{-15}$ m. As we will see in Section 11.4.3 our Fabry-Perot setup can already achieve a sensitivity of $\sim 10^{-19}$ m. This is already quite spectacular, especially given that the setup was designed for atom trapping and not for observing the thermally excited modes of the mirrors. As shown in Part II, the thermally induced motion of the mirrors can have an effect on an intracavity FORT. Our study of these modes has been limited by the level of intracavity optical power we were willing to tolerate. Since we currently have a working setup for studying single atom trapping in a high finesse cavity (see Part II), we were *very* conservative in turning up the intracavity optical power lest we damage the mirrors inadvertently. Also, the mirrors are mounted in a manner suitable for stability, and not in a way that would reduce the damping of each mode. Therefore, our sensitivity would be improved significantly by simply turning up the input power. We should be able to further improve the sensitivity by designing a better mounting scheme for the mirrors.

These effects have been studied extensively by other groups as well. Researchers in the LIGO project have studied these effects with the goal of limiting the noise in their interferometers [86]. Other groups have built cavities specifically for studying thermal noise as well. The experiment of Reference [87] is one example that has also achieved a sensitivity of $\sim 10^{-19}$ m. Their experiment used a cavity of finesse $\mathcal{F} \sim 37000$ and length $L \sim 1.06$ mm. While the sensitivity of their experiment is comparable to ours, we shall see that our setup affords a significant advantage. Because our cavity is so short ($L \approx 40$ μm) and has a very high finesse, we can observe many thermal modes, and thereby have an accurate measurement of the spectral density function for displacement due to thermal noise. I believe that our apparatus is unique in this respect.

Chapter 11

Brownian Motion and Harmonic Oscillators

11.1 Effect of Displacement on Cavity Output

11.1.1 Fabry-Perot Finesse

The finesse of a Fabry-Perot cavity is given by

$$\mathcal{F} \equiv \frac{\Delta\omega_{\mathrm{F.S.}}}{\Delta\omega_0}, \tag{11.1}$$

where $\Delta\omega_{\mathrm{F.S.}} = \frac{\pi c}{L}$ is the free spectral range of the cavity, $\Delta\omega_0 = \frac{\omega_0}{Q}$ is the full width at half maximum of the resonance at frequency ω_0, L is the cavity length and Q is the quality factor of the resonance. Therefore, the finesse can be written as

$$\mathcal{F} = \frac{\pi c Q}{L\omega_0} = \frac{\pi c}{2\kappa L}, \tag{11.2}$$

since

$$Q = \frac{\omega_0}{\Delta\omega_0} = \frac{\pi c}{\lambda\kappa}, \tag{11.3}$$

where κ is the cavity field decay rate.

11.1.2 Power Fluctuations for Length Changes

For a Fabry-Perot cavity, a displacement δL of one mirror causes a change in the resonant frequency ω_0 as follows

$$\delta\omega_0 = -\frac{\omega_0}{L_0}\delta L. \tag{11.4}$$

The measured power of the cavity output can be approximated as a Lorentzian for frequencies sufficiently near the resonance and for modes that are sufficiently separated

$$P(\omega) = \frac{P_0(\frac{\omega_0}{2Q})^2}{(\omega-\omega_0)^2 + (\frac{\omega_0}{2Q})^2}, \tag{11.5}$$

where P_0 is the measured power at the resonance ω_0. Therefore, the derivative as a function of ω_0 is given by

$$\frac{dP}{d\omega_0} = \frac{2P_0\frac{\omega_0}{2Q}(\omega-\omega_0)}{[(\omega-\omega_0)^2 + (\frac{\omega_0}{2Q})^2]^2}\left[\omega - \omega_0 + \frac{\omega_0}{2Q}\right]. \tag{11.6}$$

Evaluating this derivative at the side of the cavity (half maximum) for $\omega = \omega_0 + \kappa = \omega_0 + \frac{\Delta\omega}{2}$ then yields

$$\left.\frac{dP}{d\omega_0}\right|_{\omega_0+\kappa} = \frac{2P_0 Q}{\omega_0} = \frac{2P_0\mathcal{F}L}{\pi c}. \tag{11.7}$$

Since we have

$$\frac{d\omega_0}{dL} = \frac{\omega_0}{L_0}, \tag{11.8}$$

we then have at the side of the cavity

$$\frac{dP}{dL} = \frac{4P_0\mathcal{F}}{\lambda_0} = \frac{2P_0\omega_0\mathcal{F}}{\pi c}. \tag{11.9}$$

This yields the measured power changes for small changes in the cavity length.

11.1.3 Important Assumptions

An important assumption in this discussion is that the TEM_{00} component of the distorted optical mode reflected from the vibrating mirror surface still resonates in the Fabry-Perot cavity, and that the light scattered into other optical modes does not. This will be true if the change in resonant frequencies $\Delta\omega_n$ of the optical modes of the cavity due to the vibrations of the mirror is less than the linewidth κ of the cavity and if the transverse mode spacing is much larger than the cavity linewidth. Therefore, from Equation 11.8 we see that the change in frequency will be less than the linewidth if

$$\Delta l < \frac{\lambda_0}{2\mathcal{F}}. \tag{11.10}$$

The transverse mode spacing will also be much larger than the linewidth 2κ if

$$\mathcal{F}^2 \gg \frac{R}{8L}, \tag{11.11}$$

where $\mathcal{F}$ is the finesse of the cavity, R is the radius of curvature of the mirrors, and L is the cavity length. This condition is easily satisfied in our case, since $\mathcal{F} = 3.5 \times 10^5$ for $\lambda = 869$ nm, $R \sim 0.2$ m, and $L \sim 40\ \mu$m.

Another important effect related to the cavity linewidth is the cavity buildup time. If we are interested in a frequency greater than the inverse cavity buildup time, then the effects at that frequency will be attenuated. In our case, the linewidth (FWHM) at 869 nm is $\frac{2\kappa}{2\pi} \approx 10.7$ MHz.

11.2 Simple Harmonic Oscillator in Thermodynamic Equilibrium

As we will discuss in Section 11.2.3, the coupling of each mode, ω_n, can be parameterized in terms of an effective mass coefficient, α_n, so that the effective mass is $\alpha_n m$, where m is the actual mass of the mirror. In this way, the motion of the mirror surface can then be modelled as if it were a point mass of magnitude $\alpha_n m$ vibrating with frequency ω_n in harmonic oscillation.

11.2.1 Classical Harmonic Oscillator

For a Hooke's Law force, where the restoring force is proportional to the displacement $F = -kx$, the potential is

$$V_n = \frac{1}{2}k_n x^2 = \frac{1}{2}\alpha_n m \omega_n^2 x^2, \tag{11.12}$$

where the frequency of oscillation ω_n is given by

$$\omega_n^2 = \frac{k_n}{\alpha_n m}. \tag{11.13}$$

The energy is then given by

$$E = T + V = \frac{p^2}{2\alpha_n m} + \frac{1}{2}k_n x^2 = \alpha_n m \omega_n^2 A^2. \tag{11.14}$$

Therefore, the total energy is proportional to the square of the amplitude, and is time-independent (conservative).

The mean energy of any system in thermodynamic equilibrium is

$$\langle E \rangle = k_B T. \tag{11.15}$$

Therefore, the amplitude of displacement, Δl, for a mode of a harmonic oscillator in thermodynamic equilibrium is

$$\Delta l_n = \sqrt{\frac{k_B T}{\alpha_n m \omega_n^2}}. \tag{11.16}$$

11.2.2 Quantum Harmonic Oscillator

The classical quantities x and p are replaced by the conjugate observables X and P, where

$$[X, P] = \imath\hbar. \tag{11.17}$$

The Hamiltonian is then

$$H = \frac{P^2}{2\alpha_n m} + \frac{1}{2}\alpha_n m\omega_n^2 X^2 = -\frac{\hbar^2}{2\alpha_n m}\frac{d^2}{dx^2} + \frac{1}{2}\alpha_n m\omega_n^2 X^2. \tag{11.18}$$

For a one-dimensional quantum harmonic oscillator in thermodynamic equilibrium with a reservoir at temperature T,

$$\langle H \rangle = \frac{\hbar\omega_n}{2} + \frac{\hbar\omega_n}{e^{\frac{\hbar\omega_n}{k_B T}} - 1}. \tag{11.19}$$

For $k_B T \ll \hbar\omega_n$

$$\langle H \rangle \simeq \frac{\hbar\omega_n}{2} + \hbar\omega_n e^{-\frac{\hbar\omega_n}{k_B T}}. \tag{11.20}$$

However, for $k_B T \gg \hbar\omega_n$

$$\langle H \rangle \simeq \frac{\hbar\omega_n}{2} + k_B T(1 - \frac{1}{2}\frac{\hbar\omega_n}{k_B T} + \ldots) \tag{11.21}$$

or

$$\langle H \rangle \simeq k_B T. \tag{11.22}$$

At room temperature (300K), we have $\frac{k_B T}{2\pi\hbar} \approx 6 \times 10^{12}$ Hz. For our mirrors, the first mode occurs at $\sim$ 800 kHz. Therefore, we are definitely in a regime where $k_B T \gg \hbar\omega_n$.

11.2.3 Effective Mass Coefficients

Following Ref. [86] we can remove the dependence of the amplitudes of the displacements on the energy normalization by parametrizing the coupling of each mode in terms of an effective mass coefficient α_n defined as

$$\alpha_n = \frac{U}{m\omega_n^2 \Delta l_n^2}, \tag{11.23}$$

where m is the actual mass of the mirror, ω_n is the angular resonant frequency of the vibrational mode, Δl_n is the displacement given by Equation 11.16, and U is the energy of the mode given by E or H for the classical or quantum cases, respectively. In this way, the motion of the surface can then be modelled as if it were a point mass of magnitude $\alpha_n m$ vibrating at frequency ω_n measured by an ideal one-dimensional laser beam.

We can then use the equipartition theorem to calculate the root-mean-squared motion of a mode of the thermally excited mirror. Each mode will have an energy of $k_B T$, where k_B is Boltzman's constant and T is the temperature. Therefore, in thermodynamic equilibrium, the displacement Δl_n of each mode will be given by Equation 11.16

As a first approximation, most of the energy of the motion occurs within a bandwidth given by the quality factor of the acoustic mode. However, a better prediction can be made by applying the fluctuation dissipation theorem [25] as discussed in the next section.

11.3 Spectral Density Function for Displacement

11.3.1 Velocity Damping

In some instances, the damping force is proportional to the velocity of the particle. Examples include viscous drag on a particle suspended in a liquid and eddy currents in moving conductors. In this case, the frictional force is given by

$$F_{\text{fric}} = -\beta v, \tag{11.24}$$

where β is the friction coefficient and v is the velocity of the particle. For a harmonic oscillator the fraction of energy lost in one cycle of oscillation is $\frac{2\pi}{Q}$, where Q is the quality factor. For the velocity damping described above, the quality factor of each mode is given by $Q_n = \frac{m\omega_n}{\beta}$.

The energy lost per cycle can be found by integrating the work done by the frictional force over one cycle

$$\begin{aligned} W &= \int F_{\text{fric}} \cdot dx \\ &= \beta\pi\omega_n A^2, \end{aligned} \tag{11.25}$$

where A is the rms amplitude of displacement. Since the total energy is $E_{\text{tot}} = m\omega_n^2 A^2$, we can easily see that the fraction of energy lost per cycle is $\frac{2\beta\pi}{m\omega_n}$. Because the fraction of energy lost in one cycle of oscillation is $\frac{2\pi}{Q}$, the quality factor is $Q_n = \frac{m\omega_n}{\beta}$.

In the case of velocity damping, the spectral density function for displacement is [25]

$$S_x(f) = \sum_n \frac{4k_B T\beta}{m^2(\omega_n^2 - \omega^2)^2 + \beta^2\omega^2}. \tag{11.26}$$

The root-mean-square displacement is then found by integrating the spectral density function and then taking the square root

$$\Delta x_{\text{RMS}} = \left[\int_0^\infty S_x(f)df\right]^{1/2}. \tag{11.27}$$

We then find that in the case of velocity damping for a single resonance ω_0,

$$\Delta x_{\text{RMS}} = \sqrt{\frac{k_B T}{m\omega_0^2}}. \tag{11.28}$$

This is consistent with the equipartition theorem since in thermodynamic equilibrium the mode should have an energy of $k_B T$ and the energy of the harmonic oscillator mode would be given by $m\omega_0^2\Delta x^2$. Note that the result is independent of the friction coefficient, β.

11.3.2 Structural Damping

If we define a loss function, φ_n, where the fraction of energy lost in one cycle of oscillation at frequency ω is given by $2\pi\varphi(\omega)$, then the loss function is related to the Q of the mode by $\varphi_n(\omega_n) = \frac{1}{Q_n}$. The spectral density function of displacement due to thermal excitation can be found from the fluctuation dissipation theorem to be [86]

$$\begin{aligned} S_x(f) &= \sum_n S_{xn}(f) \\ &= \sum_n \frac{4k_BT}{\alpha_n m\omega}\left[\frac{\omega_n^2\varphi_n(\omega)}{(\omega^2-\omega_n^2)^2+\omega_n^4\varphi_n^2(\omega)}\right]. \end{aligned} \tag{11.29}$$

The root-mean-squared displacement $\Delta l_B^{\mathrm{rms}}$ for a measurement bandwidth B is then given by

$$\Delta l_B^{\mathrm{rms}} = \left[\int_{f-\frac{B}{2}}^{f+\frac{B}{2}} S_x(f)df\right]^{1/2}. \tag{11.30}$$

The spectral density function in the case of structural damping can be found from that of velocity damping by giving the frictional coefficient for each mode a frequency dependence of $\beta_n = \frac{\varphi_n m\omega_n^2}{\omega}$.

11.4 Measuring Brownian Motion in Fabry-Perot Cavities

11.4.1 Shot Noise in Photodetectors

Because there is a fundamental noise source in the measurement of the amplitude of a light source, it is common to compare measurements to this limit. This limit is the photon shot noise due to the quantum uncertainty of the light power. Shot noise arises by assuming that the arrival of electrons at a given point in a circuit is a Poissonian process. The current i will have a noise current spectral density of

$$\langle i_N\rangle = \sqrt{2ei}, \tag{11.31}$$

where $\langle i_N\rangle$ has units $\left[\frac{\mathrm{A}}{\sqrt{\mathrm{Hz}}}\right]$. The current noise for a detection bandwidth B is then given by $i_n = \langle i_N\rangle\sqrt{B}$. Note that it is possible to have situations that exhibit more or less than shot noise. For example, a battery will exhibit less than shot noise for a given average current. However, the measurements we will discuss involve photodiodes which exhibit full shot noise.

If we assume that the conversion efficiency and gain of the photodiode and circuit are constant as a function of frequency, then for a current i in the circuit, the incident optical power P_{in} required to achieve this current is $P_{in} = iR\sigma$ where $\sigma = \frac{\text{Power}}{\text{Voltage}}$ is the conversion coefficient that factors in the effect of the transimpedance amplifier. Therefore, for an incident optical power P_{in}, detection bandwidth B, circuit impedance R, and conversion coefficient σ, the optical power corresponding to the shot noise level is given by

$$\begin{aligned} P_{sn} &= i_n R\sigma \\ &= \sqrt{2eBP_{\text{in}}}R\sigma. \end{aligned} \tag{11.32}$$

11.4.2 Measuring Displacements Due to Brownian Motion

Because the mode of the cavity is approximately Lorentzian, we know that small changes in the length at the resonant frequency ω_0 will have no first-order effect on the measured output optical power. That is, from Equation 11.6, $\frac{dP}{d\omega_0}(\omega_0) = 0$. However, as we move from the center of the resonance, the slope increases and the cavity becomes more efficient at converting displacements into changes in the transmitted optical power. Therefore, to maximize the effects of Brownian motion of the mirrors, one should tune the cavity to frequency $\omega = \omega_0 + \kappa$ (i.e., the half-maximum point).

If the cavity is tuned to the half-maximum point, then we know from Equation 11.9 that the optical power, P_{opt}, due to the thermally excited mirror displacements is

$$P_{opt} = \Delta P = \frac{4P_0\mathcal{F}}{\lambda_0}\Delta l_B^{\text{rms}}, \tag{11.33}$$

where P_0 is the output power of the cavity on resonance, $\mathcal{F}$ is the finesse of the cavity, λ_0 is the wavelength of the cavity resonance, Δl_B^{rms} is the RMS displacement defined in Equation 11.30, and B is the detection bandwidth (in $\frac{\text{cycles}}{\text{sec}}$).

Experimentally, it is much easier to compare the theoretical and experimental results if they are given relative to shot noise. The optical power corresponding to the shot noise level is given by Equation 11.32. In the case of detuning the cavity to frequency $\omega = \omega_0 + \kappa$, the incident power on the detector is one half the output power of the cavity on resonance. Therefore, the signal level relative to shot noise is

$$\text{Level [dBm]} = 10 \log \left[\frac{4\mathcal{F}}{\lambda_0} \sqrt{\frac{P_0}{eR\sigma B}} \Delta l_B^{\text{rms}} \right], \tag{11.34}$$

where $\mathcal{F}$ is the finesse of the cavity, λ_0 is the wavelength of the resonant light, P_0 is the output optical power of the cavity on resonance, Δl_B^{rms} is the RMS displacement defined in Equation 11.30, e is the electric charge, R is the input impedance of the spectrum analyzer, and σ is the conversion factor that takes into account the transimpedance amplifier. It is because of our definition of the conversion factor σ, that the shot noise level depends on the input impedance, R, of the spectrum analyzer. The conversion factor is the ratio of the optical power at the detector input to the voltage generated across the input impedance of the spectrum analyzer.

11.4.3 Sensitivity of the Mechanical System

We define the sensitivity of the system to be the displacement corresponding to the optical power that represents the shot noise level. Therefore, in order to be measurable, the displacements would have to be greater than the sensitivity. Combining Equations 11.32 and 11.33, we have the sensitivity $\Upsilon_{l,B}$ in units of [m] for a measurement bandwidth of B is

$$\Upsilon_{l,B} = \frac{\lambda_0}{4\mathcal{F}} \sqrt{\frac{eR\sigma B}{P_0}}. \tag{11.35}$$

Therefore, increasing the optical power and the finesse improve the sensitivity as expected. Decreasing the measurement bandwidth B also improves the sensitivity, since this decreases the shot noise level.

For our measurements, the power transmitted through the cavity on resonance was $P_0 = 5.6\ \mu\text{W}$, for wavelength $\lambda_0 = 869$ nm, finesse $\mathcal{F} = 3.5 \times 10^5$, conversion factor $\sigma = 2.78 \times 10^{-5}\ \frac{\text{W}}{\text{V}}$, and measurement bandwidth $B = 1$ kHz. With these parameters, we see from Equation 11.35 that the sensitivity of our setup is $\Upsilon_{l,B} = 1.24 \times 10^{-19}$ m.

This is quite amazing and is yet another illustration of the extreme care that must be taken when dealing with high-finesse cavities. For other examples of this see Chapter 5.

Chapter 12

Normal Modes of Oscillation and Cavity Output

The problem of solving for the normal modes of oscillation for a solid body was understood more than a century ago. For the case of a sphere, exact solutions are known in analytic form for the case of small amplitude of oscillation. One might assume that this would make the study of the thermally excited modes of a microsphere resonator (see Part III) easier to study than those of a Fabry-Perot cavity. Unfortunately, in the case of microspheres the oscillations induce stresses that change the index of refraction. These effects are just as important as those due to the geometric deformation. Therefore, the situation is actually somewhat more complicated than the case of Fabry-Perot cavities where the only item of concern is the net displacement of the surface.

When one moves to the case of cylinders and parallelepipeds, there are exact solutions in the sense that there are series solutions which quickly converge for small mode numbers [88, 89]. These types of solutions also exist in a less sophisticated manner for the truncated quadrangular pyramids, prisms and cones [90]. The results can then be compared to various finite element analyses with excellent agreement. Also, the ‘exact’ solutions for thick plates have been successfully compared to the proper limit of a right circular cylinder as well as a finite element analysis [91]. These solutions have then been compared to various experimental results [88]. There is also a great deal of experimental work done with resonant ultrasound techniques for many of these basic geometric shapes in a range of aspect ratios and the solutions have been compared to these results with good agreement (see Reference [92]).

12.1 Normal Modes of a Cylinder

We first study the modes of a cylinder as an approximation to the more complicated case of our mirrors. The simplest approximation is to just solve for the longitudinal modes of a bar. A better approximation is found by solving the elastic wave equation for the cylinder. These modes can then be modified to account for both the lateral inertia and shear stiffness that have a large effect on the longitudinal modes of a 'thick' cylinder. Ultimately, the best solution is found by using finite element analysis to numerically solve for the eigenmodes. We use all of these methods to understand the differences and limits of each before using finite element analysis to solve for the actual case of our mirrors in Section 12.2.

12.1.1 Longitudinal Modes of a Bar

For a bar of length L, let the longitudinal displacement be $\xi(x,t)$. For a sufficiently thin bar, the displacement will be the same at all points in any particular cross section.

$$\frac{\partial^2 \xi}{\partial x^2} = \frac{1}{c^2}\frac{\partial^2 \xi}{\partial t^2}, \tag{12.1}$$

where $c = \sqrt{\frac{Y}{\rho}}$ is the speed of sound, Y is Young's modulus of elasticity, and ρ is the density. The two simplest boundary conditions are either a fixed or free end. In the case of a fixed end, there can be no displacement, so that $\xi = 0$ at that point. In the case of a free end, there can be no internal elastic forces, so that $\frac{\partial \xi}{\partial x} = 0$ at that point. Note that a solid bar is very rigid, therefore, it is difficult to provide supports of greater rigidity, and hence a fixed boundary condition is difficult to realize in practice.

For the cases of either a Free-Free or Fixed-Fixed boundary condition, the normal modes are $\omega_n = \frac{n\pi c}{L}$. For the Fixed-Free case, $\omega_n = \frac{2n-1}{2}\frac{\pi c}{L}$.

For the case of Free-Free boundary conditions with the ends located at $x = (0, L)$, the amplitude for displacement along the bar is given by

$$\xi(x) = A\cos\left(\frac{n\pi}{L}x\right). \tag{12.2}$$

The energy in the mode ω_n is given by

$$E_n = \int_0^L \rho\omega_n^2 A^2 \cos^2\left(\frac{n\pi}{L}x\right)dx = \frac{1}{2}m\omega_n^2 A^2, \tag{12.3}$$

where the displacement amplitude is A, and the mass of the bar is $m = \rho L$. The energy can now be expressed in terms of an effective mass as discussed in Section 11.2.3 to be

$$E_n = \alpha_n m\omega_n^2 A^2. \tag{12.4}$$

This implies that the effective mass coefficient will be $\alpha_n = \frac{1}{2}$ for each of these modes.

For the longitudinal modes of a bar, the phase speed is calculated using Young's modulus Y, that is, $c = \sqrt{\frac{Y}{\rho}}$. However, when the transverse dimensions of the solid are large compared to a wavelength, the bulk and shear moduli must be used in place of Young's modulus to calculate the phase speed. In that case [93],

$$c = \sqrt{\frac{B + \frac{4}{3}G}{\rho}}, \tag{12.5}$$

where B is the bulk modulus and G is the shear modulus. The substrates for our mirrors are made of BK7, for which the two relevant phase speeds are $c = \sqrt{\frac{Y}{\rho}} = 5,681\ \frac{\mathrm{m}}{\mathrm{s}}$ and $c = \sqrt{\frac{B+\frac{4}{3}G}{\rho}} = 6,032\ \frac{\mathrm{m}}{\mathrm{s}}$. Figure 12.1 is a plot of the spectral density function for the longitudinal modes of a bar of BK7 that has length $L = 0.00345$ m with free-free boundary conditions. This is a simple approximation to the mirror used in our experiment (as described in more detail in Section 12.2). Figure 12.2 is a plot of the root-mean-square displacement $\Delta l_B^{\mathrm{rms}}$ and the corresponding power fluctuations (relative to shot noise) for the spectral density function shown in Figure 12.1.

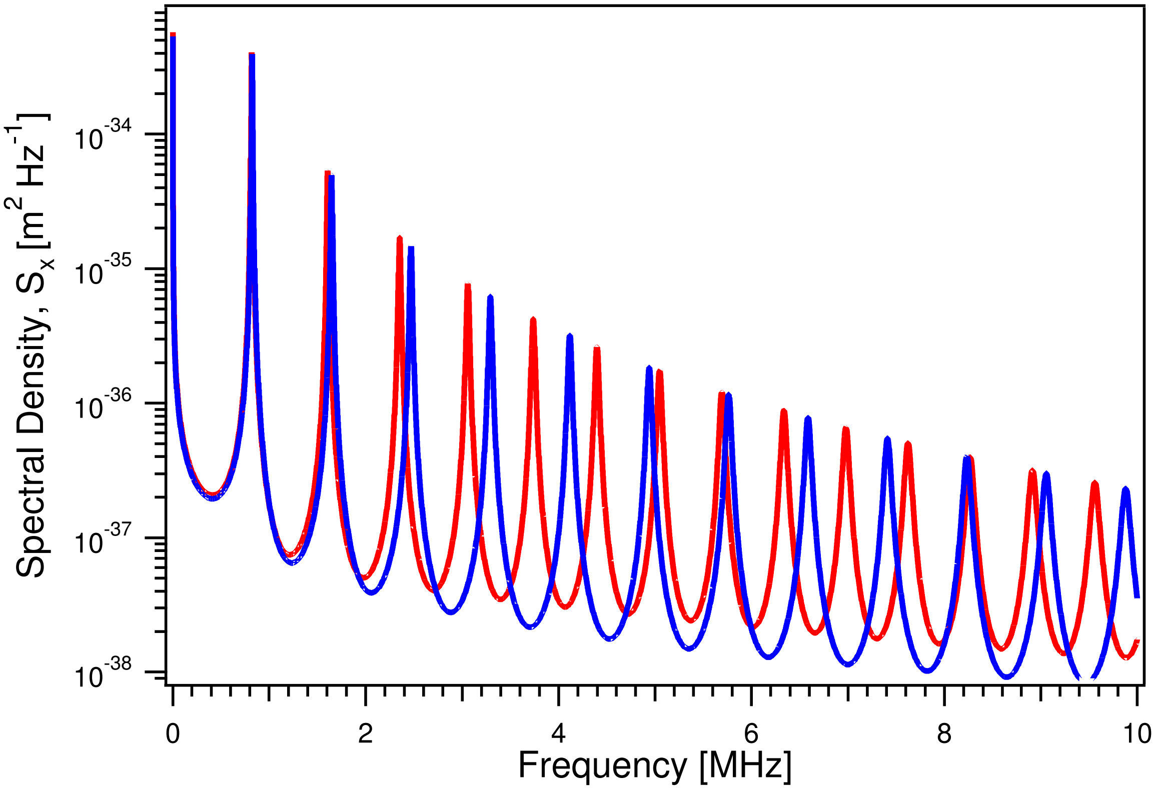

Figure 12.1: Spectral Density Function for a Bar

The spectral density function S_x $\left[\frac{\mathrm{m}^2}{\mathrm{Hz}}\right]$ for the case of structural damping (see Equation 11.29) for the longitudinal modes of a bar of BK7 with free-free boundary conditions (shown in blue). The length is $L = 0.00345$ m and each mode given by Equation 12.2 is assumed to have an effective mass coefficient of $\alpha_n = \frac{1}{2}$ and quality factor $Q = 100$. The quality factor determines the loss function in Section 11.3.2. Also shown (red) is the case of the Bishop corrections discussed in Section 12.1.3. Note that the normal modes are shifted to lower frequencies.

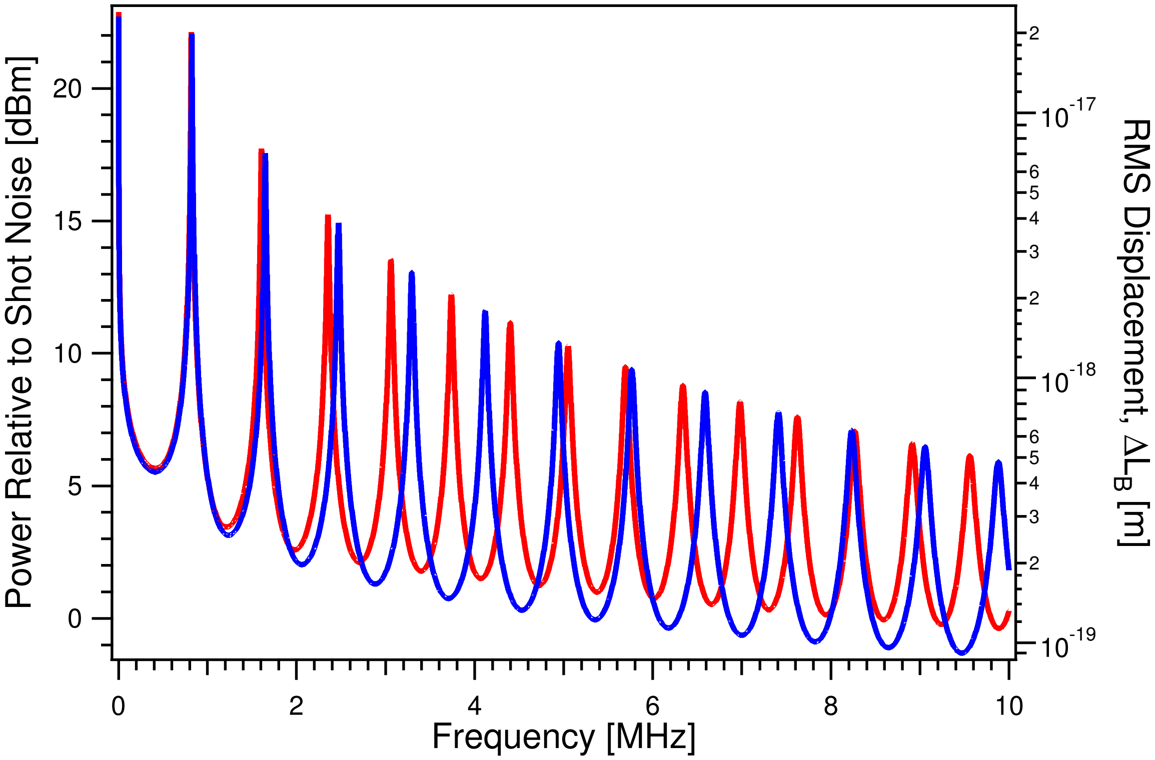

Figure 12.2: Thermal Displacement Noise for a Bar

The right axis corresponds to the root-mean-square displacement $\Delta l_B^{\mathrm{rms}}$ [m] of Section 11.3.2 for the modes of a bar of length $L = 0.00345$ m with free-free boundary conditions, as in Equations 12.2-12.5, and a measurement bandwidth $B = 1$ kHz. The left axis corresponds to the expected power fluctuations (relative to shot noise) discussed in Section 11.4.2 to be measured at the side of the cavity for the computed RMS displacement using the parameters of our system. For the measurements detailed in Section 12.2, we had an on resonance power transmitted through the cavity of $P_0 = 5.6$ μW, $\lambda_0 = 869$ nm, finesse $\mathcal{F} = 3.5 \times 10^5$, and conversion factor $\sigma = 2.78 \times 10^{-5}$ $\frac{\mathrm{W}}{\mathrm{V}}$. Also shown (red) is the case of the Bishop corrections discussed in Section 12.1.3. Note that the normal modes are shifted to lower frequencies.

12.1.2 Wave Equation in an Elastic Cylinder

For an assumed sinusoidal dependance, $e^{-i\omega t}$, the wave equation leads to the Helmholtz equation

$$\nabla^2\Psi + k^2\Psi = 0, \tag{12.6}$$

where in cylindrical coordinates we have

$$\nabla^2 = \frac{1}{r}\frac{\partial}{\partial r}\left(r\frac{\partial}{\partial r}\right) + \frac{1}{r^2}\frac{\partial^2}{\partial\varphi^2} + \frac{\partial^2}{\partial z^2}. \tag{12.7}$$

If we let $\Psi(r,\varphi,z) = R(r)\Phi(\varphi)Z(z)$, then the acoustic modes are indexed by (p,m,n) as $\Psi(r,\varphi,z) = R_{m,n}(r)\Phi_m(\varphi)Z_n(z)$, where

$$\begin{aligned} Z_p(z) &= \cos\left(\frac{p\pi}{L}z\right) \\ \Phi_m(\varphi) &= \cos(m\varphi) \\ R_{m,n}(r) &= J_m\left(\frac{x_{m,n}}{a}r\right), \end{aligned} \tag{12.8}$$

where $(p,m,n) = 0,1,2,\ldots$, and the frequencies are given by

$$\omega_{p,m,n} = \frac{c}{L}\left[x_{m,n}^2\beta^2 + p^2\pi^2\right]^{1/2}, \tag{12.9}$$

where $\beta = \frac{L}{a}$ is the aspect ratio and $x_{m,n}$ is the coordinate of the nth zero of the derivative of an mth order Bessel function. Therefore, the indices can be understood as follows: p is the number of longitudinal nodes along axis of cylinder, m is the number of radial nodal lines, and n is the number of azimuthal nodal lines. For $p = n = 0$, the only nonzero mode is $m = 1$. Also, for a given p and $m \neq 1$, all $m \neq 1$, $n = 0$ modes are degenerate in frequency to the $(p,0,0)$, which is the corresponding longitudinal mode of a bar of the same length (see Section 12.1.1).

Now, since $x_{m,0} = 0, \forall m \neq (0,1)$, we have $J_m\left(x_{m,0}\frac{r}{a}\right) = 0, \forall m \neq (0,1)$. Therefore, these are not actual eigenmodes. Using these conditions, we can then neglect the $m \neq 1$, $p = n = 0$ modes. We also neglect the $m \neq (0,1)$, $n = 0$ modes since they have zero displacement everywhere.

We now have the following classes of solutions (p, m, n) for $p, m, n \geq 1$: $(p, 0, 0)$ purely longitudinal (corresponding to the longitudinal modes of a bar); $(0, 1, 0)$ has one radial nodal line; $(0, 0, n)$ axisymmetric and purely radial; $(0, m, n)$ non-axisymmetric radial and rotational; $(p, 0, n)$ axisymmetric radial and longitudinal; (p, m, n) mixed.

Figure 12.3 is a plot of the spectral density function for these modes of a cylinder of BK7 with free boundary conditions that has length $L = 0.00345$ m and radius $a = 0.00149$ m, to improve upon the approximation of the previous section for the mirror used in our experiment (as described in more detail in Section 12.2). Figure 12.4 is a plot of the root-mean-square displacement $\Delta l_B^{\mathrm{rms}}$ and the corresponding power fluctuations (relative to shot noise) for the spectral density function shown in Figure 12.3.

12.1.3 Corrections to Cylinder Modes

There are a variety of corrections to the eigenfrequencies of a rod [94]. These corrections attempt to account for both the lateral inertia and shear stiffness. The lateral inertia *decreases* the natural frequency estimated from the elementary theory, since the lateral inertia increases the kinetic energy. However, the effect of shear stiffness is to *increase* the natural frequencies, since the shear stiffness increases the strain energy.

From the elementary theory, we know that the longitudinal modes are $\omega_n = n\frac{\pi c}{L}$. The Rayleigh correction is made to include the effects of lateral inertia [94]

$$\omega_n = n\frac{\pi c}{L}\frac{1}{\sqrt{1 + r_1^2 (n\pi)^2}}. \tag{12.10}$$

The Bishop correction is made to include both lateral inertia and shear stiffness [94]

$$\omega_n = n\frac{\pi c}{L}\sqrt{\frac{1 + r_1^2 r_2 (n\pi)^2}{1 + r_1^2 (n\pi)^2}}, \tag{12.11}$$

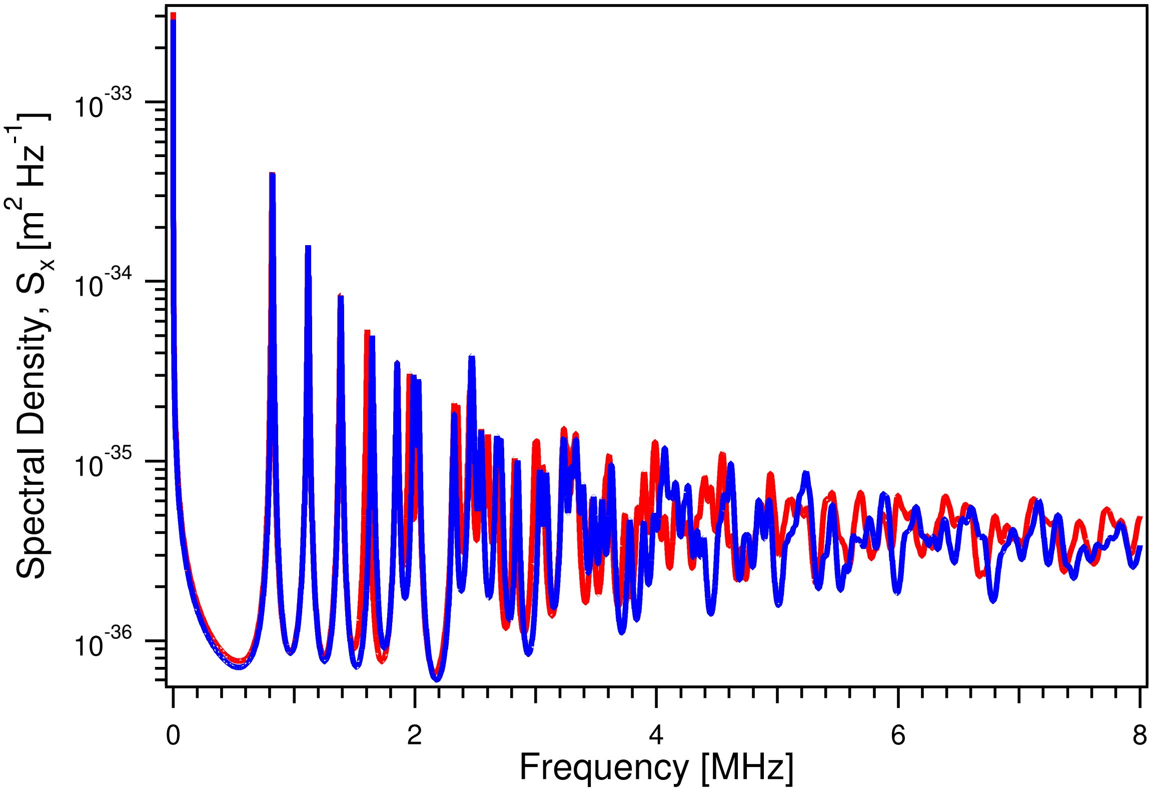

Figure 12.3: Spectral Density Function for Elastic Modes of a Cylinder
The spectral density function S_x $\left[\mathrm{m}^2\mathrm{Hz}^{-1}\right]$ (see Equation 11.29) for the elastic modes of a cylinder (given by Equation 12.9) of BK7 with free boundary conditions (shown in blue). The length is $L = 0.00345$ m, radius $a = 0.00149$ m, and effective mass coefficient is taken to be $\alpha_n = \frac{1}{2}$ for each mode with quality factor $Q = 100$. Also shown (red) is the case of the Bishop corrections discussed in Section 12.1.3.

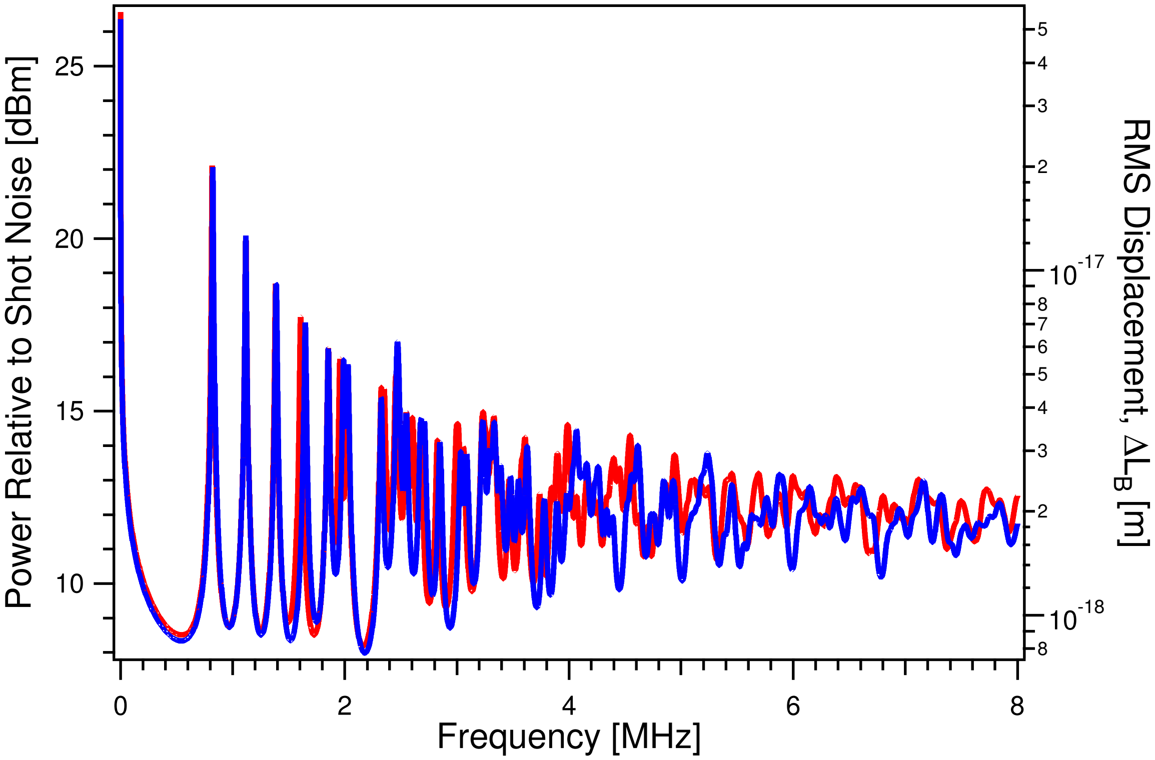

Figure 12.4: Thermal Displacement Noise for Elastic Modes of a Cylinder

The right axis corresponds to the root-mean-square displacement $\Delta l_B^{\mathrm{rms}}$ [m] of Section 11.3.2 for the elastic modes of a cylinder (given by Equation 12.9) of BK7 with free boundary conditions (shown in blue). The length is $L = 0.00345$ m, radius $a = 0.00149$ m, measurement bandwidth $B = 1$ kHz, and the effective mass coefficient is taken to be $\alpha_n = \frac{1}{2}$ for each mode with quality factor $Q = 100$. The left axis corresponds to the expected power fluctuations (relative to shot noise) discussed in Section 11.4.2 to be measured at the side of the cavity for the computed RMS displacement using the parameters of our system. For the measurements detailed in Section 12.2, we had an on resonance power transmitted through the cavity of $P_0 = 5.6$ μW, $\lambda_0 = 869$ nm, finesse $\mathcal{F} = 3.5 \times 10^5$, and conversion factor $\sigma = 2.78 \times 10^{-5}$ $\frac{\mathrm{W}}{\mathrm{V}}$. Also shown (red) is the case of the Bishop corrections discussed in Section 12.1.3.

where

$$\begin{aligned} r_1^2 &= \nu^2 \frac{r_0^2}{L^2}, \\ r_0^2 &= \frac{I_p}{A_0}, \\ I_p &= \frac{\pi}{2} R^4, \\ A_0 &= \pi R^2, \\ r_2 &= \sqrt{\frac{G}{E}}. \end{aligned} \tag{12.12}$$

For a cylinder radius a and aspect ratio $\beta = \frac{L}{a}$,

$$\begin{gathered} r_0^2 = \frac{a^2}{2} \\ r_1^2 = \frac{\nu^2}{2\beta^2} \\ r_2 = \sqrt{\frac{G}{E}} \end{gathered} \tag{12.13}$$

The correction to the eigenfrequency is then given by

$$\chi_n = \left(\frac{1 + \frac{\nu^2}{2\beta^2} \sqrt{\frac{G}{E}} (n\pi)^2}{1 + \frac{\nu^2}{2\beta^2} (n\pi)^2} \right)^{1/2} \tag{12.14}$$

so that

$$\omega_n = n \frac{\pi c}{L} \chi_n \tag{12.15}$$

The effects of these corrections for the modes of a bar and the elastic modes of a cylinder are shown in Figures 12.1 through 12.4.

12.1.4 Finite Element Analysis for a Cylinder

We want to start with the case of a right circular cylinder in order to understand the finite element analysis for our actual mirror geometry (see Figure 12.7). The analysis was done by Dennis Coyne (with the LIGO project) for a cylinder of radius

$a = 0.149$ cm and length $L = 0.345$ cm. This cylinder has a volume of 0.02406 cm^3 and a mass of 6.0397×10^{-2}gm. The finite element analysis was performed using 5004 elements (7882 nodes) of parabolic tetrahedrons. The I-Deas software package from SDRC was used to perform these calculations.

We then use the following values for BK7 [95]:

$$\text{Elastic Modulus,} \qquad E = 81 \text{ GPa} \tag{12.16}$$

$$\text{Poisson's Ratio,} \qquad \nu = 0.208 \tag{12.17}$$

$$\text{Shear Modulus,} \qquad G = \frac{E}{2(1+\nu)} = 33.5 \text{ GPa} \tag{12.18}$$

$$\text{Density,} \qquad \rho = 2.51\text{gm/cm}^3 \tag{12.19}$$

For calculating the effective mass coefficients, we use a beam waist radius of 23 μm, which corresponds to the waist in our actual measurements. The normalized axial amplitude can then be found by finding the displacement for a given energy. We can use this result to find the effective mass coefficients. Figure 12.5 is a plot of the spectral density function for these modes of a cylinder of BK7 with free boundary conditions that has length $L = 0.00345$ m and radius $a = 0.00149$ m. This can then be compared to the simple approximations discussed in the previous section. Figure 12.6 is a plot of the root-mean-square displacement Δl_B^{rms} and the corresponding power fluctuations (relative to shot noise) for the spectral density function shown in Figure 12.5.

12.2 Normal Modes of Our Mirrors

As can be seen in Figure 12.7, the analysis of our physical system is complicated by the irregular geometry of the mirrors comprising our Fabry-Perot cavity. The Finite Element Analysis was then performed using 5004 elements (7882 nodes) of parabolic tetrahedrons for the dimensions of the mirrors in our cavity. The diameter is $D_2 = 2.98$ mm, the total length is 3.85 mm, the length before the taper is $L_2 = 2.91$ mm, the length of the tapered section is $L_1 = 0.94$ mm, and the diameter of the

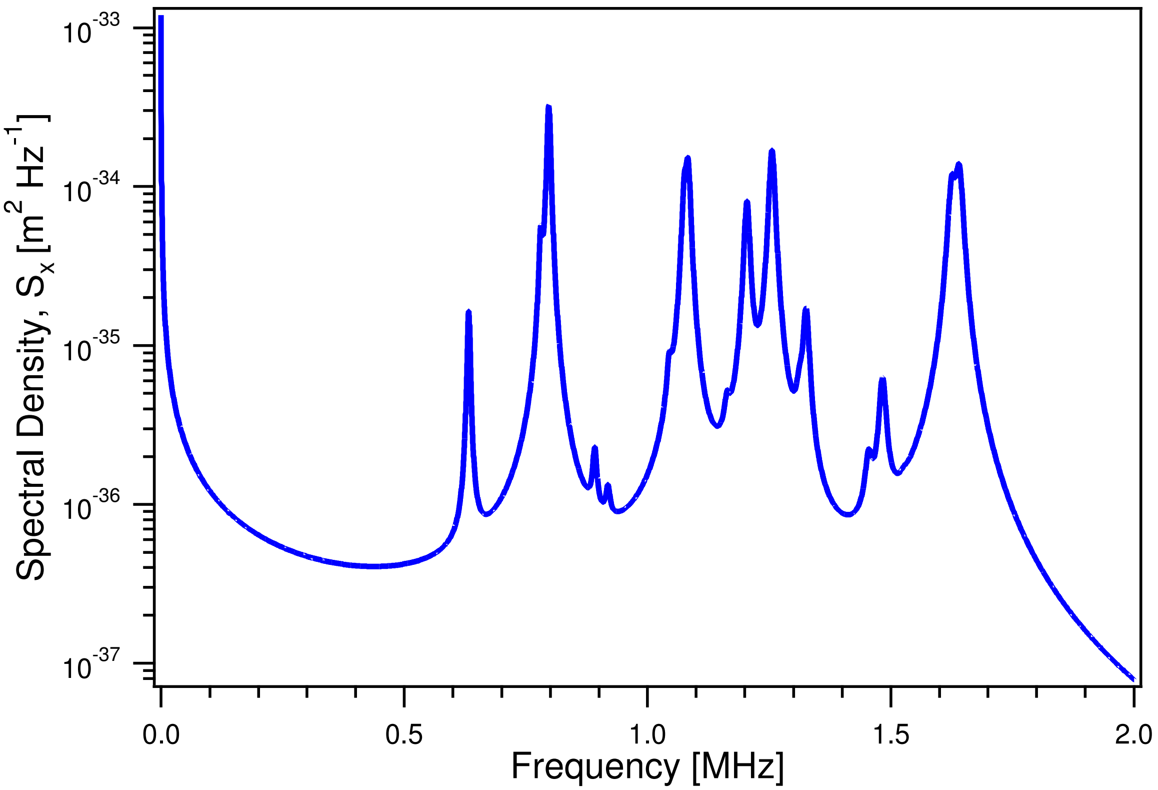

Figure 12.5: Spectral Density Function for Modes of a Cylinder
The spectral density function S_x $\left[\mathrm{m}^2\mathrm{Hz}^{-1}\right]$ for the modes of a cylinder of BK7 with free boundary conditions determined through finite element analysis as discussed in Section 12.1.4. The length is $L = 0.00345$ m, radius $a = 0.00149$ m, and effective mass coefficient is taken to be that computed through the finite element analysis with each mode given a quality factor $Q = 100$. Note that the function is computed with only the first 50 modes.

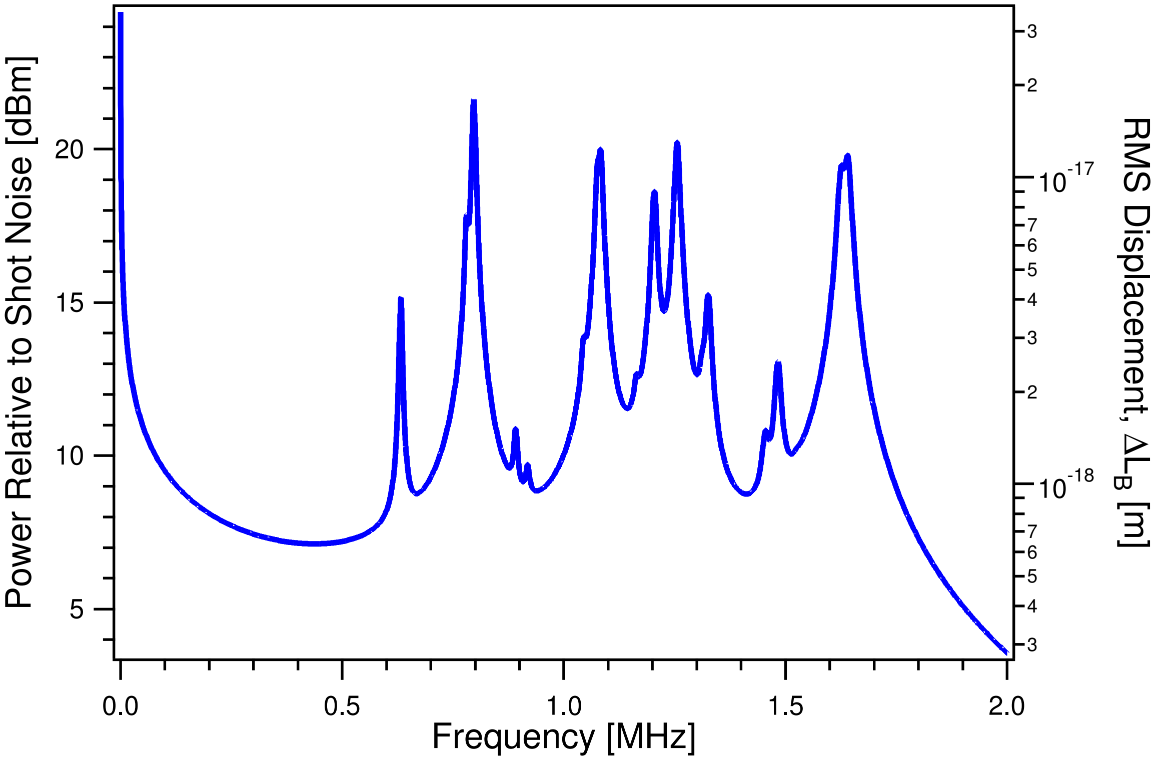

Figure 12.6: Thermal Displacement Noise for Modes of a Cylinder
The right axis corresponds to the root-mean-square displacement Δl_B^{rms} [m] of Section 11.3.2 for the modes of a cylinder of BK7 with free boundary conditions determined through finite element analysis as discussed in Section 12.1.4. The length is $L = 0.00345$ m, radius $a = 0.00149$ m, measurement bandwidth $B = 1$ kHz, and the effective mass coefficient is taken to be that determined through the finite element analysis with each mode given a quality factor $Q = 100$. The left axis corresponds to the expected power fluctuations (relative to shot noise) discussed in Section 11.4.2 to be measured at the side of the cavity for the computed RMS displacement using the parameters of our system. For the measurements detailed in Section 12.2, we had an on resonance power transmitted through the cavity of $P_0 = 5.6$ μW, $\lambda_0 = 869$ nm, finesse $\mathcal{F} = 3.5 \times 10^5$, and conversion factor $\sigma = 2.78 \times 10^{-5}$ $\frac{\text{W}}{\text{V}}$. Note that the function is computed with only the first 50 modes.

front face is $D_1 = 1.0$ mm. The volume of the straight section is then $V_2 = \pi R_1^2 L_1 = 2.0296\times10^{-2}$ cm^3 and the volume of the tapered section is $V_1 = \frac{\pi L_2}{3}(R_1^2+R_2^2+R_1R_2) = 3.1648 \times 10^{-3}$ cm^3. The total volume is then $V = V_1 + V_2 = 2.3461 \times 10^{-2}$ cm^3. This implies a mass of 5.8887×10^{-5} kg.

For determining the effective mass coefficients, we use a beam waist radius of 23 μm. The normalized axial amplitude can be found by finding the displacement for a given energy. We can use this and Equation 11.23 to find the effective mass coefficients. Figure 12.8 is a plot of the spectral density function of these modes for our mirrors (shown in Figure 12.7). This can then be compared to the simple approximations discussed in the previous sections. Figure 12.9 is a plot of the root-mean-square displacement $\Delta l_B^{\mathrm{rms}}$ and the corresponding power fluctuations (relative to shot noise) for the spectral density function shown in Figure 12.8. Figure 12.10 compares this result to the experimental results we obtained with our cavity. For the measurements shown in Figure 12.10, we had an on resonance power transmitted through the cavity of $P_0 = 5.6$ μW, $\lambda_0 = 869$ nm, finesse $\mathcal{F} = 3.5\times10^5$, and conversion factor $\sigma = 2.78 \times 10^{-5}$ $\frac{\mathrm{W}}{\mathrm{V}}$.

The theoretical results qualitatively compare favorably to the experimental results. It should be no surprise that the modes do not match up exactly, since the cavity mounting structure is actually far more complicated than we have modelled. Also, we used the same loss function for each of the mechanical modes. In reality, the quality factor of each mode will be different. We see from Figure 12.10 that we can qualitatively model the density of states and its translation into thermal noise. Therefore, we can use these results as a first attempt to model the noise and apply this to the results of Chapter 7 to see the effect on an intracavity FORT.

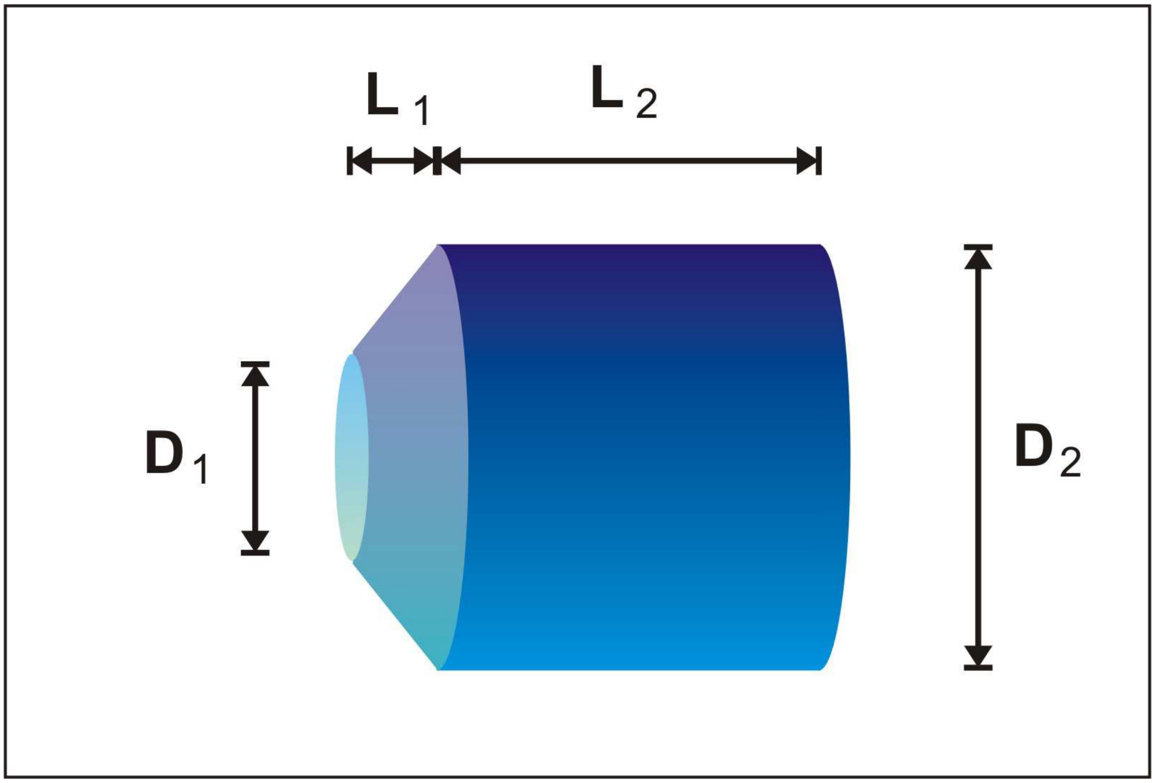

Figure 12.7: Geometry of Our Mirrors

The geometry of the mirrors comprising our Fabry-Perot cavity. The mirrors are made of a BK7 substrate with an anti-reflective coating on one side and a dielectric high reflecting coating on the other side. The diameter is $D_2 = 2.98$ mm, the total length is $L_1 + L_2 = 3.85$ mm, the length before the taper is $L_2 = 2.91$ mm, the length of the tapered section is $L_1 = 0.94$ mm, and the diameter of the front face is $D_1 = 1.0$ mm. The volume of the straight section is then $V_1 = \pi R_2^2 L_2 = 2.0296 \times 10^{-2}$ cm^3 and the volume of the tapered section is $V_2 = \frac{\pi L_1}{3}(R_1^2 + R_2^2 + R_1 R_2) = 3.1648 \times 10^{-3}$ cm^3. The total volume is then $V = V_1 + V_2 = 2.3461 \times 10^{-2}$ cm^3. This implies a mass of 5.8887×10^{-5} kg.

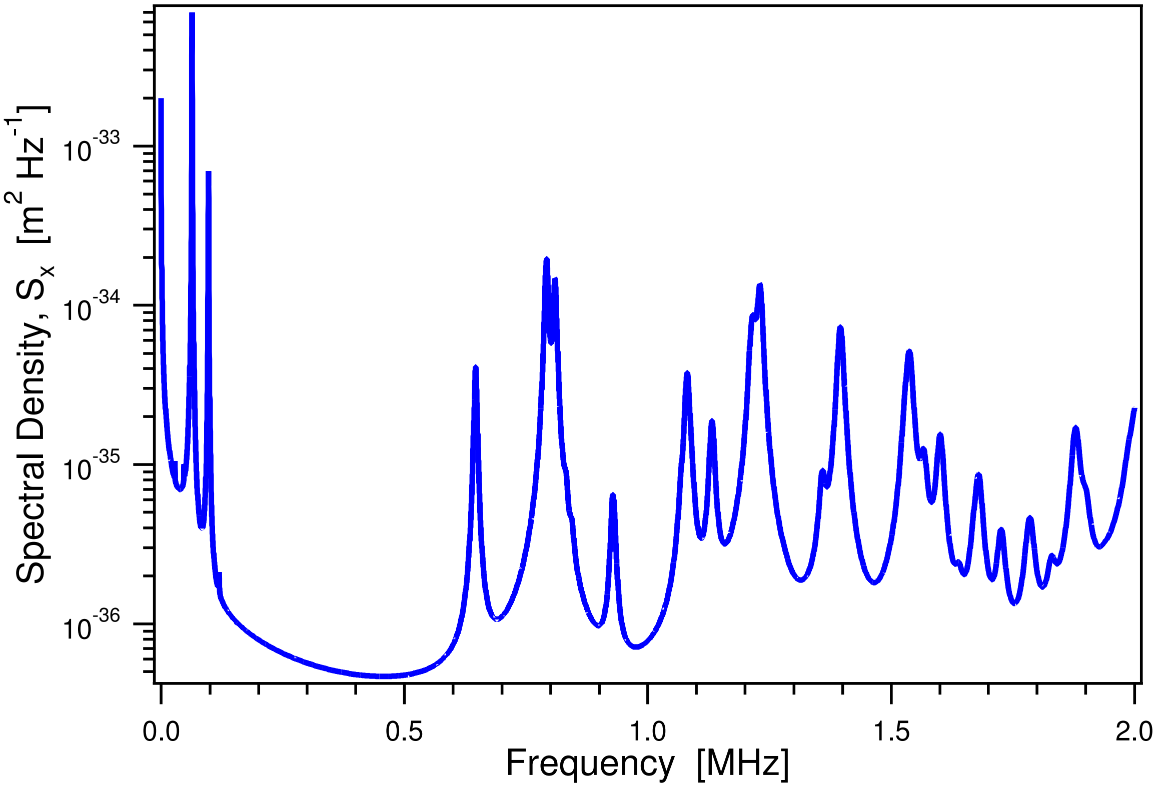

Figure 12.8: Spectral Density Function for Modes of Our Mirror

The spectral density function S_x $\left[\mathrm{m^2Hz^{-1}}\right]$ for the modes of our mirror (see Figure 12.7) comprised of BK7 determined through finite element analysis as discussed in Section 12.2. The effective mass coefficient is taken to be that computed through the finite element analysis with each mode given a quality factor $Q = 100$. The modes below 100 kHz arise from tacking down the mirror with two points at one end.

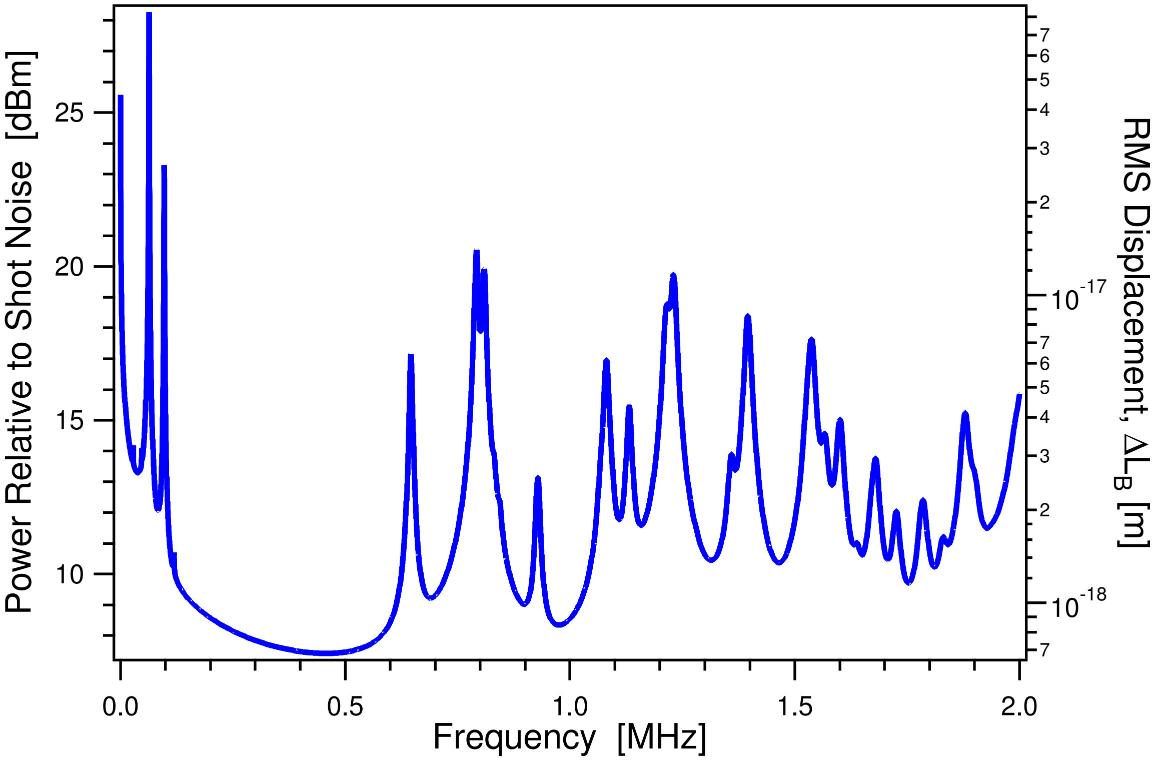

Figure 12.9: Thermal Displacement Noise for Modes of Our Mirror
The right axis corresponds to the root-mean-square displacement $\Delta l_B^{\rm rms}$ [m] of Section 11.3.2 for the modes of our mirror determined through finite element analysis as discussed in Section 12.2. The measurement bandwidth is $B = 1$ kHz, and the effective mass coefficient is taken to be that determined through the finite element analysis with each mode given a quality factor $Q = 100$. The left axis corresponds to the expected power fluctuations (relative to shot noise) discussed in Section 11.4.2 to be measured at the side of the cavity for the computed RMS displacement using the parameters of our system. For the measurements detailed in Section 12.2, we had an on resonance power transmitted through the cavity of $P_0 = 5.6\ \mu$W, $\lambda_0 = 869$ nm, finesse $\mathcal{F} = 3.5 \times 10^5$, and conversion factor $\sigma = 2.78 \times 10^{-5}\ \frac{\rm W}{\rm V}$. The modes below 100 kHz arise from tacking down the mirror with two points at one end.

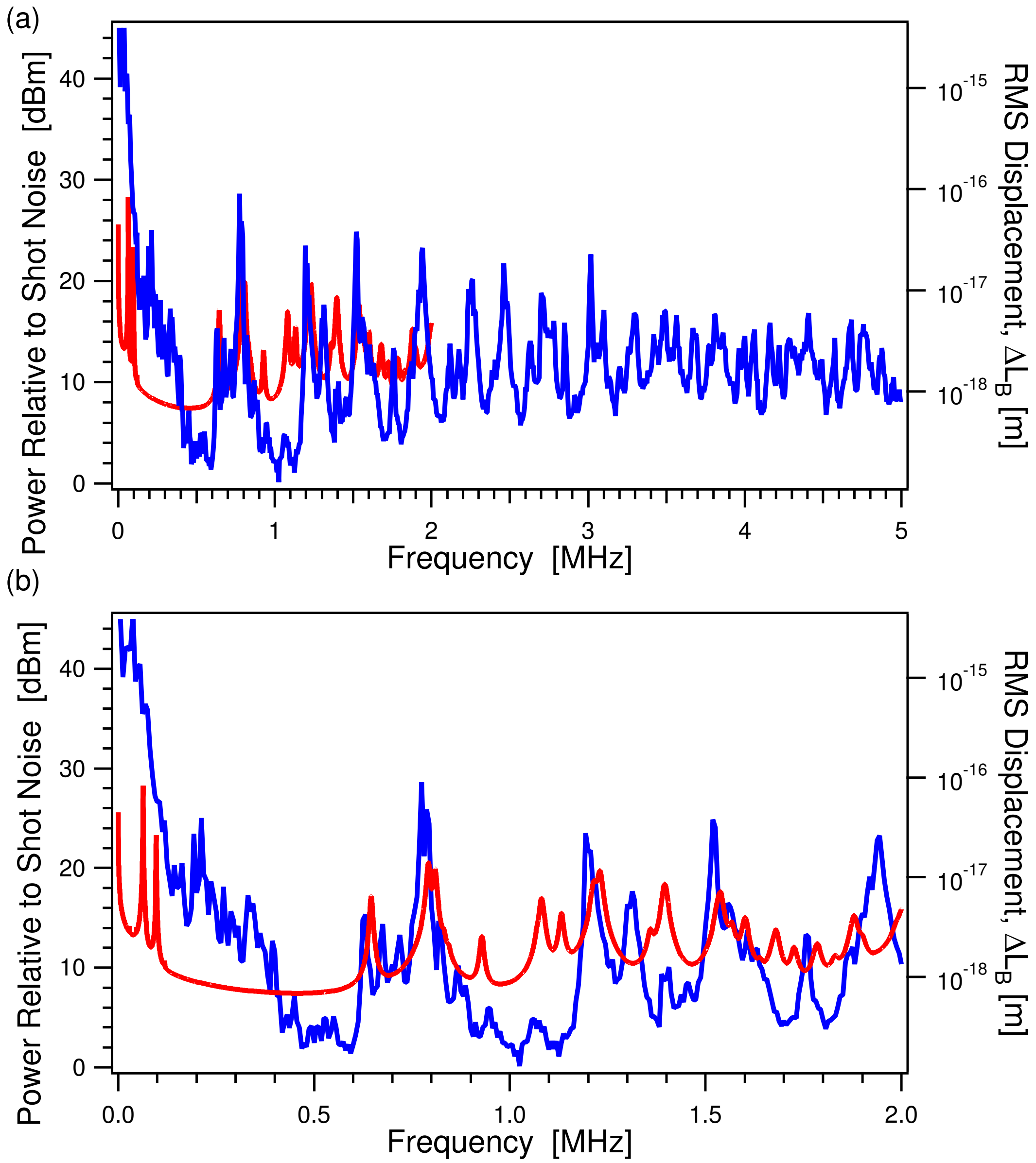

Figure 12.10: Comparison of Calculated and Measured Thermal Noise

(a) & (b) The measured power fluctuations (relative to shot noise) discussed in Section 11.4.2 measured at the side of our cavity (shown in blue). The right axis corresponds to the root-mean-square displacement $\Delta l_B^{\rm rms}$ $[m]$ of Section 11.3.2. The left axis corresponds to the power fluctuations (relative to shot noise) discussed in Section 11.4.2 measured at the side of the cavity. We had an on resonance power transmitted through the cavity of $P_0 = 5.6\ \mu$W, $\lambda_0 = 869$ nm, finesse $\mathcal{F} = 3.5 \times 10^5$, conversion factor $\sigma = 2.78 \times 10^{-5}\ \frac{\rm W}{\rm V}$, and measurement bandwidth $B = 1$ kHz. A comparison is made to the results computed in Section 12.2 using finite element analysis (shown in red). The effective mass coefficient is taken to be that determined through the finite element analysis with each mode given a quality factor $Q = 100$. The modes were only calculated up to 2.5 MHz, so the spectral density function was only computed up to 2 MHz.

Part V

Applications of Cavity QED to Communication Theory: Superadditivity

Chapter 13

Superadditivity for a Binary Quantum Alphabet: Introduction

These chapters are about achieving the maximal information transfer rate possible when information is encoded into quantum systems via the preparation of one or another of two nonorthogonal states. This might at first seem like a questionable thing to consider: for transmissions through a noiseless medium, the maximal transfer rate (or capacity) of 1 bit/transmission is clearly achieved *only* with orthogonal alphabets. This is because nonorthogonal preparations cannot be identified with complete reliability. However, there are instances in which it is neither practical nor desirable to use such an alphabet. The most obvious example is when a simple laser transmitter is located a great distance from the receiver. The receiver's field will take on the character of a very attenuated optical coherent state. Because the states become less orthogonal as the power is attenuated, one is confronted with precisely the issue considered here. In this case, one is typically stuck with trying to extract information from quantum states that are not only nonorthogonal, but almost completely overlapping.

The practical method in many situations for compensating for very weak signals is to invest in elaborate receiving stations. For instance, in microwave communication very large-dish antennas are the obvious route. Recently, however, a new quantum mechanical effect has been discovered for the decoding of nonorthogonal signals on separate quantum systems. Traditional signal processing methods have only considered fixed decoding measurements performed on the separate transmissions (see for example Ref. [96]): i.e., taking into account the intrinsic noise generated by the quantum measurement [97], one is left with a basic problem of classical information theory—coding for a discrete memoryless channel [98]. Quantum mechanics, however, allows for more possibilities than this [99]. If one is capable of doing collective measurements on blocks of transmitted signals, it is possible to achieve a greater capacity than one might have otherwise thought [100]—this is referred to as the superadditivity of quantum channel capacities. This is an effect that does not exist classically [98, Lemma 8.9.2]. The physics behind the effect relies on a kind of nonlocality dual to the famous one exhibited by entangled quantum systems through Bell inequality violations [101, 102, 103].

More precisely, a communication rate R is said to be achievable if in k transmissions there is a way of writing 2^{Rk} messages with the nonorthogonal alphabet so that the probability of a decoding error goes to zero as $k \to \infty$. The number R signifies the number of bits per transmission that can be conveyed reliably from the transmitter to the receiver in the asymptotic limit. Clearly the rates that can be achieved will depend on the class of codings used for the messages and the class of quantum measurements allowed at the receiver. The capacity C_n is defined to be the supremum of all achievable rates, where n is the number of transmissions to be saved up before performing a measurement. The meaning of superadditivity is simply that $C_n > C_1$, where the inequality is strict.

Generally it is a difficult problem to calculate C_n even with a quantum version of Shannon's noisy channel coding theorem available [100]. And it is a much more difficult task still to find codes that approach C_n. This is because the coding theorems generally give no information on how to construct codes that approach a given capacity. It turns out however that the number C_1 is rather easily calculable and, because of a recent very powerful theorem on quantum channel capacities [104, 105, 106], so is the asymptotic case C_∞ [103]. The most striking thing about these two quantities is that even though both $C_1 \to 0$ and $C_\infty \to 0$ as the overlap between the states goes to unity, the ratio C_∞/C_1 nevertheless diverges (see Figure 13.1). This means that

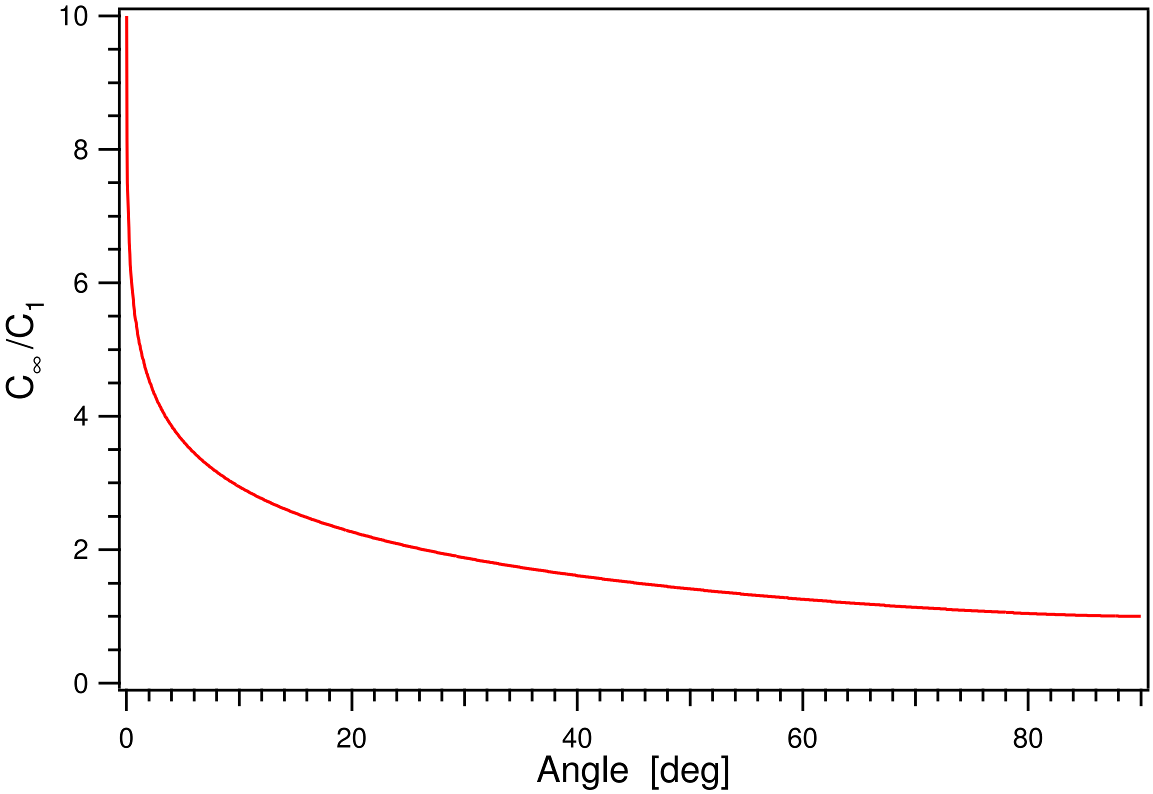

Figure 13.1: C_∞/C_1 for Nonorthogonal States
The ratio C_∞/C_1 as a function of the angle γ in degrees, where γ is the angle between the two nonorthogonal states comprising the transmission alphabet.

grossly collective measurements can, in principle at least, produce an arbitrarily large improvement in the channel capacity of very weak signals—a very desirable state of affairs and one of some serious practical import.

The problem from the practical side of the matter is that before one will be able to decode very large blocks, one must first be able to tackle the case of small blocks, preferably of just size two or three. There has already been substantial progress in this direction by Sasaki *et al.*, in a series of papers [107, 108, 109]. They explicitly demonstrate a code that uses collective decoding three transmissions at a time to achieve a communication rate R_3 greater than C_1. Nevertheless, it would be nice to demonstrate superadditivity with an even simpler scheme, namely two-shot collective measurements. Also the ratio $R_3/C_1 \to 1$ as the angle γ between the two states goes to zero for their given coding scheme. Thus just where one would be looking for the most help from superadditivity (in the very weak signal regime), one loses it for this code.

We improve on the work of Sasaki *et al.*, by showing that in fact $C_2 > C_1$ for angles $\gamma \lesssim 19^\circ$, and moreover that this superadditivity is sustained and only strengthened as $\gamma \to 0$. On the down side, the improvement in capacity is not great—only 2.82 percent—but is definitely there and not so small as to be forever invisible. In this vein, we propose an experimental demonstration that relies on near-term laboratory capabilities for implementation. For our two nonorthogonal quantum states, we use low photon-number coherent states $|\alpha\rangle$ and $|-\alpha\rangle$ with the separate signals carried on different circular polarizations. The two-shot signal decoding is performed with atomic state measurements on a single Cesium atom in a high-finesse optical cavity via the technique of quantum jumps in fluorescence similar to those demonstrated on ions in References [110, 111, 112].

Chapter 14

Deriving Superadditivity for Two-Shot Collective Measurements

14.1 Quantum Shannon Noisy Coding Theorem

Following the discussion of the previous chapter, we will take as an alphabet for all communication schemes a fixed set of two nonorthogonal quantum states $|\psi_0\rangle$ and $|\psi_1\rangle$ characterized by the single parameter γ:

$$\langle\psi_0|\psi_1\rangle = \cos\gamma\ . \tag{14.1}$$

We would like to know what communication rates R_n can be achieved with this alphabet when decoding measurements are performed n transmissions at a time.

This in general is a very difficult problem, especially if one is also confronted with the issue of explicitly demonstrating codes for achieving those rates. However, if one can be contented in knowing the number C_n itself and the quantum measurements required to achieve that (i.e., without knowing the coding scheme explicitly), then a great simplification arises because of a quantum extension to the Shannon noisy coding theorem [98] due to Holevo [100].

We shall state the result of this theorem presently. Let the variable x denote the binary strings of length n that index the set of all messages $|\Psi_x\rangle = |\psi_{x_1}\rangle|\psi_{x_2}\rangle\cdots|\psi_{x_n}\rangle$, let the function $p(x)$ denote a probability distribution over those messages, and let

$$\rho = \sum_x p(x)|\Psi_x\rangle\langle\Psi_x| \tag{14.2}$$

denote the resultant density operator of that distribution. We shall use the notation E to denote a generalized quantum measurement or positive operator-valued measure (POVM) [113] on the message Hilbert space $\mathcal{H}_n$, i.e., $E = (E_k)$ is an infinite sequence of operators on $\mathcal{H}_n$ with only a finite number of $E_k \neq 0$ such that $\langle\psi|E_k|\psi\rangle \geq 0$ for all k and $|\psi\rangle$, and the E_k's form a decomposition of the identity operator on $\mathcal{H}_n$. In order to find C_n, it is enough to perform the following maximization:

$$C_n = \frac{1}{n} \max_{p(x)} \max_{\mathrm{E}} \left[H_{\mathrm{E}}(\rho) - \sum_x p(x) H_{\mathrm{E}}(|\Psi_x\rangle) \right] , \tag{14.3}$$

where

$$H_{\mathrm{E}}(\rho) = -\sum_k (\mathrm{tr}\rho E_k) \log(\mathrm{tr}\rho E_k) \tag{14.4}$$

and

$$H_{\mathrm{E}}(|\Psi_x\rangle) = -\sum_k \langle\Psi_x|E_k|\Psi_x\rangle \log\langle\Psi_x|E_k|\Psi_x\rangle \tag{14.5}$$

are the Shannon informations for the various probability distributions generated by the measurement E. (In these expressions we have used the base-two logarithm so that information is measured in bits.) For any rate $R_n = C_n - \epsilon$, $\epsilon > 0$, there *exists* a code that will achieve that rate. Moreover, if E is fixed and only the maximization over $p(x)$ is performed in Equation (14.3), then the resulting expression will define the capacity that can be reached with the given measurement.

14.2 Limiting Cases for C_n

There are two limiting cases where the calculation of C_n becomes tractable, $n = 1$ and $n = \infty$. In the first case, one can use References [114, 115, 103] to find rather easily that

$$\begin{aligned} C_1(\gamma) = & \frac{1}{2}\left[1+\sqrt{1-\cos^2\gamma}\right]\log\left[1+\sqrt{1-\cos^2\gamma}\right] \\ & +\frac{1}{2}\left[1-\sqrt{1-\cos^2\gamma}\right]\log\left[1-\sqrt{1-\cos^2\gamma}\right] . \end{aligned} \tag{14.6}$$

For the limit where arbitrarily many collective measurements are made, one can use the powerful theorem of Ref. [104] to find that the channel capacity per bit is given by [103]

$$\begin{aligned} C_\infty(\gamma) = & - \frac{1}{2}(1-\cos\gamma)\log\frac{1}{2}(1-\cos\gamma) \\ & - \frac{1}{2}(1+\cos\gamma)\log\frac{1}{2}(1+\cos\gamma) . \end{aligned} \tag{14.7}$$

For all cases in between, there is nothing better to be done than an explicit search over all probabilities $p(x)$ and all measurements E.

As stated in Chapter 13, one can see from Equations (14.6) and (14.7), that

$$\lim_{\gamma\to 0}\frac{C_\infty(\gamma)}{C_1(\gamma)} \longrightarrow \infty . \tag{14.8}$$

So the incentive to use collective measurements in the decoding of these signals is great.

14.3 R_2: Rate for Two-Shot Collective Measurements

Therefore, let us specialize to the case of collective measurements on two transmissions at a time. In this case, with respect to the decoding observables we have an effective alphabet consisting of the tensor-product states

$$\begin{aligned} |a\rangle &= |\psi_0\rangle|\psi_1\rangle && (14.9)\\ |b\rangle &= |\psi_1\rangle|\psi_0\rangle && (14.10)\\ |c\rangle &= |\psi_0\rangle|\psi_0\rangle && (14.11)\\ |d\rangle &= |\psi_1\rangle|\psi_1\rangle\ , && (14.12) \end{aligned}$$

with the consequent inner products

$$\langle a|c\rangle = \langle b|c\rangle = \langle a|d\rangle = \langle b|d\rangle = \cos\gamma\ , \qquad (14.13)$$

and

$$\langle a|b\rangle = \cos^2\gamma\ . \qquad (14.14)$$

It turns out that these states can already exhibit superadditivity even when the collective observables are taken to be simple von Neumann measurements: i.e., by taking $E_k = |e_k\rangle\langle e_k|$ where the $|e_k\rangle$ are four orthonormal vectors. Taking p_i to be a probability distribution on the effective alphabet states, we must attempt to maximize the rate

$$\begin{aligned} R = \quad & H_{\rm E}(\rho) - p_a H_{\rm E}(|a\rangle) - p_b H_{\rm E}(|b\rangle) - p_c H_{\rm E}(|c\rangle) \\ & - p_d H_{\rm E}(|d\rangle) \qquad (14.15) \end{aligned}$$

with

$$\rho = p_a|a\rangle\langle a| + p_b|b\rangle\langle b| + p_c|c\rangle\langle c| + p_d|d\rangle\langle d|\ , \qquad (14.16)$$

$$H_{\rm E}(\rho) = -\sum_k \langle e_k|\rho|e_k\rangle \log\langle e_k|\rho|e_k\rangle\ , \qquad (14.17)$$

and

$$H_{\rm E}(|a\rangle) = -\sum_k |\langle e_k|a\rangle|^2 \log|\langle e_k|a\rangle|^2 \qquad (14.18)$$

and likewise for $|b\rangle$, $|c\rangle$, and $|d\rangle$. The rate R_2 we will be interested in is then

$$R_2 = \frac{1}{2} \max_{p_i} \max_{|e_k\rangle} R\ . \tag{14.19}$$

We have thoroughly studied R_2 numerically with a steepest descent and simulated annealing technique. As one might guess, the optimal solution to Equation (14.19)—for sufficiently small angles ($\gamma \lesssim 19^\circ$)—appears to obey the following symmetries

$$\begin{aligned} p_d &\rightarrow 0, \\ p_a &= p_b \equiv p, \\ p_c &\equiv 1 - 2p. \end{aligned} \tag{14.20}$$

Therefore we make the following *Ansatz* (see Figure 14.1)

$$\begin{aligned} \langle c|e_3\rangle &= \cos\eta \\ \langle a|e_1\rangle &= \langle b|e_2\rangle \\ \langle a|e_3\rangle &= \langle b|e_3\rangle \\ \langle c|e_1\rangle &= \langle c|e_2\rangle \end{aligned} \tag{14.21}$$

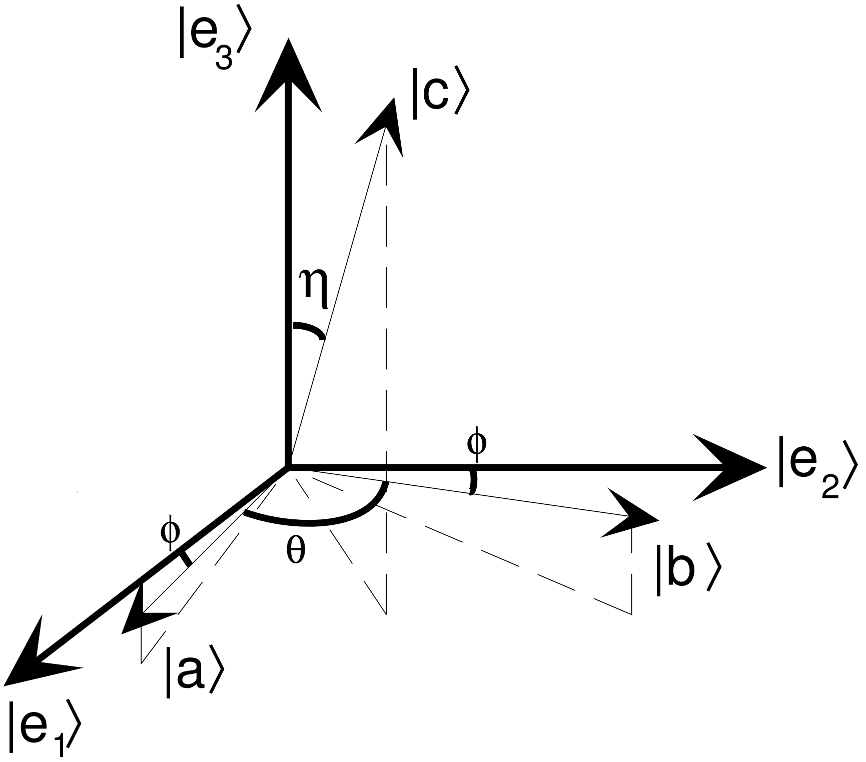
$|e_3\rangle$
$|c\rangle$
η
ϕ
$|e_2\rangle$
ϕ
θ
$|b\rangle$
$|a\rangle$
$|e_1\rangle$

Figure 14.1: Effective Alphabet Projection
The effective alphabet for our implementation represented in an orthogonal measurement basis. The projections are in the $|e_1\rangle$,$|e_2\rangle$ plane.

14.4 Measurement Basis and Limit for R_2

Taking these symmetries as a more analytic starting point, we can expand the measurement basis as a function of η, γ, and the alphabet states (see Figure 14.1):

$$\begin{aligned}
|e_1\rangle = \quad & \frac{\cos\eta + 1}{2\sin\gamma}|a\rangle + \frac{\cos\eta - 1}{2\sin\gamma}|b\rangle \\
& + \frac{\sqrt{2}\sin\eta\sin\gamma - 2\cos\eta\cos\gamma}{2\sin\gamma}|c\rangle \\
|e_2\rangle = \quad & \frac{\cos\eta - 1}{2\sin\gamma}|a\rangle + \frac{\cos\eta + 1}{2\sin\gamma}|b\rangle \\
& + \frac{\sqrt{2}\sin\eta\sin\gamma - 2\cos\eta\cos\gamma}{2\sin\gamma}|c\rangle \\
|e_3\rangle = \quad & -\frac{\sqrt{2}\sin\eta}{2\sin\gamma}|a\rangle - \frac{\sqrt{2}\sin\eta}{2\sin\gamma}|b\rangle \\
& + \frac{\sqrt{2}\sin\eta\cos\gamma + \cos\eta\sin\gamma}{\sin\gamma}|c\rangle
\end{aligned} \tag{14.22}$$

Thus the rate can now be expressed as

$$R_2(\gamma) = \max_{\eta,p} R(\eta, p, \gamma) \tag{14.23}$$

Even with these strong assumptions and simplifications, $R_2(\gamma)$ does not yield a simple analytic expression. We must instead content ourselves with a numerical study as depicted in Figure 14.2. Note in particular that as $\gamma \to 0$ the superadditivity does not dwindle away:

$$\lim_{\gamma\to 0} \frac{R_2(\gamma)}{C_1(\gamma)} \quad \longrightarrow \quad 1.02818\ . \tag{14.24}$$

This contrasts with the rate R_3 exhibited by Sasaki *et al.* [107, 108, 109] for which the ratio R_3/C_1 goes to one within the very weak signal regime.

Note that we use the notation R_2 rather than C_2 because our favored quantity can only be asserted as a *lower bound* to the two-shot capacity. The symmetry assumptions on the probabilities along with the specialization to symmetric von Neumann measurements could turn out to be overly restrictive. However, further numerical investigations seem to indicate that any further improvement is likely to be very

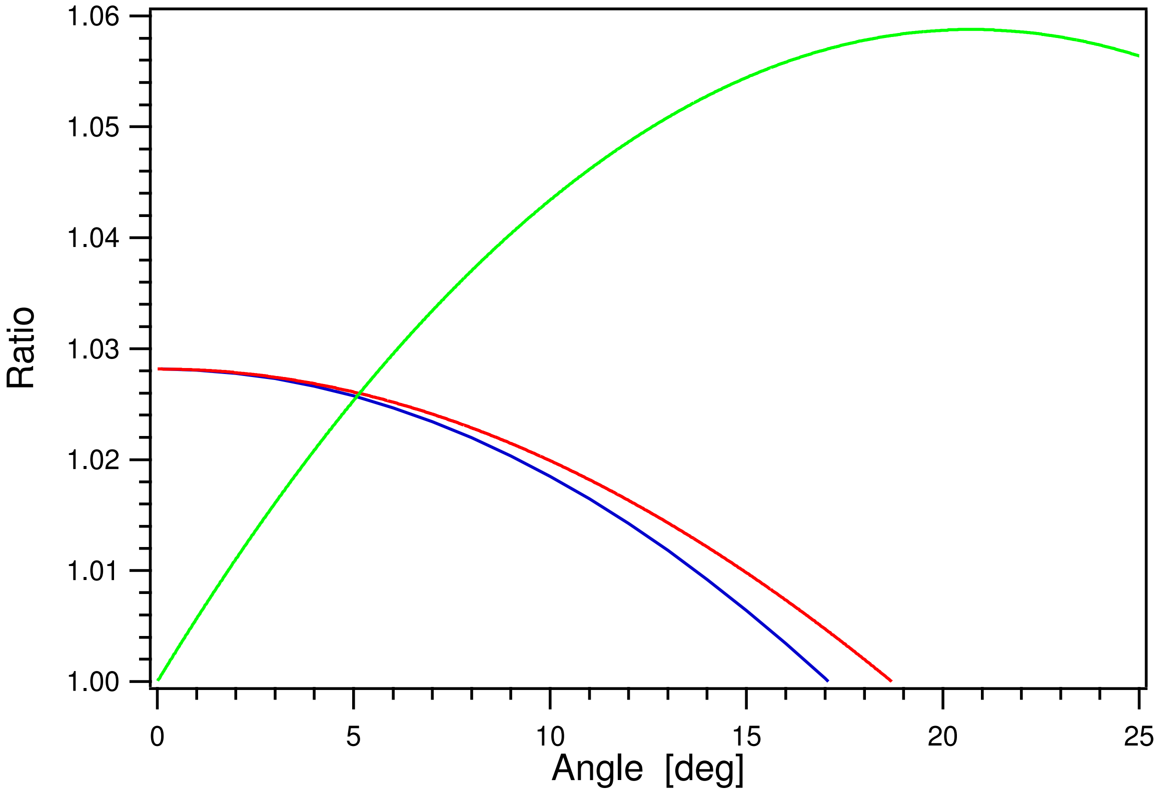

Figure 14.2: Comparison of Superadditivity
The red line represents the ratio R_2/C_1 as a function of γ. The blue line represents the ratio obtained using the experimentally feasible but nonoptimal basis discussed in Section III. The green line represents R_3/C_1 obtained by Sasaki *et al.* in References [107, 108, 109].

small [116]. Also we should emphasize that demonstrating that $R_2 > C_1$ does not give an automatic means for finding a code that comes within ϵ of this rate: the channel capacity theorem Equation (14.3) is only an existence proof of such a code. However, the noise model that our alphabet and measurement leads to—i.e., a simple stochastic transition diagram on three letters—has been extensively studied in classical information-theory literature, and good codes for this problem are likely to exist.

Finally, let us mention one more quantification of the superadditivity due to our nonorthogonal alphabet; this is the simple difference between the two-shot rate and

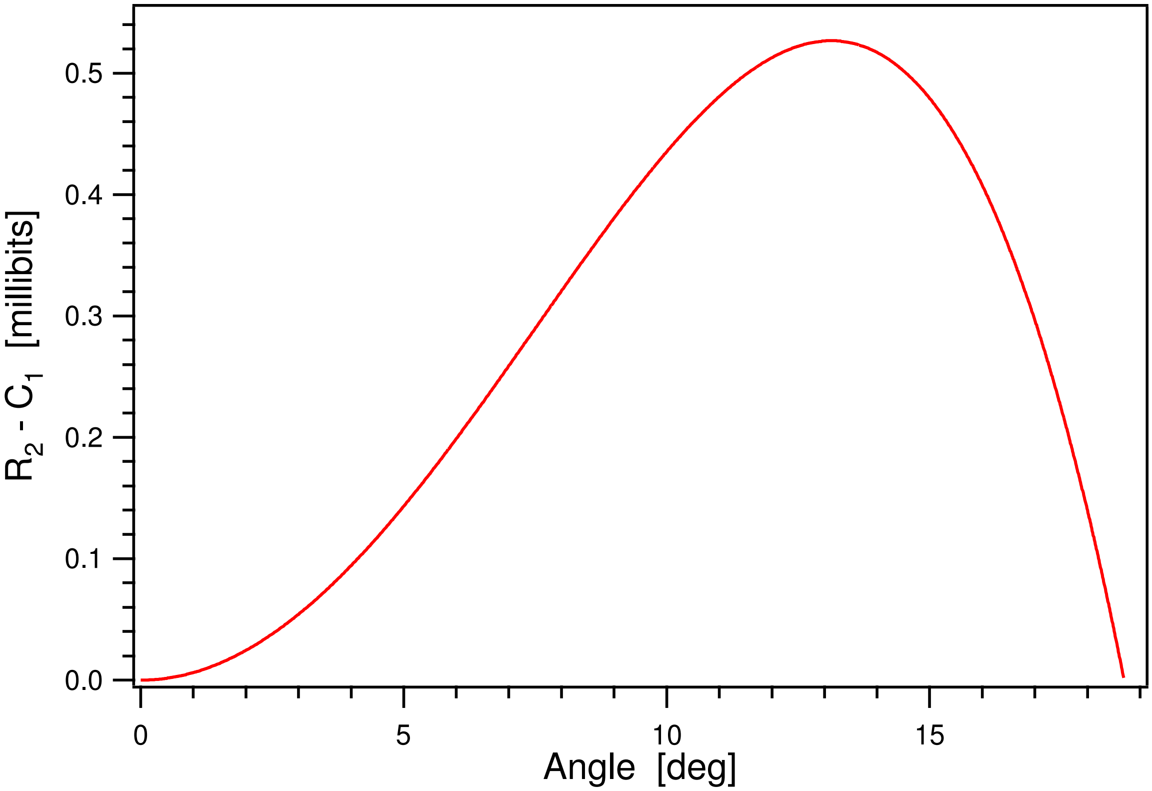

Figure 14.3: Difference in Communication Rates $(R_2 - C_1)$
The difference in rates $R_2 - C_1$ as a function of the angle γ.

the one-shot rate. We plot $R_2 - C_1$ in Figure 14.3. It has been suggested in Ref. [103] that the differences $C_n - C_1$ can help define various notions of when two quantum states are most "quantum" with respect to each other (and hence least "classical"). When one goes to the limit $C_\infty - C_1$ one finds a well-behaved notion: two states are most quantum with respect to each other when they are 45° apart. Figure 14.3 seems to indicate that $R_2 - C_1$ plays no such simple role: at the very least, it means that this difference does a poor job of ferreting out the quantumness of two states in the geometrical sense already supplied by Hilbert space.

Chapter 15

Experimental Proposal for Achieving Superadditivity

15.1 Basis for Experiment

Let us now focus on the case we are most interested in for our experimental proposal: two very low photon-number coherent states $|\alpha\rangle$ and $|-\alpha\rangle$ of a particular field mode. We choose α real so that the mean photon number in that mode is α^2. For the angles for which we demonstrated superadditivity, i.e., $\gamma \lesssim 19^\circ$, this translates to a mean photon number less than 0.03 in each transmission. In this case, we are well warranted in making the approximation

$$\begin{aligned} |\psi_0\rangle &= |\alpha\rangle \cong \frac{1}{\sqrt{1+\alpha^2}}|0\rangle + \frac{\alpha}{\sqrt{1+\alpha^2}}|1\rangle \\ |\psi_1\rangle &= |-\alpha\rangle \cong \frac{1}{\sqrt{1+\alpha^2}}|0\rangle - \frac{\alpha}{\sqrt{1+\alpha^2}}|1\rangle \ , \end{aligned} \tag{15.1}$$

where $|0\rangle$ and $|1\rangle$ denote the zero- and single-photon states of the mode, respectively. Moreover, we have

$$\alpha \cong \sqrt{\frac{1-\cos\gamma}{1+\cos\gamma}}\ . \tag{15.2}$$

In order to keep track of the separate transmissions, we encode each transmission in a different mode. For our purposes it is convenient to choose two orthogonal circular polarizations.

Expanding the measurement basis in terms of the photon number states, we thus have

$$\begin{aligned} |e_1\rangle = \quad & \frac{\sqrt{2}\sin\eta + 2\alpha\cos\eta}{2(1+\alpha^2)}|0\rangle_+|0\rangle_- \\ & + \frac{\alpha\sqrt{2}\sin\eta - \cos\eta + \alpha^2\cos\eta - 1 - \alpha^2}{2(1+\alpha^2)}|0\rangle_+|1\rangle_- \\ & + \frac{\alpha\sqrt{2}\sin\eta - \cos\eta + \alpha^2\cos\eta + 1 + \alpha^2}{2(1+\alpha^2)}|1\rangle_+|0\rangle_- \\ & + \frac{\alpha^2\sqrt{2}\sin\eta - 2\alpha\cos\eta}{2(1+\alpha^2)}|1\rangle_+|1\rangle_- \end{aligned} \tag{15.3}$$

$$\begin{aligned} |e_2\rangle = \quad & \frac{\sqrt{2}\sin\eta + 2\alpha\cos\eta}{2(1+\alpha^2)}|0\rangle_+|0\rangle_- \\ & + \frac{\alpha\sqrt{2}\sin\eta - \cos\eta + \alpha^2\cos\eta + 1 + \alpha^2}{2(1+\alpha^2)}|0\rangle_+|1\rangle_- \\ & + \frac{\alpha\sqrt{2}\sin\eta - \cos\eta + \alpha^2\cos\eta - 1 - \alpha^2}{2(1+\alpha^2)}|1\rangle_+|0\rangle_- \\ & + \frac{\alpha^2\sqrt{2}\sin\eta - 2\alpha\cos\eta}{2(1+\alpha^2)}|1\rangle_+|1\rangle_- \end{aligned} \tag{15.4}$$

$$\begin{aligned} |e_3\rangle = \quad & \frac{\cos\eta - \alpha\sqrt{2}\sin\eta}{(1+\alpha^2)}|0\rangle_+|0\rangle_- \\ & + \frac{\sqrt{2}\sin\eta(1-\alpha^2) + 2\alpha\cos\eta}{2(1+\alpha^2)}|0\rangle_+|1\rangle_- \\ & + \frac{\sqrt{2}\sin\eta(1-\alpha^2) + 2\alpha\cos\eta}{2(1+\alpha^2)}|1\rangle_+|0\rangle_- \\ & + \frac{\alpha\sqrt{2}\sin\eta + \alpha^2\cos\eta}{(1+\alpha^2)}|1\rangle_+|1\rangle_- \end{aligned} \tag{15.5}$$

The $+$ and $-$ subscripts in these equations refer to righthand and lefthand circularly polarized light, respectively.

The measurement basis above is, of course, orthonormal. However, after optimizing over η as in the previous section, one finds that the coefficient of each $|1\rangle_+|1\rangle_-$ component turns out to be of order α while the other terms are of order one. Because one is free to choose any measurement basis, we choose to ignore the small $|1\rangle_+|1\rangle_-$ term for each $|e_i\rangle$. This new basis $|\tilde{e}_i\rangle$ is close to the optimal basis $|e_i\rangle$ but allows the great simplification of not having to worry about how to distinguish $|1\rangle_+|1\rangle_-$ from $|0\rangle_+|1\rangle_-$ and $|1\rangle_+|0\rangle_-$. We may then focus on experiments based on the absorption of at most a single photon.

The final step for defining our measurement scheme is to re-orthogonalize the vectors $|\tilde{e}_i\rangle$. A simple convenient technique for this is the one introduced in Ref. [117]. Let

$$M = \sum_{i=1}^{3} |\tilde{e}_i\rangle\langle\tilde{e}_i| \, . \tag{15.6}$$

Then clearly the vectors

$$|e_i'\rangle = M^{-\frac{1}{2}}|\tilde{e}_i\rangle \tag{15.7}$$

form an orthonormal set. It is this basis that we will use in the experimental proposal, the main point of interest about it being that it contains no two-photon contributions. Of course, the new basis cannot be optimal for achieving the rate R_2 already calculated, but for small α it becomes arbitrarily good. In fact, it is already sufficient for demonstrating superadditivity for $\gamma \lesssim 17^\circ$ (see Figure 14.2).

15.2 Experimental Protocol

We now turn to the task of realizing the measurement explored in the last section. To carry this out, we need the ability to perform an entangled measurement on two wave packets at a time. We can achieve this collective decoding by mapping the orthonormal measurement basis in Equation (15.7) onto a set of orthonormal superpositions of three sublevels of a single atom (see Figure 15.1). Note that only two levels would be required to perform the optimal (unentangled) measurement to distinguish $|\alpha\rangle$ and $|-\alpha\rangle$ [118].

The basic idea is to first transfer the information from the propagating light fields to photons inside an optical cavity and subsequently map the information from the cavity field to a single atom inside that cavity. In order to make sure the photon wavepacket enters the cavity, rather than being reflected off the cavity mirror, we make use of the adiabatic passage scheme of [119, 120]. This means that the laser fields

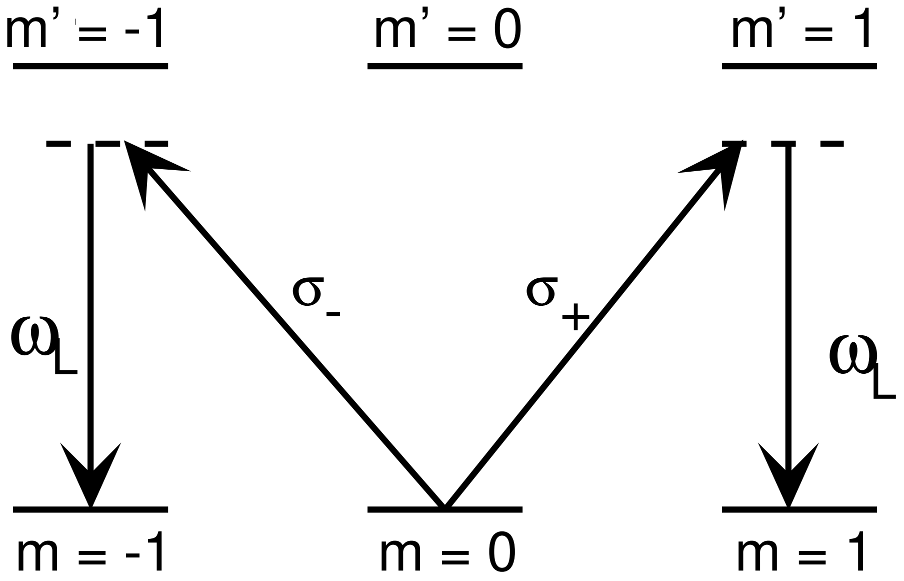

Figure 15.1: Transition Diagram for Experimental Implementation
Transition diagram for our implementation: a π-polarized laser field with frequency ω_L is applied to a single atom inside an optical cavity. The laser will induce a Raman transition from the initial state $|m = 0\rangle$ to $|m = +1\rangle$ or $|m = -1\rangle$ in the presence of a single σ^+ or σ^- polarized cavity photon, with frequency $\omega_C = \omega_L$. No transition is induced in the absence of a cavity photon, as the $m = 0 \leftrightarrow m' = 0$ transition is forbidden. Note that π-polarized modes are not supported by the cavity.

taking care of the mapping process (for details see below) actually have to be turned on *before* the wavepacket arrives at the cavity. Alternatively, one might consider the scheme of [8] using symmetric photon wavepackets. However, this relies on the ability to maintain symmetric wavepackets, which is impractical for long distance communication.

15.2.1 Mapping the Photon States to an Atom

The mapping is then accomplished as follows: First, the atom is prepared in a ground state with $|m = 0\rangle$ by optical pumping. The presence of a single σ^+ polarized cavity photon is then more than sufficient to induce a Raman transition to the $|m = 1\rangle$ state with the help of a π-polarized laser field (in fact, the advances in cavity QED have increased the atom-cavity coupling to such a large degree that the saturation photon number for optical transitions is very small [77]; in particular, for the $(6S_{\frac{1}{2}}, F = 4, m = 4) \rightarrow (6P_{\frac{3}{2}}, F = 5, m = 5)$ transition in Cesium it is only 2.3×10^{-4} [33]). Similarly, the presence of a single σ^- photon will induce the transition to $|m = -1\rangle$, while if no cavity photon is present, the atom will stay in $|m = 0\rangle$. Thus, the measurement scheme is based on the mapping

$$\begin{aligned} |0\rangle_+|0\rangle_-|m=0\rangle &\longmapsto |0\rangle_+|0\rangle_-|m=0\rangle, \\ |0\rangle_+|1\rangle_-|m=0\rangle &\longmapsto |0\rangle_+|0\rangle_-|m=-1\rangle, \\ |1\rangle_+|0\rangle_-|m=0\rangle &\longmapsto |0\rangle_+|0\rangle_-|m=+1\rangle. \end{aligned} \tag{15.8}$$

This mapping must be executed within the cavity lifetime (a typical lifetime for high-finesse optical cavities is $\kappa^{-1} \sim 0.1\ \mu$s [121]). Once this mapping has been performed, we no longer rely on cavity fields.

In order to avoid any disturbing effects from the laser field on level $|m = 0\rangle$ in the absence of a cavity photon, we require the transition $|m = 0\rangle \mapsto |m' = 0\rangle$ to be forbidden, which is easily accomplished by choosing $\delta F = 0$ transitions. For example, one might consider the following transition between hyperfine multiplets in Cesium

$$6S_{\frac{1}{2}}, F = 3 \quad \longleftrightarrow \quad 6P_{\frac{1}{2}}, F = 3. \tag{15.9}$$

Moreover, the frequency ω_L of the laser field is chosen such that we are on two-photon resonance with the $|m = 0\rangle \leftrightarrow |m = \pm 1\rangle$ Raman transitions, but far off resonance with respect to the excited states. Therefore, the latter will not be populated and no further transitions from $|m = 1\rangle$ or $|m = -1\rangle$ will occur.

15.2.2 Transforming the Measurement Basis

Once the information has thus been transferred from the polarizations to the atom in the cavity, the measurement basis is an orthonormal *superposition* of the three relevant atomic ground states $|m = -1\rangle$, $|m = 0\rangle$, and $|m = 1\rangle$. Making a measurement of a superposition of these states is far more difficult than measuring the states themselves. Therefore, we first apply a unitary operation that transforms the basis of Equation (15.7) into the physical measurement basis. This operation can be performed by a series of at most 16 appropriately timed Raman pulses [122, 123]. In general, for an N level system, with N even, the unitary evolution can be controlled with a sequence of N^2 pulses consisting of two distinct perturbations in an alternating sequence [123]. While this scheme is not optimal for $N = 3$, it does give an upper bound for the required number of pulses.

15.2.3 Measuring the Projection in the Physical Basis

Once this transformation of basis has been performed, the only remaining task is to measure the projection onto each of the three possible hyperfine levels of our physical measurement basis. To perform this measurement, a magnetic field is turned on adiabatically, causing a splitting of the energy of these otherwise degenerate hyperfine levels. Next, we use the technique of optical shelving to make a measurement of the levels [110, 111, 112]. With this technique, a Raman pulse is applied to cause a transition from the $|m = 1\rangle$ state into a secondary state that can then be driven on resonance to yield a large number of photons. If the atom fluoresces at the driven frequency, the measurement outcome is $m = 1$, and the measurement is finished. Otherwise, if no fluorescence is detected, the atom will not be affected by this driving laser and the process is then repeated for the $|m = 0\rangle$ and $|m = -1\rangle$ states.

At the time the work for our paper was done [21], atoms could only be held in a cavity for times exceeding 250μs [121], which was nearly sufficient for the measurements and laser manipulations discussed to be performed. Now as discussed earlier in this thesis, we are able to hold atoms for approximately 3 seconds. This improvement has greatly relaxed the conditions on timing necessary to carry out the manipulations needed to demonstrate superadditivity. Therefore, the ability to hold single atoms in a cavity for a sufficient period of time will open up a world of possibilities for the field of communication [8, 124, 125].

Bibliography

[1] E. T. Jaynes and F. W. Cummings. *Proc. IEEE*, **51**:89, (1963).

[2] J. Ye, D. W. Vernooy, and H. J. Kimble. *Phys. Rev. Lett.*, **83**:4987, (1999).

[3] For a review, see contributions in the special issue of Phys. Scr. **T76**, 127 (1998).

[4] J. McKeever, J. R. Buck, A. D. Boozer, A. Kuzmich, H.-C. Nägerl, D. M. Stamper-Kurn, and H. J. Kimble. *Phys. Rev. Lett.*, **90**:133602, (2003).

[5] C. J. Hood, T. W. Lynn, A. C. Doherty, A. S. Parkins, and H. J. Kimble. *Science*, **287**:1457, (2000).

[6] T. W. H. Pinkse, T. Fischer, P. Maunz, and G. Rempe. *Nature*, **404**:365, (2000).

[7] T. Pellizzari, S. A. Gardiner, J. I. Cirac, and P. Zoller. *Phys. Rev. Lett.*, **75**:3788, (1995).

[8] J. I. Cirac, P. Zoller, H. J. Kimble, and H. Mabuchi. *Phys. Rev. Lett.*, **78**:3221, (1997).

[9] S. J. van Enk, J. I. Cirac, and P. Zoller. *Fortschr. Phys.*, **46**:689, (1998).

[10] C. Cabrillo, J. I. Cirac, P. Garcia-Fernandez, and P. Zoller. *Phys. Rev. A*, **59**:1025, (1999).

[11] S. Bose, P. L. Knight, M. B. Plenio, and V. Vedral. *Phys. Rev. Lett.*, **83**:5158, (1999).

[12] A. S. Parkins and H. J. Kimble. *Journal Opt. B: Quantum Semiclass. Opt.*, **1**:496, (1999).

[13] H. J. Kimble *et al. Laser Spectroscopy XIV*, page 80. World Scientific, Singapore, (1999).

[14] H. Katori, T. Ido, and M. Kuwata-Gonokami. *J. Phys. Soc. Jpn.*, **68**:2479, (1999).

[15] T. Ido, Y. Isoya, and H. Katori. *Phys. Rev. A*, **61**:061403, (2000).

[16] S. J. van Enk, J. McKeever, H. J. Kimble, and J. Ye. *Phys. Rev. A*, **64**:013407, (2001).

[17] M. L. Gorodetsky, A. A. Savchenkov, and V. S. Ilchenko. *Opt. Lett.*, **21**:453, (1996).

[18] D. W. Vernooy, V. S. Ilchenko, H. Mabuchi, E. W. Streed, and H. J. Kimble. *Opt. Lett.*, **23**:247, (1998).

[19] D. W. Vernooy and H. J. Kimble. *Phys. Rev. A*, **55**:1239, (1997).

[20] D. W. Vernooy, A. Furusawa, N. Ph. Georgiades, V. S. Ilchenko, and H. J. Kimble. *Phys. Rev. A*, **57**:R2293, (1998).

[21] J. R. Buck, S. J. van Enk, and C. A. Fuchs. *Phys. Rev. A*, **61**:032309, (2000).

[22] K. G. Libbrecht and J. L. Hall. *Rev. Sci. Instr.*, **64**:2133, (1993).

[23] C. C. Bradley, J. Chen, and R. G. Hulet. *Rev. Sci. Instr.*, **61**:2097, (1990).

[24] J. R. Buck and H. J. Kimble. *Phys. Rev. A*, **67**:033806, (2003).

[25] P. R. Saulson. *Phys. Rev. D*, **42**(8):2437, (1990).

[26] P. A. M. Dirac. *Proc. Roy. Soc. A*, **114**:243, (1927).

[27] M. O. Scully and M. S. Zubairy. *Quantum Optics.* Cambridge University Press, United Kingdom, (1997).

[28] P. W. Milonni. *The Quantum Vacuum.* Academic Press, San Diego, (1994).

[29] C. Cohen-Tannoudji, B. Diu, and F. Laloe. *Quantum Mechanics.* John Wiley & Sons, New York, (1977).

[30] R. J. Thompson, G. Rempe, and H. J. Kimble. *Phys. Rev. Lett.*, **68**:1132, (1992).

[31] Q. A. Turchette, C. J. Hood, W. Lange, H. Mabuchi, and H. J. Kimble. *Phys. Rev. Lett.*, **75**:4710, (1995).

[32] H. Mabuchi, Q. A. Turchette, M. S. Chapman, and H. J. Kimble. *Opt. Lett.*, **21**:1393, (1996).

[33] C. J. Hood, M. S. Chapman, T. W. Lynn, and H. J. Kimble. *Phys. Rev. Lett.*, **80**:4157, (1998).

[34] C. J. Hood, J. Ye, and H. J. Kimble. *Phys. Rev. A*, **64**:033804, (2001).

[35] C. J. Hood. *Real-time Measurement and Trapping of Single Atoms by Single Photons.* Phd thesis, California Institute of Technology, Pasadena, CA, 2000.

[36] H. J. Metcalf and P. van der Straten. *Laser Cooling and Trapping.* Springer-Verlag, New York, (1999).

[37] H. J. Kimble. *Phil. Trans. R. Soc. Lond. A*, **355**:2327, (1997).

[38] L. A. Orozco, H. J. Kimble, A. T. Rosenberger, L. A. Lugiato, M. L. Asquini, M. Brambilla, and L. M. Narducci. *Phys. Rev. A*, **39**:1235, (1989).

[39] G. R. Guthohrlein, M. Keller, K. Hayasaka, W. Lange, and H. Walther. *Nature*, **414**:49, (2001).

[40] J. Eschner, Ch. Raab, F. Schmidt-Kaler, and R. Blatt. *Nature*, **413**:495, (2001).

[41] A. E. Siegman. *Lasers.* University Science Books, Sausalito, California, (1986).

[42] D. W. Vernooy. *Cold Atoms in Cavity QED for Quantum Information Processing.* Phd thesis, California Institute of Technology, Pasadena, CA, 2000.

[43] C. Monroe, W. Swann, H. Robinson, and C. Wieman. *Phys. Rev. Lett.*, **65**:1571, (1990).

[44] J. Dalibard and C. Cohen-Tannoudji. *J. Opt. Soc. Am. B*, **6**:2023, (1989).

[45] G. Nienhuis, P. van der Straten, and S-Q. Shang. *Phys. Rev. A*, **44**:462, (1991).

[46] R. Grimm, M. Weidemller, and Yu. B. Ovchinnikov. *Adv. At. Mol. Opt. Phys.*, **42**:95, (2000).

[47] J. P. Gordon and A. Ashkin. *Phys. Rev. A*, **21**:1606, (1980).

[48] J. D. Miller, R. A. Cline, and D. J. Heinzen. *Phys. Rev. A*, **47**:R4567, (1993).

[49] J. Dalibard and C. Cohen-Tannoudji. *J. Opt. Soc. Am. B*, **2**:1707, (1985).

[50] I. H. Deutsch and P. S. Jessen. *Phys. Rev. A*, **57**:1972, (1998).

[51] D. Cho. *J. Korean Phys. Soc.*, **30**(2):373, (1997).

[52] K. L. Corwin, S. J. M. Kuppens, D. Cho, and C. E. Wieman. *Phys. Rev. Lett.*, **83**:1311, (1999).

[53] M. Fabry and J. R. Cussenot. *Can. J. Phys.*, **54**:836, (1976).

[54] T. A. Savard, K. M. O'Hara, and J. E. Thomas. *Phys. Rev. A*, **56**:R1095, (1997).

[55] C. W. Gardiner, J. Ye, H. C. Nagerl, and H. J. Kimble. *Phys. Rev. A*, **61**:045801, (2000).

[56] H. J. Kimble. *Physica Scripta*, **T76**:127, (1998).

[57] J. McKeever and H. J. Kimble. *Laser Spectroscopy XIV*. World Scientific, (2002).

[58] A. Kuhn, M. Hennrich, and G. Rempe. *Phys. Rev. Lett.*, **89**:067901, (2002).

[59] D. Boiron, A. Michaud, P. Lemonde, Y. Castin, C. Salomon, S. Weyers, K. Szymaniec, L. Cognet, and A. Clairon. *Phys. Rev. A*, **53**:R3734, (1996).

[60] V. B. Braginsky and V. S. Ilchenko. *Sov. Phys. Dokl.*, **32**:307, (1987).

[61] H. Mabuchi and H. J. Kimble. *Opt. Lett.*, **19**:749, (1994).

[62] M. L. Gorodetsky and V. S. Ilchenko. *Opt. Commun.*, **113**:133, (1994).

[63] F. Treussart, J. Hare, L. Collot, V. Lefèvre-Seguin, D. S. Weiss, V. Sandoghdar, J. M. Raimond, and S. Haroche. *Opt. Lett.*, **19**:1651, (1994).

[64] J. C. Knight, N. Dubreuil, V. Sandoghar, J. Hare, V. Lefèvre-Seguin, J. M. Raimond, and S. Haroche. *Opt. Lett.*, **20**:1515, (1995).

[65] J. C. Knight, N. Dubreuil, V. Sandoghar, J. Hare, V. Lefèvre-Seguin, J. M. Raimond, and S. Haroche. *Opt. Lett.*, **21**:698, (1996).

[66] W. Jhe and J. W. Kim. *Phys. Rev. A*, **51**:1150, (1995).

[67] H. Chew. *J. Chem. Phys.*, **87**:1355, (1987).

[68] V. V. Klimov and V. S. Letokhov. *Opt. Commun.*, **122**:155, (1996).

[69] V. V. Klimov, M. Ducloy, and V. S. Letokhov. *J. Mod. Opt.*, **43**:549, (1996).

[70] W. Klitzing, R. Long, V. S. Ilchenko, J. Hare, and V. Lefvre-Seguin. *New J. of Phys.*, **3**:14, (2001).

[71] M. M. Mazumder, D. Q. Chowdhury, S. C. Hill, and R. K. Chang. *Optical Processes in Microcavities*, volume 3. World Scientific, Singapore, (1996).

[72] A. J. Campillo, J. D. Eversole, and H-B. Lin. *Optical Processes in Microcavities*, volume 3. World Scientific, Singapore, (1996).

[73] R. E. Slusher and U. Mohideen. *Optical Processes in Microcavities*, volume **3**. World Scientific, Singapore, (1996).

[74] A. B. Matsko, S. P. Vyatchanin, H. J. Kimble, and H. Mabuchi. *Phys. Lett. A*, **192**:175, (1994).

[75] D. J. Norris, M. Kuwata-Gonokami, and W. E. Moerner. *Appl. Phys. Lett.*, **71**:297, (1997).

[76] X. Fan, A. Doran, and H. Wang. *Appl. Phys. Lett.*, **73**:3190, (1998).

[77] H. J. Kimble. *Cavity Quantum Electrodynamics.* Academic Press, San Diego, (1994).

[78] J. A. Stratton. *Electromagnetic Theory.* McGraw Hill, New York, (1997).

[79] R. D. Richtmyer. *Journ. Appl. Phys.*, **10**:391, (1939).

[80] M. Bass, editor. *Handbook of Optics*, volume II, chapter 33, page 63. McGraw Hill, New York, 2 edition, (1995).

[81] C. Lin. *Handbook of Microwave and Optical Components.* Wiley, New York, (1991).

[82] V. V. Datsyuk. *Appl. Phys. B*, **54**:184, (1992).

[83] H-B. Lin, J. D. Eversole, and A. J. Campillo. *Optics Comm.*, **77**:407, (1990).

[84] M. L. Gorodetsky and V. S. Ilchenko. *J. Opt. Soc. Am. B*, **16**:147, (1999).

[85] A. Abramovici, W. E. Althouse, R. W. P. Drever, Y. Gursel, S. Kawamura, F. J. Raab, D. Shoemaker, L. Sievers, R. E. Spero, K. S. Thorne, R .E. Vogt, R. Weiss, S. E. Whitcomb, and M. E. Zucker. *Science*, **256**:325, (1992).

[86] A. Gillespie and F. Raab. *Phys. Rev. D*, **52**(2):577, (1995).

[87] Y. Hadjar, P. F. Cohadon, C. G. Aminoff, M. Pinard, and A. Heidmann. *Europhys. Lett.*, **47**(5):545, (1999).

[88] J. R. Hutchinson. *J. Appl. Mech.*, **47**:901, (1980).

[89] J. R. Hutchinson and S. D. Zillmer. *J. Appl. Mech.*, **50**:123, (1983).

[90] P. G. Young and S. M. Dickinson. *Transactions of the ASME*, **62**:706, (1995).

[91] J. R. Hutchinson. *J. Appl. Mech.*, **51**:581, (1984).

[92] R. G. Leisure and F. A. Willis. *J. Phys.: Condens. Matter*, **9**:6001, (1997).

[93] L. E. Kinsler, A. R. Frey, A. B. Coppens, and J. V. Sanders. *Fundamentals of Acoustics.* John Wiley & Sons, New York, (1982).

[94] J. S. Rao. *Advanced Theory of Vibration.* John Wiley & Sons, New York, (1992).

[95] M. Bass, editor. *Handbook of Optics*, volume II, chapter 33, page 50. McGraw Hill, New York, 2 edition, (1995).

[96] C. M. Caves and P. D. Drummond. *Rev. Mod. Phys.*, **66**:481, (1994).

[97] A. S. Kholevo. *Prob. Inf. Transm.*, **9**:110, (1973).

[98] T. M. Cover and J. A. Thomas. *Elements of Information Theory.* John Wiley & Sons, New York, (1991).

[99] A. S. Kholevo. *Rep. Math. Phys.*, **12**:273, (1977).

[100] A. S. Kholevo. *Prob. Inf. Transm.*, **15**:247, (1979).

[101] A. Peres and W. K. Wootters. *Phys. Rev. Lett.*, **66**:1119, (1991).

[102] C. H. Bennett, D. P. DiVincenzo, C. A. Fuchs, T. Mor, E. Rains, P. W. Shor, J. A. Smolin, and W. K. Wootters. *Phys. Rev. A*, **59**:1070, (1999).

[103] C. A. Fuchs. *Quantum Communication, Computing, and Measurement 2.* Plenum Press, New York, (1998).

[104] P. Hausladen, R. Jozsa, B. Schumacher, M. Westmoreland, and W. K. Wootters. *Phys. Rev. A*, **54**:1869, (1996).

[105] A. S. Holevo. *IEEE Trans. Inf. Theor.*, **44**(1):269, (1998).

[106] B. Schumacher and M. D. Westmoreland. *Phys. Rev. A*, **56**:131, (1997).

[107] M. Sasaki, K. Kato, M. Izutsu, and O. Hirota. *Phys. Lett. A*, **236**:1, (1997).

[108] M. Sasaki, K. Kato, M. Izutsu, and O. Hirota. *Phys. Rev. A*, **58**:146, (1998).

[109] M. Sasaki, T. Sasaki-Usuda, M. Izutsu, and O. Hirota. *Phys. Rev. A*, **58**:159, (1998).

[110] W. Nagourney, J. Sandberg, and H. G. Dehmelt. *Phys. Rev. Lett.*, **56**:2797, (1986).

[111] Th. Sauter, W. Neuhauser, R. Blatt, and P. E. Toschek. *Phys. Rev. Lett.*, **57**:1696, (1986).

[112] J. C. Bergquist, R. G. Hulet, W. M. Itano, and D. J. Wineland. *Phys. Rev. Lett.*, **57**:1699, (1986).

[113] A. Peres. *Quantum Theory: Concepts and Methods.* Kluwer Academic, Dordrecht, (1993).

[114] L. B. Levitin. *Quantum Communications and Measurement.* Plenum Press, New York, (1995).

[115] C. A. Fuchs and C. M. Caves. *Phys. Rev. Lett.*, **73**:3047, (1994).

[116] J. A. Smolin. Private communication.

[117] L. P. Hughston, R. Jozsa, and W. K. Wootters. *Phys. Lett. A*, **183**:14, (1993).

[118] M. Sasaki, T. S. Usuda, O. Hirota, and A. S. Holevo. *Phys. Rev. A*, **53**:1273, (1996).

[119] T. Pellizzari. *Phys. Rev. Lett.*, **79**:5242, (1997).

[120] S. J. van Enk, H. J. Kimble, J. I. Cirac, and P. Zoller. *Phys. Rev. A*, **59**:2659, (1999).

[121] H. Mabuchi, J. Ye, and H. J. Kimble. *Appl. Phys. B*, **68**:1095, (1999).

[122] C. K. Law and J. H. Eberly. *Opt. Expr.*, **2**(9):368, (1998).

[123] G. Harel and V. M. Akulin. *Phys. Rev. Lett.*, **82**:1, (1999).

[124] S. J. van Enk, J. I. Cirac, and P. Zoller. *Science*, **279**:205, (1998).

[125] S. J. van Enk, J. I. Cirac, and P. Zoller. *Phys. Rev. Lett.*, **78**:4293, (1997).